

**Molecular dynamics insights into nanovoid behavior in metals: from sparsely-arranged
nanovoids to densely-arranged nanopores**

by

Yi Cui

A thesis submitted in partial fulfillment of the requirements for the degree of

Doctor of Philosophy

Department of Mechanical Engineering
University of Alberta

© Yi Cui, 2017

Abstract

Atomistic-level study of void behavior in metallic materials is a difficult task for continuum-based methods. In contrast, MD method serves as an ideal tool for real-time computer simulation of all kinds of atomistic phenomena. More and more researchers become aware of this and a few have pioneered in the area of nanovoid simulation. Many problems were nicely addressed, yet not every stone has been turned. Particularly, we provided new understanding to the “shear impossibility” debate in light of our MD investigation. In this work, molecular dynamics simulation is applied to uncover mechanisms regarding the nucleation, growth and coalescence of nanovoids.

Molecular dynamics results are examined by using the “relative displacement” of atoms. In doing so, the homogenous elastic deformation has been excluded. The “relatively farthest-travelled” (RFT) atoms characterize the onset of interfacial debonding and void growth due to dislocation formation. Our results indicate that the initiation of interfacial debonding is due to the high surface stress in an initially dislocation-free matrix. Through this approach, we also justified the feasibility of void growth induced by shear loops/curves. At a smaller scale, the formation and emission of shear loops/curves contributes to the local mass transport. At a larger scale, a new mechanism of void growth via frustum-like dislocation structure is revealed. A phenomenological description of void growth via frustum-like dislocation structure is also proposed. As for the shape effect, the simulation results reveal that the initial void geometry has substantial impact on the stress response during void growth, especially for a specimen with a relatively large initial porosity. During void coalescence, the void shape combination is found more influential than the intervoid ligament distance (ILD) on the strength and damage development. The critical stress to trigger the dislocation emission is found in line with the

Lubarda model. The dislocation density calculated from simulation is qualitatively consistent with the experimental measurement. For densely-arranged pores, the diamond-array-pore sample exhibits a superior stress response at the same initial porosity. The onset of plasticity is investigated for differently-structured nanoporous samples, which could shed light on the novel designs of nanoporous structure with enhanced structural integrity.

Main contributions of this work can be summarized as follows. First, we show that the shape and the arrangement of nanovoids have a great impact on the mechanical performance of nanoporous metals. Secondly, the “relative displacement” is employed to visualize atom movement during interfacial debonding and dislocation formation. Thirdly, the “shear impossibility” debate is preliminarily settled. Fourthly, the Lubarda model for critical stress to trigger dislocation emission is extended to the case of nanoporous geometry.

Preface

A version of Chapter 2 of this thesis has been published as Cui, Y.; Chen, Z. Void initiation from interfacial debonding of spherical silicon particles inside a silicon-copper nanocomposite: A molecular dynamics study. *Modell. Simul. Mater. Sci. Eng.* 2017, 25, 025007. Dr. Chen was the supervisory author and was responsible for concept formation, checking results and revising the manuscript. I was responsible for conducting numerical simulations, data analysis, writing the manuscript and also contributed to concept formation.

A version of Chapter 3 of this thesis has been published as Cui, Y.; Chen, Z. Molecular dynamics modeling on the role of initial void geometry in a thin aluminum film under uniaxial tension. *Modell. Simul. Mater. Sci. Eng.* 2015, 23, 085011. Dr. Chen was the supervisory author and was responsible for concept formation, checking results and revising the manuscript. I was responsible for conducting numerical simulations, data analysis, writing the manuscript and also contributed to concept formation.

A version of Chapter 4 of this thesis is submitted as Cui, Y.; Chen, Z. Void growth via atomistic simulation: will the formation of shear loops still grow a void under different thermo-mechanical constraints? Dr. Chen was the supervisory author and was responsible for concept formation, checking results and revising the manuscript. I was responsible for conducting numerical simulations, data analysis, writing the manuscript and also contributed to concept formation.

A version of Chapter 5 of this thesis has been published as Cui, Y.; Chen, Z. Material transport via the emission of shear loops during void growth: A molecular dynamics study. *J. Appl. Phys.* 2016, 119, 225102. Dr. Chen was the supervisory author and was responsible for concept

formation, checking results and revising the manuscript. I was responsible for conducting numerical simulations, data analysis, writing the manuscript and also contributed to concept formation.

A version of Chapter 7 of this thesis has been published as Cui, Y.; Chen, Z. Molecular dynamics simulation of the influence of elliptical void interaction on the tensile behavior of aluminum. *Comput. Mater. Sci.* 2015, 108,103-113. Dr. Chen was the supervisory author and was responsible for concept formation, checking results and revising the manuscript. I was responsible for conducting numerical simulations, data analysis, writing the manuscript and also contributed to concept formation.

A version of Chapter 8 of this thesis is submitted as Cui, Y.; Chen, Z. Simulation of mechanical response of nanoporous FCC copper under compression with pores mimicking some crystalline arrays. Dr. Chen was the supervisory author and was responsible for concept formation, checking results and revising the manuscript. I was responsible for conducting numerical simulations, data analysis, writing the manuscript and also contributed to concept formation.

Acknowledgements

The most sincere appreciation and deepest gratitude goes to my supervisor, Dr. Zengtao Chen, for his critical insights, unwavering supports, enthusiasm and commitment to the highest levels of academic excellence over the past three years and beyond.

Special thanks to Dr. Tian Tang for the inspiring course along with those helpful discussions she offered, which helps deepen my understanding in molecular dynamics. Special thanks to Dr. Chongqing Ru for his kind help and recognition in my TA assignment.

My gratitude is extended to those generous scholarships I received, particularly, the support from University of Alberta Doctoral Recruitment Scholarship and RR Gilpin Memorial Scholarship.

No matter how far away, the support and nagging from my mother and father is always so refreshing. You make me stronger.

Despite being a long, arduous and solitary journey, I enjoyed every minute in my PhD adventure, which is truly memorable for a lifetime.

Table of Contents

Abstract	ii
Preface	iv
Acknowledgements	vii
List of Tables	xi
List of Figures	xii
List of Abbreviations	xxiv
Chapter 1: Introduction	
1.1. Background	1
1.2. Literature Review	2
1.2.1. Experimental Observations	2
1.2.2. Molecular Dynamics Simulations	6
1.2.3. Theoretical Understanding	10
1.3. Outline of Problems	13
1.4. Objectives of Research	14
1.5. Thesis Structure	15
Chapter 2: Void Initiation from Nano-Inclusion	16
2.1. Introduction	16
2.2. Simulation Methodology	16
2.3. Results and Discussions	18
2.3.1. Energies of Cu-Si Interface for Planar Configuration	18
2.3.2. The Particle-Matrix Case	21
2.3.3. The Size Effect	38
2.3.4. The Strain Rate Effect	47
2.4. Conclusions	50
Chapter 3: The influence of Initial Void Shape on the Void Growth	52
3.1. Introduction	52
3.2. Simulation Methodology	54
3.3. Results and Discussions	55

3.3.1. Effect of the z-Direction Thickness	56
3.3.2. The Cases with Unfixed Intervoid Ligament Distance	59
3.3.3. The Cases with Fixed ILDs	70
3.3.4. Comparison with the Analytical Model	76
3.4. Conclusions	79
Chapter 4: The Impact of Thermo-Mechanical Constraints on the Void Growth	81
4.1. Introduction	81
4.2. The MD Simulation Technique	83
4.3. Results and Discussions	86
4.3.1. Simulations with Temperature Control	86
4.3.2. Dynamic Simulations without Temperature Control	97
4.3.3. Miscellaneous Factors in Simulation	105
4.4. Conclusions	110
Chapter 5: Void Growth via Shear Loop Emission	112
5.1. Introduction	112
5.2. The Molecular Dynamics Simulation Methodology	114
5.3. Material Transport Observation: Void Growth and Material Transport	115
5.3.1. The Basic Case	115
5.3.2. Additional Cases	125
5.4. Theoretical Considerations	130
5.4.1. Material Transport Equation for the Prismatic Loop	130
5.4.2 Feasibility of Material Transport via Shear Loop Emission	131
5.4.3. A Phenomenological Description of Void Growth by Dislocation Emission	135
5.5. Conclusions	141
Chapter 6: Theoretical Calculations of Void Growth due to Shear Loops	142
Chapter 7: The Influence of Ellipticity to the Void Coalescence	153
7.1. Introduction	153
7.2. Simulation Methodology	157
7.3. Results and Discussions	158
7.3.1. The Onset of Dislocation Emission Compared with the Lubarda Model	160
7.3.2. The Overall Stress Response	166

7.3.3. The Porosity Accumulation and Void Shape Evolution.....	169
7.4. Conclusions	177
Chapter 8: Simulation of Nanoporous Metal with Pores Mimicking Crystalline Arrays	179
8.1. Introduction	179
8.2. Simulation Specifications	181
8.3. Results and Discussions	183
8.3.1. The Overall Stress Response	183
8.3.2. The Onset of Dislocation Emission and the Comparison of Yield Stresses.....	185
8.3.3. Evolution of Dislocations, Hardening and Early Densification	194
8.4. Concluding Remarks	202
Chapter 9: Conclusions and Future Perspectives.....	204
9.1. Conclusions	204
9.2. Future Perspectives	206
9.2.1. Critical Stress for Dislocation Emission	206
9.2.2. Void Shape Effect with More Considerations	207
9.2.3. Void Growth due to Dislocation Loops	207
9.2.4. Bridging the Gap Between MD Results and Continuum Damage Models	208
9.2.5. Modeling Designed Nanoporous Structures	209
Bibliography	210
Appendix A: The Relative Displacement	233
Appendix B: List of Publications during PhD thesis work	236

List of Tables

Table 2.1: Interface and Fracture Energies for the Cu-Si Interface	21
Table 3.1: Geometry Specifications for Virtual Specimens 1-6	60
Table 3.2: Geometry Specifications for Virtual Specimens 7-9	71
Table 3.3: Geometry Specifications for Virtual Specimens 10-12	78
Table 4.1: Dislocation Angles Compared with the Lubarda Model	90
Table 7.1: Details about the Computation Geometry	159
Table 8.1: Geometry of Nanoporous Copper Samples for Atomistic Simulation	183
Table 8.2: Finalized Dislocation Geometries for the Theoretical Calculation. The Burgers Vector b is in the Unit of Lattice Constant. The Parameter ρ is set as 1 in $w=\rho b$	189
Table 8.3: The Critical Stresses for Dislocation Emission Predicted by Classical Dislocation Theory Compared with those by Atomistic Simulation. The Gliding P-K Force due to Image Stress is balanced by that due to External Load	192

List of figures

Figure 1.1: Decohesion of second-phase particle in high-strength Al alloys [16]. (Reprinted with permission from Liu et al. 2003. Copyright 2003, Taylor & Francis)	3
Figure 1.2: Void growth with surrounding slips [19] (Reprinted with permission from Meyers and Aifantis 1983. Copyright 1983, Elsevier)	4
Figure 1.3: Octahedral void formed in a spall test [20] (Reprinted with permission from Stevens 1972. Copyright 1972, AIP Publishing LLC)	4
Figure 1.4: Fractograph (f) and 3D visualization from tomographic reconstructions (a-e) of void coalescence [21] (Reprinted with permission from Hosokawa et al. 2013. Copyright 2013 Elsevier)	5
Figure 1.5: Void growth and interaction of shear loops emitted from void [26] (Reprinted with permission from Traiviratana et al. 2013. Copyright 2013, Elsevier)	6
Figure 1.6: Void coalescence and generated dislocations [37] (Reprinted with permission from Potirniche et al. 2006. Copyright 2006, Elsevier).....	8
Figure 1.7: (a) Void growth via prismatic dislocation loop. (b) Void growth via shear dislocation loops. [18] (Reprinted with permission from Lubarda et al. 2004. Copyright 2004, Elsevier).....	10
Figure 2.1: Two periodic planar geometries with sizes of $11.57 \text{ nm} \times 11.57 \text{ nm} \times 11.57 \text{ nm}$ for (a) and $23.14 \text{ nm} \times 11.57 \text{ nm} \times 11.57 \text{ nm}$ for (b). The geometries (a) and (b) are essentially identical due to periodicity.....	20
Figure 2.2: Cubic simulation box halved showing Silicon spherical particle (gray) embedded inside Copper matrix (yellow).	22
Figure 2.3: The stress-strain relation, void volume fraction under a simulation size of $26.03 \text{ nm} \times 26.03 \text{ nm} \times 26.03 \text{ nm}$ with a spherical particle of 7.5 nm in diameter embedded under a strain	

rate of $2 \times 10^9 \text{ s}^{-1}$	22
Figure 2.4: Relative displacement (magnitude) during the interfacial debonding. The formula to compute relative displacement (magnitude) can be found in Ref. [87]. The cutting plane is yoz plane. The unit of color bar is Å.	24
Figure 2.5: Local normal stress at different location inside a spherical shell of matrix covering the particle. The spherical shell has been divided into 12 zones (numbered from 1 to 12) longitudinally and the projection of individual zone onto the xoy plane is an annulus.....	26
Figure 2.6: Movement of the RFT copper atoms (in yellow) near the Cu-Si interface. Snapshot has been projected onto the yoz plane. The critical length is set as 2.0 \AA to identify the RFT atoms. The blue atoms represent silicon particle atoms.	29
Figure 2.7: Dislocation network and RFT atoms after dislocation emission. Blue atoms represent particle-matrix/void-matrix interface/surface, while the blue and green rendered lines represent dislocation lines. The critical length is set as 2.0 \AA to identify the RFT atoms.	31
Figure 2.8: Critical stresses by Lubarda model compared with MD results.....	34
Figure 2.9: Relative displacement (magnitude) after dislocation emission. The coordinate origin for matrix is attached on the simulation box. The coordinate origin for the particle is its center. The cutting plane is yoz plane. Snapshots are plotted by ATOMEYE. The unit of color bar is Å	35
Figure 2.10: Interfacial debonding with pre-existed dislocations inside matrix. Dislocation network is shown in (a), where blue atoms represent particle-matrix/void-matrix interface/surface, the blue and green rendered lines represent dislocation lines and the red atoms show the stacking fault area. The cutting plots (b) and (c) show the interfacial debonding	37

Figure 2.11: Average stress in the loading direction with different volume fraction of particle	39
Figure 2.12: Local normal stress at different location inside a spherical shell of matrix covering the particle for $V_{fit}=10\%$ case. Same zones are divided here as in Figure 2.5.	40
Figure 2.13: Nucleated void volume fraction under different particle volume fraction	41
Figure 2.14: Growth and coalescence of the nucleated void under different particle volume fraction ($\epsilon=0.2$ and cutting plane is yoz plane). Snapshots are plotted by ATOMVIEWER [100]. The cutting plane is the yoz plane at the box center. The modified bond-angle distribution (BAD) method, originally introduced by Ackland and Jones [101] is applied to color the atoms. Red atoms here are not RFT atoms	43
Figure 2.15: Average stress in the loading direction with different-sized simulation box	44
Figure 2.16: Nucleated void volume fraction with different-sized simulation box.....	45
Figure 2.17: Growth of the nucleated void with different simulation box size at $\epsilon=0.19$. The cutting plane is xoz plane. The simulation boxes are with three different lengths, namely, 13.01nm, 26.02 nm and 52.06 nm in (a-c). Snapshots are colored in the same way as Figure 2.14	46
Figure 2.18: Average stress in the loading direction under different strain rate	47
Figure 2.19: Nucleated void volume fraction under different strain rate	48
Figure 2.20: Growth of the nucleated void under different strain rate at $\epsilon=0.19$ (The cutting plane is xoz plane). Snapshots are colored in the same way as Figure 2.14.....	49
Figure 3.1: Stress-strain relation with 5% initial porosity under different z-direction thickness	56
Figure 3.2: The early stage of dislocation emission (stacking fault atoms in red are made visible	

and the dislocation lines are in dark blue or gray, while the stacking fault atoms are in red) under different z-direction thickness (thickness is in the unit of lattice constant of aluminum)57

Figure 3.3: The dislocation structure (stacking fault atoms are made invisible) at the ultimate strength point under different z-direction thickness (thickness is in the unit of lattice constant of aluminum).....58

Figure 3.4: Three void shape cases with 5% initial porosity60

Figure 3.5: The early stage of dislocation emission61

Figure 3.6: Gliding of a part of the initially formed dislocation lines (x-elongated void)61

Figure 3.7: The dislocation structure at the ultimate strength62

Figure 3.8: The void shape and dislocation structure at 0.2 strain of 5% initial porosity62

Figure 3.9: Stress-strain relation under 5% initial porosity64

Figure 3.10: The early stage of dislocation emission (magnified)66

Figure 3.11: The dislocation structure at the ultimate strength67

Figure 3.12: Dislocation kinks (inside the left black circle) and jogs (inside the right black circle) near the surface of the y-elongated void (green arrow is the Burgers vector).....67

Figure 3.13: The void shape and dislocation structure at 0.2 strain of 1% initial porosity68

Figure 3.14: Stress-strain relation with 1% initial porosity69

Figure 3.15: Specimens 7, 8, 9 with fixed ILD.....71

Figure 3.16: The early stage of dislocation emission72

Figure 3.17: The dislocation structure at the ultimate strength73

Figure 3.18: The way of void expansion in specimen 7 (The snapshots are only truncated horizontally)73

Figure 3.19: The evolved void geometry of specimen 8 and 9 at 0.2 strain74

Figure 3.20: Stress-strain relation of specimen 2, 7, 8 and 9.....75

Figure 3.21: Illustration of the void-dislocation geometry from Ref. [91] (Reprinted with permission from Lubarda. Copyright 2011, Elsevier)77

Figure 3.22: The critical stresses for dislocation emission predicted by MD are compared to the minimum critical stress predicted analytically [91]. The hollow, horizontally half-filled, filled scattered and vertically half-filled symbols are the MD results with 1%, 2.5%, 5%, 20% initial porosity, respectively. The integer right to the individual symbol inside the legend is the corresponding specimen number. Geometric mean radius $\bar{R} = \sqrt{a_1 a_2}$ is used for the non-circular voids. A scale break is introduced horizontally to accommodate the largest void size.78

Figure 4.1: Initial configuration of simulation box (26×26×26 nm) and central spherical void84

Figure 4.2: The dislocation density and the corresponding void growth88

Figure 4.3: The dislocation emission angles of the uniaxial strain. Red atoms here are stacking fault atoms while the light blue atoms represent the void surface. Gray and blue rendered lines represent dislocation lines90

Figure 4.4: The dislocation structure and the RFT atoms (in red) for the uniaxial-strain case (NVT). The RFT atoms are made invisible in (d-f). Light blue atoms in (a-c) represent void surface. The red and blue rendered lines represent dislocation lines. The stacking faults areas are colored in gray. The critical length is set at 1.0 Å to identify the RFT atoms93

Figure 4.5: The dislocation structure and the RFT atoms (in red) for the uniaxial-stress case (NPT). The RFT atoms are made invisible in (d-f). Light blue atoms in (a-f) represent the void surface. The red and blue rendered lines represent dislocation lines. The stacking faults areas are colored in gray. The critical length is set as 1.0 Å to identify the RFT atoms.....95

Figure 4.6: Shape evolution of the void by its size in all the three directions for both the uniaxial-strain and uniaxial-stress cases under a temperature of 0.1K.....97

Figure 4.7: The dislocation density and the corresponding void growth with initial temperature 300K and no thermostat applied98

Figure 4.8: The surface growth and shrinkage for the uniaxial-stress case. The halved void surfaces at two different strains have been plotted in a combined way. The dark blue atoms represent the void surface at the strain 7.68% while the dark red atoms represent those at the strain 7.92%. Dark red area indicates growth area while the dark blue area indicates the opposite100

Figure 4.9: The dislocation structure and the RFT atoms (in red) for the uniaxial-strain case (NVE) under an initial temperature of 300K. The RFT atoms are made invisible in (d-f). Light blue atoms in (a-c) represent void surface. The rendered lines in blue, red and gray represent dislocation lines. The stacking faults areas are colored in gray. The critical length is set at 1.0 Å to identify the RFT atoms101

Figure 4.10: The dislocation structure and the RFT atoms (in red) for the uniaxial-stress case (NPH). The RFT atoms are made invisible in (d-f). Light blue atoms represent the void surface. The blue lines represent dislocation lines. The stacking faults areas are colored in gray. The critical length is set at 1.0 Å to identify the RFT atoms103

Figure 4.11: Shape evolution of the void by its size in all three directions for both the uniaxial-strain and uniaxial-stress cases under an initial temperature of 300K.....104

Figure 4.12: The void volume fraction with different equilibration durations105

Figure 4.13: The void volume evolution with different sizes of simulation box106

Figure 4.14: Material transport visualized by the RFT atoms with different sizes of simulation box. Light blue atoms in (a-c) represent the void surface (almost invisible in (b) and (c)). The red and blue lines represent dislocation lines. The stacking fault areas are colored in light gray. The critical length is set at 2.0 Å to identify the RFT atoms. The strains in (a-c) are 6.7%, 5.9% and 5.8%, respectively. The snapshots are not proportional to their actual sizes. Equilibration duration in (b) is 3 ns107

Figure 4.15: The void volume evolution at different strain rates108

Figure 4.16: Material transport visualized by the RFT atoms with different strain rates. Light blue atoms in (a-c) represent void surface (almost invisible). The red and blue lines represent dislocation lines. The stacking faults areas are colored in gray. The critical length is set at 2.0 Å to identify the RFT atoms. The strains in (a-c) are 5.09%, 5.1% and 7.4%, respectively. The case of $\dot{\epsilon}=2\times 10^8 \text{ s}^{-1}$ is shown in Figure 4.14(b)109

Figure 5.1: Initial configuration of simulation box (26×26×26 nm) and central spherical void (r=3.5 nm) inside (only atoms on the surface of void are shown)114

Figure 5.2: The correlation of void growth and the dislocation density. Engineering strain is used116

Figure 5.3: The Displacement field (magnitude) by MD simulation and the relative displacement field (magnitude) by MD simulation at the strain 0.05 (right before the dislocation emission). All the colored scale bars are in the unit of Å. The cutting plane is the xoz plane at the simulation box center118

Figure 5.4: The relative displacement field (magnitude) by MD simulation at the strain 0.052 (the onset of dislocation emission) and 0.058. All the color bars are in the unit of Å. The cutting plane is the xoz plane at the box center119

Figure 5.5: The rapid development of dislocation structure before it meets the periodic boundary. Blue atoms represent void surface while the red and blue rendered lines represent dislocation lines. The stacking faults areas are colored in gray.....120

Figure 5.6: The “relatively farthest-travelled” atoms (in red) inside the dislocation network at the strain of 5.92% and 6%. Blue atoms in (c) represent void surface while the red and blue rendered lines represent dislocation lines. The stacking faults areas are colored in gray. Three different critical lengths, namely $d_{crit}= 1.0, 2.0, \text{ and } 3.0 \text{ \AA}$, are used to identify the “relatively farthest-travelled” atoms.....121

Figure 5.7: Number of the relatively farthest-travelled atoms identified by different critical length under different strains122

Figure 5.8: Displacement field (magnitude) and relative displacement field (magnitude) by the MD method plus the relative displacement field (magnitude) by the finite element (FE) simulation at the strain of 5.92% and 6%. All the color bars are in the unit of \AA . White dotted lines indicate the slip planes124

Figure 5.9: The cases of an irregular-shaped void with an initial system temperature 0.1 K. Here we show (a) the dislocation network along with void surface depicted by light blue atoms and (b) the “relatively farthest-travelled” atoms inside the dislocation network at the strain 0.046. The critical length to identify the relatively farthest-travelled atoms is 1.0 \AA . The rendered blue lines represent dislocation lines. The stacking faults areas are colored in light gray in (a)126

Figure 5.10: Displacement field (magnitude) and relative displacement field (magnitude) by the MD method at the strain 0.046 with an irregular initial void. All the color bars are in the unit of \AA . White dotted lines indicate the slip planes.....127

Figure 5.11: The case of spherical void with initial temperature of 300K. Here shows (a) the

dislocation network alone with void surface depicted by light blue atoms and (b) the “relatively farthest-travelled” atoms inside the dislocation network at the strain 0.0488. The critical length to identify the relatively farthest-travelled atoms is 1.0 Å. The rendered red and blue lines represent dislocation lines. The stacking faults areas are colored in gray.....129

Figure 5.12: Forming of prismatic loop with quadrangular-prism slip surface. The figure is reproduced [56] (Reprinted with permission from Bulatov et al. 2010. Copyright 2010, Elsevier)130

Figure 5.13: A zoomed-in snapshot of Figure 5.6 with cutting plane [0 1 -1] at the box center. The red atoms still represent the relatively farthest-travelled atoms while the other atoms are in green. Only a small fraction of the void is shown. The blue filled circle is the rendered shear loop front.....132

Figure 5.14: Analytical solution of displacement field caused by a circular shear loop. Here shows the contour plot of u_1 in the unit of Burgers vector at the plane $x_2=0$ for a circular shear dislocation loop, reproduced from Ohr [60] (Reprinted with permission from Ohr 1972. Copyright 1972, Taylor & Francis). The circular shear loop is inside the plane $x_3=0$ and the Burgers vector is in the x_1 direction. Here involves different convention for the Burgers vector133

Figure 5.15: Schematic material transport via the emission/formation of a shear dislocation loop/curve135

Figure 5.16: Three-dimensional schematic diagram of material transport via a square-frustum like structure consisting of dislocation loops/curves on the slip plane. Symmetry only applies for the spherical void case. The loading direction here is assumed vertical136

Figure 5.17: Two-dimensional schematic diagram of material. Different cutting plane at the box

center has been chosen in (a) and (b). Here view angle of (a) corresponds to Figure 5.13 and (b) corresponds to Figure 5.8(d).....138

Figure 6.1: Closed dislocation loop C and its bounding surface A from [57] (Reprinted with permission from Hirth Copyright 1982, Hirth). The close loop is denoted as C , the normal of surface A is \mathbf{n} , the segment vector of loop is $d\mathbf{l} = \xi d\mathbf{l}$ and the motion of dislocation loop is $\delta\mathbf{r}$ 143

Figure 6.2: Schematic of the corresponding geometry. The center of the circular shear loop with a radius of R coincides with the coordinate origin. The spherical void of a same radius R is centered at the coordinates $(1.1R, 0, 1.05R)$. The ratio b/R is set as 0.1.....147

Figure 6.3: Deformed slice plot of the magnitude of total displacement \mathbf{u} with the cutting plane at $x_2=0$. Growth of the nanovoid towards the shear loop can be clearly seen (Deformation has been magnified by a scale factor of 2). The color bar is in the unit of R148

Figure 6.4: Incremental material transport from $\epsilon=5.8\%$ to $\epsilon=5.92\%$ during the emission of eight sets of shear curves/loops. The light blue atoms represent the current void surface while the red atoms are the incremental RFT atoms. The rendered blue and red curves are dislocation curves. The critical magnitude of displacement to identify the incremental RFT atoms is 1.02 \AA , which is the averaged magnitude of Burgers vectors belonging to the eight front shear curves. Snapshots are plotted by software ATOMVIEWER .Loading is applied in x direction. Figure (d) shows a cutting view of (c).....151

Figure 7.1: Schematic of idealized void interaction geometry reproduced from [157]: (a) oblate-oblate combination; (b) prolate-prolate combination156

Figure 7.2: Schematic of the empirical criterion for void coalescence (the critical ILD is larger than zero)157

Figure 7.3: Simulation Geometry containing two non-uniformly distributed elliptical voids (Periodicity are applied on all the three dimensions).....	159
Figure 7.4: The void-dislocation geometry under uniaxial tension reproduced from [91]. (Reprinted with permission from Lubarda. Copyright 2011, Elsevier)	161
Figure 7.5: The centrosymmetry parameter coloring (CPC) plots indicating the onset of dislocation emission for each specimen.....	162
Figure 7.6: The critical stress by MD simulation compared to the minimum critical [91]. Geometric mean radius $\bar{R} = \sqrt{a_1 a_2}$ is used for the elliptical void.....	164
Figure 7.7: Strain-stress curves to reflect the influence of void shape combination	167
Figure 7.8: Strain-stress curves to reflect the influence of ILD_0	168
Figure 7.9: Porosity evolution reflecting the influence of void shape combination	170
Figure 7.10: Porosity evolution to reflect the influence of ILD_0	171
Figure 7.11: The void shape evolution of each specimen	173
Figure 7.12: The gliding of the material along the dislocations to grow the void.....	174
Figure 7.13: The shrinkage of the ILD during the deformation	175
Figure 7.14: The effect of ILD_0 and void shape combination on the coalescence porosity	176
Figure 8.1: Nanoporous copper sample for atomistic simulation and finite element simulation	182
Figure 8.2: Stress-strain relation for different crystalline arrays of pores with the same initial porosity. Colored arrows indicate the start of dislocation emission correspondingly for each sample	183
Figure 8.3: Dislocation emissions at the yield point of four samples via atomistic simulation. The post-processing software ATOMVIEWER [85] is employed. Figures (a), (b), (c) and (d)	

belong to the diamond, BCC, FCC and HCP array of pores, respectively. From up to down show firstly the snapshots with full atoms (bulk atoms in dark blue), secondly the cutting views with only surface atoms left (in light blue) and thirdly the local magnification (blue rendered curves are Shockley partial dislocations and red atoms represent stacking fault). The corresponding strains are 6.24% for (a), 2.80% for (b), 1.40% for (c) and 1.05% for (d)186

Figure 8.4: 3D Schematic of incipient curved dislocation for the theoretical calculation.....188

Figure 8.5: Magnitude of the shear component $\mathbf{b} \cdot \boldsymbol{\sigma}^* \cdot \mathbf{n}$ on the slip planes by finite element simulation, where $\boldsymbol{\sigma}^*$ is the stress field induced by remote stress and \mathbf{n} is the unit normal vector of slip plane. The z-direction remote stresses in (a-d) are all controlled to 117.3MPa, same to the critical stress that initiates dislocation emission for the HCP-array-pore sample. The solid black curves inside represent the dislocation segments.....193

Figure 8.6: Ensuing evolution of dislocation network. Blue, pink, red and green rendered curves present Shockley partial, Frank partial, stair-rod partial and perfect dislocations, respectively. Red atoms represent stacking fault atoms while blue atoms represent surface atoms. Diamond-array-pore specimen in (a-c) is strained to 6.36%, 7.14% and 15.6%, respectively. BCC-array-pore specimen in (d-f) is strained to 3.83%, 5.30% and 15.6%, respectively. FCC-array-pore specimen in (g-i) is strained to 2.80%, 7.80% and 15.6%, respectively. HCP-array-pore specimen in (j-l) is strained to 2.80%, 7.80% and 15.6%, respectively.....195

Figure 8.7: Flow stress versus accumulated dislocation density since dislocation emission. Since the strain increment is even, wider horizontal gap between points indicates faster-pace increase in the dislocation density.199

Figure 8.8: The decrease of porosity due to compression. Porosities after relaxation run is slightly smaller than the as-created values.....201

List of Abbreviations

BCC:	Body-centered cubic
CMD	Classical molecular dynamics
CPC:	Centrosymmetry parameter coloring
DFT:	Density functional theory
EAM:	Embedded atom method
FCC:	Face-centered cubic
FE:	Finite element
GLD:	Gologanu–Leblond–Devaux
GTN:	Gurson-Tvergaard-Needleman
HCP	Hexagonally close-packed
ILD	Intervoid ligament distance
MD:	Molecular dynamics
MEAM:	Modified embedded atom method
RFT:	Relatively-farthest travelled
TEM:	Transmission electron microscopy

Chapter 1: Introduction

1.1. Background

Void behavior in metallic materials is a vital and active topic. It is of great interest in industrial situations such as ductile tearing of gas pipelines over hundreds of meters, crack propagation in large nuclear vessels, or ductile tearing of aircraft fuselage [1].

Due to heterogeneity, metals sometimes fail prematurely through ductile fracture. The pre-existing second-phase particles and inclusions in metal alloy offer sites where damage can nucleate in the form of microvoids. Void initiation from the second-phase particles or other impurities is the first stage of void evolution. Large second-phase particles can determine the moment and location of ductile fracture, but they are not essential to the fracture process itself [2]. On the contrary, smaller particles appeared to govern the fracture process [2]. The size of these small particles, as so-referred in the early work of Broek [2], is in the range of a few hundred nanometers. With continued deformation, nucleation of damage will proceed, accompanied by the growth of the existing voids. At a certain stage of deformation, the interaction of neighbouring voids triggers void coalescence which eventually leads to the formation of cracking and failure in the form of ductile fracture [3]. In the micro- and macro-level, this type of failure mode has been extensively studied. However, mechanistic models regarding nucleation, growth and coalescence of nanovoids are under continuous development and not yet fully satisfying, partly owing to the difficulty in a real-time experimental observation at nano-scale.

Nanovoids inside the metal material can stem from a number of sources such as radiation damage [4] or void initiation during the propagation of crack tip under stress [5]. It is of great

scientific significance to understand the behavior of nanovoids inside the metallic materials, not only to prevent structural damage but also to pave the way towards novel functional designs. For instance, nano-porous, nano-crystalline or nano-layered structures have been proposed to be radiation tolerant media as a new design concept due to the fact that their nano-sized pores, grain boundaries or interfaces could act like a sink to store or absorb radiation-induced damages [6, 7]. Besides, nanoporous metals are emerging as strong versatile candidates with great potentials in other diverse applications. The inner morphology of nanoporous materials, which is the very feature to distinguish them from traditional bulk materials, can be tailored for different needs. For example, bi-continuous nanoporous metals foam, whose inner morphology reassembles a forest of nanowires, exhibit a high specific strength. Their high surface-to-volume ratio can provide more active area for reactant molecules and improve the electron mobility with solid ligaments [8-10]. Other possible applications and advantages include electrochemical sensor, energy conversion/storage system [8, 11, 12], exceptional mechanical properties with light weight [6, 13].

1.2. Literature Review

1.2.1. Experimental Observations

Void can be nucleated by the debonding or cracking of second-phase particles or inclusions from matrix material as shown in Figure 1.1. Void nucleation is strongly related to the size and shape of second-phase particles. Large micrometer particles are prone to cracking at lower strains, while smaller sub-micron particles are prone to debonding [14]. Nucleation mechanisms are proposed to be either stress- or strain-controlled. The stress-controlled mechanisms state that the dispersoid/matrix decohesion occurs once the interfacial strength exceeds a critical level

which depends on the properties of dispersoid and matrix. For strain-controlled mechanisms, the debonding of dispersoid is considered related to dislocation kinetics [15]. Although dislocation pile-ups could form by particles, yet giant pile-up will not occur [2]. The mere presence of dislocation loops around particles without high stresses and strains is insufficient for void initiation [2]. These void nucleation models are typically continuum-based, capturing averaged nucleation process of dispersoid/matrix system. Shortcoming or not, calibration of specific parameters in these models are often inevitable [3].

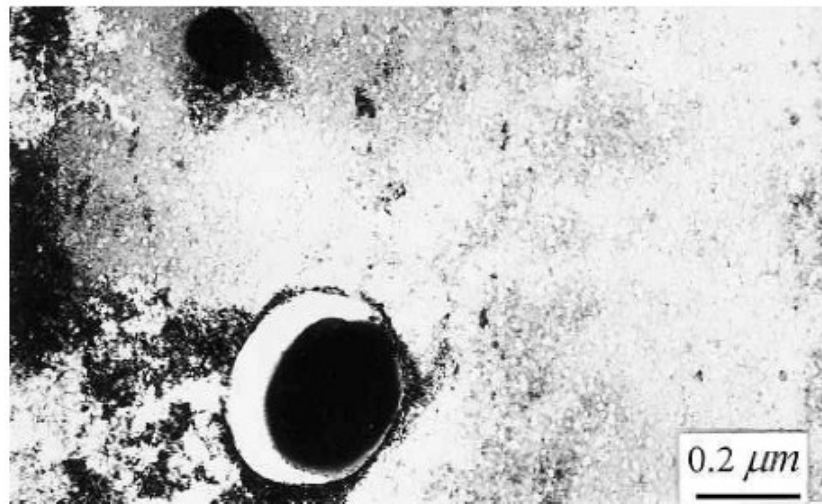


Figure 1.1: Decohesion of second-phase particle in high-strength Al alloys [16] (Reprinted with permission from Liu et al. 2003. Copyright 2003, Taylor & Francis).

In a continuum view, void growth is the most understood stage of ductile fracture, which is assumed a continuum process not like void nucleation or coalescence [17]. Voids are typically assumed cylindrical, elliptical, spherical or ellipsoidal and change shape during growth. The void growth rate and shape evolution are intrinsically linked as void shape induces anisotropy, altering stress state and growth rate in a non-linear fashion [3]. Understanding void growth under extreme high strain rate could contribute to the design analysis of structures potentially

sustaining explosive or projectile impacts [18]. The dislocation emission has been proposed to be a primary cause of the void growth under high strain rate [18]. Dislocation activity around growing void was reported by Meyers and Aimone [19] as shown in Figure 1.2. During a spall test, void will evolve into octahedral shape as seen in Figure 1.3 [20].

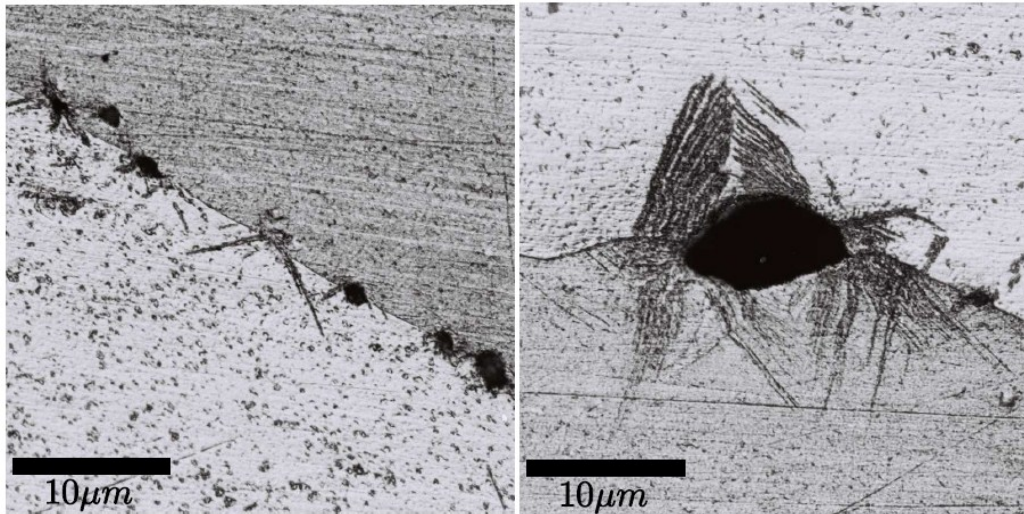


Figure 1.2: Void growth with surrounding slips [19] (Reprinted with permission from Meyers and Aimone 1983. Copyright 1983, Elsevier).

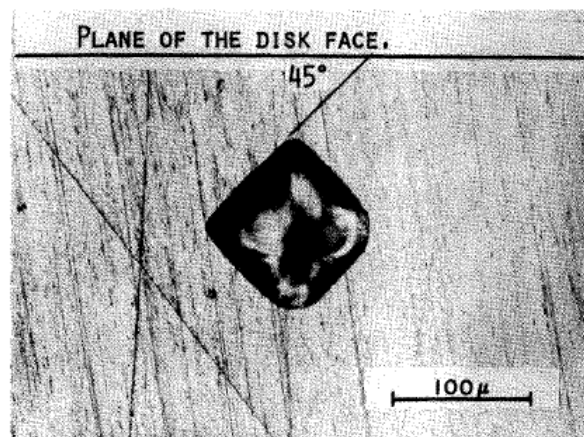


Figure 1.3: Octahedral void formed in a spall test [20] (Reprinted with permission from Stevens 1972. Copyright 1972, AIP Publishing LLC).

Compared with void growth, void coalescence in a continuum view is a sudden and rapid phenomenon where voids link up to form cracks that propagate throughout the material. Void coalescence relates to many factors such as initial porosity, void size, void shape, spacing and material hardening [3]. Recent experiment with fully 3D array of drilled artificial microvoids demonstrated that intervoid distance could keep decreasing during coalescence between centroids of voids (see Figure 1.4) [21]. Inspection of fracture surfaces indicates that the coalescence involves secondary populations of smaller voids [22-24]. These smaller voids nucleate between larger microvoids and interlink to cause rapid failure by compromising the integrity of ligament and hastening its collapse [3]. The role played by these secondary voids on ductile fracture can no longer be ignored and has since become an active subject of research [25]. Besides, these smaller secondary voids are more readily to model with the current computational power for atomistic simulation.

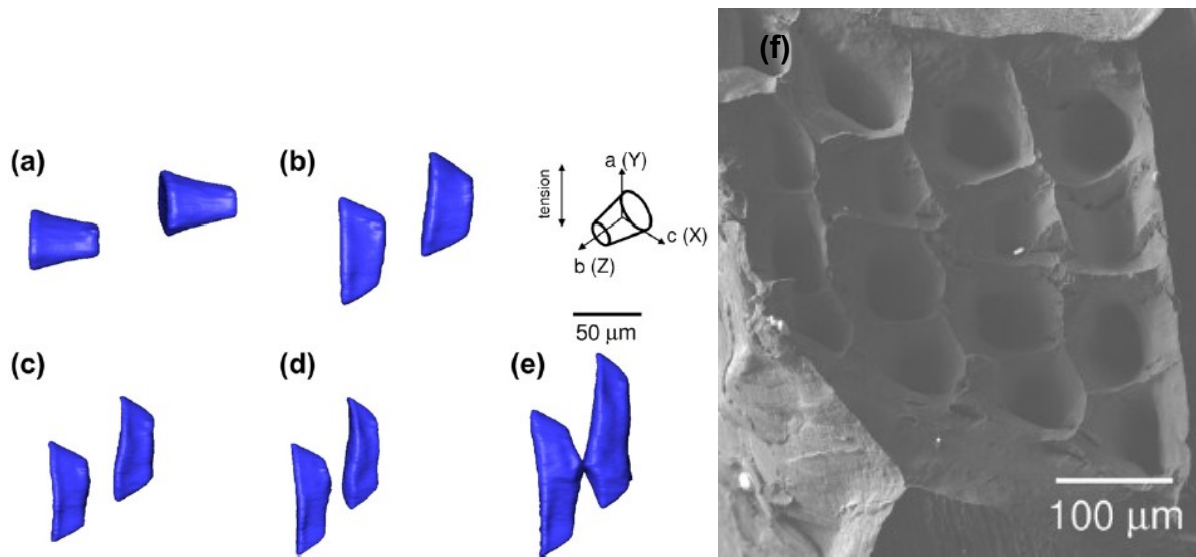


Figure 1.4: Fractograph (f) and 3D visualization from tomographic reconstructions (a-e) of void coalescence [21] (Reprinted with permission from Hosokawa et al. 2013. Copyright 2013

Elsevier).

1.2.2. Molecular Dynamics Simulation

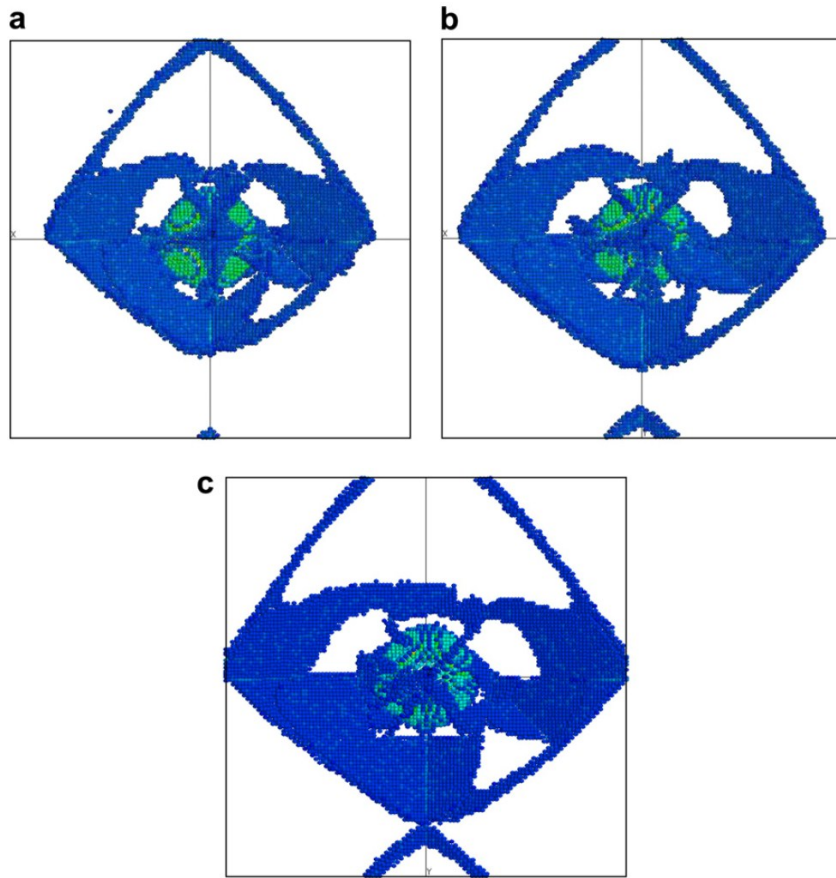


Figure 1.5: Void growth and interaction of shear loops [26] (Reprinted with permission from Traiviratana et al. 2013. Copyright 2013, Elsevier).

Regarding void nucleation from composites, molecular dynamics simulation does not require pre-defined quantities or assumptions about the interface unlike a number of other numerical approaches. The initial interfacial bonding is directly achieved through relaxation run of the system including atoms comprising the interface until the system reaching an equilibrium state. Regarding the MD work for composite materials, the reported simulations focused extensively on the debonding of planar or nanocrystalline composites. Gall et al. [27] investigated the planar atomic interface of the aluminum-silicon system. They observed that the

interfacial fracture occurs at the positions where the local displacement of interface atoms creates a rippled structure in the absence of vacancies, dislocations, impurities and other defects. Ward et al. [28] showed that Al-Si nanocrystalline thin films fail primarily along the Al/Si interface at high local tensile stress. Tomar and Zhou [29] analyzed the tensile deformation of nanocrystalline α -Fe₂O₃+FCC-Al composites via MD simulation. They also concluded that the strength of the composite is strongly affected by interfaces between the phases, and the interface effect is strongest for smallest grains. Agreement with experimental observation was reached only for the grain sizes above a critical value. For small grains, interfacial stresses are important for predicting the strength of the composite. Further, they suggested that dislocation emission plays a secondary role for small grains. For large grains, dislocations contribute significantly to the deformation. Noreyan et al. [30] found that the critical shear stress of Al/Si interface is significantly lower than the tensile critical stresses and the fracture by shear is only confined in Al phase near the Al/Si interface. The MD simulation of Dongare et al. [31] showed that voids nucleate from the Al-Si interface, which is attributed to mechanical separation and sliding at the Al/Si interface rather than the dislocation pile-up. Shadlou and Wegner [32] recently investigated the effect of nano-structural shape on the mechanical response of SiC/Cu nanocomposites. They found that the spherical shape leads to superior mechanical properties. To sum up, the nanoparticles in the above research are all sized below 10nm. The size effect of nano-particles, which is essential to the nanoworld [33-36], has not been reported to our best knowledge. More importantly, no study has linked the individual motion of atom to the onset of debonding and correlates the dislocation emission to the subsequent debonding. Not to mention clarifying what roles have the accumulated stress and plastic strain played in the interfacial debonding of nanoparticles. With rising capability of computational resources, it is now feasible to simulate

larger spherical nanoparticles up to, for example, 30 nm in diameter. Based on the knowledge from the planar and nanocrystalline composites, the objective of the present work is to examine the process of interfacial debonding of spherical silicon nanoparticle from an initially defect-free and dislocation-free copper matrix. The role of interfacial stress and dislocation emission in interfacial debonding, subsequent growth and coalescence of the nucleated void will be investigated. Based on a new interpretation of MD results, the material transport during the interfacial debonding and void growth will be highlighted for a better understanding of damage mechanism.

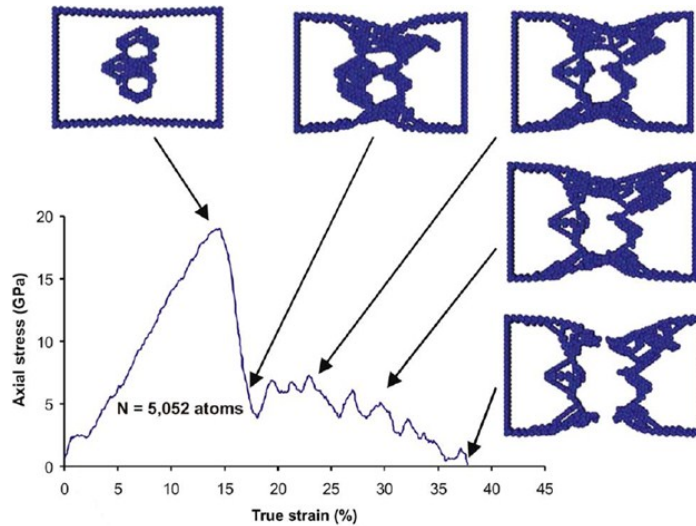


Figure 1.6: Void coalescence and generated dislocations [37] (Reprinted with permission from Potirniche et al. 2006. Copyright 2006, Elsevier).

The void growth and coalescence mechanisms in face-centered cubic metals have been widely studied by atomistic simulations. Traiviratana, et al. [26] carried out MD simulation in monocrystalline and bicrystalline copper and confirmed that the emission of shear dislocation loop is the primary mechanism of void growth (see Figure 1.5). The work of Bringa, et al. [38] applied MD method to investigate the effect of loading orientation in nanocrystalline FCC

copper. Marian, et al. [39] applied the quasi-continuum method to study the void expansion of FCC aluminum and indicated that dislocation emission is the primary mechanism. Potirniche et al. [37] employed the MD method to study growth and coalescence of circular nanovoids in single crystal nickel (see Figure 1.6). Their results reflected the size-scale dependence of the nanovoids. Tang et al. [40] investigated growth and coalescence of circular void in single-crystal magnesium.

It has been acknowledged that the initial void shape has a considerable influence on void growth, coalescence and material softening [41-43]. Some detailed studies regarding the effect of initial void shape via FE method have been carried out in [42-44]. They concluded that the effect of void shape can be substantial on the porosity evolution and influential on the stress-strain relation. Indeed, some analytical models such as the Gologanu–Leblond–Devaux model [45] model or its more sophisticated variants [41, 46, 47] have already included the influence of void shape phenomenologically. However, in MD simulations, most authors adopted circular or spherical void shape as a geometric simplification. The effect of initial void shape on the dislocation-void interaction and void has not yet been addressed via MD simulation in the literature. Though the FE approach is capable of modeling the void growth with different initial geometry, the applied phenomenological material model generally cannot capture the dislocation-void interaction. Moreover, the interviod ligament is only allowed to neck down to a point but never fracture due to the limitation of the FE method.

1.2.3. Theoretical Understanding

The first stage is void nucleation. Gurson [48] proposed that nucleation of voids can be expressed in terms of equivalent plastic strain based on Gurland's measurements [49]. Following

Gurson's work, Chu and Needleman [50] formulated the stress- or strain-controlled nucleation model by using normal distributions, respectively

$$\dot{f}_{\text{nucleation}} = \frac{f_n}{s_N \sigma_y \sqrt{2\pi}} \exp \left[-\frac{1}{2} \left(\frac{\dot{\sigma}_n - \sigma_N}{s_N \sigma_y} \right)^2 \right] \dot{\sigma}_n \quad (1.1)$$

$$\dot{f}_{\text{nucleation}} = \frac{f_n}{s_N \sqrt{2\pi}} \exp \left[-\frac{1}{2} \left(\frac{\bar{\varepsilon}^p - \varepsilon_N}{s_N} \right)^2 \right] \dot{\bar{\varepsilon}}^p, \quad (1.2)$$

where $\dot{f}_{\text{nucleation}}$ is time derivative of the porosity due to void nucleation, f_n is the volume fraction of void-nucleating particles, σ_y is the yield stress, σ_n is the critical interface stress [51-53], $\bar{\varepsilon}^p$ is the equivalent plastic strain, σ_N or ε_N is the nucleation burst stress or strain where maximum number of voids are nucleated according to the normal distribution and s_N is the standard deviation.

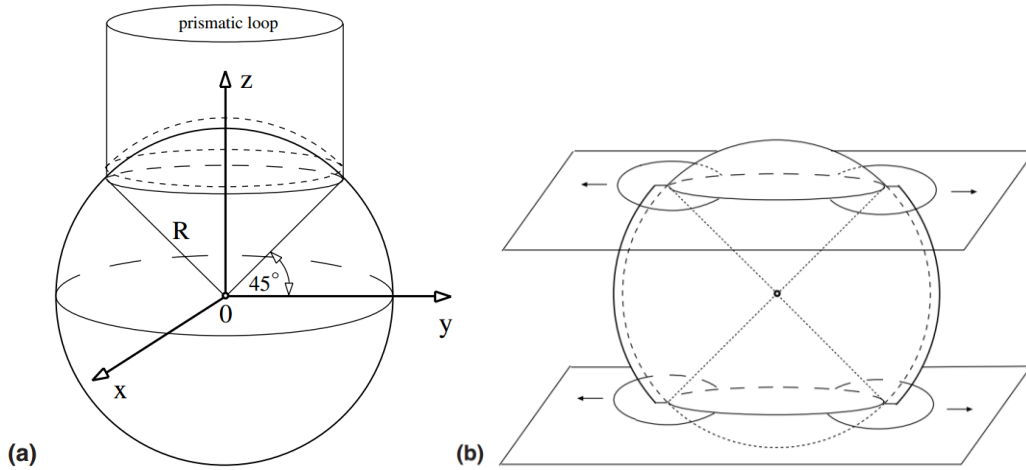


Figure 1.7: (a) Void growth via prismatic dislocation loop. (b) Void growth via shear dislocation loops [18] (Reprinted with permission from Lubarda et al. 2004. Copyright 2004, Elsevier).

The second stage is void growth. The focus here is the void growth under high strain rate, of which dislocation emission is suggested to be a primary cause [18]. Ashby [54] suggested that geometrically necessary dislocations are responsible for the compatible deformation between multiple solid phases in addition to statistically-stored dislocations. Regarding void growth, two geometrically necessary dislocations are proposed: prismatic and shear loops (see Figure 1.7) [18]. The void growth increment due to these dislocations is given by [55]

$$\Delta V = \Delta V^{\text{pl}} + \Delta V^{\text{el}}, \quad (1.3)$$

which consists of two parts: the plastic growth (mass transferred) due to the formation of dislocation loops and the elastic growth due to the elastic deformation caused by existing dislocation loops. For prismatic dislocation loops, the plastic growth is straightforwardly $\pi\rho^2b$, where ρ is the radius of the loop and b is magnitude of the Burgers vector. For shear dislocation loop, the plastic growth is more complicated and not yet well-understood (still a debate). Bulatov et al. [56], who claimed the impossibility of the shear loop to grow the void, emphasized the mass conservation over the loop surface as

$$\Delta V^{\text{pl}} = \int_{\text{loop}} \mathbf{b} \cdot d\mathbf{S} = \int_{\text{loop}} (\mathbf{b} \cdot \mathbf{n}) dS, \quad (1.4)$$

where ΔV^{pl} is the incremental void growth induced by the dislocation loop, \mathbf{b} is the Burgers vector of the dislocation loop, \mathbf{n} is the norm of the loop plane and dS is the differential element of the surface. However, the original equation for material removed [57] is expressed in terms of a differential volume element over an arbitrary surface A :

$$\delta V = \mathbf{b} \cdot \mathbf{n} dA. \quad (1.5)$$

As defined in [57], “any surface A bounded by loop C could be used for the operation”. Indeed, Figure 4-2 in the text book [57] clearly shows that a pure edge dislocation could be generated by different possible cuts. This idea can be easily extended to a shear loop. One side of the surface cut A is displaced by \mathbf{b} relatively and the material on both side of the cut are rejoined afterwards [57, 58]. The inner product $\mathbf{b} \cdot \mathbf{n}$ therefore highly depends on the shape of surface A . In the comments of Bulatov et al. [56], the flat area encircled by the loop C was chosen as this surface A . It is only under this premise that their asserted condition $\mathbf{b} \cdot \mathbf{n} = 0$ [56] is valid. In other words, Burgers vector \mathbf{b} and \mathbf{n} will not be perpendicular to each other everywhere if the surface A is not a flat one. Besides, the plastic void growth (mass transfer) is not invariant with respect to arbitrary surface cut for an incomplete loop. To determine the possible shape of the surface A , other information is required. Such information could, for example, come from atomistic simulations. We shall clarify this “shear impossibility” debate in Chapter 6 and Chapter 7. Apart from plastic deformation, the displacement due to the introduction of an arbitrary dislocation loop is given as the Volterra formula [59]

$$u_{i,j}(\mathbf{x}) = \int_S C_{klmn} b_m G_{ik,lj}(\mathbf{x} - \mathbf{x}') n_n dS(\mathbf{x}'), \quad (1.6)$$

where C_{ijkl} is the elastic tensor, b_m is the Burgers vector, $G_{kp}(\mathbf{x})$ is the Green function, n_n is the normal vector of the slip area S . However, solving such an equation in the presence of a nearby void is nontrivial. Ahn et al. [55] studied the elastic interaction between a prismatic loop and a void. Ohr [60] solved the displacement field around a circular shear loop. However, the elastic void growth due to the presence of a shear dislocation loop was not reported to our best knowledge.

The third is void coalescence. Tvergaard and Needleman [61] proposed a phenomenological coalescence model to identify the onset of coalescence by relying on a critical porosity. In this approach, the accumulated porosity shifts to a faster increase, once reaching the specified critical porosity. The resulting effective porosity reads

$$f^* = \begin{cases} f & f \leq f_c \\ f_c + \frac{f_u^* - f}{f_f - f_c} (f - f_c) & f > f_c \end{cases} \quad (1.7)$$

where f_c is the critical porosity, f_f is the porosity at failure when all material strength vanishes, and f_u^* is equal to $1/q_1$ with no physical significance. The most widely-used GTN (Gurson-Tvergaard-Needleman) model adopts the critical porosity and porosity at failure as 0.15 and 0.25, respectively. The parameter q_1 can be assumed 1.25 for example [62]. Nowadays, it is a universal consensus that critical porosity is not a just material constant but a function of the initial porosity, void shape, stress state and material properties [44, 63, 64].

1.3. Outline of Problems

Atomistic-level study of void behavior in metallic materials is a difficult task for continuum-based methods. In contrast, MD method serves as an ideal tool for real-time computer simulation of all kinds of atomistic phenomena. More and more researchers become aware of this and a few have pioneered in the area of nanovoid simulation. Many problems were nicely addressed, yet not every stone has been turned. Of a great significance is perhaps the debate whether the shear dislocation loop can grow the nanovoid or not. Surprisingly, this rather fundamental debate is still unsettled, despite extensive simulation efforts in this field over a decade. This debate, started between two groups of high-profile researchers, is utterly important since it is essential to the

role dislocations played in the void growth and would help improve continuum models once clarified. Besides, the mass transfer pattern, which is crucial to void growth, was commonly overlooked in the post-processing of MD results. In addition, the role of initial void geometry remains unclear in the nanovoid behavior, which has been extensively focused for microvoid through continuum-based methods. For a single void, ellipticity could bring considerable influence to stress response as suggested by continuum-based studies. For multiple nanovoids or even nanoporous case, this geometry effect could be more general, i.e., the arrangement of certain amount of voids or pores, and still remains unclear unsurprisingly. All these problems are of both scientific and engineering significance to solve in our current research.

1.4. Objectives of Research

The objective of this research is to provide more critical insights into the mechanical behavior of nanovoid in metals by primarily performing MD simulation to deepen our understanding to the following major issues:

1. The void nucleation from bi-material interface and subsequent growth at atomic level,
2. The debate of “shear impossibility” and mass transport during void growth,
3. The effect of initial shape of nanovoids on the void growth, coalescence and stress response of material and
4. The dislocation mechanism and stress response in novelty-designed nanoporous structure.

Some secondary objectives are to examine the effect of constraint in MD simulation, compute the elastic void growth due to the presence of a shear loop, probe the possible shape of

surface cut to create a shear loop and extend the Lubarda model to a fully 3D case for nanoporous structure.

1.5. Thesis Structure

The thesis consists of the following chapters. After the brief introduction of the thesis work in Chapter 1, Chapter 2 reveals the void initiation mechanism in a nano-inclusion embedded, initially dislocation-free matrix. Chapter 3 reflects the role of void shape on nanovoid growth. Chapter 4 investigates the impact of thermo-mechanical constraints on nanovoid growth. Chapter 5 concerns the nanovoid growth mechanism via shear dislocation formation. Chapter 6 theoretically calculates the nanovoid growth due to shear loop formation. Chapter 7 deals with the influence of ellipticity on nanovoid coalescence. Chapter 8 explores the structural integrity of differently-arranged, nanoporous structure by using both MD simulation and finite element method. Chapter 9 presents the conclusions and recommendation for future work.

Chapter 2: Void Initiation from Nano-Inclusion*

2.1. Introduction

It is of great importance to understand the interfacial debonding and related material fracture at the bi-material interfaces in order to model the mechanical response of a broad range of engineering composite materials [27]. For example, the silicon or aluminum-oxide inclusions are found to be fatigue crack nucleation sites in Al-Si casting [65]. Void initiation from the second-phase particles or other impurities is the first stage of void evolution during damage accumulation. Large second-phase particles can determine the moment and location of ductile fracture, but they are not essential to the fracture process itself [2]. On the contrary, smaller particles appeared to govern the fracture process [2]. The size of these small particles, as so-referred in the early work of Broek [2], is already in the range of a few hundred nanometers. On the other hand, nanoparticle composites have shown their potential in many aspects. Nanoparticle reinforcements have been explored for enhanced strength and ductility [66-68]. Nanoparticle-loaded nanocomposite is emerging as a promising candidate for superior energy storage [69-72]. Also, functionalized nanoparticles are ideal catalysts due to their higher surface-to-volume ratio [73-76]. Understanding the fundamental mechanical behavior of nanoparticle composite would thus help to improve the design in terms of structure integrity.

2.2. Simulation Methodology

The MD simulations are performed by the Large-scale Atomic/Molecular Massively Parallel Simulator (LAMMPS) [77] from Sandia National Labs. The atomistic interaction is

* A version of this chapter has been published. Reprinted with permission from Cui, Y.; Chen Z. Void initiation from interfacial debonding of spherical silicon particles inside a silicon-copper nanocomposite: A molecular dynamics study. *Modell. Simul. Mater. Sci. Eng.* 2017, 25, 025007. Copyright 2017 IOP Publishing Ltd.

modeled by the modified embedded atom method (MEAM) [78, 79]. The total energy E of a system is approximated as the sum of the atomic energies:

$$E = \sum_i \left[F_i(\bar{\rho}_i) + \frac{1}{2} \sum_{j \neq i} \phi_{ij}(r_{ij}) \right], \quad F_i(\bar{\rho}_i) = \begin{cases} A_i E_i^0 \bar{\rho}_i \ln(\bar{\rho}_i) & \bar{\rho}_i \geq 0 \\ -A_i E_i^0 \bar{\rho}_i & \bar{\rho}_i < 0 \end{cases} \quad (2.1)$$

where F_i is the embedding function, $\bar{\rho}_i$ is the background electron density at the site of atom i , $\phi_{ij}(r_{ij})$ is the pair potential between atoms, E_i^0 is the sublimation energy and parameter A_i depends on the element type of atom i [79]. The background electron density $\bar{\rho}_i$ takes the form [79]

$$\bar{\rho}_i = \begin{cases} \rho_i^{(0)} \sqrt{1 + \Gamma_i} / \rho_i^0 & \Gamma_i \geq -1 \\ -\rho_i^{(0)} \sqrt{1 + \Gamma_i} / \rho_i^0 & \Gamma_i < -1 \end{cases}, \quad \Gamma_i = \sum_{k=1}^3 t_i^{(k)} \left(\frac{\rho_i^{(k)}}{\rho_i^{(0)}} \right)^2 \quad (2.2)$$

where ρ_i^0 is the composition-dependent electron density scaling, $t_i^{(k)}$ is the average weighting factors, $\rho_i^{(0)}$, $\rho_i^{(1)}$, $\rho_i^{(2)}$ and $\rho_i^{(3)}$ are zeroth and higher-order densities given in [79]. Unlike embedded atom method (EAM), the electron densities in MEAM depend on the displacement vector rather than only the scalar distance between atoms.

It is crucial that the atomistic potential chosen must accurately reproduce pertinent features of the resulted energy curves, such as the unstable stacking fault energy [80]. The unstable stacking fault energy is an important parameter of the barrier for partial dislocation nucleation [81]. Jelinek et al. [79] improved the previously proposed MEAM parameters [27] in an effort to achieve better agreement with the generalized stacking fault energy curves. Their new MEAM potentials were validated towards density functional theory (DFT), classical MD (CMD) and experimental data in crucial aspects such as the formation energies of defects, equilibrium

volumes and elastic moduli [79]. Therefore the Cu-Cu, Si-Si and Cu-Si interactions in our simulation are modeled by their MEAM potentials.

As a physical simplification of periodically-arranged second-phase particles inside matrix material, periodic cubic simulation box is created to represent uniformly-distributed particles inside an infinite matrix. The particle is generated by removing the copper atoms from a desired region and refilling it with silicon atoms. Energy minimization using a conjugate gradient algorithm is performed to attain the minimum energy configuration especially for the interface, followed by the relaxation step to reach an equilibrium-state configuration. The relaxation is performed at 300K with zero outside stress via the Nose-Hoover thermostat and barostat [82, 83]. Equilibrium run is important to ensure a good initial bonding of the interface. The adopted equilibrium duration is 20 ps [28] by considering tradeoff between the validity and computation cost. Based on the relaxed configuration, a load of fixed engineering tensile strain is applied in the z-direction with strain-confined lateral boundaries. Both the software ATOMEYE [84] and ATOMVIEWER [85] are employed in post-processing the MD data to identify the dislocation network and Burgers vectors. ATOMVIEWER combines the modified Nye-tensor method and the dislocation line extraction method to derive Burgers vectors and dislocation network without constructing Burgers circuits explicitly [85].

2.3. Results and Discussions

2.3.1. Energies of Cu-Si Interface for Planar Configuration

The surface energies here are evaluated in a similar way as in Ref. [28]. The major difference in this work is the elimination of the fixed end in the loading direction. In an effort to reproduce an identical boundary condition as will be applied in the later spherical-particle

simulation, the periodicity is not only applied in the lateral directions as in [28] but also in the loading direction for the planar configuration. The advantage of doing so is the elimination of the unknown energy associated with the fixed end, while the disadvantage is the introduction of the additional interface. The total clean surface energy for the Cu-Si system per unit area is [28]

$$\gamma_{CS} = \frac{E_T^{CS} - E_B^{Cu} - E_B^{Si}}{2A} \quad (2.3)$$

The total energy E_T^{CS} is the sum of the bulk Cu and bulk Si energies and surface energies for each block with sufficient separation between the surfaces. The bulk cohesive energies are $E_B^{Cu} = n_{Cu}e_B^{Cu}$, $E_B^{Si} = n_{Si}e_B^{Si}$, where n_{Cu} is the number of copper atoms and e_B^{Cu} is the cohesive energy per atom. The energy of as-created interfaces for the Cu-Si system per unit area is [28]

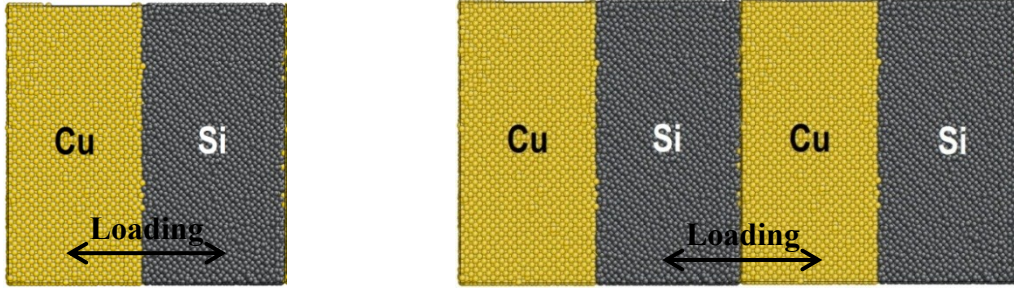
$$\gamma_I = \frac{E_T^I - E_B^{Cu} - E_B^{Si}}{2A} \quad (2.4)$$

The total energy E_T^I here refers to the one right after the equilibrium run to form the interface. Once the periodicity in the loading direction is applied, the number of interfaces becomes two as seen in Figure 2.1a. In order to determine the fracture energy, one needs to eliminate the energy of the still bonded interface due to the periodicity in the loading direction. Once the specimen is loaded to fracture, only one interface in Figure 2.1a will break and thus leaves the bonding energy of the remaining interface as unknown. Our strategy is to create another periodic geometry with one more repeat in the loading direction as seen in Figure 2.1b. Due to the periodicity, this new geometry with four interfaces is physically identical to the two-interface one up till the point of fracture. The total energies for these two geometries, at the point of fracture, are

$$E_T^F = E_B^{Cu} + E_B^{Si} + \gamma_F A + \gamma_I' A \quad (2.5)$$

$$E_T^F = E_B^{Cu} + E_B^{Si} + \gamma_F A + 3\gamma_I' A \quad (2.6)$$

where γ_I' is the unit area energy of the still bonded interface. The total energy E_T^F and the cohesive energy like E_B^{Cu} are of different values in Eqs. (2.5,2.6) for the two specimens. The fractured surface energy γ_F can thus be determined by solving Eqs. (2.5,2.6).



(a) Two interfaces due to periodicity

(b) Four interfaces due to periodicity

Figure 2.1: Two periodic planar geometries with sizes of $11.57 \text{ nm} \times 11.57 \text{ nm} \times 11.57 \text{ nm}$ for (a) and $23.14 \text{ nm} \times 11.57 \text{ nm} \times 11.57 \text{ nm}$ for (b). The geometries (a) and (b) are essentially identical due to periodicity.

Based on the fractured energy and the as-fabricated interface energy, the work of fracture for the actual separated interfaces can be calculated as

$$W_S = \gamma_F - \gamma_I \quad (2.7)$$

The Griffith work of fracture associated with the perfect cleavage fracture can be calculated as

$$W_G = \gamma_{CS} - \gamma_I \quad (2.8)$$

Given these two fracture work, the “toughness enhancement factor” can be thus defined as [28]

$$T = W_s/W_G \quad (2.9)$$

Table 2.1: Interface and Fracture Energies for the Cu-Si Interface

γ_F (eV/Å ²)	γ_{CS} (eV/Å ²)	γ_I (eV/Å ²)	W_s (eV/Å ²)	W_G (eV/Å ²)	T
0.4277	0.3938	0.3598	0.0679	0.0340	2.0

It is worth noting that the “toughness enhancement factor” calculated in Table 2.1 is very close to that in [28] ($T=2.2$) for the interface with the same crystallographic orientation. The surface fracture with $T > 1$ is characterized as “ductile” and these “ductile” interfaces were further categorized into two types of failure: those fail after or before dislocation emission [28]. Although the (1 0 0) interface tends to debond after dislocation emission for the one dimensional planar configuration [28], it remains unclear for the case of a spherical particle inside matrix as the preferred slip plane of FCC metal is not in the (1 0 0) direction. Thus, there could be the competition of the break of atomic bond at the (1 0 0) interface due to the maximum interface stress there and that due to the dislocation emission with preferred slip type {111}. This competition determines which one would trigger the interfacial debonding of the spherical particle from an initially dislocation-free matrix.

2.3.2. The Particle-Matrix Case

As illustrated in Figure 2.2, the periodic simulation box in all three dimensions is employed to represent the copper nanocomposite with uniformly-distributed silicon nanoparticles. Different simulation specimens including varying simulation-box size and different volume fraction of Si nanoparticle are also tested. The volume fraction of the spherical particles varies from 0.15625%

to 10%. The largest simulation box contains a spherical particle of 30 nm in diameter with a total of 11.9 million atoms in the system.

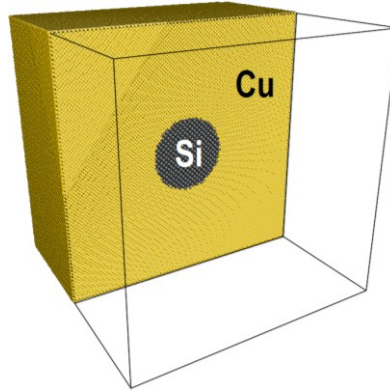


Figure 2.2: Cubic simulation box halved showing Silicon spherical particle (gray) embedded inside Copper matrix (yellow).

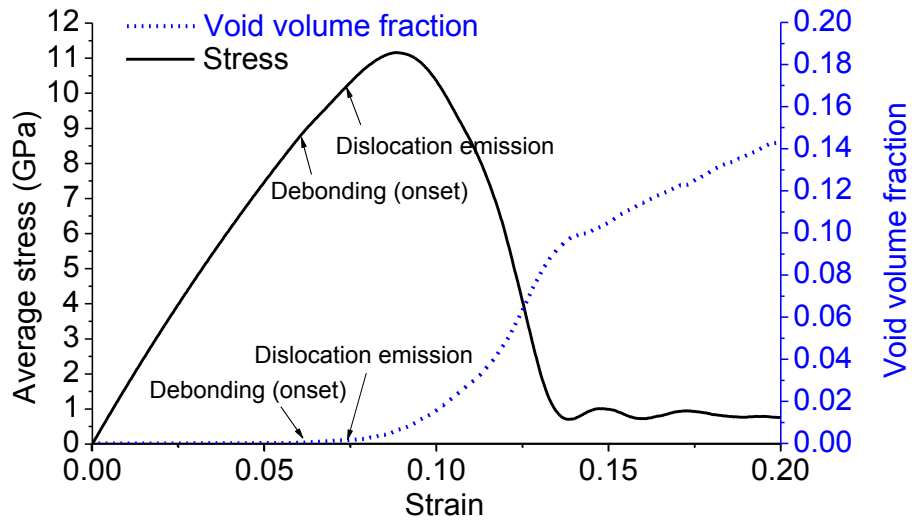


Figure 2.3: The stress-strain relation, void volume fraction under a simulation size of 26.03 nm × 26.03 nm × 26.03 nm with a spherical particle of 7.5 nm in diameter embedded under a strain rate of $2 \times 10^9 \text{ s}^{-1}$.

Figure 2.3 shows the average stress and void volume fraction versus strain for the primary simulation case. The ultimate strength of the composite material is reached after initiation of

both events of interfacial debonding and the dislocation emission. It appears that dislocation emission has little impact on the onset of interfacial debonding from an initially dislocation-free matrix, but plays an important role in the subsequent debonding and growth of the nucleated void. After the ultimate strength, the continuing decrease of the load-carrying capacity is due to the fast-rising void volume fraction and dislocation population. At the end of loading, the average stress stabilizes at a level below 1 GPa. Calculation of the volume fraction of nucleated voids from interfacial debonding is a non-trivial issue. The first step is the recognition of different-type atoms on each side of the interface. However, the interfacial debonding will leave a few silicon atoms “glued” on the nucleated void surface comprised of copper atoms. These atoms should therefore be excluded from the recognized particle surface. The second step is to apply the Delaunay triangulation method [86] to: (1) surface copper atoms to calculate the hollow volume inside the matrix, and (2) surface silicon atoms to calculate the current particle volume. The difference of these two volumes gives the volume of nucleated void. At higher strain with excessive void growth, the recognition method could be rather time-consuming due to the increasing number of surface atoms. An alternative approach would be counting those voided volumes inside the meshed simulation box with lattice-sized volumetric elements. In Figure 2.3, the volume fraction of nucleated voids starts to increase rapidly after the onset of dislocation emission. From the start of rapid void growth till a strain of 0.13, the void gains more volume than the total volume increase of the simulation box. This implies that the tightened atomic bonds during elastic deformation in some region have been relaxed. The void volume increasing rate is gradually approaching that of the simulation box. This is mainly due to the strain-confined lateral boundary condition, which is analogous to a plane strain dynamic loading, such as that in a spall test.

2.3.2.1. Initial Debonding During the Elastic Regime

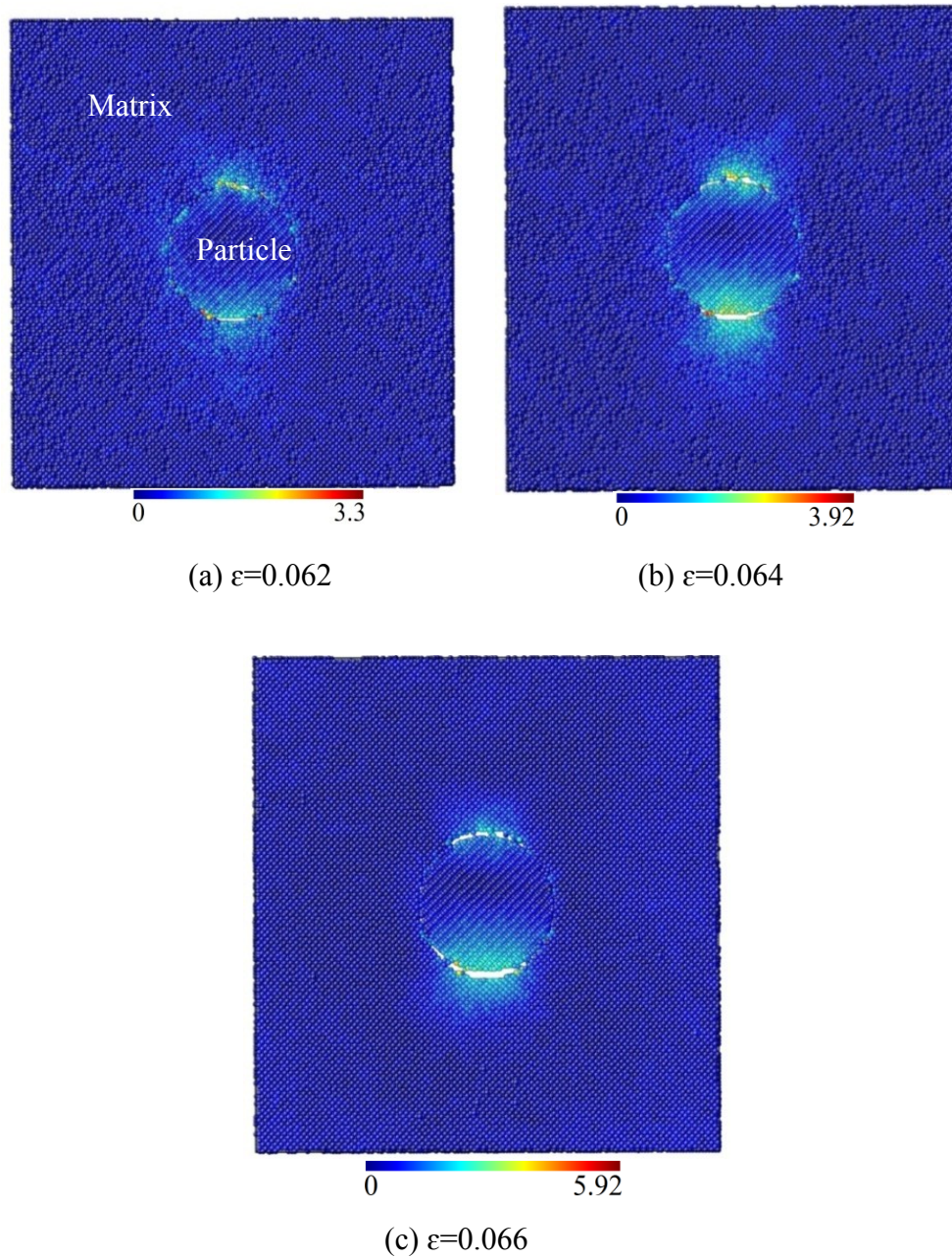


Figure 2.4: Relative displacement (magnitude) during the interfacial debonding. The formula to compute relative displacement (magnitude) can be found in the Appendix. The cutting plane is yoz plane. The unit of color bar is Å.

In this subsection, the localized material transport within the strain range from 0.060 to 0.066 will be further investigated. A better understanding of material transport during the interfacial debonding will help us build an insightful mechanism of this vital event. Atomic displacement can be calculated in terms of the difference between the current and initial positions of atoms. Since periodic boundary condition is involved, attention should be paid to the situation when atoms are crossing the periodic boundary and re-entering in the other side. The displacement for those atoms should be the difference between their initial position and their periodic image of the current position. This straightforward subtraction for the atomic displacement depends on the selection of the coordinate origin. However, the “relative displacement” field, as proposed in Ref. [87], is independent of the choice of the coordinate origin as long as it is attached on the stretched simulation box. Once the homogenous elastic deformation is excluded by using this relative displacement, the remainder is the deformation due to the presence of silicon particle. The magnitude of this relative displacement field during interfacial debonding is plotted Figure 2.4. It can provide a general picture of relative atomic motions during the onset of interfacial debonding.

The initial bonding of interface is achieved by equilibrium run under zero stress. A test has been performed to ensure that the debonding strain is insensitive to the equilibrium duration applied. Atoms of highest magnitude of relative displacement are found at both the upper and lower sides of the Cu-Si interface. The local decohesion initiates on the part of interfacial circumference facing the loading direction. This is consistent with experimental observations under normal tensile loading [16]. The incipient interfacial debonding in Figures 2.4a-c occurs at both upper and lower sides of the interface. Due to the initial perfect bonding between silicon particle and the copper matrix, the silicon particle has also been stretched and deformed

elastically in Figure 2.4a. Heterogeneous deformation builds up inside Si particle during the debonding process in Figures 2.4a-c. This elastic deformation of Si particle has not been recovered until significant interfacial separation. No fracture or void nucleation has been observed inside the silicon particle. It is worth noting that the relative displacement in Figure 2.4 is evaluated with respect to the same origin attached on the box for both matrix and particle since there has not been a translation of the particle with respect to the simulation box.

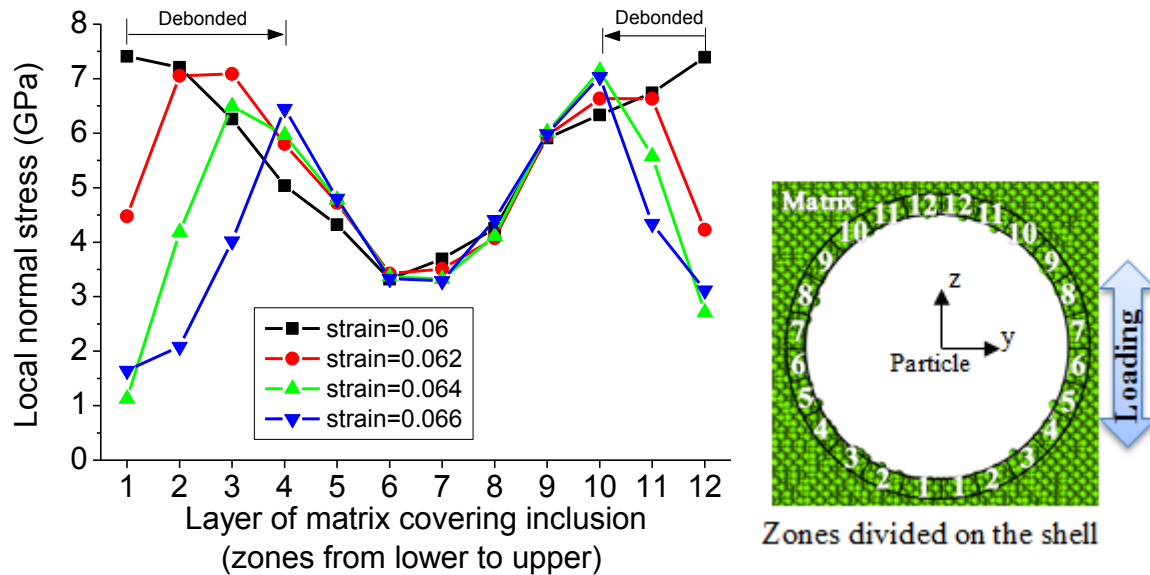


Figure 2.5: Local normal stress at different location inside a spherical shell of matrix covering the particle. The spherical shell has been divided into 12 zones (numbered from 1 to 12) longitudinally and the projection of individual zone onto the xoy plane is an annulus.

Figure 2.5 shows the local normal stresses in thin, annular matrix layers around the particle at different strains. The stress tensor at the atomic scale is measured by the virial stress [88]. The average normal stress is then calculated as the average over each divided annular zone. This atomic “normal stress” distribution is not defined on the spherical interface but on a spherical

shell. Therefore, this normal stress could decrease to a small value but not necessarily zero for the debonded zone. Noreyan et al. [30] showed that shear stress could only induce sliding at the aluminum-silicon interface but not interfacial debonding. Hence, the current attention is only paid to the relation between the normal stress and interfacial debonding. Prior to debonding, the normal stresses at zones 1 and 12 keep rising and thus deteriorate the bonding there. At $\varepsilon=0.06$, right before the interfacial debonding, the normal stresses at upper and lower zones 1 and 12 have already been lowered slightly. The higher normal stresses at the upper and lower regions trigger the local decohesion indicated by a significant decrease in the normal stresses. At $\varepsilon=0.066$, the interfacial debonding has spread from zone 1 to zone 4 (lower side) and also from zone 12 to zone 10 (upper side).

The stress field of a plate with embedded disc is given in [89] under uniaxial tension. For arbitrary biaxial loading, the solution can be easily extended by superposition.

$$\sigma_r = \frac{\sigma}{2} \left[(1+k) \left(1 - \frac{\gamma R^2}{r^2}\right) + (1-k) \left(1 - \frac{2\beta R^2}{r^2} - \frac{3\delta R^4}{r^4}\right) \cos 2\theta \right] \quad (2.10)$$

$$\sigma_\theta = \frac{\sigma}{2} \left[(1+k) \left(1 + \frac{\gamma R^2}{r^2}\right) - (1-k) \left(1 - \frac{3\delta R^4}{r^4}\right) \cos 2\theta \right] \quad (2.11)$$

$$\tau_{r\theta} = -\frac{\sigma}{2} (1-k) \left(1 + \frac{\beta R^2}{r^2} + \frac{3\delta R^4}{r^4}\right) \sin 2\theta \quad (2.12)$$

$$\beta = -\frac{2(G_0 - G_1)}{G_1 + G_0 \kappa_1} \quad (2.13)$$

$$\gamma = \frac{G_1(\kappa_0 - 1) - G_0(\kappa_0 - 1)}{2G_0 + G_1(\kappa_0 - 1)} \quad (2.14)$$

$$\delta = \frac{G_0 - G_1}{G_1 + G_0 \kappa_1} \quad (2.15)$$

where σ is the remote stress in the direction of the uniaxial-strain loading, k ($k < 1$) is the ratio of the stress in the lateral direction over that in the loading direction, R is the radius of the particle, G_0 is the shear modulus for the particle, G_1 is the shear modulus for the matrix and $\kappa_0 = 3 - 4\nu_0$ is for the plane strain case. The normal stress at the interface becomes

$$\sigma_r = \frac{\sigma}{2} [(1+k)(1-\gamma) + (1-k)(1-2\beta-3\delta) \cos 2\theta] \quad (2.16)$$

It has a maximum value at $\theta = 0^\circ$ and $\theta = 180^\circ$ (the upper and lower loading directions) and a minimum value at $\theta = 90^\circ$ (the lateral direction). As seen in Figure 2.5, the maximum and minimum locations of the black curve for the perfectly-bonded particle are consistent with the prediction of Eq. (2.16). This could be taken as a form of validation of MD simulation towards the elasticity theory for inclusion problem.

The magnitude field of relative displacement in Figure 2.4 cannot capture the direction of atomic motion. Fortunately, atomic information such as displacement vector of individual atom, which seems experimentally inaccessible, can be readily acquired from MD simulation. As plotted in Figure 2.6, the displacement vector of the specific atoms may provide more insights into the interfacial debonding.

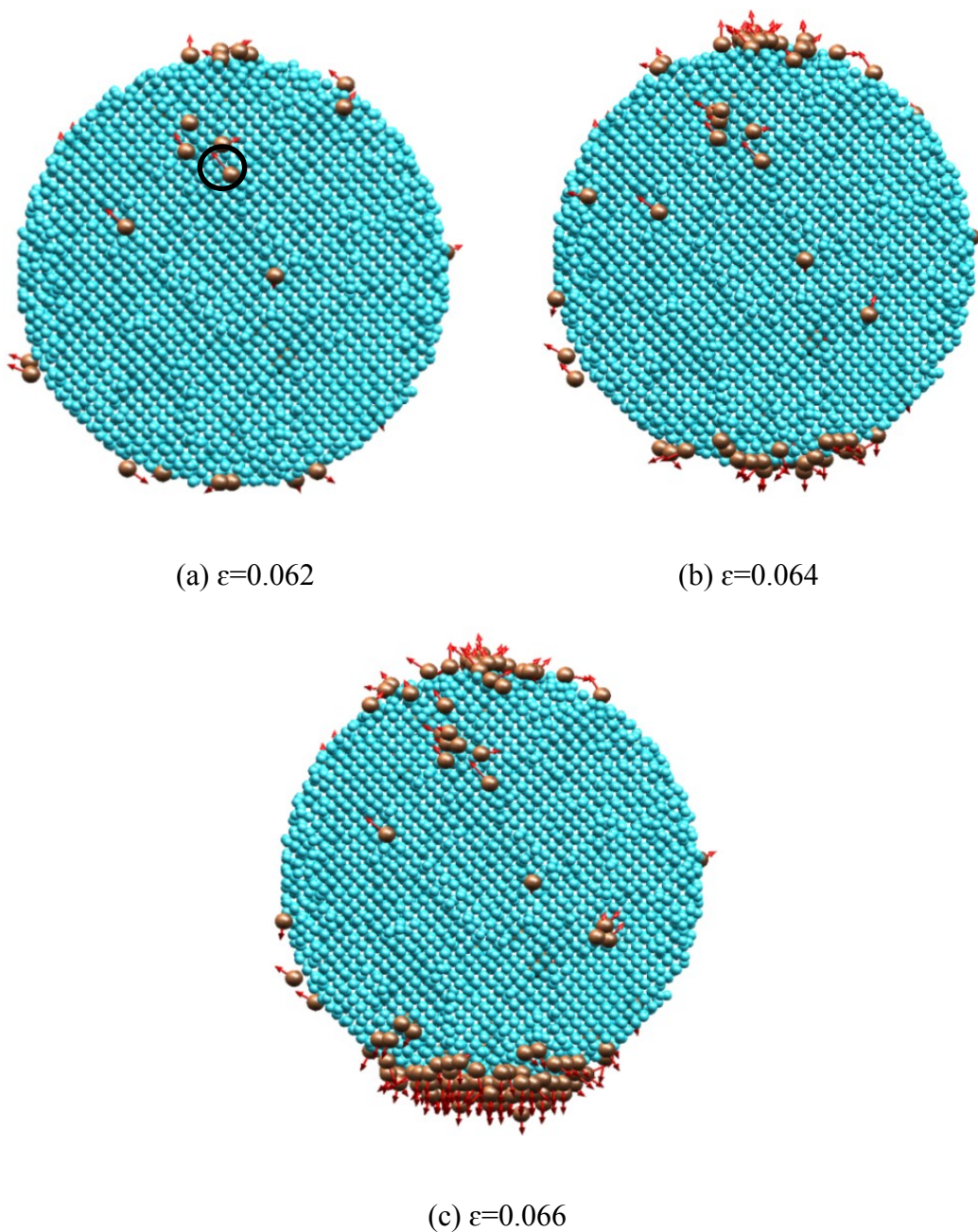


Figure 2.6: Movement of the Relatively-farthest travelled (RFT) copper atoms (in yellow) near the Cu-Si interface. Snapshot has been projected onto the yoz plane. The critical length is set as 2.0 \AA to identify the RFT atoms. The blue atoms represent silicon particle atoms.

Although interfacial debonding has already occurred in Figure 2.6a, the RFT copper atoms are rather scattered and so are their displacement vectors. In Figure 2.6b, the RFT copper atom

with the longest displacement arrow is not found at either of the two debonding sites. This implies that the interfacial debonding is not a local event at the atomic scale. Rather, interfacial debonding should be attributed to a cluster of atoms with higher-than-average displacements. Figures 2.6a-c illustrate the competition between the two debonding sites. Initially, RFT atoms appear first at the upper side. In Figure 2.6b, the lower side has started gaining more RFT atoms than the upper side. Finally in Figure 2.6c, the number of RFT atoms at lower side remarkably surpasses that at the upper side. More importantly, the displacement arrows at the lower side shift into a highly-ordered alignment. These two facts lead to a larger separation at the lower side than the upper side, as shown in Figure 2.4c.

2.3.2.2. The Subsequent Debonding and Void Growth after Dislocation Emission

The dislocation emission begins at the strain of 0.074. The gray dislocation lines on the interface are induced by the mismatch between the lattices of the two materials, as shown in Figure 2.7a. They appear and continue to evolve from the beginning of loading. The onset of dislocation emission is recognized only at the time when the dislocation curves protrude out of Si particle like the blue one in Figure 2.7a. The newly-formed dislocation structure facilitates not only the growth of the nucleated void but also the subsequent debonding. Next, we will study the evolution of the dislocation network and the corresponding relative displacement.

The subsequent development of the dislocation structure inside the matrix is somehow similar to the case of a pre-existing void inside an FCC metal. Shear dislocation curves emitted from the nucleated void grow and glide on four slip planes to form a frustum-like structure at the upper region, as shown in Figure 2.7b. Secondary dislocation structures form subsequently at the lower and lateral sides in Figure 2.7b. This frustum-like structure of dislocations growing from

the particle is highly asymmetric. The asymmetric dislocation structure here could be associated with the irregular shape of the nucleated void. Similar to the pre-existing void case [87], the frustum-like dislocation structure here also induces the local material transport. Those red RFT atoms illustrate the material transport related to the dislocation emission. As demonstrated in Ref. [87], shear curves are capable of inducing local material transport. In Figure 2.7b, the appearance of red atoms inside the upper frustum-like structure of dislocations indicates that material can move away from the particle surface with the aid of dislocation structure. In the absence of frustum-like structure shown in Figure 2.7a, the nucleated void grows elastically.

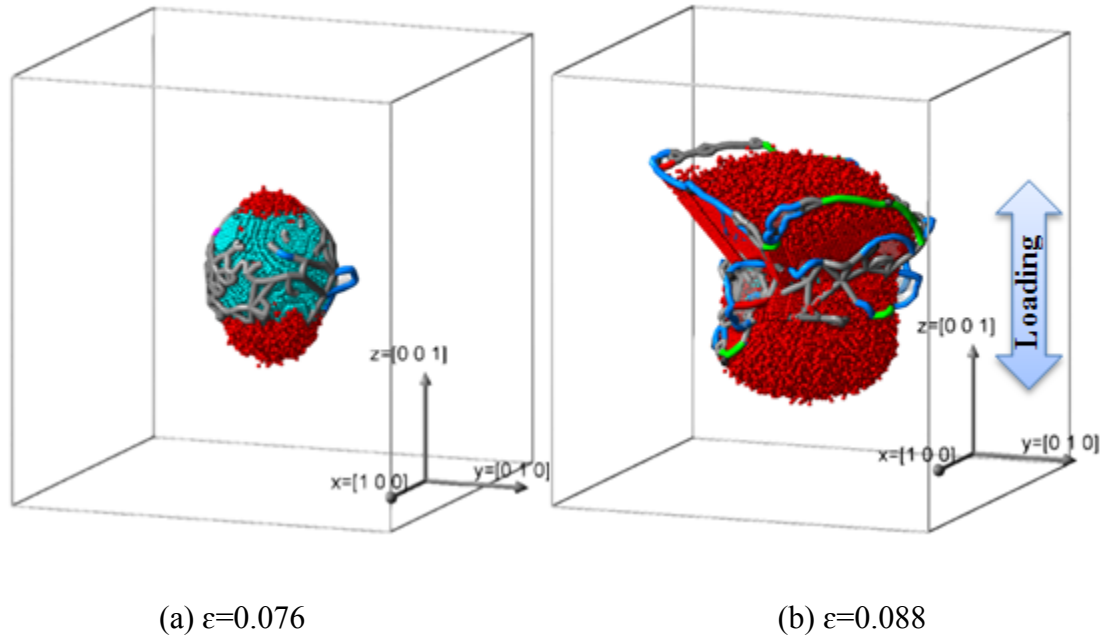


Figure 2.7: Dislocation network and RFT atoms after dislocation emission. Blue atoms represent particle-matrix/void-matrix interface/surface, while the blue and green rendered lines represent dislocation lines. The critical length is set as 2.0 \AA to identify the RFT atoms.

The stress component of image field due to a perfectly-bonded particle on a nearby dislocation can be calculated from [90]

$$\sigma_x = \frac{G_1 b_y}{\pi(\kappa_1 + 1)R} \left[\frac{A+B}{\bar{r}(\bar{r}^2 - 1)} - \frac{A-1+M(\kappa_0 + 1)}{\bar{r}^3} \right] \quad (2.17)$$

$$\tau_{xy} = -\frac{G_1 b_x}{\pi(\kappa_1 + 1)R} \left[\frac{A+B}{\bar{r}(\bar{r}^2 - 1)} + \frac{3A-B}{\bar{r}^3} \right] \quad (2.18)$$

$$\sigma_y = -\frac{G_1 b_y}{\pi(\kappa_1 + 1)R} \left[\frac{A+B}{\bar{r}(\bar{r}^2 - 1)} - \frac{A-1+M(\kappa_0 + 1)}{\bar{r}^3} \right] \quad (2.19)$$

where $\bar{r} = r/R$ and the constants are given as [90]

$$A = \frac{G_1 - G_0}{G_1 + G_0 \kappa_1} \quad (2.20)$$

$$B = \frac{G_1 \kappa_0 - G_0 \kappa_1}{G_1 \kappa_0 + G_0} \quad (2.21)$$

$$M = \frac{G_1 G_0 (\kappa_1 + 1)}{(G_1 \kappa_0 + G_0)(G_1 \kappa_0 - G_1 + 2G_0)} \quad (2.22)$$

Thus, the Peach-Koehler force exerted by the perfectly-bonded particle on the dislocation can be computed by [57]

$$\mathbf{F} = (\boldsymbol{\sigma} \cdot \mathbf{b}) \times \mathbf{e}_z \quad (2.23)$$

Rewriting Eq. (2.23) by using the stress components, we have

$$F_\rho = b\tau_{xy} \cos 2\theta + b(\sigma_y - \sigma_x) \sin \theta \cos \theta \quad (2.24)$$

The corresponding shear stress along the slip plane of dislocation by applying the remote stress is

$$\tau = (\sigma_{\theta} - \sigma_r) \sin \theta \cos \theta + \tau_{r\theta} (\cos^2 \theta - \sin^2 \theta) \quad (2.25)$$

Once substituting the stress components σ_{θ} , σ_r and $\tau_{r\theta}$ as given by Eqs. (2.10-2.12) into Eq. (2.25), Eq. (2.25) can be rewritten as

$$\tau = \sigma f(r, \theta) \quad (2.26)$$

where the rather lengthy function $f(r, \theta)$ can be easily determined through using Eqs. (2.10-2.12). Lubarda et al. [18, 91] defined the critical stress for dislocation emission as once the remote stress balances the attraction force from the inclusion as

$$\tau b + F_{\rho} = 0 \quad (2.27)$$

By assuming the dislocation site is near but not falls on the interface, the critical remote stress can be derived as

$$\sigma_{cr} = \frac{-F_{\rho}}{b \cdot f(r, \theta)} \Big|_{x=\frac{\sqrt{2}R}{2} + \rho b, y=\frac{\sqrt{2}R}{2}} \quad (2.28)$$

This predefined dislocation position is given in [18]. It is proposed that the dislocation will likely be emitted from void once the equilibrium distance is less than the dislocation core width ρb . Therefore, the remote stress is required to balance the attractive force exerted by the inclusion/void at $(\sqrt{2}R/2 + \rho b, \sqrt{2}R/2)$. Once setting $G_0 = 0$ for the inner particle, Eq. (2.28) is reduced to the critical stress for dislocation emission with an embedded void. Thus, Eq. (2.28) becomes a simply generalized version for either a perfect-bonded particle or a void inside the matrix. In our calculation, the shear moduli are $G_1=48$ GPa for copper and $G_1=47$ GPa for silicon [92], $b=0.255$ nm is the magnitude of the dislocation Burgers vector for copper, the Poisson's

ratios are $\nu_1=0.34$ for copper and $\nu_0=0.27$ [93] for silicon, the stress ratio k is found to be 0.65 for the concerned strains and the core cutoff parameter ρ is set as 1 [18].

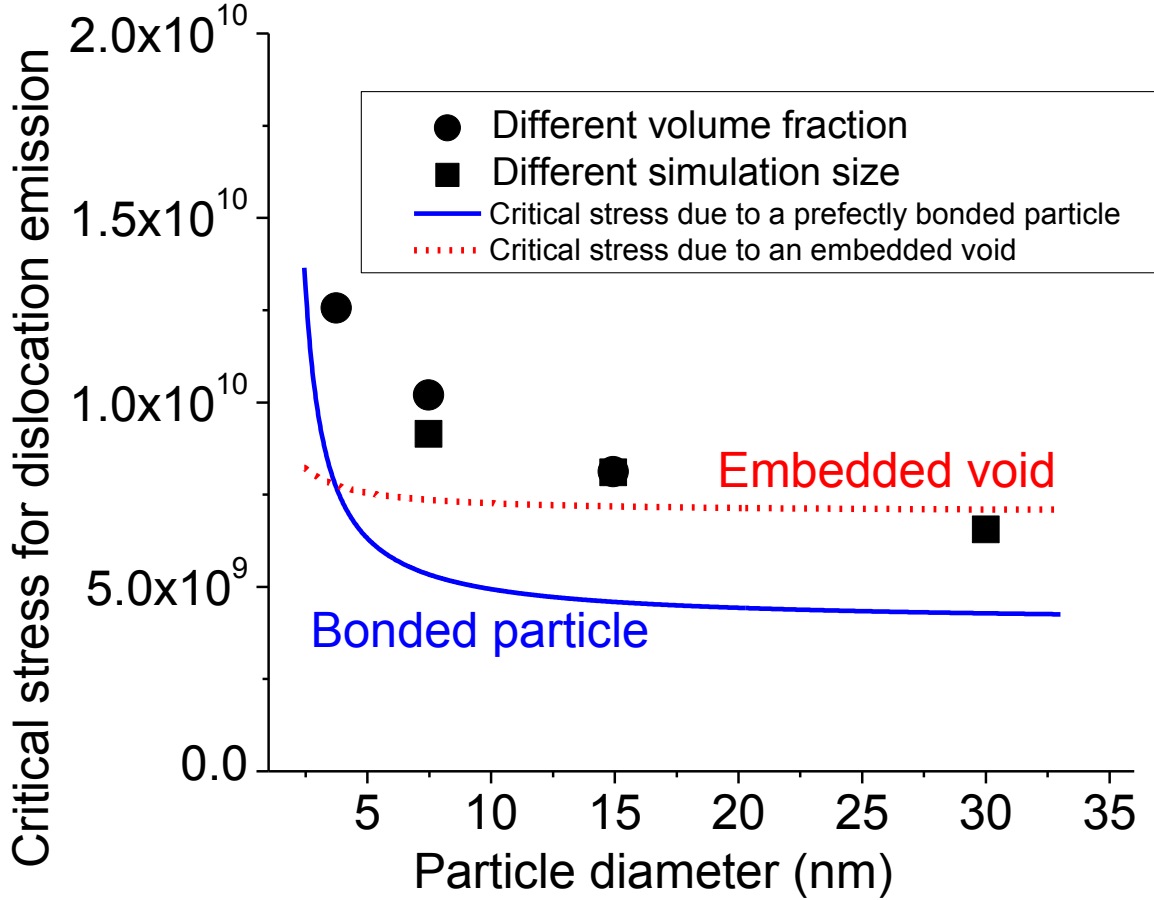


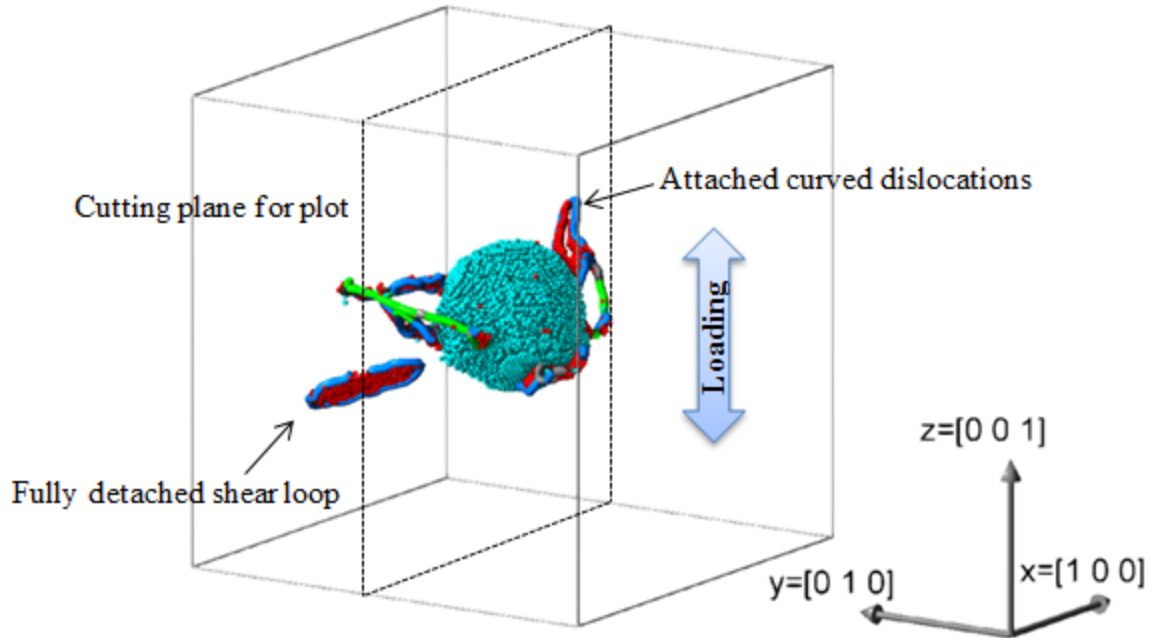
Figure 2.8: Critical stresses by Lubarda model compared with MD results.

Figure 2.8 shows the onset stress for dislocation emission of MD simulation compared with the critical stress predicted by the generalized Lubarda model. The filled circle points are the particles of different volume fraction but inside a same-sized simulation box and the filled square points are those of the same volume fraction but inside different-sized simulation box from 13.01 nm to 52.06 nm in its length. Both the two groups result in a variation of the particle size. In general, the dislocations are emitted after the interfacial decohesion if the matrix is initially

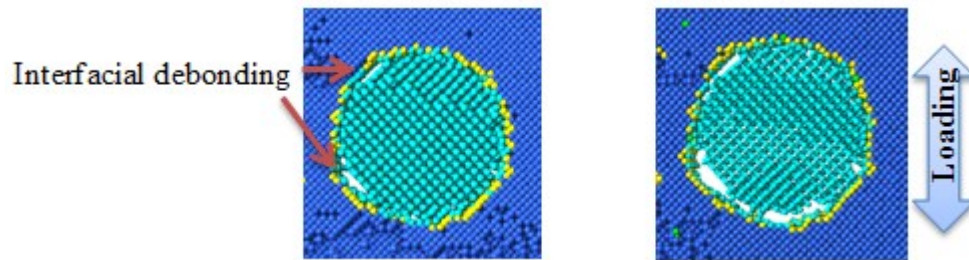
lower side of particle facilitates the void nucleation. However, the interfacial debonding at the upper side is gradually healed from Figure 2.9a to Figure 2.9b. This healing process can be understood as follows. The interatomic force, for atoms being small distance apart but not far away, could enable them to rejoin. Of course, the premise is that the wider separation at the lower side has eased the local stress at the upper side. The break of symmetry for interfacial debonding, started in Figure 2.4c, has since been enhanced. The interfacial separation at the lower side causes not only the healing of upper separation but also the translation of the particle with respect to the simulation box. To single-phase material transport, any origin as long as attached on the simulation box will result in the same relative displacement [87]. However, it is a different scenario when there is a translation of a second-phase particle. The relative displacement inside the particle should now be separately evaluated by using the particle center as the origin to eliminate the effect of this rigid-body translation. The mild change of displacement field inside the Si particle indicates that the elastic deformation gradually recovers. The outside load can barely be transmitted from the matrix to particle due to severe separation between the particle and matrix at the lower side. For the copper matrix, dislocation lines cause strong discontinuity in the relative displacement field as seen in Figure 2.9b. The formed dislocation structure, mainly shear curves, facilitates the mass transfer and therefore grows the nucleated void. It is the formation of dislocations, rather than the conservative motion of dislocation loops that helps transfer the mass. The mass transfer caused by the motion of a dislocation loop is given in [57]

$$\delta V = \oint_C \mathbf{b} \cdot (\delta \mathbf{r} \times d\mathbf{l}) \quad (2.29)$$

The triple product in Eq. (2.29) is zero when the motion is a pure slip, i.e. the three vectors \mathbf{b} , $\delta\mathbf{r}$ and $d\mathbf{l}$ are in a same plane.



(a) $\epsilon=0.056$



(b) $\epsilon=0.04$

(c) $\epsilon=0.056$

Figure 2.10: Interfacial debonding with pre-existing dislocations inside matrix. Dislocation network is shown in (a), where blue atoms represent particle-matrix/void-matrix interface/surface, the blue and green rendered lines represent dislocation lines and the red atoms show the stacking fault area. The cutting plots (b) and (c) show the interfacial debonding.

Neither the conservative motion of a shear loop as seen in Figure 2.10 nor that of a prismatic loop can cause mass transfer. Figure 2.10a specifically shows the case when there are pre-existing dislocations before the major tensile loading. Given all the other simulation specifications the same, we first preload the specimen with 0.08 tensile strain and then compress it back with the same amount of strain. The dislocation structure formed during this preloading and certainly will not disappear after the compressive load. Then, equilibrium run of 50 ps is applied to bond the interface again and removes the residual stress. The new tensile loading is then applied on this unstrained specimen with pre-existing dislocations. With new tensile load up to a strain of 0.04, interfacial debonding (see Figures 2.10b and c) now not only starts earlier but also aligns at a near 45° (or 135°) angle to the loading direction under the influence of pre-existing dislocations. This angle, close to that of the slip system in FCC metal, clearly indicates the influence of pre-existing dislocations (see in Figure 2.10a) on the onset of interfacial debonding.

2.3.3. The Size Effect

The scope of the MD simulation could be limited by two key factors: length scale and time scale. As for the length scale, various testing techniques have demonstrated that the decreasing sample size could substantially increase the stress response of the testing material [33-36]. In addition to the characteristic size of nanoparticle, the volume fraction of particle is also important to the particle-matrix geometry. The first to be examined is the effect of particle volume fraction on the stress response, which is achieved by fixing the size of the cubic simulation box. The second to be examined is the effect of intrinsic simulation size on the stress response, which is through fixing the volume fraction of particles.

2.3.3.1. Different Volume Fraction V_{fr} of Particle inside a Same-Sized Simulation Box

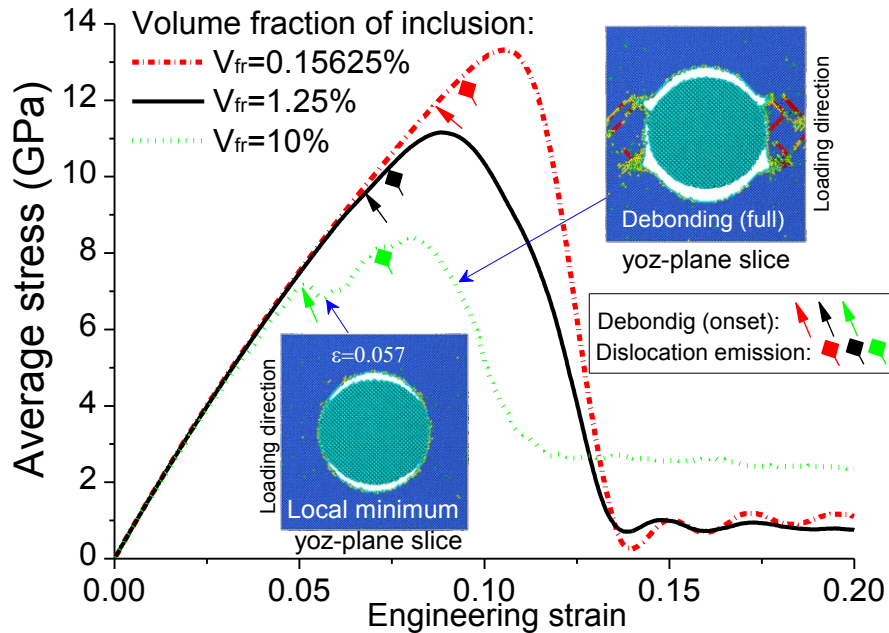


Figure 2.11: Average stress in the loading direction with different volume fraction of particle.

Figure 2.11 shows the average stress curve under different volume fractions of particles with the same box size. The strain of interfacial debonding (onset) clearly depends on volume fraction of particles. Larger particles nucleate voids at lower strains. This observation is consistent with both established experimental and theoretical studies [94-96]. The critical stress required for dislocation emission is also inversely related to the particle size. This relation is the same as observed in the simulations with pre-existing voids [97]. Recent experiment shows that the local volume fraction of second-phase particles can strongly promote damage formation and lower the yield stress as well [98]. The 10%-particle case exhibits considerable difference than the other two curves. Due to its much larger lateral spacing, the interfacial debonding, despite a yet small nucleated void, can effectively influence the overall stress-strain relation and create a local minimum at $\epsilon = 0.057$ in Figure 2.11. The local normal stress around the matrix layer surrounding

the particle in Figure 2.12 indicates that the maximum at $\epsilon=0.057$ is the lowest among the five different strain cases. Before $\epsilon=0.057$, the interfacial bonding is strong at zones 4 and 9. However, a shift of these strong bonding sites occurs at $\epsilon=0.057$. From $\epsilon=0.057$ to $\epsilon=0.059$, the strong bonding sites have shifted to zones 5 and 8. The recovered interfacial bonding at these new sites thus regains the load-carrying capacity of the composite. The strong recovery from this local minimum is also due to the relatively slow growth of void volume fraction.

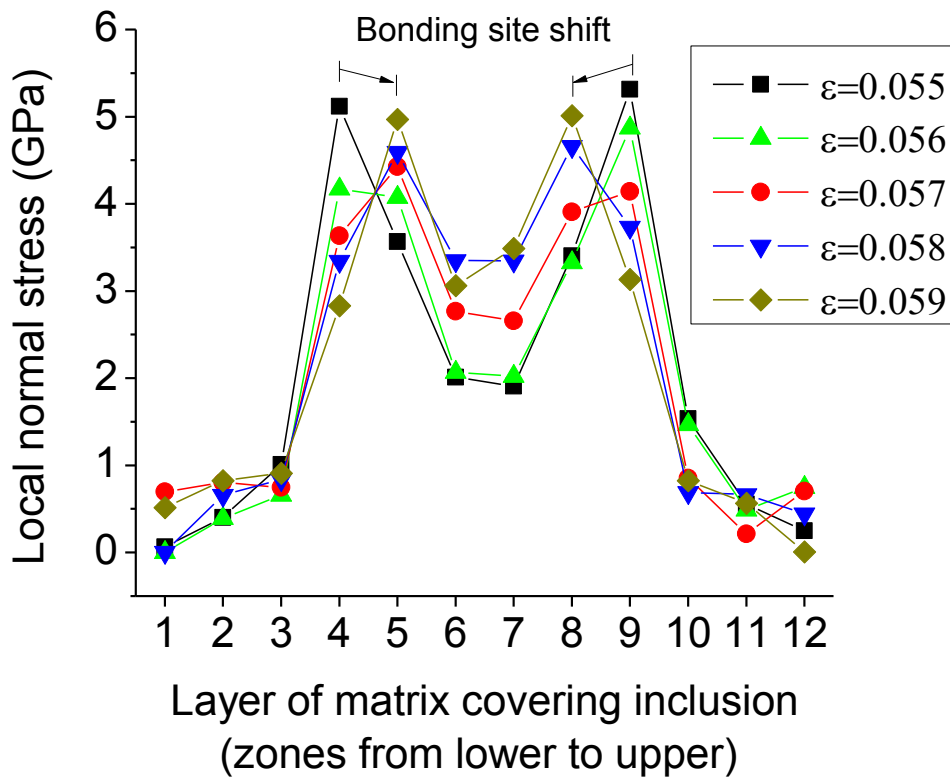


Figure 2.12: Local normal stress at different location inside a spherical shell of matrix covering the particle for $V_{fr}=10\%$ case. Same zones are divided here as in Figure 2.5.

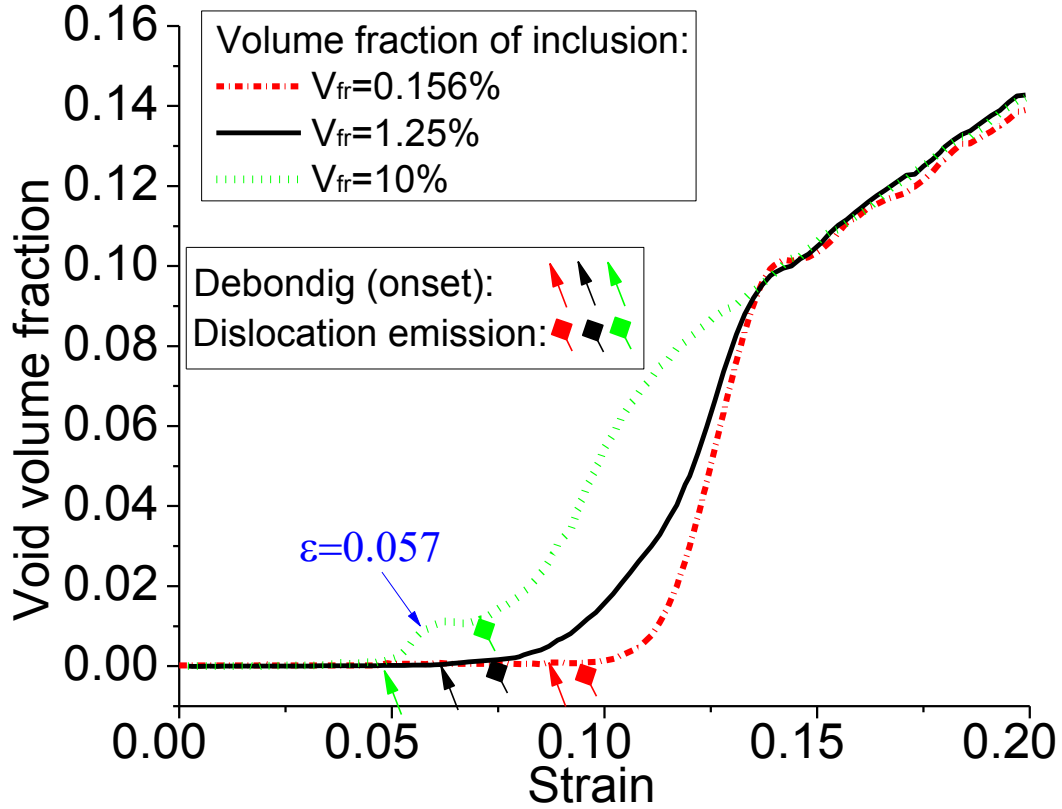


Figure 2.13: Nucleated void volume fraction under different particle volume fraction.

In Figure 2.13, very limited void growth is seen from $\epsilon=0.057$ to the onset strain of dislocation emission (marked by the green quadrilateral arrow). Shortly after, the rapid buildup of dislocation structure accelerates the void growth and lowers the average stress. This stress drop during debonding process has also been predicted using the cohesive-zone method [99]. In that study, the primary case with 13% volume fraction shows a considerable sudden drop of stress during debonding, and the increasing particle volume fraction further enhances the stress drop [99]. This positive correlation is also true to our MD simulation. The only difference is that, in the present simulation, the sudden stress drop is not related to the dislocation emission. However, dislocation emission does contribute to the interfacial debonding in the lateral direction for the $V_{fr}=10\%$ specimen up to $\epsilon=0.09$. The sliced snapshot showing a full debonding

can be found in the inset of Figure 2.11. Four cleavages are created from the dislocation emission sites. The total debonding is only inside the yoz plane, and helped by the spacing created by dislocation emission. However, the particle still partly bonds to the matrix if viewed by the xoz plane.

All ultimate strengths of the three cases are reached after both the onset of interfacial debonding and dislocation emission. The rising volume fraction of particles dramatically lowers the ultimate strength of the composite. However, the average stress of the 10% particle case retains a higher load-carrying capacity at the end of loading. Since the final void volume fractions are very close among the three cases, the higher final stress of the 10%-particle specimen is mainly attributed to its thicker intervoid ligament as well as the shape of void. The shape of nucleated void from the 10%-particle specimen appears close to a sphere, while the nucleated voids from the other two specimens are severely elongated in the lateral directions.

For the two specimens with smaller particle volume fractions, observable void growth only appears after dislocation emission. The void volume created by debonding before dislocation emission is only significant for the $V_{f1}=10\%$ specimen. It has been stabilized at a certain porosity level until dislocation emission occurs. Up to $\epsilon=0.15$, the three specimens result in a very close volume fraction of the nucleated voids. This can be attributed to the strain-confined lateral boundary condition.

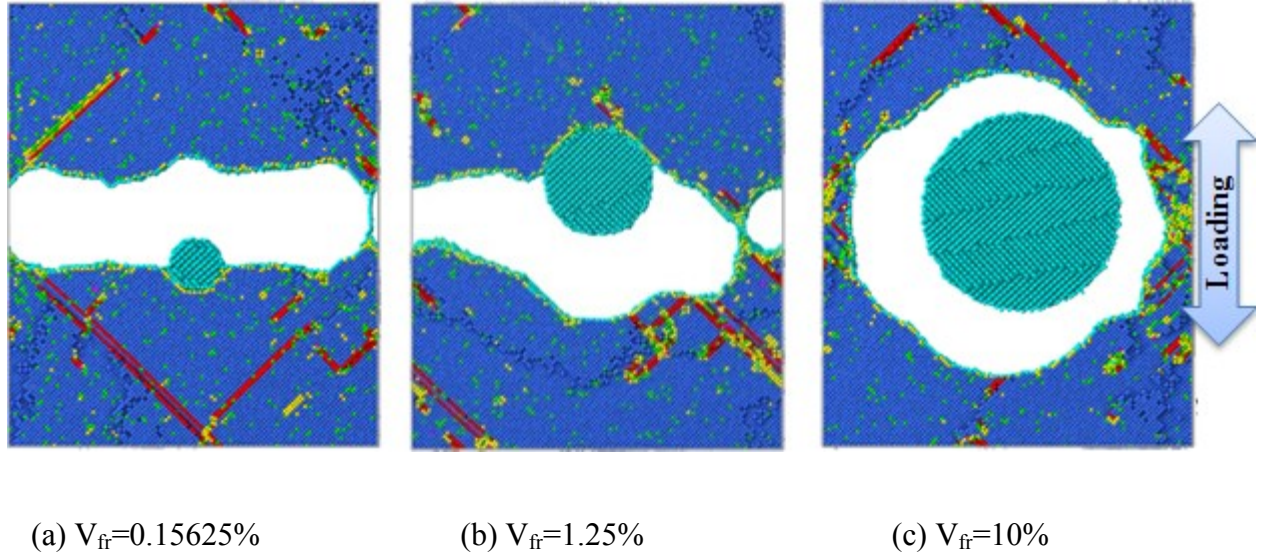


Figure 2.14: Growth and coalescence of the nucleated void under different particle volume fraction ($\epsilon=0.2$ and cutting plane is yoz plane). Snapshots are plotted by ATOMVIEWER [100]. The cutting plane is the yoz plane at the box center. The modified bond-angle distribution (BAD) method, originally introduced by Ackland and Jones [101] is applied to color the atoms. Red atoms here are not RFT atoms.

Light blue atoms, with less than 10 neighbours, are classified as the free surfaces which apply to the atoms on both surfaces of the silicon particle and nucleated void. The red atoms, with 12 neighbours and only three straight bonds, represent the stacking fault atoms (They are not RFT atoms here). Dark blue atoms are the regular, face-centered-cubic atoms. The dislocation lines and large number of disordered atoms help grow the void towards its periodic neighbors in the lateral directions. The present MD simulation illustrates that second-phase particles can induce void nucleation, growth and coalescence, the same as described by the classical ductile fracture theory, despite the applied ultra-high strain rate. In Figure 2.14, a prominent feature is the different shapes of the nucleated voids. The $V_{fr}=0.156\%$ specimen leads to the most elongated void in the lateral direction. In contrast, the $V_{fr}=10\%$ specimen results in a

sphere-like void. Hence, the volume fraction plays a dominant role in the shape evolution of the nucleated void from interfacial debonding. The difference in final stress level can be attributed to the difference in the final void shape given that their porosities are quite close. Indeed, investigation of void shape effect clearly demonstrates that voids elongated in the transverse direction of loading will significantly lower the load-carrying capacity [97, 102].

2.3.3.2. Different Simulation Box Size V_{box} with Particle Volume Fraction $V_{\text{fr}}=10\%$

As the effect of particle volume fraction has been studied, the further attention will be paid to the particle size effect while keeping volume fraction the same. As the $V_{\text{fr}}=10\%$ specimen implies that relatively large particles (clustering effect) can enhance the impact of interfacial debonding on the stress-strain curve, it is then of great interest to investigate the size effect while keeping V_{fr} as large as 10%.

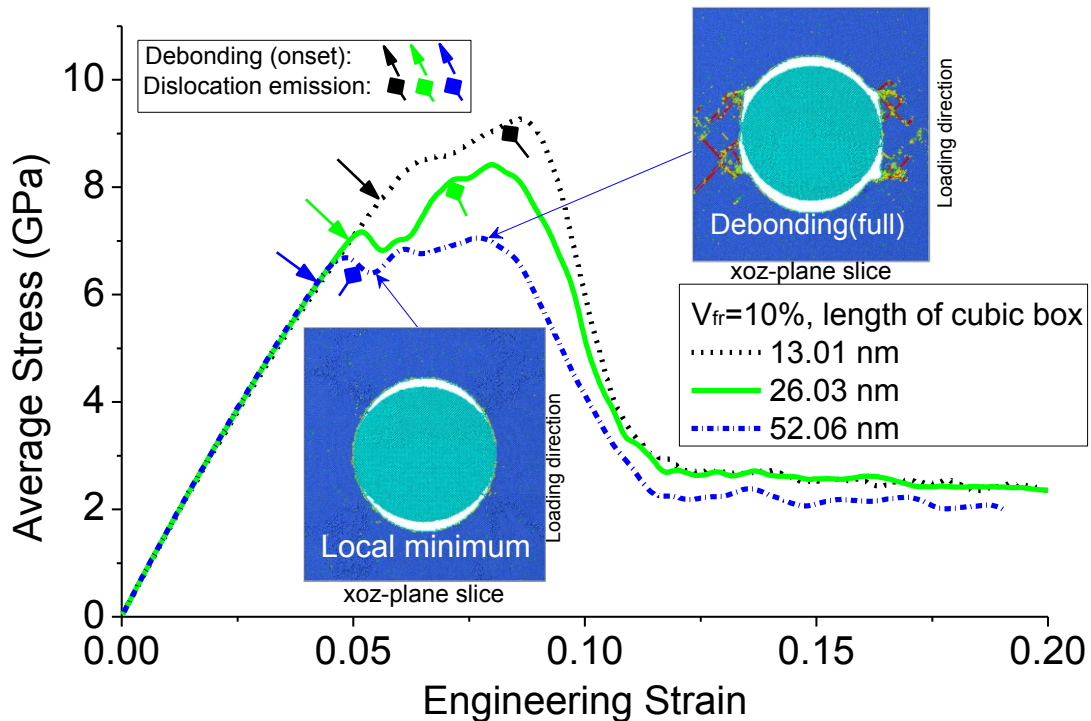


Figure 2.15: Average stress in the loading direction with different-sized simulation box.

As Figure 2.15 shows, the inverse relation between the debonding strain and the particle size also holds here. The critical stress to trigger dislocation emission is also inversely related to the particle size. The debonding strain and dislocation emission stress are inversely related to both volume fraction of particles and the side length of the simulation box. However, the debonding strain appears more strongly related to the volume fraction than the simulation size. A higher volume fraction plays a stronger role in promoting interfacial debonding than the overall size of the nanocomposite. Among the three cases with 10% volume fraction of particle, the stress-strain curve of the largest size becomes more flat during debonding process. The reason is its earlier dislocation emission compared with the other two specimens. As shown in Figure 2.16, the earlier dislocation emission of the 52.06 nm specimen facilitates the growth of the nucleated void. Thus, the resulted higher porosity lowers the otherwise higher stress response recovered from the local minimum in Figure 2.15.

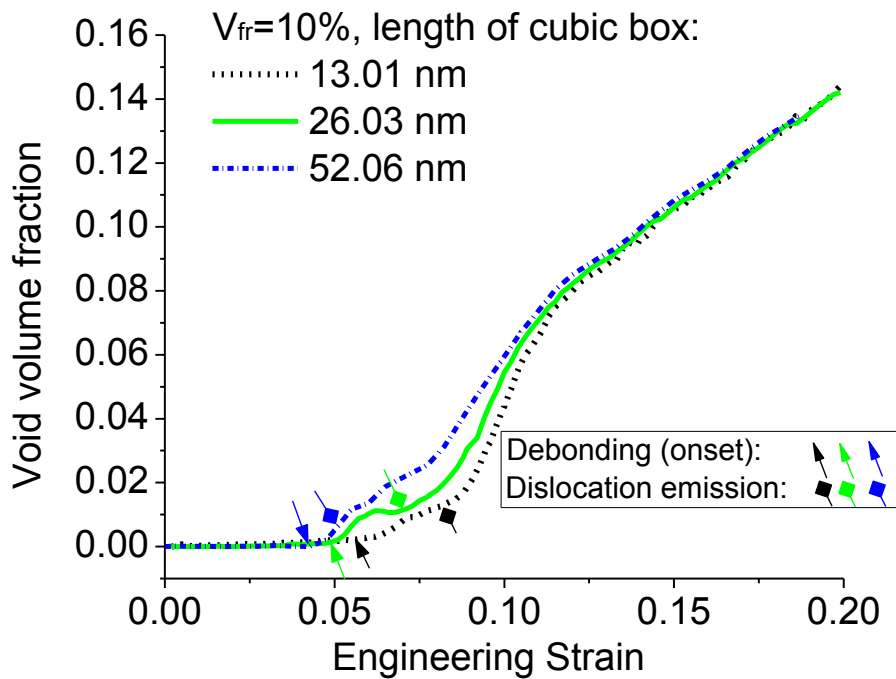


Figure 2.16: Nucleated void volume fraction with different-sized simulation box.

Due to high volume fraction of particles, all three specimens in Figure 2.16 have already nucleated voids with an observable volume fraction before dislocation emission. Once dislocation structures start to build, the porosity accumulation will shift into a faster pace. In all three cases, a similar porosity level is approached at the end of loading due to the strain-confined lateral boundaries.

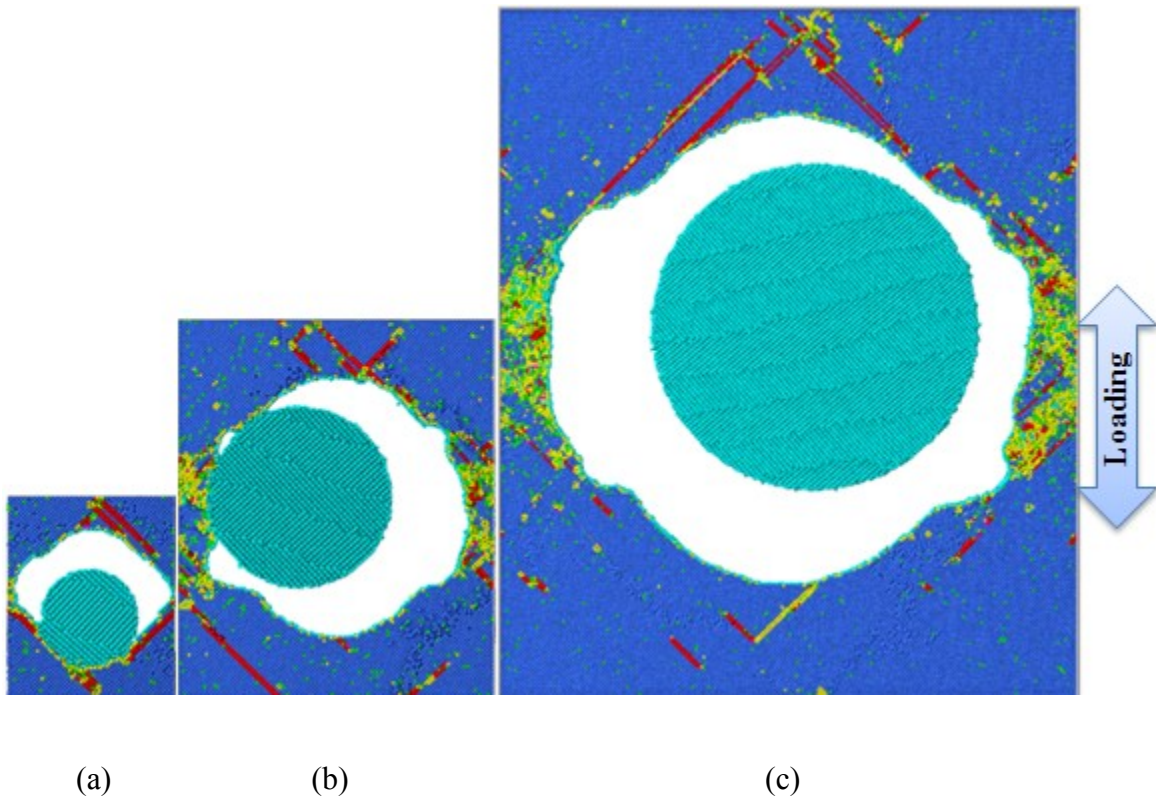


Figure 2.17: Growth of the nucleated void with different simulation box size at $\epsilon=0.19$. The cutting plane is xoz plane. The simulation boxes are with three different lengths, namely, 13.01nm, 26.02 nm and 52.06 nm in (a-c). Snapshots are colored in the same way as Figure 2.14.

For the 13.01 nm specimen, the similar re-bonding of particle-matrix interface on the lower side can be seen in Figure 2.17a. For the 26.02 nm specimen, a 3D shape of nucleated void can be envisaged by combining Figure 2.17b with Figure 2.14c. The particle appearing totally

debonded from matrix in Figure 2.14c is actually still weakly attached if viewed in the xoz plane as shown in Figure 2.17b. The nucleated void from the smallest simulation size evolves into an octahedral shape. For the two larger simulation sizes, both nucleated voids evolve into a more spherical shape. The final void shape relates to the dislocation lines (represented by those red atoms) as shown in Figure 2.17. Despite the similar porosity level among the three cases at the end of loading, the relatively high remaining stress of the 13.01 nm specimen is due to the lower density of disordered atoms at the intervoid ligament and its smaller intrinsic length.

2.3.4. The Strain Rate Effect

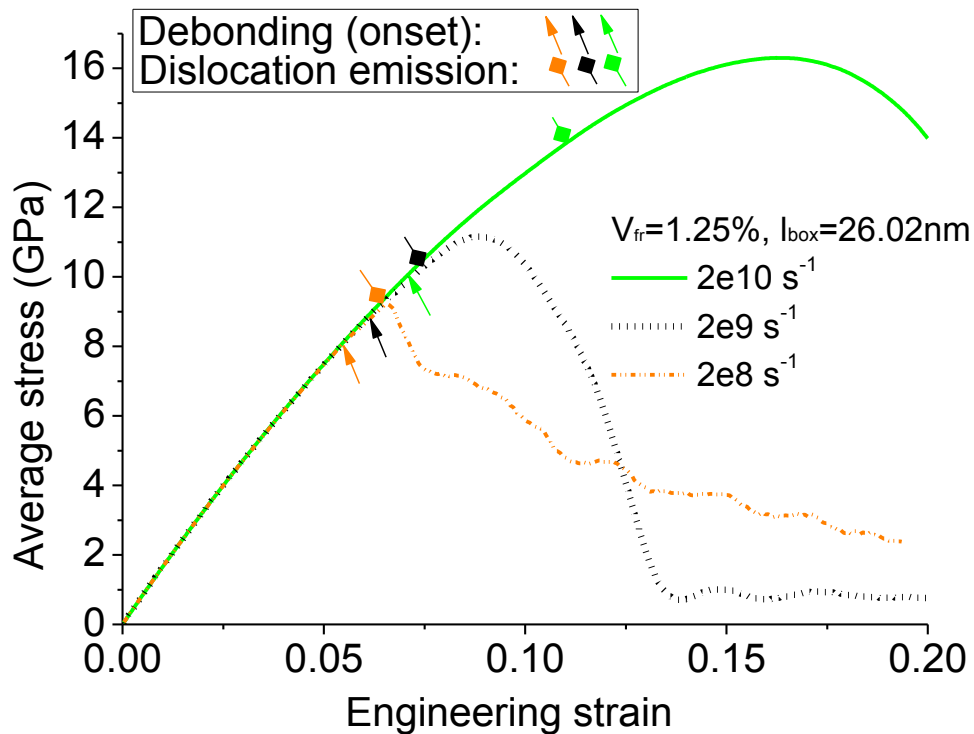


Figure 2.18: Average stress in the loading direction under different strain rate.

The strain rate determines the time scale of the simulation for a given tensile strain. The achievable strain rate by MD simulation is comparable to that of a ballistic loading or a laser

spall test. The dependence of stress response on strain rate could be stronger for the void-embedded specimen compared with the void-free case [103]. The present simulations have shown a similar size dependence of dislocation emission between the particle-embedded and void-embedded specimen [97]. Hence, it is of great importance to also examine the strain rate effect regarding the particle-embedded specimens.

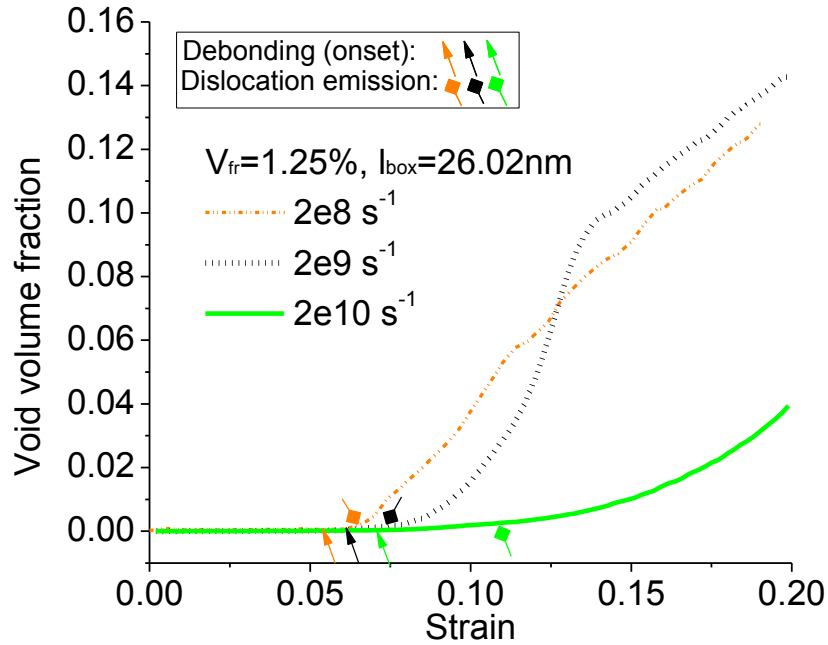


Figure 2.19: Nucleated void volume fraction under different strain rate.

The stress-strain curves under three different strain rates, namely, $2 \times 10^8 \text{ s}^{-1}$, $2 \times 10^9 \text{ s}^{-1}$ and $2 \times 10^{10} \text{ s}^{-1}$ are plotted in Figure 2.18. The debonding strain is lowered by decreasing the strain rate. Higher strain rate not only increases the stress response but also allows the interface to sustain a larger normal stress. For all strain rates concerned, initiation of debonding starts at polar areas of the particle and this event happens prior to dislocation emission if the matrix is initially dislocation-free. The ensuing debonding process features the continuous widening of the separation for all three cases. However, the onset strain of dislocation emission is dramatically

delayed by applying a strain rate of $2 \times 10^{10} \text{ s}^{-1}$. The even larger difference lies in its pattern of dislocation emission. Large dislocation structures are absent under a strain rate of $2 \times 10^{10} \text{ s}^{-1}$, which delays the growth of nucleated void in Figure 2.19. Compared with the $\dot{\epsilon} = 2 \times 10^9 \text{ s}^{-1}$ case, the $\dot{\epsilon} = 2 \times 10^8 \text{ s}^{-1}$ case retains a higher stress level near the end of loading. The higher stress response of the $\dot{\epsilon} = 2 \times 10^{10} \text{ s}^{-1}$ case could also be attributed to its low porosity level throughout the loading.

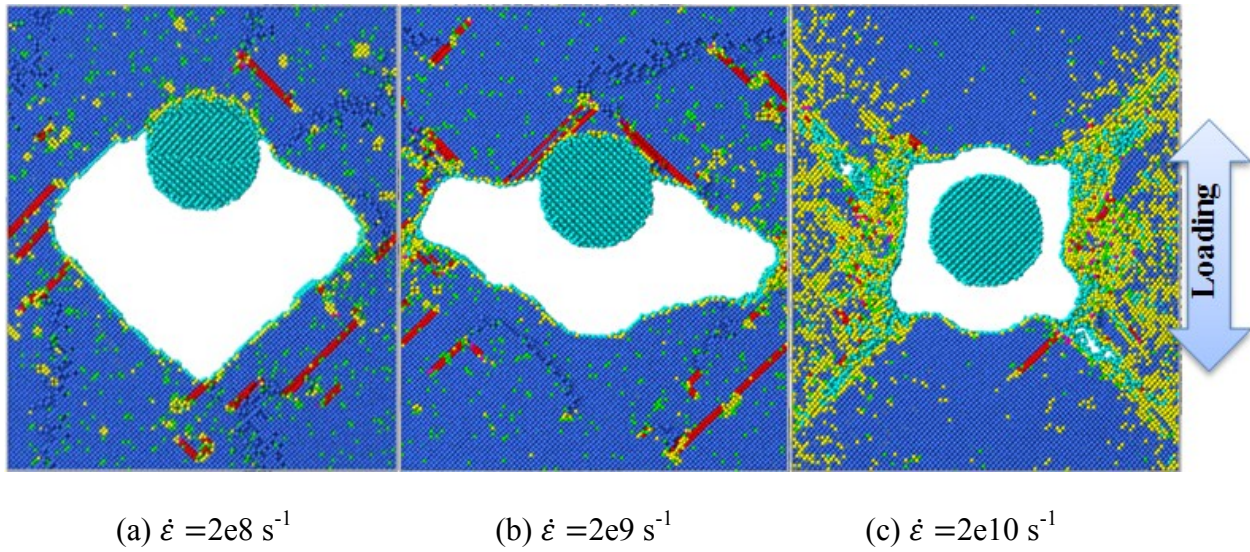


Figure 2.20: Growth of the nucleated void under different strain rate at $\epsilon=0.19$ (The cutting plane is xoz plane). Snapshots are colored in the same way as Figure 2.14.

For all three cases, the rapid growth of nucleated void is associated with dislocation emission. Similar frustum-like dislocation structures have been observed for both the $\dot{\epsilon} = 2 \times 10^8 \text{ s}^{-1}$ and $\dot{\epsilon} = 2 \times 10^9 \text{ s}^{-1}$ cases shortly after dislocation emission. For reference, the strain rate of $2 \times 10^8 \text{ s}^{-1}$ for a void-embedded specimen also results in a frustum-like dislocation structure [87]. Similar mechanism of material transport via these dislocation structures is responsible for the rapid void growth. The dislocation emission of the $\dot{\epsilon} = 2 \times 10^{10} \text{ s}^{-1}$ case features the simultaneous generation of large population of disordered atoms. In Figure 2.20c, these disordered atoms and defects give

birth to some secondary small voids. The very different pattern of dislocations could be responsible for its much lower porosity during the loading.

2.4. Conclusions

MEAM potential is employed to perform the MD simulation of interfacial debonding of silicon particles from copper matrix. Inside an initially dislocation-free matrix, the onset of interfacial debonding is triggered by the normal stress at the interface. However, the pre-existing dislocations could considerably affect the onset of interfacial debonding. Very similar to a normal tensile test [16], the simulated local decohesion initiates on the part of interfacial circumference facing the loading direction. Although the “toughness enhancement factor” indicates that the (1 0 0) silicon-copper interface is strongly “ductile”, the simulation of spherical-particle-embedded geometry suggests that the higher normal stress at the “polar” area of the silicon particle is responsible for the initial decohesion if there has been no initial dislocation inside matrix. In terms of atomic motion, interfacial debonding features a cluster of atoms with higher-than-average displacement. The displacement vectors of atoms at the primary debonding site form highly-ordered alignment. The Lubarda model to evaluate the critical stress for dislocation emission for void-embedded matrix has been straightforwardly generalized to a perfectly-bonded particle case. For particles with smaller size, their onset stresses for dislocation emission are close to the prediction by assuming a perfectly-bonded particle. For particles with larger size up to 30 nm in diameter, their onset stresses for dislocation emission are close to the prediction by assuming an embedded void. In the subsequent development of dislocation network, the gradually less regular shape of void nucleated from debonding causes an asymmetric dislocation structure. The frustum-like dislocation structure emitted from the nucleated void induces the local material transport in a way similar to the pre-existing void case.

Although the initiation of interfacial debonding is triggered by the normal stress at the interface with the initial-dislocation-free assumption, dislocation emission also contributes to the subsequent debonding in the lateral direction. The dislocation lines and the large number of disordered atoms help grow the void towards its periodic neighbours in the lateral directions, and thus promote void coalescence. As for the size effect, larger particles lower the onset strains for both interfacial debonding and dislocation emission. Compared with the simulation size, the volume fraction plays a stronger role in lowering the onset strain of decohesion. A stress drop is observed for relatively large particles during the interfacial debonding. This stress drop has also been predicted by using strain-gradient plasticity theory with cohesive-zone method [99]. As for that strain rate effect, the decreasing strain rate tends to lower the onset strain for decohesion and the dislocation emission.

Chapter 3: The Influence of Initial Void Shape on the Void Growth*

3.1. Introduction

Nanovoids inside the metal material can stem from a number of sources such as radiation damage [4] or void initiation during the propagation of crack under stress [5]. It is of scientific significance to understand the behavior of these voids inside the metallic film as it relates to the structure integrity and perhaps novel designing. For instance, nanostructures containing thin Cu/Nb multilayer films have been proposed to be radiation tolerant media as a new design concept due to the fact that their interface could act like sink to store radiation induced damages. As for the microelectronic device, the failure of the aluminum or copper based thin films causes a major reliability concern [104]. A major driving force of this failure comes from the thermomechanical stress induced by the difference in thermal expansion between the layers [105]. A better understanding of the defect formation and stress evolution in the metallic films also contributes to the enhanced reliability in the mechanical aspects of microelectronic devices [106]. Vella et al. [107] investigated the mechanical properties of nanostructured thin films with multilayered CuNb, FeB and FeTi. In their work, the increased nano-voiding is found to decrease the hardness of the film. As they stated, the multilayer interface itself is not expected to affect the movement of atoms on either side of the interface. Therefore it seems reasonable to simplify the simulation geometry to an only one-layer case. Gungor et al. [106, 108] studied the void growth inside the ductile FCC metallic thin films under tensile loading. Their simulations suggest that the evolution of void morphology is accompanied by blunting due to dislocation emission. The

* A version of this chapter has been published. Reprinted with permission from Cui, Y.; Chen Z. Molecular dynamics modeling on the role of initial void geometry in a thin aluminum film under uniaxial tension. *Modell. Simul. Mater. Sci. Eng.* 2015, 23, 085011. Copyright 2016 IOP Publishing Ltd.

step pattern formation on the film surface reveals a possible mechanism of interfacial delamination for encapsulated metallic thin films used in microelectronics. Kolluri et al. [109] reported an analysis of void nucleation mechanism inside strained ultrathin films of FCC metals. They concluded that the nucleation of nanovoid inside the ultrathin film is due to the emission and propagation of multiple dislocation half-loop and the formation and clustering of vacancies due to dislocation interactions and gliding of jogged dislocations. It is therefore meaningful to carry out simulation to further investigate the situation with specifically-shaped void inside thin metallic film and its pertinent pattern of dislocation emission and growth mechanism.

The dislocation emission has been proposed to be a primary cause of the void growth under high strain rate [18]. The understanding of void growth under extreme high strain rate contributes to the design analysis of structures potentially sustained explosive or projectile impacts [18]. Recently, Feng et al. [5] observed via transmission electron microscopy (TEM) the nucleation and growth of the void of tens of nanometer to propagate the crack. Besides, dislocation emission and migration are spotted to accumulate ahead of the crack tip regions in their study. Lubarda, et al. [18] revealed that the dislocation emission could be the primary cause of void expansion and proposed critical stress for dislocation emission under high strain rate. Their early work focused on the biaxial tension case. Later, Lubarda [91] generalized their original work to the cases under combined loading. The newly proposed dislocation emission angle is no longer confined to a 45 degree from the void surface. Instead, the minimum critical stress is physically obtained by minimizing the critical stress with respect to the two angular variables. Several of these theoretically proposed mechanisms such as the dislocation emission angle and critical stress, are supported by the later MD simulations [26, 38, 39].

As a theoretic approach, it is feasible to first simplify the problem to the case with only matrix material. Future attention could be paid to the void initiation in the presence of second phase inclusion. In this work, the simulation is confined to the pre-existing void case. The shape of embedded elliptical void varies from “x-elongated” to “y-elongated” by altering the aspect ratio. The initial porosity fraction is controlled by cutting different size of void out of a fixed simulation box. The ILLD, known to be important for the void coalescence, is set fixed or unfixed in creating the void geometries. This work will shed some light on better understanding the role of the void geometry.

3.2. Simulation Methodology

The Large-scale Atomic/Molecular Massively Parallel Simulator (LAMMPS) is utilized in the simulation. The atomistic interaction is modeled by the embedded atom method (EAM) [110]. It is crucial that the EAM potential chosen for atomistic simulations must accurately reproduce pertinent features of the resulted energy curves, such as the unstable stacking fault energy [80]. The unstable stacking fault energy is an important parameter of the barrier for partial dislocation nucleation [81]. Simulation with qualified EAM potential is able to reflect dislocation nucleation and interaction phenomena [111]. Mishin, et al. [112, 113] reported the EAM potentials for aluminum and copper, respectively. These potentials demonstrated accurate intrinsic and unstable stacking fault energy and have been extensively applied in MD simulations [26, 38, 39, 111, 114]. Hence, EAM potential for aluminum [112] is selected to carry out the simulation.

As for the computational geometry, a periodic void-embedded simulation box is selected to represent a cluster of uniformly distributed voids. The 3-D simulation box with a thin thickness

in z-direction is employed. The atoms inside the void are removed to create a specifically-shaped embedded hole. Energy minimization using a conjugate gradient algorithm is first performed to attain the minimum energy configuration, followed by the relaxation step to reach an equilibrium state configuration. Based on that, the load of fixed engineering tensile strain is applied in the x direction and with strain-confined lateral boundary. The MD simulation is performed with the isothermal-isobaric ensemble under room temperature via the Nose-Hoover thermostat [82, 83], representing a system in thermal contact with a bath of constant temperature. According to LAMMPS user manual, the Nose-Hoover thermostat could bring the undesirable oscillation of pressure and/or temperature to the atomic system. Therefore, a proper drag force is applied upon the thermostat to damp this oscillation.

The software ATOMVIEWER [85] is applied in the post-processing of the LAMMPS outputs. ATOMVIEWER is a visualization and analysis tool for molecular dynamics simulations, which is capable of featuring the detection and characterization of dislocations and their Burgers vectors. It utilizes a novel way to identify dislocations and Burgers vectors by the decomposition of dislocation density tensor [85].

3.3. Results and Discussion

Elliptical void of different aspect ratio and initial porosity is embedded in a periodical simulation box. The 3D simulation geometry with a central void cut throughout its z direction represents a physical model of sheet tensile specimen containing penetrating holes. During the simulation, uniaxial load is applied at both ends of x-direction. The x-y aspect ratio of the elliptical void varies from 2 to 1/2. The stress-strain relation is monitored during the growth of the void under applied tractions. The vertical ILDs are allowed to change in subsection 3.3.2 but will be fixed in subsection 3.3.3.

3.3.1. Effect of the z-Direction Thickness

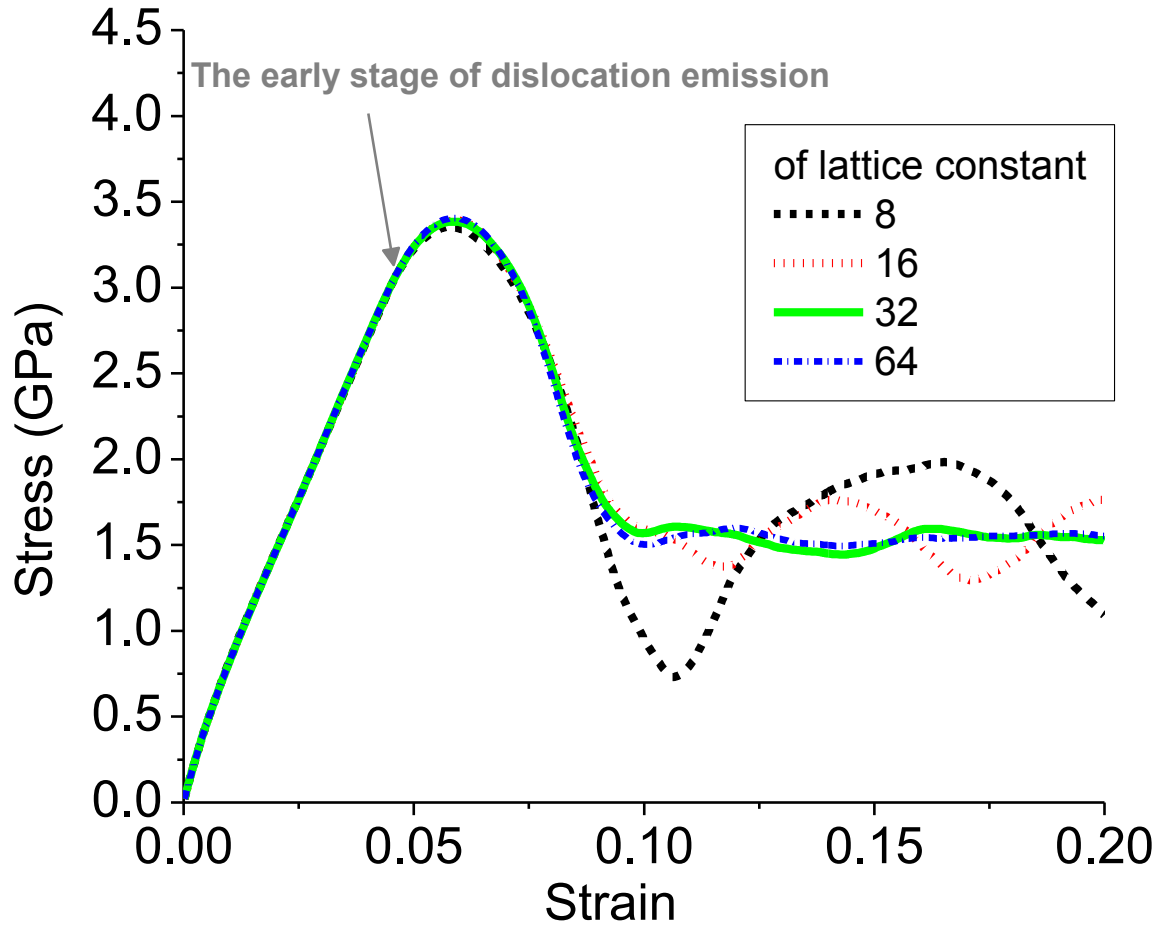
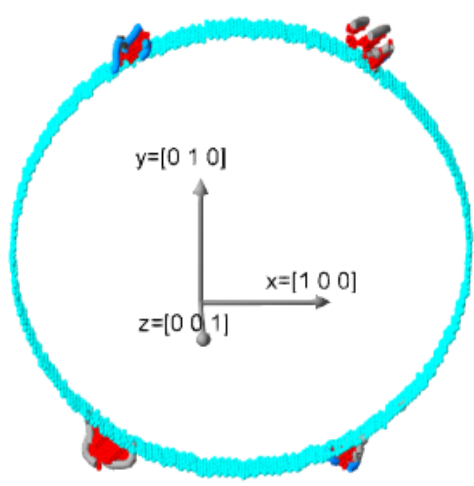
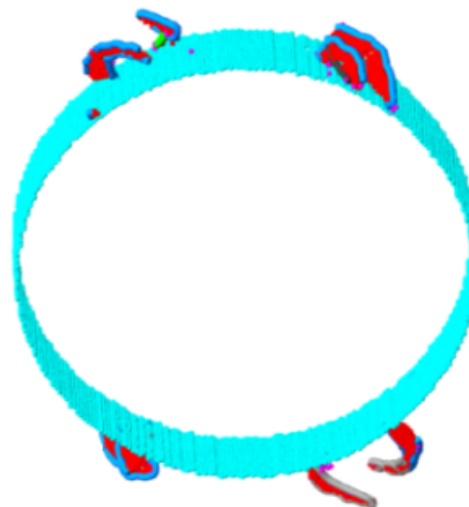


Figure 3.1: Stress-strain relation with 5% initial porosity under different z-direction thickness.

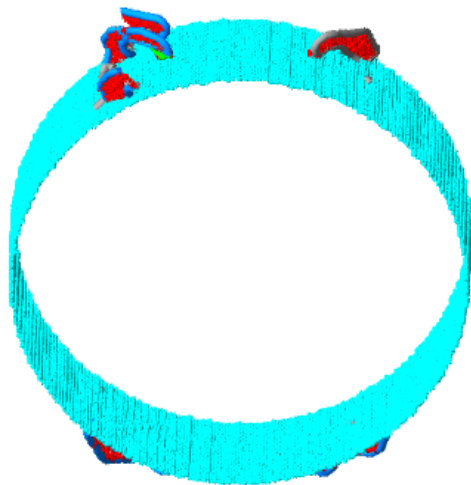
To limit the influence of the z-direction thickness on our simulation results, we first perform an analysis upon the simulation cells with varying z-direction thickness. The z-direction thickness is increased from 8 lattice constants of aluminum (3.24 nm) to 64 lattice constants (25.92 nm), while fixing the size in the other two directions. The resulted atom numbers increase from around 2 million up to 16 million. The strain rate is chosen as $2e9 \text{ s}^{-1}$, which is within the commonly adopted range [26, 37, 40].



(a) 8



(b) 16



(c) 32



(d) 64

Figure 3.2: The early stage of dislocation emission (stacking fault atoms in red are made visible and the dislocation lines are in dark blue or gray, while the stacking fault atoms are in red) under different z-direction thickness (thickness in (a-d) is in the unit of lattice constant of aluminum).

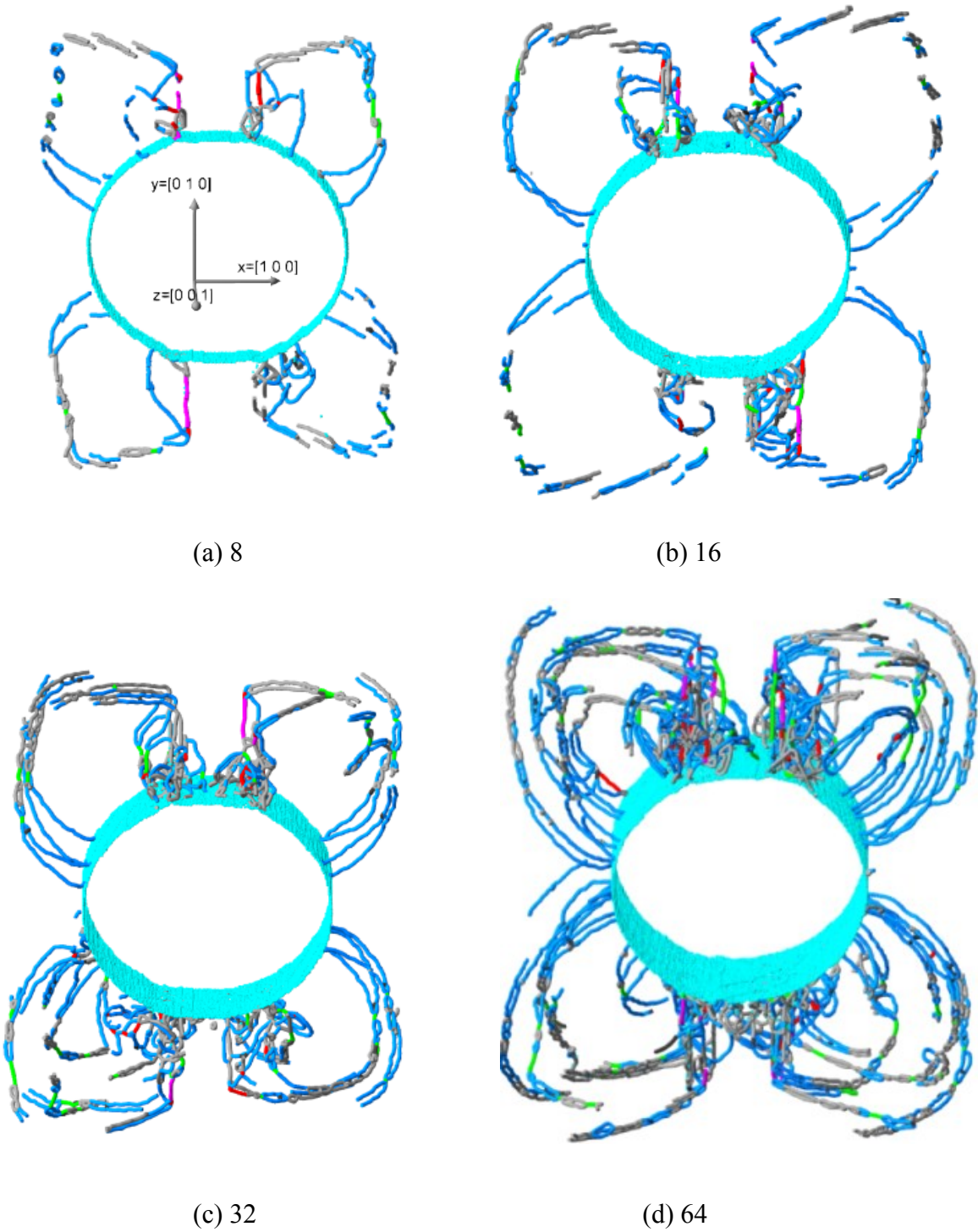


Figure 3.3: The dislocation structure (stacking fault atoms are made invisible) at the ultimate strength point under different z-direction thickness (thickness in (a-d) is in the unit of lattice constant of aluminum).

The stress-strain relation depicted in Figure 3.1 reveals little difference before a strain around 0.075. Given this fact, it is not surprising to find that the onset strain of dislocation emission is almost unaffected by the change of the z-direction thickness. However, the stress-strain curves diverge after the ultimate strength. As the z-direction thickness is doubled, the corresponding stress response gradually converges and shows less dependence on the thickness. In this sense, a thickness of 32 seems good enough to limit the influence of the thickness. Next, the newly formed dislocations at the early stage are shown in Figure 3.2. Except for the thinnest case, the other three cases exhibit similar activated slip system. There appears to be enough spacing for the dislocation loop to develop and detach from the void surface in the last two cases. At the ultimate strength, more complicated dislocation structures are formed out of the interaction between the dislocations in Figure 3.3. Similar features in Figure 3.3c and d such as the shape of dislocation loops and the congregation of the dislocations around the “polar” areas of the voids suggest that a thickness of 32 would be a fair trade-off. For a comprehensive consideration of the stress-strain relation and dislocation pattern, a thickness of 32 is therefore selected and will be used below.

3.3.2. The Cases with Unfixed Intervoid Ligament Distance

The pertinent void geometries are illustrated in Figure 3.4 and detailed in Table 3.1. The uniaxial load is applied corresponding to a constant engineering strain of the square simulation box in the x-direction. The initial porosity is chosen as either 5% or 1%. Apparently, changing the void aspect ratio while fixing the initial void fraction inside a square simulation box leads to varying vertical ILDs. Among all the void shapes, the vertical ILD of the “y-elongated” elliptical void is the shortest. The terms “x-elongated” and “y-elongated” stand for “elliptical shape with

its major axis lying in the horizontal direction” and “elliptical shape with its major axis lying in the vertical direction”, respectively.

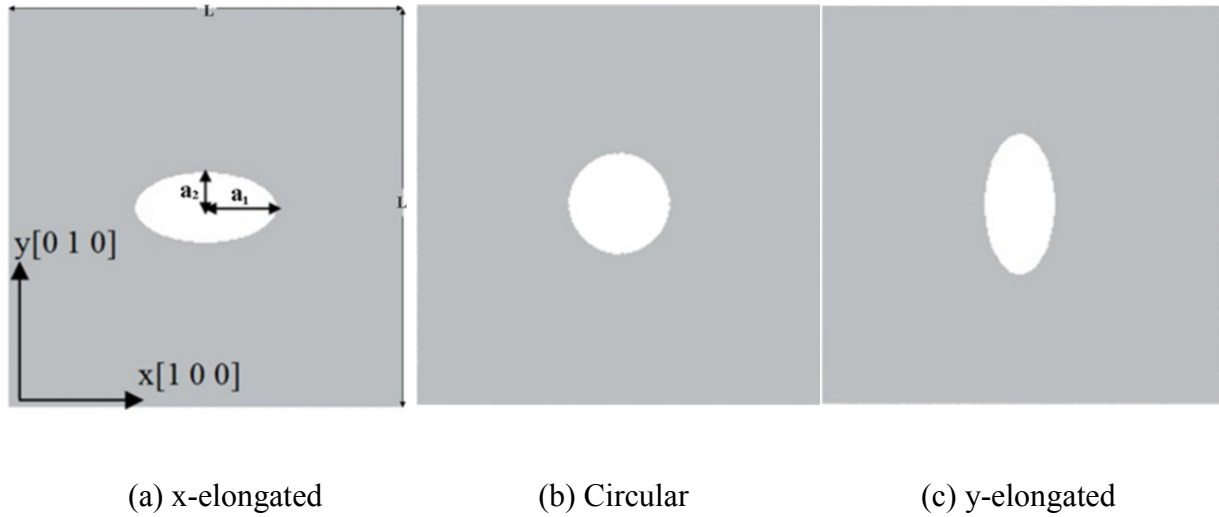


Figure 3.4: Three void shape cases with 5% initial porosity.

Table 3.1: Geometry Specifications for Virtual Specimens 1-6

Specimen	L (nm)	Thickness (nm)	Aspect ratio a_1/a_2	Initial porosity	Void's major diameter (nm)
1	104	12.96	2	5%	36.9
2	104	12.96	1	5%	26.1
3	104	12.96	0.5	5%	36.9
4	104	12.96	2	1%	16.5
5	104	12.96	1	1%	11.7
6	104	12.96	0.5	1%	16.5

3.3.2.1. The Cases with 5% Initial Void Volume Fraction

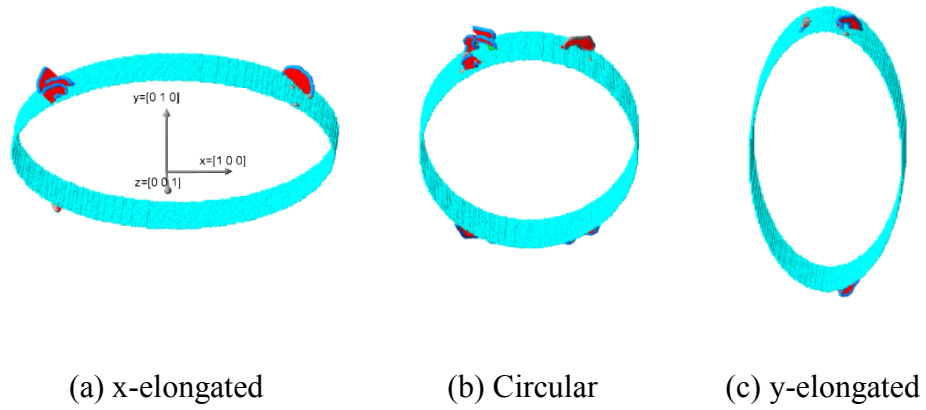
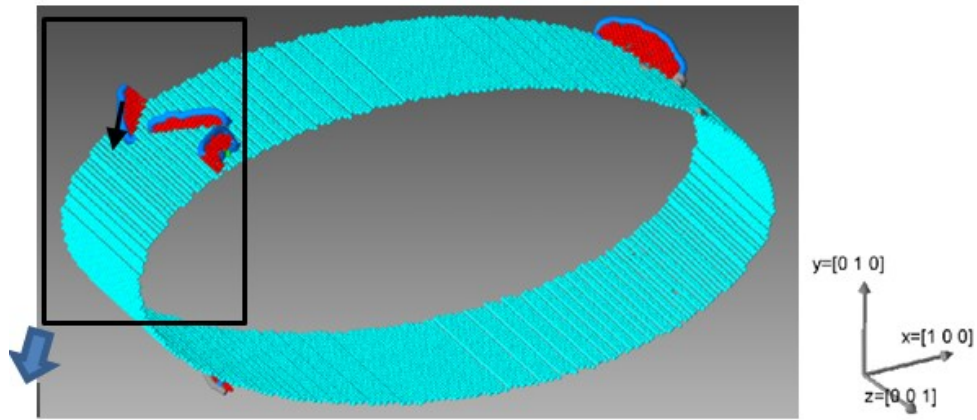
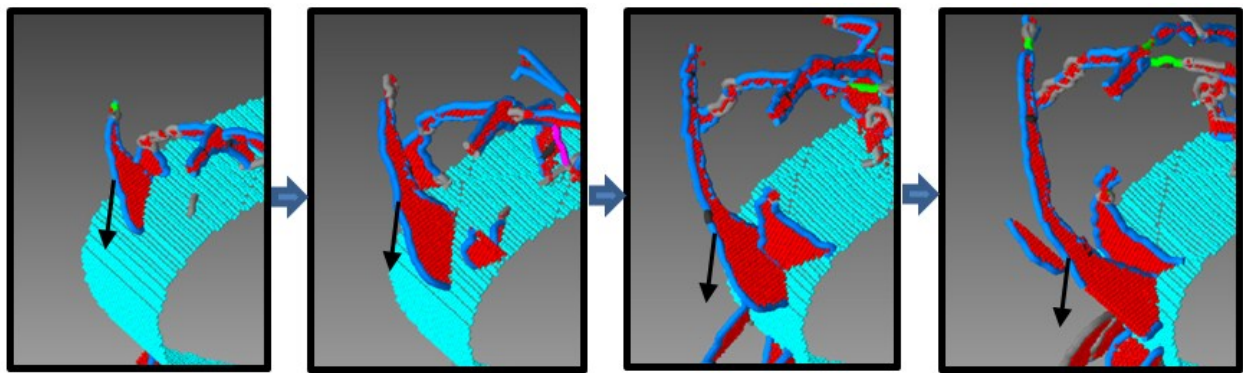


Figure 3.5: The early stage of dislocation emission.



(a) $\varepsilon = 0.056$



(b) 0.058

(c) 0.06

(d) 0.062

(e) 0.064

Figure 3.6: Gliding of a part of the initially formed dislocation lines (x-elongated void).

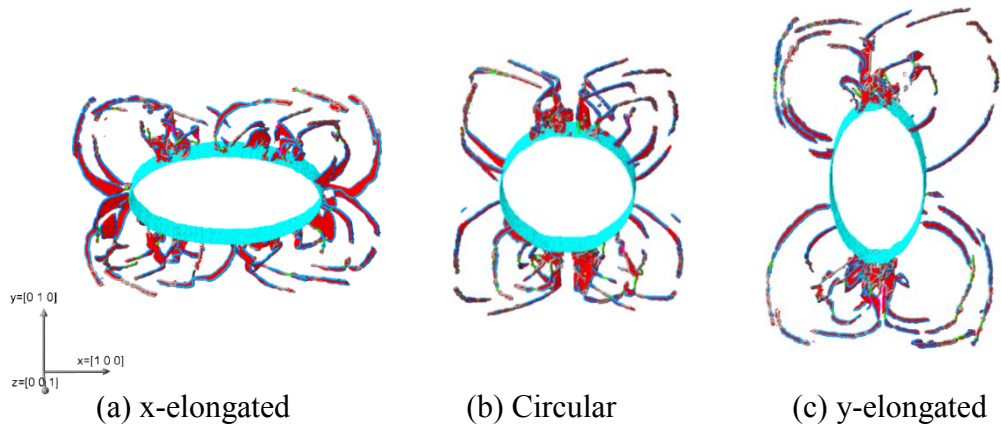
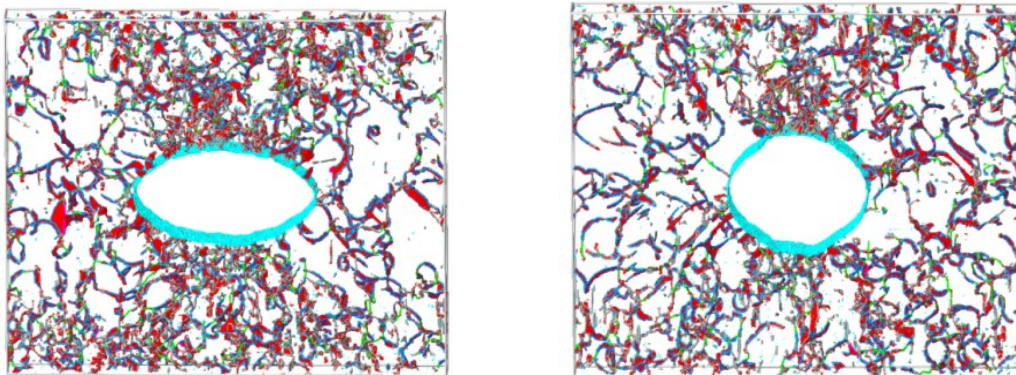
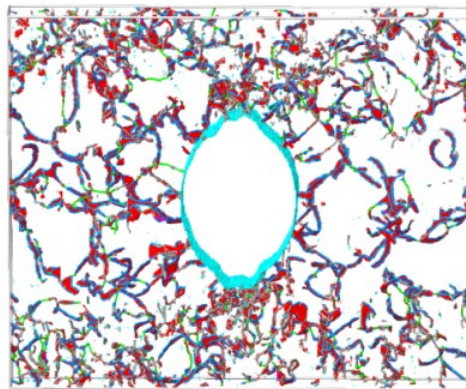


Figure 3.7: The dislocation structure at the ultimate strength.



(a) x-elongated

(b) Circular



(c) y-elongated

Figure 3.8: The void shape and dislocation structure at 0.2 strain of 5% initial porosity.

The early stage of dislocation emission refers to the snapshot by ATOMVIEWER taken very shortly after the onset of dislocation emission, which is determined by having non-zero dislocation number in the dislocation network output file of ATOMVIEWER. Very little trace of dislocation emission can be spotted prior to this early stage. In Figure 3.5, the light blue atoms identify the void surface and the red stacking fault atoms are bounded by the dislocation lines (colored in dark blue). The slip system of type $\{111\}$ is activated. The dislocation lines start at the four sites on the void surface and their location are subject to the void shape. In Figure 3.9, the y-elongated void starts its dislocation emission at a much lower strain than the other two shapes. As the x-y aspect ratio of the void changes from 2 to 0.5, the distance between the two dislocation emission sites at the upper and lower surface of the void are narrowed. No immediate plastic deformation is found at the moment of the emission of dislocations. Hence, the horizontal expansions of the voids in Figure 3.5 are so far elastic. The dislocation structures at the ultimate strength are shown in Figure 3.7. Under this strain, the dislocation lines are not restricted at the initial dislocation sites. Four sets of dislocation loops with comparable size to the void are formed by connecting the initial dislocation sites to near the equator of the void. Taking the x-elongated shape for example, the mechanism of forming this structure is through the gliding of the dislocation lines as illustrated in Figure 3.6. On the upper void surface in Figure 3.6a, the dislocation loop at the left and its stacking fault atoms inside start to glide in the arrow direction. From Figure 3.6b to Figure 3.6e, this dislocation group grows and moves, leaving visible trace behind on the void surface. The rest of the initially emitted dislocation lines stay around its initial position. Given those two sets of dislocation lines, the glided ones connect back to its “birthplace” (either directly or passing the periodical boundary indirectly) to form larger ring-like narrow loops at the four corners. It is the similar case for the other two void shapes which

also develop such a dislocation structure (Figure 3.7). The void shape affects the distance between the dislocation lines and therefore promotes or limits the dislocation interaction at the sites. For the y-elongated void, the dislocation sites at the “polar” area of the void have merged into one and led to localized plastic deformation there due to the vicinity of its initial dislocation sites. For the other two void shapes, the two dislocation sites at the upper and lower void surface are still separated. As the emission and interaction continues, the dislocations spread across the whole simulation cell as in Figure 3.8. The x-elongated void tends to retain its shape while the y-elongated void tends to extrude in its “polar” area.

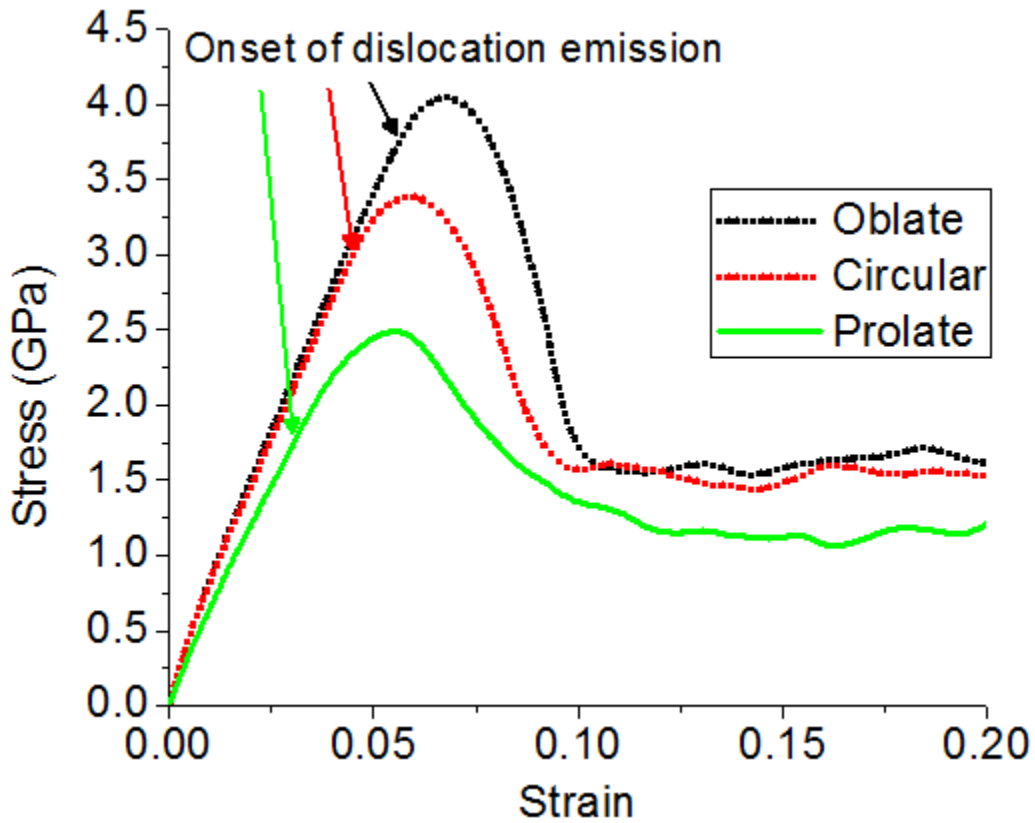


Figure 3.9: Stress-strain relation under 5% initial porosity.

Both Pardoen and Hutchinson [44] and Tvergaard [43] have reported FE investigations of void shape effect in ductile metals. In Tvergaard’s work, a trivial difference in stress response between the x-elongated, circular and y-elongated voids was found during the strain hardening

period with void aspect ratios varying from 3 to 1/3. In Pardoen and Hutchinson's work, a slightly bigger difference in stress response is observed under uniaxial load with void aspect ratios varying from 6 to 1/6. An insufficiency of the FE method is the incorporation of the phenomenological material model, which is inherently inadequate to reflect the dislocation mechanism arising at the atomic level. The previous figures have shown diverse dislocation patterns with respects to different void shapes. Hence, it is not surprising that the MD results bring some new insight into the influence of the void shape on the stress response. Indeed, the ultimate tensile strengths differ remarkably for the three void shapes in Figure 3.9, which is not case for the FE simulation. As the void shape changes from x-elongated to y-elongated, the apparent elastic stiffness, the onset strain of dislocation emission and the ultimate tensile strength are all lowered. In Figure 3.9, the stress response is not immediately deteriorated at the onset of dislocation emission. Yet the slopes of the stress-strain curves diminish right after the emerging of dislocations, especially for the y-elongated shape. All the curves drop quickly after the ultimate strength point but remain at a level around 1-2 GPa, implying that the material still maintains a certain load carrying capacity. The stress response of the x-elongated void and circular void are quite close at the end of loading, while it is the lowest for the y-elongated one. During loading, the dislocation structure grows to reach the periodical boundary of the simulation cell (in x and y direction) at the strain of around 0.09 for the x-elongated shape, 0.08 for the circular and 0.07 for the y-elongated shape. Below these strains, the void is free from the dislocation interaction of its periodical neighbors. In Figure 3.9, the differences between the curves tend to narrow from the strain of around 0.08, especially for the x-elongated and circular voids, when the void becomes no longer isolated from its neighbors.

3.3.2.2. The Cases with 1% Initial Void Volume Fraction

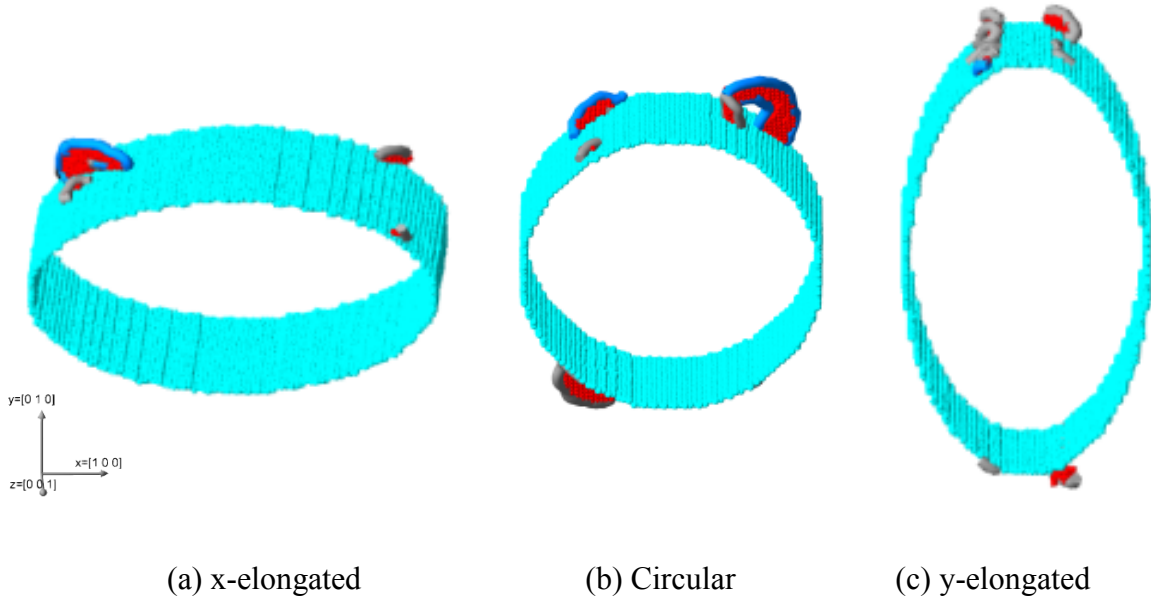
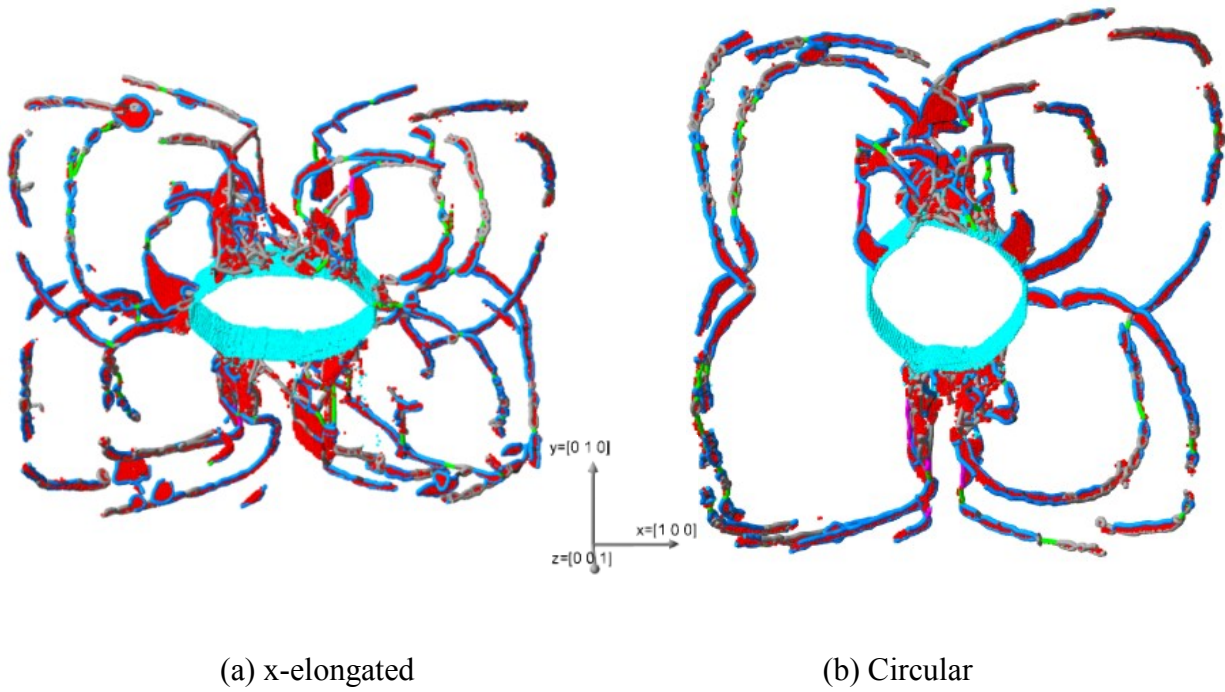
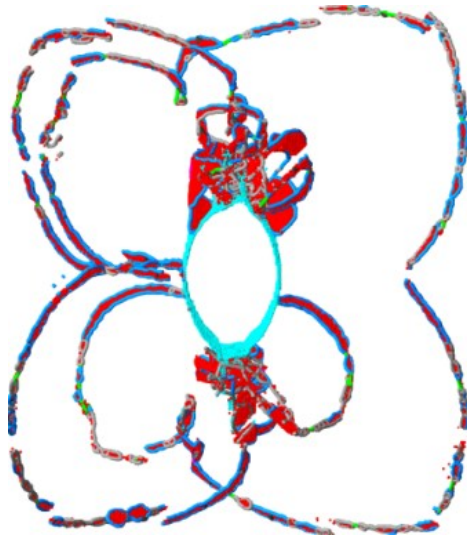


Figure 3.10: The early stage of dislocation emission (magnified).





(c) y-elongated

Figure 3.11: The dislocation structure at the ultimate strength.

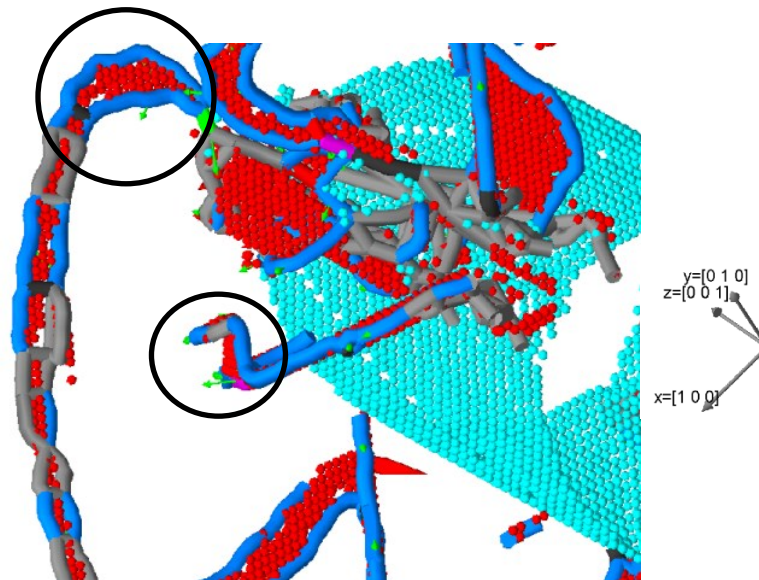
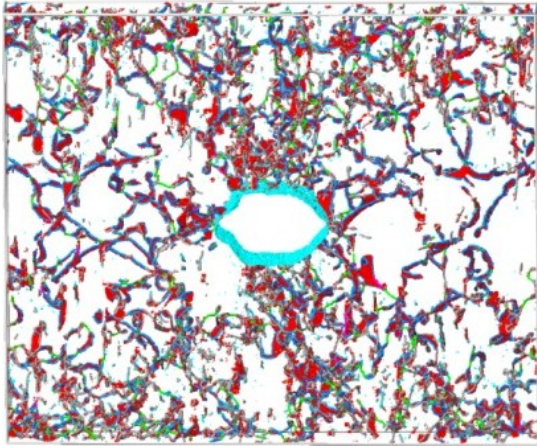
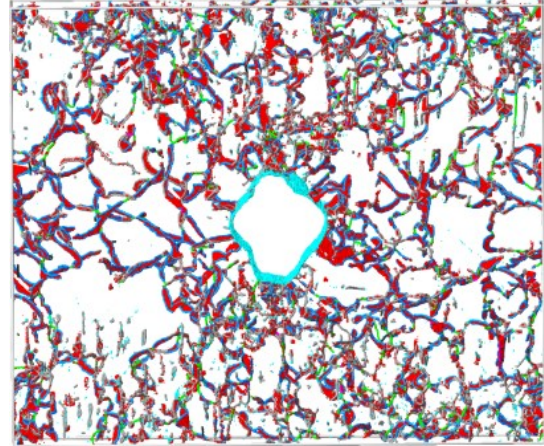


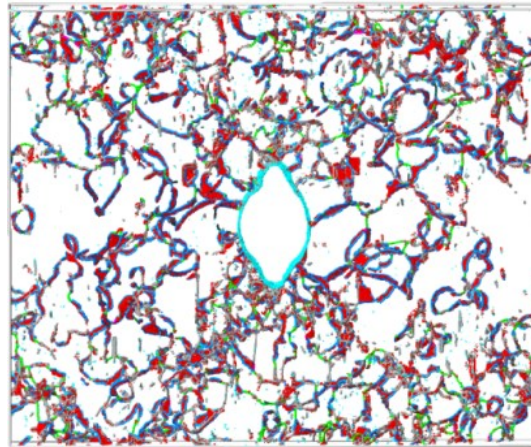
Figure 3.12: Dislocation kinks (inside the left black circle) and jogs (inside the right black circle) near the surface of the y-elongated void (green arrow is the Burgers vector).



(a) x-elongated



(b) Circular



(c) y-elongated

Figure 3.13: The void shape and dislocation structure at 0.2 strain of 1% initial porosity.

Next is the 1% initial porosity case. The void shape still determines the initiation position of dislocations on the void surface in the same way. Yet, the distance between the dislocation sites is shortened proportionally corresponding to the size of the void. Similarly, the gliding of the dislocation lines away from its initiation position is still responsible for changing dislocation structure from Figure 3.10 to Figure 3.11. Due to a shortened distance between the dislocation

initiation sites, even the upper dislocation sites of the circular shape have merged into one and led to a stronger dislocation interaction there. A distinctive feature in Figure 3.11b is that a larger dislocation loop in the left of the circular case is formed by directly connecting the dislocation sites from the upper and lower “polar” area of the void. There are no longer four sets of loops at the four corner of the void like that in Figure 3.7b but just three due to the interaction between the dislocation loops. This is also true for Figure 3.11c. During the evolution of the dislocation structure, some typical dislocation interactions such as the dislocation kinks and jogs are spotted in Figure 3.12. Compared to the cases with 5% initial porosity, the discrepancy is that the distortions of the void shapes are not only noticeable for the y-elongated shape but also for the circular shape and even the x-elongated shape. A plausible explanation is that there is more spacing for the initially smaller void to grow inside the size-fixed simulation box.

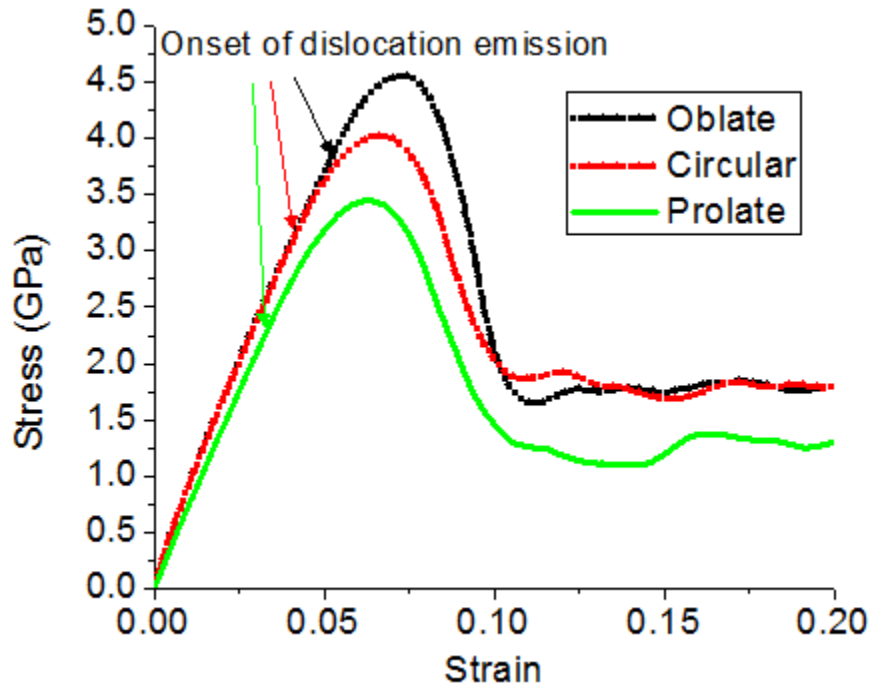


Figure 3.14: Stress-strain relation with 1% initial porosity.

Even though the initial porosity is lowered to 1%, the stress-strain curves in Figure 3.14 still suggest a strong influence of the initial void shape. From the very beginning to the ultimate strength point, the difference among the stress curves gradually widens. Following the drop after the ultimate strength, the discrepancy between the x-elongated void and the circular void narrows and yields nearly the same value at the end of loading. However, the stress response of the y-elongated void decreases to a much lower value and yet the specimens still possess a certain load carrying capacity at the end.

3.3.3. The Cases with Fixed ILDs

It has been reported that ILD plays an important role in determining the onset of void coalescence [115]. The coalescence of neighboring voids is the direct consequence of the consumption of the intervoid ligament vertical to the loading direction. The changing ILDs, as a consequence of the changing void shape, may play a certain role in affecting the material response. Therefore, the aim of this subsection is to assess the void shape effect while excluding the influence of ILDs. In order to keep the same initial void volume fraction as well as the same ILD, it is inevitable to alter the aspect ratio of the simulation box. The y-elongated void here is still embedded in a square simulation box. As a consequence, the circular void has to be embedded in a rectangular box with an x-y aspect ratio of 2 and thus double the total number of atoms from 8 million to 16 million. We know from the previous simulation cases that the x-elongated void has the highest stress response and thus is the safest in terms of its load carrying capacity. As a result, the x-elongated shape is here excluded to save the computation cost. Once ILDs are fixed, the primary consequence of changing the shape is the altering of the aspect ratio and the “polar” curvature of the void in Figure 3.15. The lenticular void is created to yield both the same initial porosity and the same ILD. The initial void shape is not smooth in real

engineering materials. It may contain sharp tips. Yet for the sake of simplicity, void is often treated as smooth in modeling. The comparison between the y-elongated void and the lenticular void serves the very purpose to evaluate the influence of the initial shape irregularity on the dislocation emission and mechanical response of the material. More information regarding the three specimens is detailed in Table 3.2.

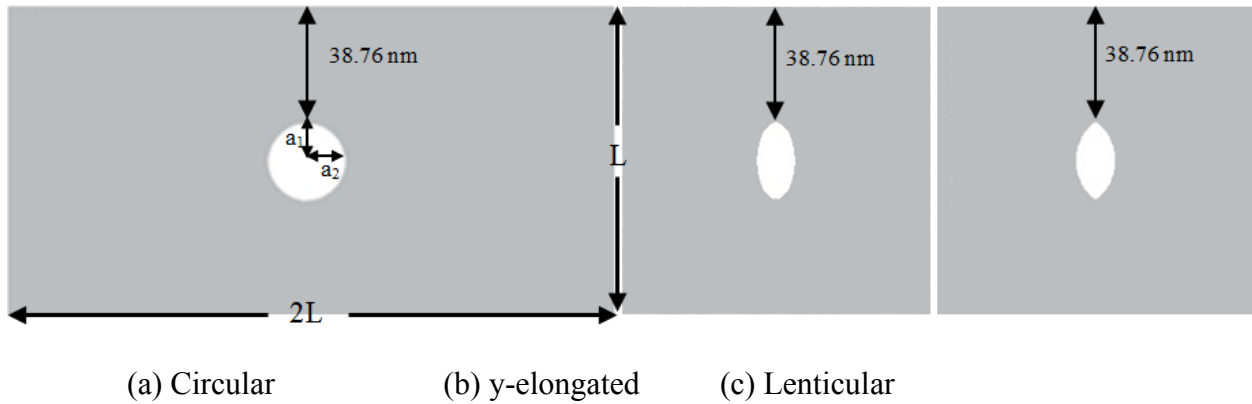


Figure 3.15: Specimens 7, 8, 9 with fixed ILD.

Table 3.2: Geometry Specifications for Virtual Specimens 7-9

Specimen	L (nm)	Thickness (nm)	Aspect ratio a_1/a_2	Initial porosity	Void's major diameter (nm)
7	104	12.96	1	2.5%	26.1
8	104	12.96	0.5	2.5%	26.1
9	104	12.96	0.55	2.5%	26.1

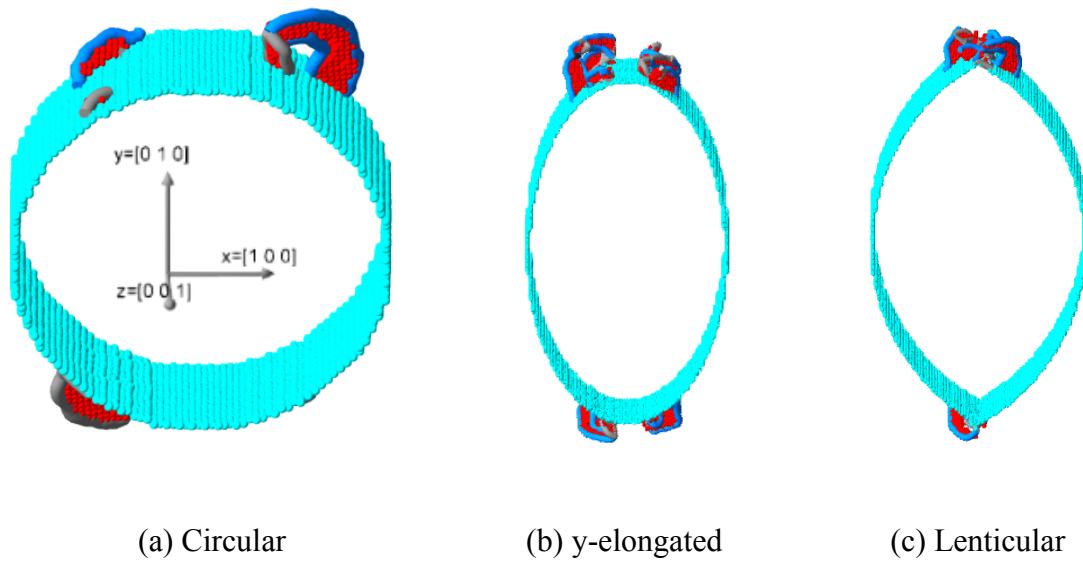
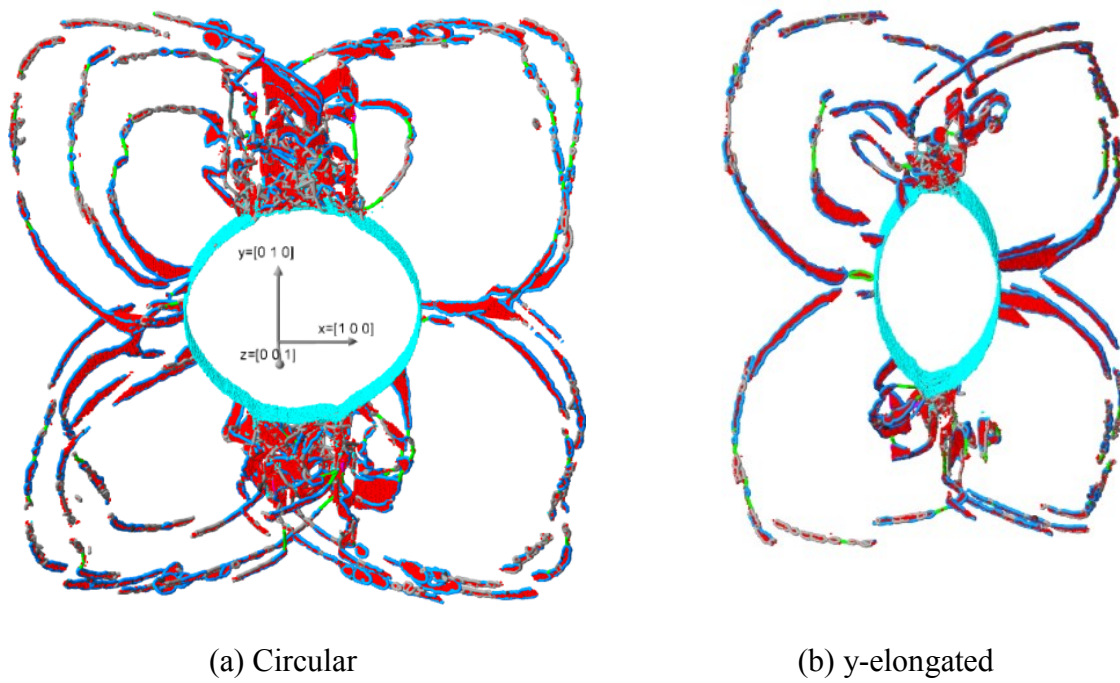
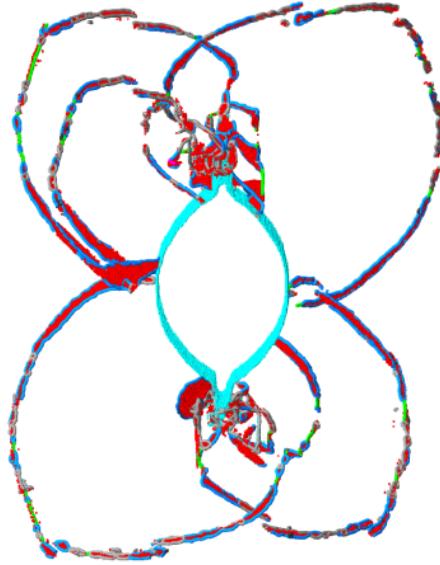


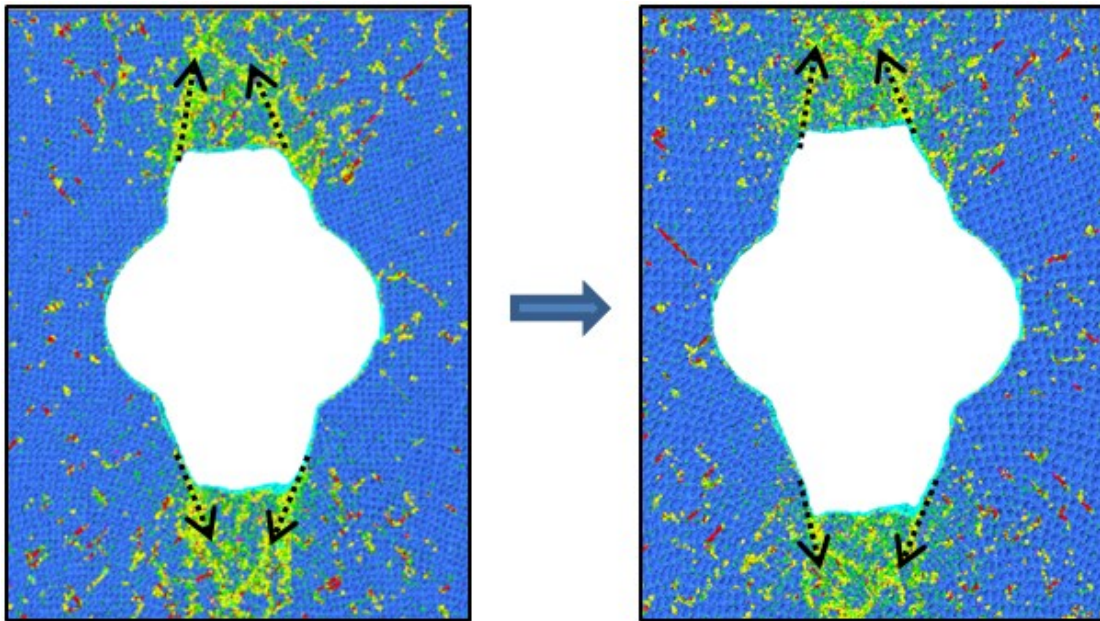
Figure 3.16: The early stage of dislocation emission.





(c) Lenticular

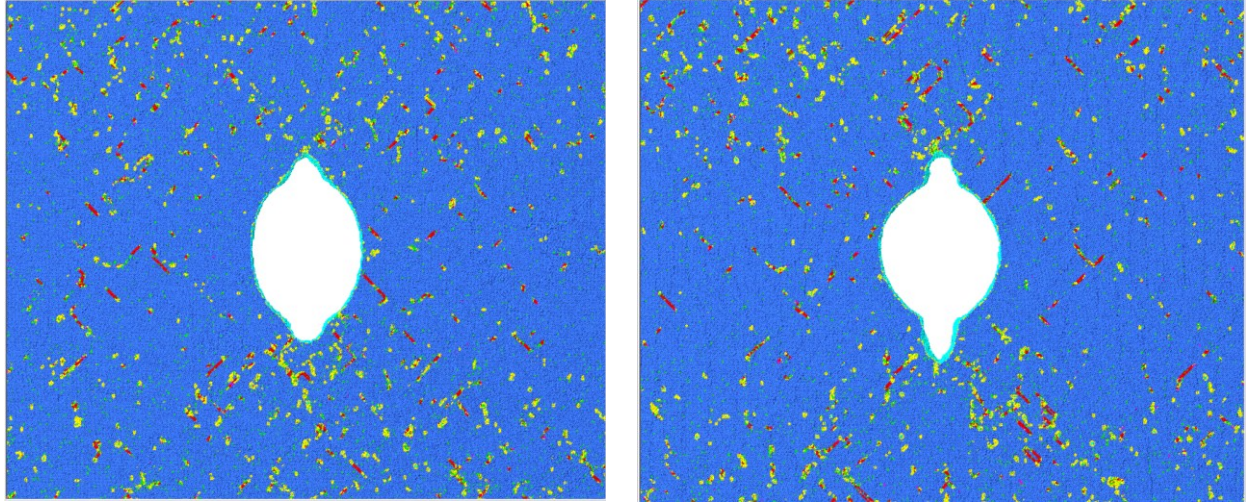
Figure 3.17: The dislocation structure at the ultimate strength.



(a) 0.15 strain

(b) 0.2 strain

Figure 3.18: The way of void expansion in specimen 7 (The snapshots are only truncated horizontally).



(a) y-elongated

(c) Lenticular

Figure 3.19: The evolved void geometry of specimen 8 and 9 at 0.2 strain.

Under the fixed ILD, the void shape again alters the position of the dislocation initiation sites in a similar way as in Figure 3.16. Only one initial dislocation site is observed at either tip of the lenticular void, which makes its total initial dislocation sites halved compared with the other shapes. The dislocation lines are found gathering at the tips of the lenticular void once emerging. At the ultimate strength point in Figure 3.17, the dislocation sites at the “polar” area of the voids all merge into one, which differs from the cases with 5% initial void volume fraction. As for the void deformation, two cleavages have been formed at the tips of the lenticular void. As the loading process continued, the circular void exhibits a distinctive way to grow its volume (see Figure 3.18). The matrix material moves away along the traces with high concentration of the disordered atoms and defects to grow the void. The disordered atoms and defects in Figure 3.18 are identified by the configuration of its nearest neighbor atoms [100]. However, this phenomenon cannot be found in Figure 3.19 and the void growth of the other two shapes is far

less than that in specimen 7. In Figure 3.19b, the cleavages from the tips of the lenticular void further extrude to consume the intervoid ligaments which may suggest an early void coalescence.

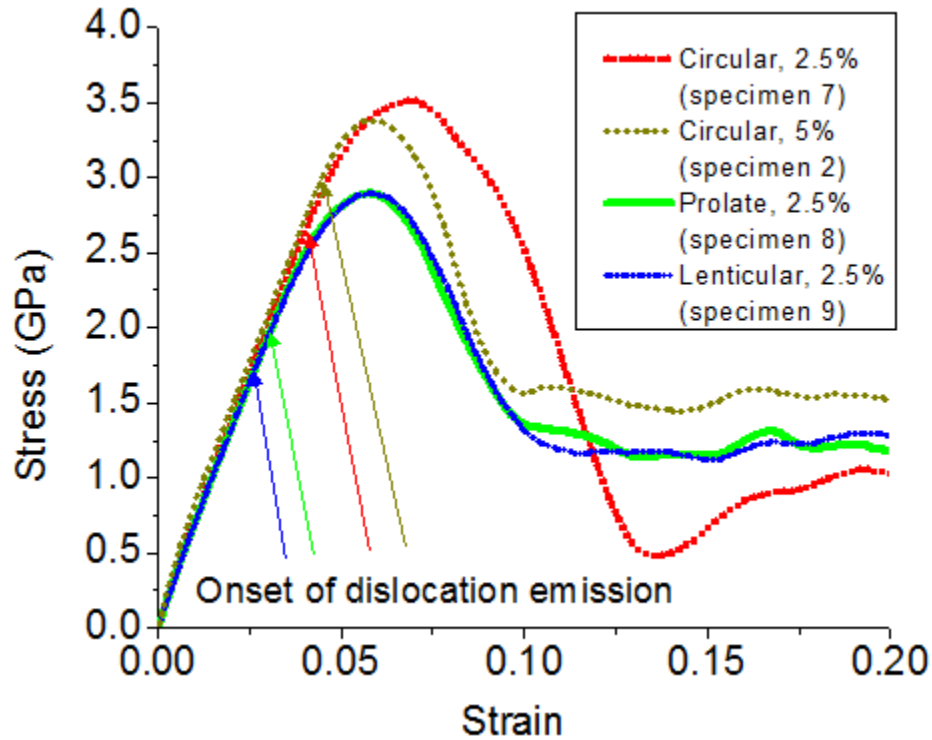


Figure 3.20: Stress-strain relation of specimen 2, 7, 8 and 9.

Given the same initial void volume fraction and ILD, the void shape still highly affects the stress-strain response of the specimens in Figure 3.20. The dislocation emission from the lenticular void is the earliest, which suggests that bigger “polar” curvature of the void promotes the dislocation initiation. The increase of the initial void volume fraction tends to postpone the dislocation emission by comparing the two circular voids. The y-elongated and lenticular voids result in a considerable deterioration of the ultimate stress compared with that of the circular void of 2.5% initial porosity. Unlike the continuum theory, there is no geometrical singularity at the atomic level. The tips of lenticular void are of finite width in the MD geometry. As a result, the “singularity” at the lenticular void tips has very limited influence on the stress response of the

specimen in Figure 3.20. In this sense, a less smooth void shape could be readily approximated by an elliptical shape in modeling. The stress response of specimen 7 is about the highest before the strain of around 0.1 due to the fact that it is circular and has halved initial porosity of specimen 2. However, since the specimen 7 has a distinctive way to excessively grow the void volume after a strain of 0.1, the corresponding stress response is significantly lowered.

3.3.4. Comparison with the Analytical Model

During the post-processing of MD simulations, we have identified the onset of dislocation emission by checking the dislocation network file output by ATOMVIEWER. Based on that, the MD results could be compared with the theoretically predicted critical stress for the dislocation emission. Lubarda, et al. [18] obtained the critical stress required to trigger dislocation emission by balancing the remote stress to the dislocation attraction force from the void. Later, Lubarda [91] extended the original model to account for combined loading cases. His analytical model utilized a cylindrical void geometry embedded in an infinitely large material. Similar to his early work, the critical stress for the initiation of dislocation emission is determined by balancing the applied stress to the image force on the dislocation exerted by the void surface. As shown in Figure 3.21, the equilibrium distance ρ from the surface of the void is set equal to the dislocation core cut-off radius ρ_0 [116] and ρ_0 is set equal to the magnitude of the dislocation Burgers vector [91]. The resulted critical stress is still associated with the angles ϕ and θ as illustrated in Figure 3.21. Therefore, the actual minimum critical stress requires to be determined through the minimization with respect to ϕ and θ . The critical stress $\sigma_{cr} = \sigma_{cr}(\phi, \theta)$ takes the form as in [91]

$$\sigma_{cr} = \frac{Gb/R}{2\pi(1-\nu)} \frac{\sin 2(\theta-\varphi)}{h} \left(\frac{r_0^4}{R^2(r_0^2-R^2)\sin\theta} - \frac{2(r_0^2-R^2)\sin\theta}{r_0^2} \right) \quad (3.1)$$

$$h = - \left[\frac{r_0^2}{R^2} - \left(3 \frac{R^2}{r_0^2} - 2 \right) \cos 4(\theta-\varphi) \right] \sin 2(\theta+\phi) - \left[\left(3 \frac{R^2}{r_0^2} - 2 \right) \sin 4(\theta-\varphi) \right] \cos 2(\theta+\phi) + \sin 2(\theta-\varphi) \quad (3.2)$$

$$r_0^2 = R^2 + \rho_0^2 + 2R\rho_0 \cos\theta \quad (3.3)$$

$$\sin(\theta-\varphi) = R \sin\theta/r \quad (3.4)$$

Where

G is the shear modulus, and $G=25.5$ GPa [117] for aluminum,

b is the magnitude of the dislocation Burgers vector, and $b=0.286$ nm [118] for aluminum,

ν is Poisson's ratio, and is set as 0.33; and other geometry quantities are as illustrated in

Figure 3.21.

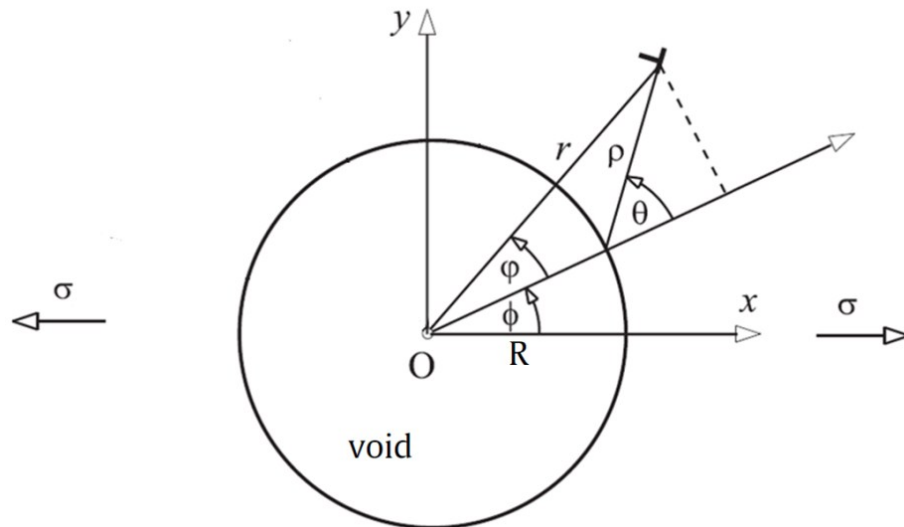


Figure 3.21: Illustration of the void-dislocation geometry from Ref. [91] (Reprinted with permission from Lubarda. Copyright 2011, Elsevier).

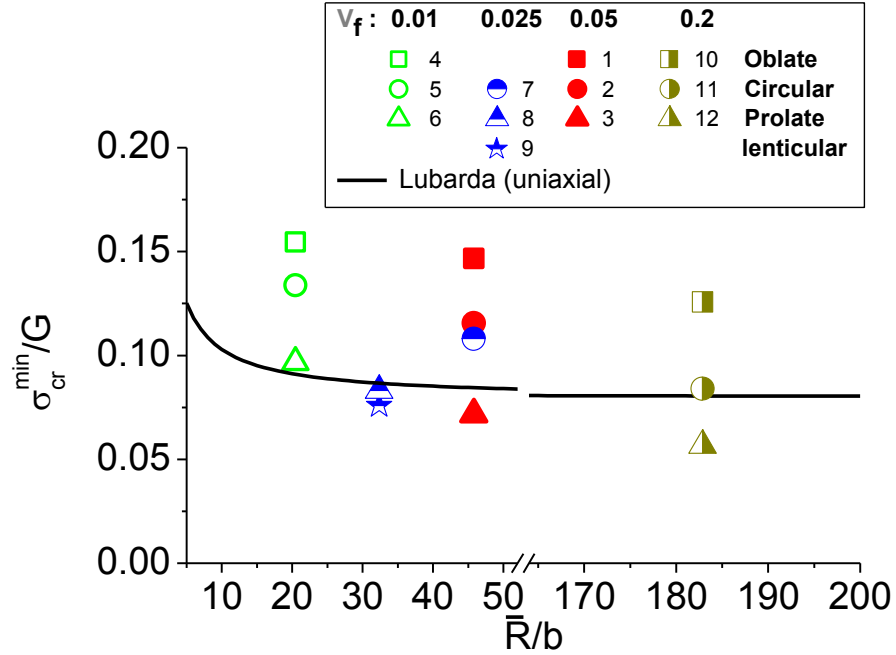


Figure 3.22: The critical stresses for dislocation emission predicted by MD are compared to the minimum critical stress predicted analytically [91]. The hollow, horizontally half-filled, filled scattered and vertically half-filled symbols are the MD results with 1%, 2.5%, 5%, 20% initial porosity, respectively. The integer right to the individual symbol inside the legend is the corresponding specimen number. Geometric mean radius $\bar{R} = \sqrt{a_1 a_2}$ is used for the non-circular voids. A scale break is introduced horizontally to accommodate the largest void size.

Table 3.3: Geometry Specifications for Virtual Specimens 10-12

Specimen	L (nm)	Thickness (nm)	Aspect ratio a_1/a_2	Initial porosity	Void's major diameter (nm)
10	207	12.96	2	20%	148.0
11	207	12.96	1	20%	104.6
12	207	12.96	0.5	20%	148.0

For the voids with same area, a bigger x-y aspect ratio leads to a larger critical stress. Our simulated dislocation cutting angle ϕ for the circular void appears smaller than that of the theoretically predicted value 89° [91]. In Figure 3.22, the tendency of the critical stress predicted by MD is in fair agreement with the prediction of the Lubarda model. Three much larger specimens as detailed in Table 3.3 are dedicated to better examining the influence of void size. The diameter of the circular void inside specimen 11 is 104.6 nm and the major diameter of the elliptical voids reaches 148.0 nm. The critical stress required by this largest circular void to initiate dislocation agrees well with the limiting value predicted by the Lubarda model for large voids. More importantly, our MD simulation reveals that the shape of large submicron voids continues to play a role in the dislocation initiation stress. The same applies to the ultimate tensile stress obtained by the simulation. The corresponding dislocation emission pattern and evolution is quite similar to the previous cases, except for now more spacing available for the dislocation line to migrate. The minor discrepancy between the theoretical critical stress and our simulated value could be attributed to two points. First, the critical stress of void under an applied strain rate of $2 \times 10^8 \text{ s}^{-1}$ is slightly lower (not displayed). It implies that the difference between the simulated results and the Lubarda model could be smaller if a lower strain rate is used. Second, the interaction among dislocations, which is neglected in the analytical model, may hinder or facilitate the emission so as to bring uncertainty to the threshold stress level [91].

3.4. Conclusion

The influence of initial void geometry on void growth under uniaxial load is studied. Dislocation emission is found to be the precursor of both the stress deterioration and the void growth under the considered strain rate. The following conclusions are drawn for the pertinent simulation conditions.

1. Large open-ring structure composed by dislocation loops is formed by the gliding of the dislocation lines. During the evolution of the dislocation structure, some typical dislocation interactions such as kink and jog are spotted before the ultimate strength is reached. The traces with high concentration of disordered atoms and defects facilitate the void expansion.

2. Initial void shape substantially affects the stress-strain response. The y-elongated void leads to considerable deterioration of the ultimate strength. Initial void shape not only alters the sites of the dislocation emission, but also determines the stress threshold for dislocation emission. The influence of initial porosity is intertwined with the influence of the initial void shape on the stress-strain relation. For circular void and y-elongated void, their stress-strain responses are relatively close to each other at the high strain range. The MD approach demonstrates a stronger effect of the void shape on stress-strain relation than that predicted by the FE approach.

3. The MD results are consistent with the Lubarda model in predicting the critical stress to trigger the dislocation emission. The x-elongated void tends to elevate the critical stress for the dislocation emission, while the y-elongated void shape does the opposite.

4. Under a fixed intervoid ligament distance, the shape of the void still plays an important role in affecting the critical stress for the dislocation initiation, the position of dislocation sites and the stress-strain relation. The singularity at the tips of the lenticular void considerably lowers the critical stress for dislocation emission but has very limited influence on the stress-strain relation.

Chapter 4: The Impact of Thermo-Mechanical Constraints on the Void Growth*

4.1. Introduction

Voids of nano-size inside the metal materials stem from a number of sources such as radiation damage [4]. These nanovoids are very suitable for MD simulation due to their small size. Molecular dynamics has proven to possess a great potential in uncovering the fundamental mechanisms of nanovoid development. Over the years, quite a number of atomistic simulations have been dedicated to the understanding of the growth mechanism of nanovoids. Traiviratana et al. [26] performed the MD simulation to study the void growth in both monocrystalline and bicrystalline copper. The emission and reaction of dislocation by the presence of the void are well detailed in their work. Zhao et al. [119] modeled the growth of nano-sized, cylindrical void under uniaxial-stress state with the NPT ensemble. Zhao et al. [120] studied the effect of multi-axial stress state on the nano-porous, single-crystalline copper. Their simulation revealed quadrangular-prismatic dislocation loops formed near the void under the hydrostatic loading and a dislocation structure of square-frustum under the uniaxial tension. Bringa et al. [38] studied the effect of loading orientation and nanocrystalline on the void initiation and growth. They confirmed the mechanism of void nucleation and growth by dislocations. Bhatia et al. [103] investigated the nanovoid growth in single-crystal aluminum under the NVT ensemble. They found that the growth rate of the nanovoid is insensitive to the initial lattice orientation. Dislocations are found closely related to the void growth. Recently, Farkas et al. [121] applied both Nose-Hoover thermostat and barostat to study the mechanical response of nanoporous gold.

* A version of this chapter of this thesis is submitted as Cui, Y.; Chen, Z. Void growth via atomistic simulation: will the formation of shear loops still grow a void under different thermo-mechanical constraints?

Of all the aforementioned papers, different mechanical and thermal constraints have been involved in the MD simulation of nanovoids inside metal material. Despite the short duration due to ultra-high strain rates, mechanical constraints on lateral boundaries could also affect the behavior of a nano-specimen. Laser shock test of a 250-nm nickel sample measures a shock velocity of 6.28 nm/ps and a shock wave rise time 5.5 ps for the free surface velocity [122]. This implies that the speed of shock wave may allow the lateral relaxation of a specimen of tens of nanometers during, for example, a 1000ps simulation time. For an MD simulation of tensile testing with free lateral boundaries, nano-specimens undergo contraction in the lateral directions [123]. A periodic representation of nano-structure inherently involves the use of mechanical constraint, and thereby, creates a difference in the predicted void growth. In light of this concern, a comparison of mechanical/thermal constraint will help to elucidate the difference they caused and thus could guide the selection of the mechanical/thermal constraint with respect to particular situation. This issue has been a general concern regarding the mechanical aspect of molecular dynamics simulation. For instance, the effect of stress control has been studied for the mechanical testing of polymers via molecular dynamics [124]. However, similar work has not yet been reported for void growth in metals. In addition to the comparison of mechanical and thermal constraints, another perspective of this chapter is the role dislocations played in the void growth. Lubarda et al. [18] has demonstrated that both prismatic loop and shear loop can grow the void under median to high strain rate. Void growth mechanism via prismatic loop is a classic, textbook understanding [57]. Despite the debate over the years, a recent MD simulation has proved the feasibility of void growth mechanism via shear loop [87]. This simulation is performed without thermostat and barostat activated along with unchanged simulation size and strain rate in loading [87]. To further explore the universality of this mechanism, new

simulations are performed and examined in the present study with different mechanical constraints, thermal constraints, sizes of simulation box and strain rates. Our focus is on the mass transport during the burst of void growth from the onset of dislocation emission.

This chapter is organized as follows. First is a brief description of the methodology to perform the mechanical and thermal constraints in molecular dynamics simulation. Second is the comparison of different mechanical constraints with thermostat activated under a temperature of 0.1K. The main purpose of selecting this low temperature is to avoid thermal activation and thermo-mechanical interaction. Third is the comparison of different mechanical constraints without temperature control under an initial temperature of 300K. Through using the software ATOMVIEWER [85], void growth pattern would be characterized by the RFT atoms inside the dislocation network. Our simulation results are dedicated to examining the difference in void growth caused by the stress/temperature control and mass transport via shear loops/curves.

4.2. The MD Simulation Technique

The temperature and stress control are sometimes essential as a lot of experimental measurements are performed at specific temperature and/or stress state rather than constant energy. Nosé [83] extended the canonical ensemble MD method to the NPT ensemble by advancing the constant pressure MD method of Andersen [125]. Martyna et al. [126] rewrote the Hamiltonian and the equations of motion for the Nosé-Hoover NPT method and introduce a fully flexible simulation cell with a modular invariant of momentum to the barostat. The software LAMMPS [77] implements the equations of Martyna et al. [126] and Shinoda et al. [127] to form the equations of motion for the NVT and NPT ensembles¹. The applied time integration schemes

¹ See the fix nvt command in the LAMMPS manual (Jun 28, 2014 version)

closely follow the time-reversible, measure-preserving Verlet and rRESPA integrators, as derived by Tuckerman et al. [128]. If no thermostat or barostat is active, the simulation will be run under NVE ensemble. The NVE integration updates the position and velocity for atoms at each time step, which creates a system trajectory consistent with the microcanonical ensemble². The deformation in the loading direction is imposed by stretching the simulation box and remapping all the coordinates of atoms. For the tensile loading of uniaxial strain, the two non-loading lateral boundaries of the simulation box are fixed. For the tensile loading of uniaxial stress, the loading dimension is decoupled from the other two directions in performing the stress control. The microcanonical (NVE) and canonical (NVT) ensembles are employed to achieve the uniaxial-strain state while the isoenthalpic-isobaric (NPH) and the isothermal-isobaric (NPT) ensembles are for the uniaxial-stress simulations. These simulations are further divided into two categories: with or without the use of thermostat under different temperatures. The dynamic simulations under NVE and NPH ensembles are run without thermostat and start at T=300K. The simulations under the NVT and NPT ensembles at near zero Kelvin are designed to eliminate thermal activation and thermo-mechanical interaction. It should be noted that the barostat and the volume/length control are only applied to non-loading directions.

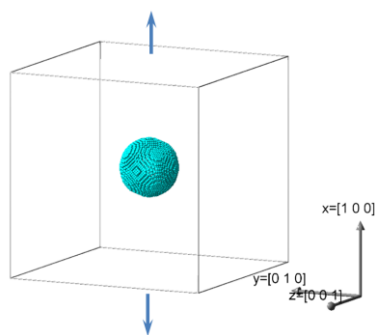


Figure 4.1: Initial configuration of simulation box ($26 \times 26 \times 26$ nm) and central spherical void ($r=3.5$ nm) inside (only atoms representing the surface of void are shown).

² See the fix nve command in the LAMMPS manual (Jun 28, 2014 version)

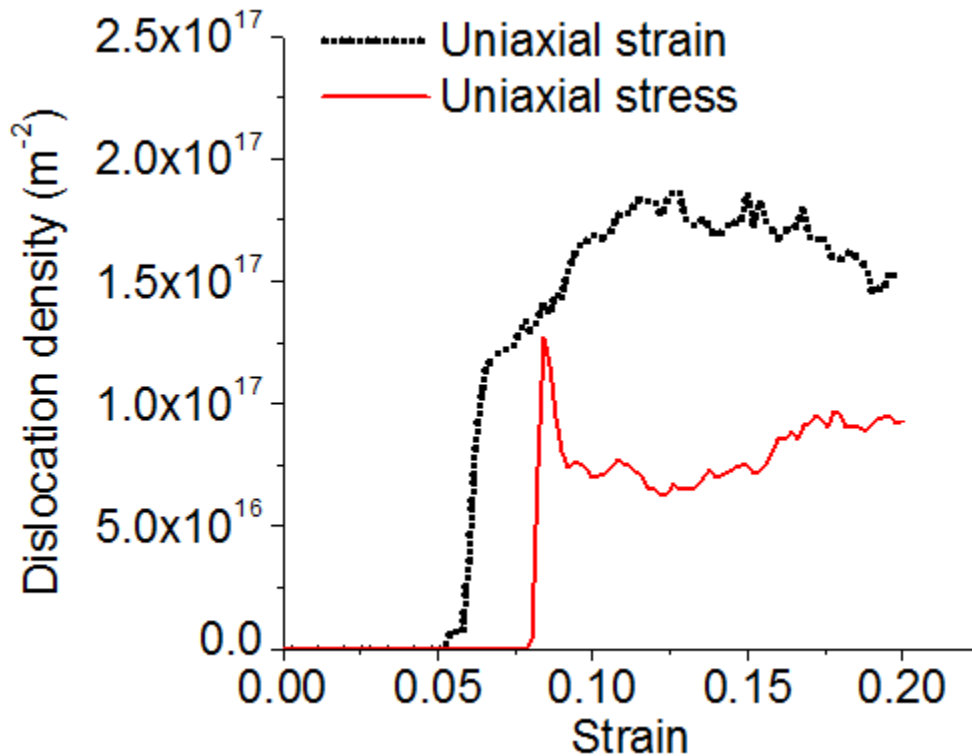
The Large-scale Atomic/Molecular Massively Parallel Simulator (LAMMPS) is used in our simulations. Atomic interaction is modeled by the embedded atom method (EAM) [110]. Mishin et al. [112, 113] reported the EAM potentials for aluminum and copper, respectively. These potentials demonstrated accurate intrinsic and unstable stacking fault energy such that they have been extensively applied in MD simulations [26, 38, 97, 102, 103, 111, 114]. Hence, this EAM potential for copper [113] is chosen to carry out all the simulations here. The void-embedded geometry is created by removing the atoms within a spherical region inside the cubic simulation box as shown in Figure 4.1. The total atom number is approximately 1.5 million. The initial void volume fraction is 1%. The boundaries of the simulation box are made periodic for all the three directions. A fixed time step of 1fs is applied in the simulation. Energy minimization is first performed by using a conjugate gradient algorithm to attain a minimum energy configuration, followed by a relaxation step to reach an equilibrium-state configuration under the designed temperature. The uniaxial load with a strain rate of $2e8 \text{ s}^{-1}$ is applied at both ends in the x direction. The two lateral directions are decoupled with the loading direction in using the barostat for the NPH and NPT cases. For the NVT and NPT ensemble cases, the temperature is constrained to 0.1 K during the loading process through the Nosé-Hoover thermostat. For the NVE and NPH cases, the initial temperature for dynamic run is 300K. The MD post-processing software ATOMVIEWER [85] is employed in post-processing the MD data to identify the dislocation network and Burgers vectors. It combines the modified Nye-tensor method and the dislocation line extraction method to derive Burgers vectors and dislocation network without constructing Burgers circuits explicitly [85]. We refer to the work of Begau et al. [85] for details. With the help of the MD software ATOMVIEWER, the computation of the overall dislocation density becomes feasible.

4.3. Results and Discussions

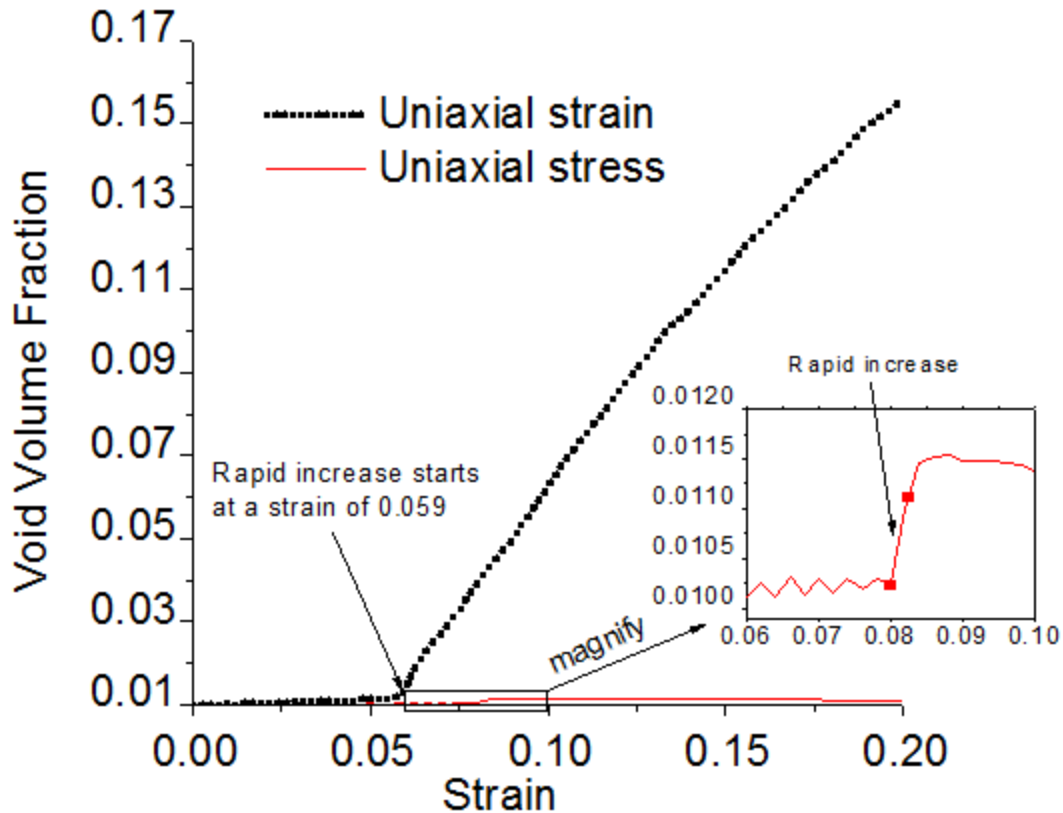
4.3.1. Simulations with Temperature Control

At some point during the loading, a direct visualization of the dislocation network would become difficult once the dislocation forest spreads all over the whole simulation box. It is then more convenient to characterize the dislocation curves by their density. The dislocation density by definition is the length summation of the entire dislocation population divided by the containing volume. The software ATOMVIEWER outputs the dislocation network files which contain the number of dislocations and the node information for each dislocation segment. The dislocation density could then be obtained by summing up the distance between the nodes belonging to each dislocation segment and dividing it by the current system volume. Attention has been paid to prevent misconnecting the nodes due to the periodicity of the simulation box in finding the length of individual dislocation segment. In Figure 4.2a, the strain for the onset of dislocation emission is 0.052 for the uniaxial-strain case by applying the NVT ensemble and 0.078 for the uniaxial-stress case by applying the NPT ensemble. The dislocation initiation is then defined as the moment when dislocation number calculated by the software ATOMVIEWER is first found non-zero. In Figure 4.2a, both the dislocation density curves have a burst of increase shortly after the onset of dislocation emission. The uniaxial-strain curve keeps climbing despite a little fluctuation. After reaching the peak value, it develops a mild decline to the end of loading. The uniaxial-stress curve declines sharply by around a half after reaching its peak value and regains a mild growth at some points later towards the end of loading. This difference between the dislocation density curves comes from the different spacing in the lateral directions. Additional simulation with constant system volume under NVT ensembles results in a very similar dislocation density evolution compared with the uniaxial-stress case (not shown for

brevity). This implies that it is not the barostat itself but the confined spacing in the lateral directions that causes the difference. Due to less spacing in the non-loading lateral boundaries, more dislocation annihilations happen so as to lower the entire dislocation population of the uniaxial-stress case. However, both two curves show a certain saturation tendency. Neither significant increase nor decrease is found at a higher strain range. The pertinent theoretical models for the dislocation density evolution (Schall et al., 1999; Malygin, 1990) also predict a saturation feature after a burst of growth. In this sense, both cases are qualitatively consistent with these models. Quantitatively, our calculated total dislocation density agrees with that from a recent MD simulation ($\sim 10^{17} \text{m}^{-2}$) [129].



(a) Dislocaiton density



(b) Void growth

Figure 4.2: The dislocation density and the corresponding void growth.

The void is recognized by identifying the atoms belonged to its surface and the Delaunay triangulation method [86] is applied to calculate the void volume through the recognized nodes. This void volume calculation method has been validated in a quasi 2D case as it is then alternatively feasible to directly measure the void size through image processing. Marked by the dislocation emission, the void growth can be divided into two regimes: elastic and inelastic regimes. Rapid void growth of both regimes starts shortly after the onset of dislocation emission. The correlation between the dislocation density and the void growth is clear: the burst of dislocation density results in a rapid void growth. During the rapid void growth, the void gain

more volume than the total volume increase of the simulation box. This implies that the tightened atomic bonds due to the elastic deformation have been relaxed in some certain region. The material transport pattern during the rapid growth of the void will be investigated later. For the uniaxial-stress case, its peak void volume fraction is merely 15% its initial value. By comparison, the void growth under uniaxial strain is as high as over 15 times its initial size. The pace of void growth under uniaxial strain gradually approaches the pace of volume increase of the simulation box. From the standpoint of strain gradient plasticity theory, Wu et al. [130] suggested that void with radius under 10nm as embedded in an infinitely large material would stop growing. A fact is that the MD simulation box is periodic and its size could not be deemed as infinitely large with respect to the void. Since the plastic deformation is volume-preserving, the excessive increase of the system volume under the uniaxial strain case inevitably leads to the excessive growth of the nanovoid. By comparison, the uniaxial-stress case results in no forcible increase of the simulation box volume and ends up with nearly no void growth. Although our simulation condition does not totally resemble that in Wu et al. [130] our result at least explains that the excessive void growth under the uniaxial-strain case is due to the excessive increase of system volume. The need to dissipate the mechanical energy, once the dislocation motion begins, induces a fluctuation to the system temperature under the NPT and NVT ensembles. Rather than explicitly rescaling the velocity of the atoms, the Nose-Hoover thermostat acts like an imaginary heat bath [83]. It efficiently regulates the system back to 0.1K while still allows a short temperature rise and fall due to a too fast mechanical energy buildup.

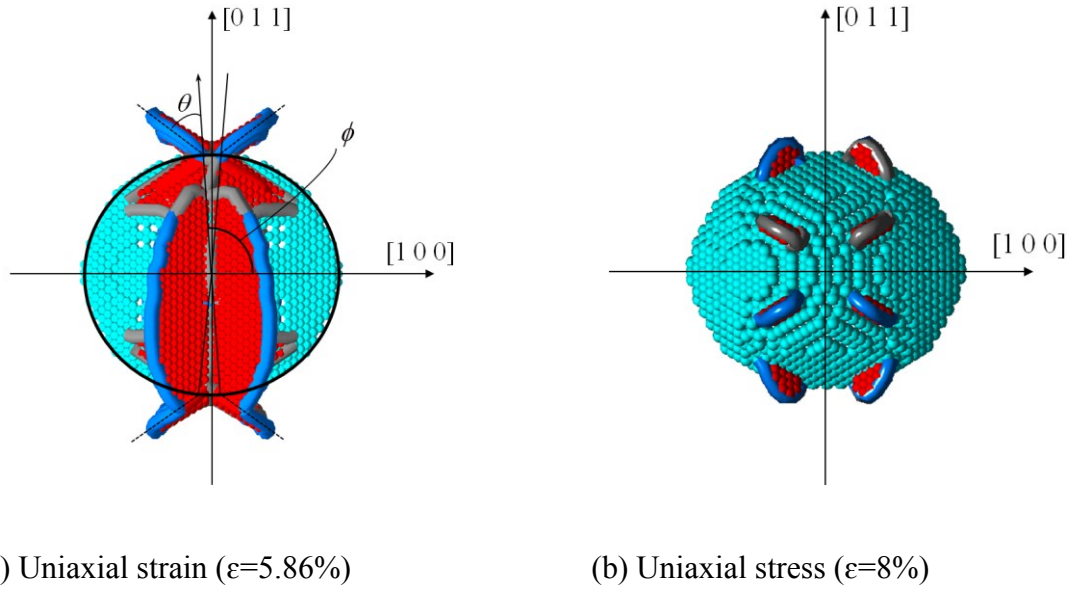


Figure 4.3: The dislocation emission angles of the uniaxial strain. Red atoms here are stacking fault atoms while the light blue atoms represent the void surface. Gray and blue rendered lines represent dislocation lines.

Table 4.1: Dislocation Angles Compared with the Lubarda Model

	Uniaxial strain	Analytical $k=1.047$
ϕ_{cr}	94°	87°
θ_{cr}	55°	49°

Lubarda [91] proposed a theoretical model for dislocation emission from void under a combined loading case. The minimum critical stress is obtained by minimizing the critical stress with respect to two angular variables. In the meantime, these two emission angles, denoted by θ and ϕ , have also been determined during the minimization process as detailed in Ref. [91]. With the temperature regulated to 0.1K, the early dislocation emission as shown in Figure 4.3 exhibits relatively high order of symmetry. This very regular shape of dislocation emission under low

temperature makes it feasible to measure the pertinent emission angles. Axes and auxiliary lines have been added onto the original dislocation snapshots to measure the emission angles. For the uniaxial-stress case, the cutting angle θ is approximately zero as seen from Figure 4.3b. Uniaxial strain implies a triaxial stress state to the system. In order to calculate the two emission angles according to Lubarda [91], the corresponding stress state must first be determined. In Figure 4.3a, the projection of the stress onto the $[0\ 1\ 1]$ and $[1\ 0\ 0]$ directions approximates a combined in-plane stress state with a ratio of $k=1.047$ under the corresponding strain. Nevertheless, the ratio k only has a relatively limited impact on the two dislocation emission angles as predicted by the Lubarda model. By comparison, the simulation with lateral directions under NPT ensemble produces a uniaxial stress state as it efficiently keeps a zero stress on the lateral boundaries. In Table 4.1, a good agreement of the dislocation emission angles can be found between the theoretical model and our simulation results for the uniaxial-strain case. However, it is not the same scenario for the uniaxial-stress case. Its emission angle ϕ simply cannot be measured under a same viewing angle.

An important measurement to investigate the material transport is perhaps the displacement field. In continuum theory, this displacement field is calculated by relating the deformed configuration to the initial configuration at each material point. At atomic level, the concept of material points embody as individual atoms inside the lattice structure. This atomic displacement field, like the one in continuum theory, could be quantified through comparing the current positions of the atoms to their initial positions. Such calculated displacement field would contain both the elastic and plastic deformation and also be subject to the established coordinates. Hence, the idea of “relative displacement” is created to exclude this homogeneous elastic deformation due to the stretch (see Appendix). The reason not to seek the decomposition of the strain tensor is

that the displacement field in atomic scale is already not smooth and may contain strong discontinuity once dislocations emerge. The strain field, as the derivative of the displacement field, would then be rather difficult to obtain. As a compromise, the relative displacement readily reflects the inelastic and heterogeneous deformation. The RFT atoms are defined once the relative displacement of some certain atoms exceeds a critical level. These atoms represent a part of the material with strong inelastic/heterogeneous deformation. The atom IDs dumped by LAMMPS are employed to link the current atom positions to their initial positions. In order to examine the relevance between the dislocation network and the material transport at atomic level, the software ATOMVIEWER is employed. It is capable of separately displaying both high-resolution 3D-rendered entities of dislocations and those RFT atoms at the same time. This composite plot can be seen in Figures 4.4d, e, and f, for example.

After the onset of dislocation emission, small tetrahedron-like structures form at the four corners of the void. In Figure 4.4a, shear dislocation curves start to emerge from between these tetrahedron-like structures. Gradually, intersection lines are created by the interaction among the shear curves. Two frustum-like structures then form along the loading direction in a quite symmetric fashion. Even with simulation box doubled, there is still no sign of these shear dislocation curves turning into prismatic loops. The reaction mechanism of in-plane dislocation loops could be found in the work of Traiviratana et al. [26] and Bringa et al. [38]. Our focus here is then how the dislocation structures induce the material transport and help to grow the void.

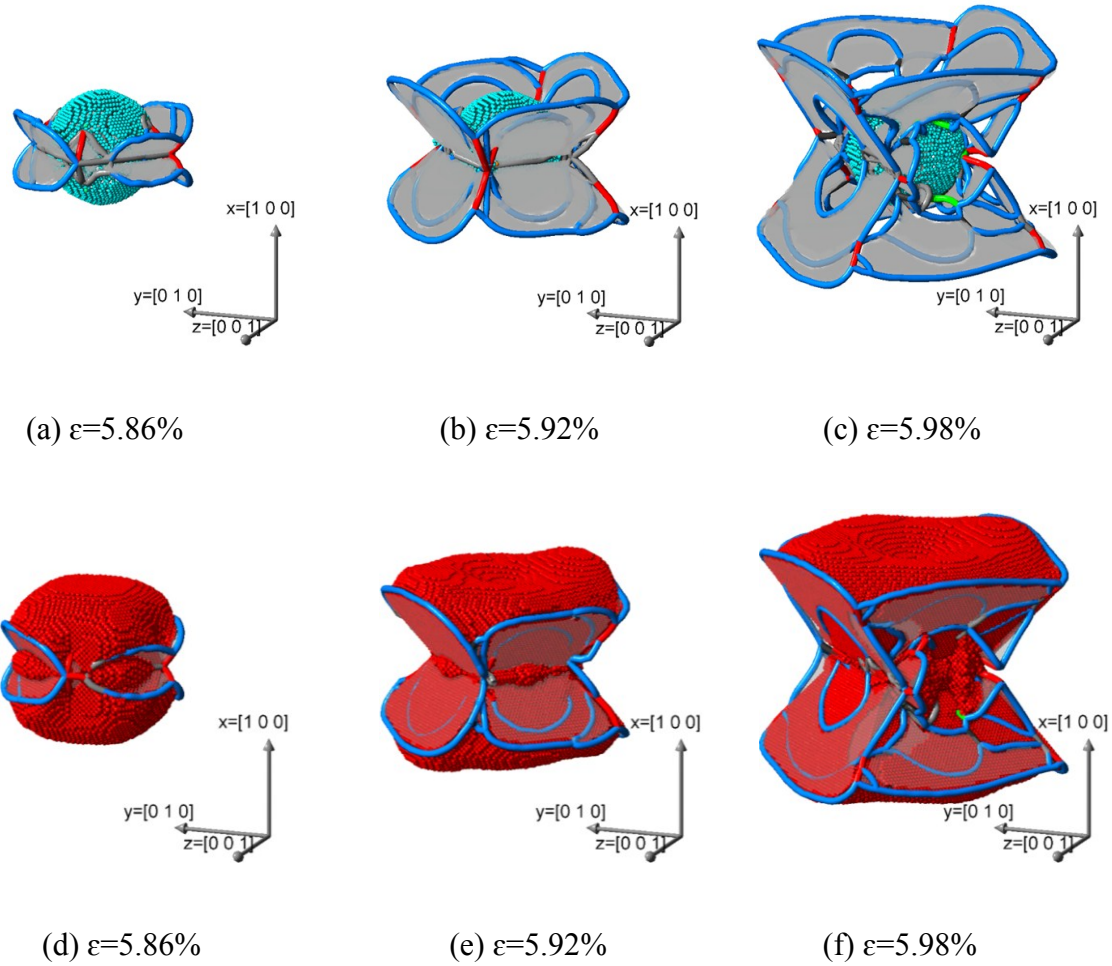


Figure 4.4: The dislocation structure and the RFT atoms (in red) for the uniaxial-strain case (NVT). The RFT atoms are made invisible in (d-f). Light blue atoms in (a-c) represent void surface. The red and blue rendered lines represent dislocation lines. The stacking faults areas are colored in gray. The critical length is set at 1.0 \AA to identify the RFT atoms.

During the elastic regime, the void growth is due to the stretch of the atomic bonds. After the onset of dislocation emission, the dominating growth pattern is still elastic. The RFT atoms are few in number and only found near the void surface facing the loading direction. It is then until about a strain of 5.86% that a rapid growth of the void is discovered in Figure 4.2b. At this strain, the shear loops and frustum-like structures emerge. In Figure 4.4d, the RFT atoms in red

are partly caused by the elastic deformation since the dislocation structures are still in the incipient stage. The number of identified RFT atoms in Figure 4.4d is fewer than those in Figures 4.4e and f. Furthermore, the maximum magnitude of the relative displacement in Figure 4.4d is only about one-fourth of that in Figure 4.4e. The rapid void growth is accompanied by the rapid extension of the shear curve front and the development of frustum-like structures. If the critical length rises from 1.0\AA to 3.0\AA , the identified RFT atoms will gather around the shear-loop planes attaching at the void surface. The detailed mechanism is that shear loops on the slip plane help to move the material away from the void surface. The forming of the larger frustum-like structure further facilitates the void growth. After the strain 5.98%, the dislocation structures start to interact with those from the periodic neighbors and make the correlation between the dislocation and void growth hard to observe.

Compared to the uniaxial-strain case, the uniaxial-stress state induces quite different slip systems in Figure 4.5a. Sixteen dislocation emission sites emerge on the void surface. Unlike the uniaxial-strain case, the emission angles under the uniaxial-stress are not in line with the theoretical prediction. The emitted dislocation curves in Figures 4.5a-c keep spreading and enlarging their stacking fault areas. Noticeably, a newly formed frustum-like structure facing the loading direction can be observed in Figure 4.5c. In Figure 4.5c, there is also another frustum-like structure at the lower side of x direction (view blocked) similar to the upper one. These two newly-formed frustum-like structures are less symmetric compared to those of the uniaxial-strain case. This difference in the dislocation buildup between the uniaxial-strain and uniaxial-stress cases is caused by the difference between their system volumes. The uniaxial-strain case increases the system volume much higher than that of the uniaxial-stress case. Additional simulation with constant system volume under NVT ensemble results in a triaxial stress state but

a very similar dislocation structure compared with the uniaxial-stress case (not shown for brevity). The discrepancy in both the dislocation development and the system volume eventually lead to the discrepancy in the void growth for the two cases.

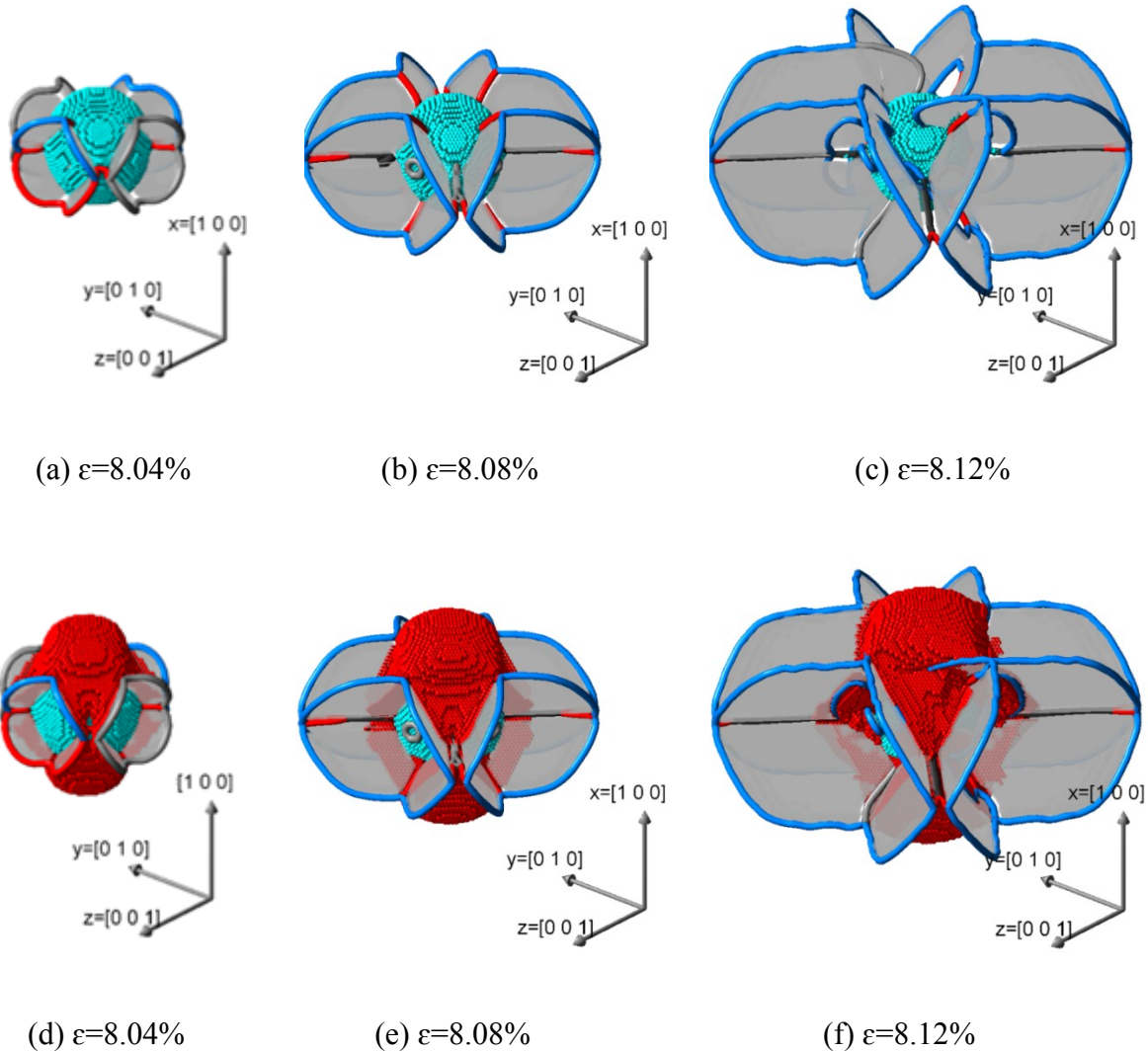


Figure 4.5: The dislocation structure and the RFT atoms (in red) for the uniaxial-stress case (NPT). The RFT atoms are made invisible in (d-f). Light blue atoms in (a-f) represent the void surface. The red and blue rendered lines represent dislocation lines. The stacking faults areas are colored in gray. The critical length is set as 1.0 \AA to identify the RFT atoms.

The rapid void growth for the uniaxial-stress case begins at a strain of 8% as shown in Figure 4.2b. The RFT atoms in Figure 4.5d are only inside the enclosing dislocation structures facing the loading direction. In Figure 4.5f, the newly formed frustum-like structure not only contains more RFT atoms but also results in a much higher maximum magnitude of the relative displacement. The strongest atomic material transport still happens near the dislocation curves attached to the void surface. The contributors of the material transport are still the multiple shear curves on the corresponding slip planes.

In Figure 4.6, the anisotropic growth of the voids is displayed. Under the elastic regime, voids under both the two cases elongate mostly in the loading direction. Once entering the inelastic regime, the uniaxial-strain case exhibits a much faster pace of elongation in all the directions. It is worth noting that the rapid growth of the void under the uniaxial stress from strain 0.08 to 0.082 is due to the sudden length increase in both the loading and the lateral directions in Figure 4.6. In most of the time, the uniaxial-stress case results in void growing in the loading direction and contraction in the lateral directions. The final 3D void shapes at the end of loading are shown inside Figure 4.6. For the uniaxial-strain case, the void evolves into an octahedron shape. Put the stress response aside, the evolved void shape under the uniaxial stress is similar to the common observation in a normal tensile test: an elongated ellipsoid in the loading direction. The elongation of this void in the loading direction and the shrinkage in the lateral directions could be explained by the same change in aspect ratio of the simulation box.

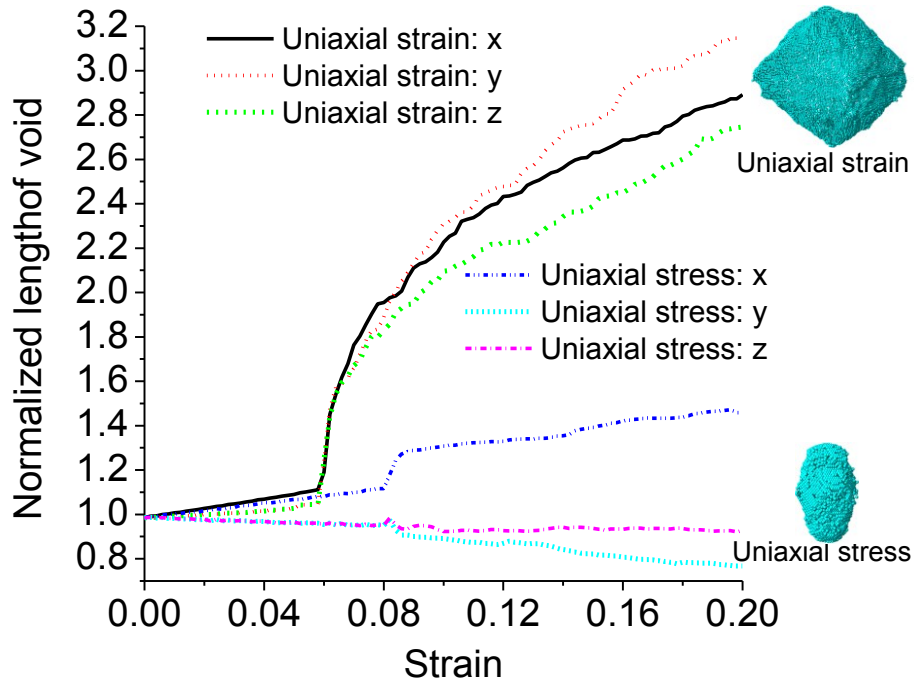
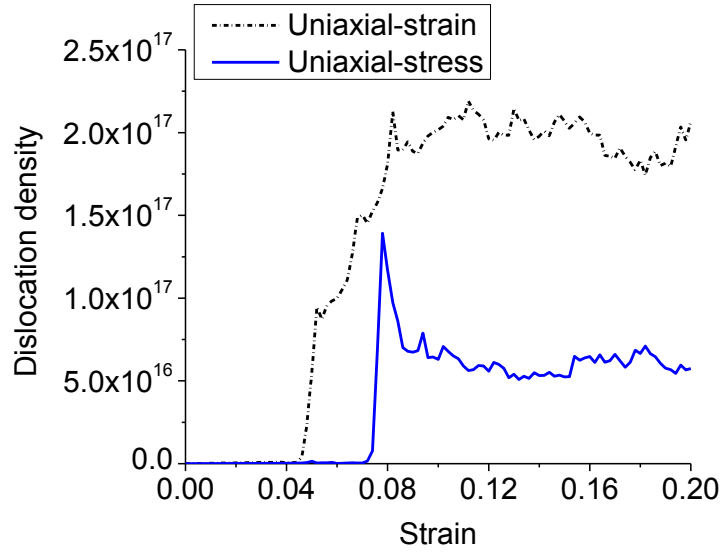


Figure 4.6: Shape evolution of the void by its size in all the three directions for both the uniaxial-strain and uniaxial-stress cases under a temperature of 0.1K.

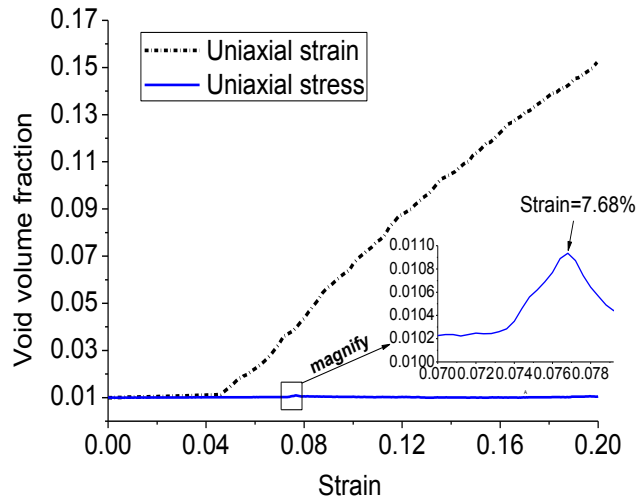
4.3.2. Dynamic Simulations without Temperature Control

A thermostat has been applied in the previous subsection to regulate the system temperature to 0.1K. Additional simulations (not shown) without the use of a thermostat started at the same temperature 0.1K have also been conducted, respectively, for both the uniaxial-strain/uniaxial-stress cases. The temperature rises, only after the dislocation buildup, to about 100K at the end of loading. The overall difference is trivial regarding the void growth, dislocation evolution and even the stress-strain relation. Hence, these results are not shown for brevity. As substitute, the simulation cases in the present subsection are run under an initial temperature of 300K. Particularly, the temperature control in the previous subsection only serves as an imaginary situation to exclude the thermal activation and thermo-mechanical interaction. For a more

realistic situation under $T=300\text{K}$, removal of the temperature control appears to be more physical although the discrepancy is rather insignificant. Hence, the simulations in this subsection are run under an initial temperature of 300K and without applying the thermostat.



(a) Dislocaiton density



(b) Void growth

Figure 4.7: The dislocation density and the corresponding void growth with initial temperature 300K and no thermostat applied.

Without the temperature control, the correlation between the dislocation density and the void growth is still clear for the dynamic situation: the burst of dislocation density results in a rapid void growth. The magnitude and the saturation feature of the dislocation density curve are close to that under a temperature of 0.1K. For the uniaxial-strain case under $T=300\text{K}$, the formation of its dislocation structure is less symmetric and less regular than that under $T=0.1\text{K}$. The sudden growth of its dislocation density is therefore less smooth than that under $T=0.1\text{K}$. For the uniaxial-strain case under NVE ensemble, its system temperature elevates to about 453K at the end of loading only after a strain of 7%. The sudden temperature rise of the uniaxial-strain case under NVE ensemble is very similar to that reported in Bringa et al. [38]. The need to dissipate the mechanical energy during the dislocation development elevates the temperature. For the uniaxial-stress case under NPH ensemble, the temperature elevates to about 394K at the end of loading only after a strain of 7.54%. The void growth under uniaxial strain is about 16 times its initial size. The void growth pace of the uniaxial-strain case still approaches the pace of volume increase of the simulation box under higher strain. By comparison, the peak void volume fraction under uniaxial stress is merely 9% its initial value, which is even smaller than the corresponding case under $T=0.1\text{K}$. Another prominent feature is the decrease of the void volume fraction as highlighted inside Figure 4.7b. The range of this declining is from 7.68% to 7.92% in strain. For further investigation, the halved void surfaces at the strain of 7.68% and 7.92% are plotted in a combined way in Figure 4.8. The dark blue atoms indicate the current void surface at the strain 7.68% while the dark red atoms indicate the current void surface at the strain 7.92%. Atoms in a certain color cover the others only when they are “outside”. Bearing this in mind, Figure 4.8 implies that the shrinkage area (in dark blue) is larger than the growth area (in dark red) on the void surface. This decrease of void size is also affected by the dislocation network as the

shrinkage and growth regions are related to dislocation structures attached on void surface. Until this strain range, the dislocation interaction between the central void and its periodic neighbors has created an interconnected dislocation complex through the periodic boundaries. The major material transport is then not only restricted to the inside of dislocation structures facing the loading direction. The newly developed dislocation structures towards the lateral directions help to impose the shrinkage of the simulation box in lateral directions onto the void surface.

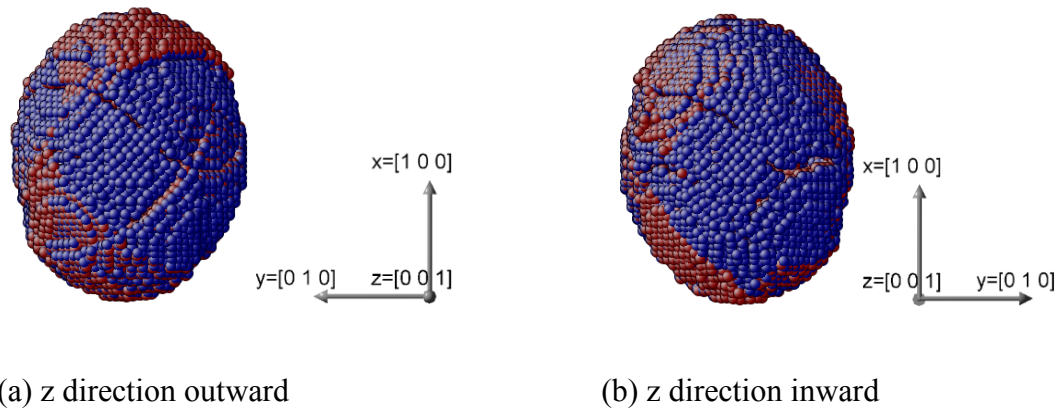
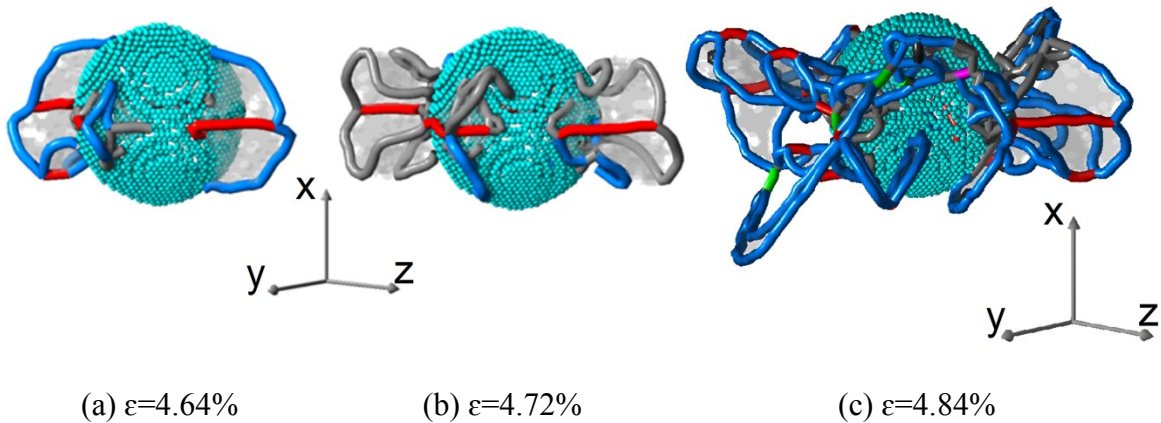


Figure 4.8: The surface growth and shrinkage for the uniaxial-stress case. The halved void surfaces combining two different strains have been plotted in a combined way. The dark blue atoms represent the void surface at the strain 7.68% while the dark red atoms represent those at the strain 7.92%. Dark red area indicates growth area while the dark blue area indicates the opposite.



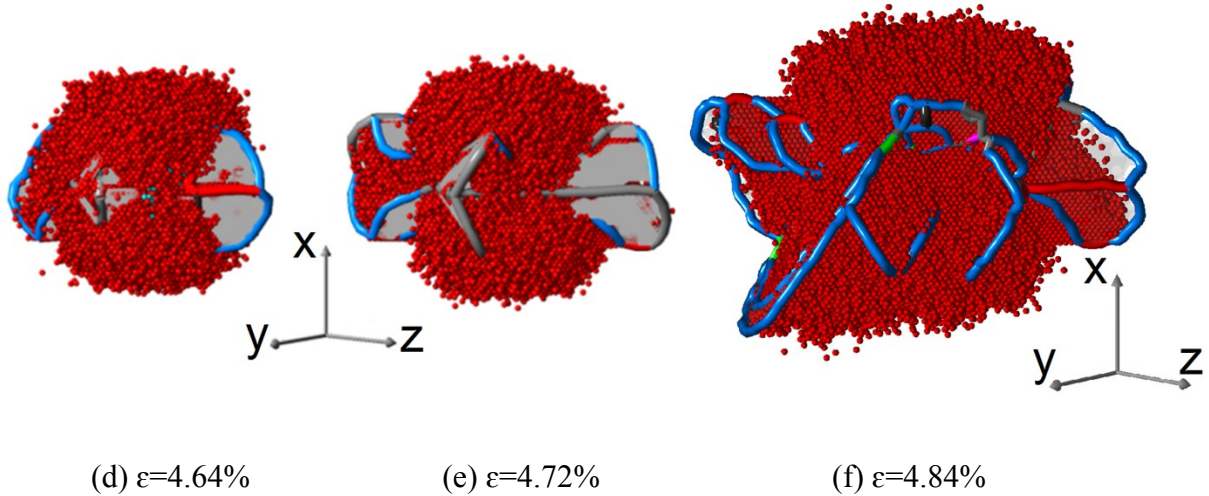


Figure 4.9: The dislocation structure and the RFT atoms (in red) for the uniaxial-strain case (NVE) under an initial temperature of 300K. The RFT atoms are made invisible in (d-f). Light blue atoms in (a-c) represent void surface. The rendered lines in blue, red and gray represent dislocation lines. The stacking faults areas are colored in gray. The critical length is set at 1.0 Å to identify the RFT atoms.

The development of dislocation structures with an initial temperature of 300K is quite different from those under a temperature of 0.1K for the uniaxial-strain case. No tetrahedron-like structure forms at the four corners of the void at the very beginning. In Figure 4.9a, highly asymmetric dislocation structures composed of shear dislocation curves extrude from the void surface. Two prism-like structures form along the y direction in Figure 4.9b. These structures are soon replaced by more complicated structures through the interaction between the dislocation curves. Two structures with opening angle, which appear to be variants of the frustum shape, form along the loading direction in Figure 4.9c. Notably, a large extruding shear loop is spotted in Figure 4.9c towards the $[-1 \ 1 \ 0]$ direction in the lower side. Under an initial temperature of 300K, the rapid void growth starts earlier (4.7% in strain) after the dislocation emission (4.5% in

strain) than that controlled at a temperature of 0.1K (5.9% and 5.2% in strain, respectively). The RFT atoms in Figure 4.9e are found inside the prism-like structure towards the lateral directions, which is different from that shown in Figures 4.5d-f. The large extruding shear loop in Figure 4.9f affects the material transport at one side of its loop plane. However, the void growth pace of the uniaxial-strain case in Figure 4.7b is found slower than that in Figure 4.2b. The formation of the larger and more regular frustum-like dislocation structures in Figure 4.4 for the low-temperature uniaxial-strain case appear responsible for the difference in the void growth pace. Once the dislocations interact with those from the periodic voids, the correlation between the dislocation structure and void growth becomes even more difficult to capture, and therefore, would be the focus of the future work.

The slip systems of the uniaxial-stress case under an initial temperature of 300K are neither similar to the uniaxial-strain case under same temperature, nor to the uniaxial-stress case under $T=0.1K$. Only two shear loops emit from the void surface in Figure 4.10. The rapid void growth for this case starts at a strain of about 7.3% as shown in Figure 4.7b. Figure 4.10 illustrates how the transition of void growth happens with the emergence of the shear loops. With initially $T=300K$, the RFT atoms are much more scattered than those in Figure 4.5 under $T=0.1K$. In addition, the same conclusion can be drawn when comparing Figure 4.9 with Figure 4.4. Given this highly-scattered pattern of atomic material transport, the strain field derived from the MD data may not be as reliable as the RFT atoms. This is the exact reason why the so-called RFT atoms are adopted as a better measurement for material transport in atomic level.

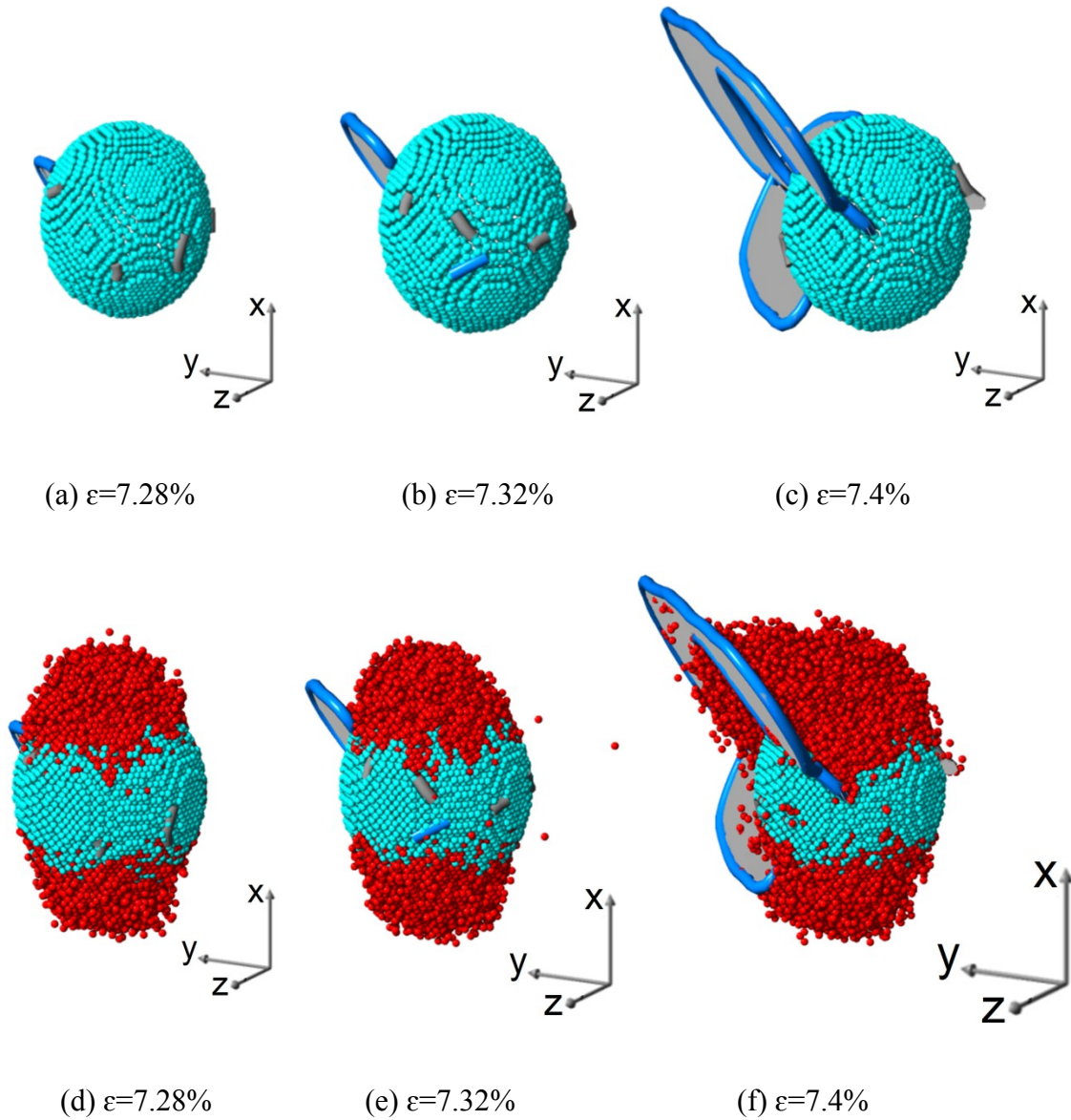


Figure 4.10: The dislocation structure and the RFT atoms (in red) for the uniaxial-stress case (NPH). The RFT atoms are made invisible in (d-f). Light blue atoms represent the void surface.

The blue lines represent dislocation lines. The stacking faults areas are colored in gray. The critical length is set at 1.0 \AA to identify the RFT atoms.

Figure 4.10f demonstrates that a single shear loop, even not forming a dislocation structure, is still capable of affecting the local material transport and hence influences the void growth. It

should be noted that the material transport via shear loops does not violate mass conservation. Based on Hirth [57], the surface cut to create a dislocation loop is not necessary its loop plane, and hence does not contradict our observation here.

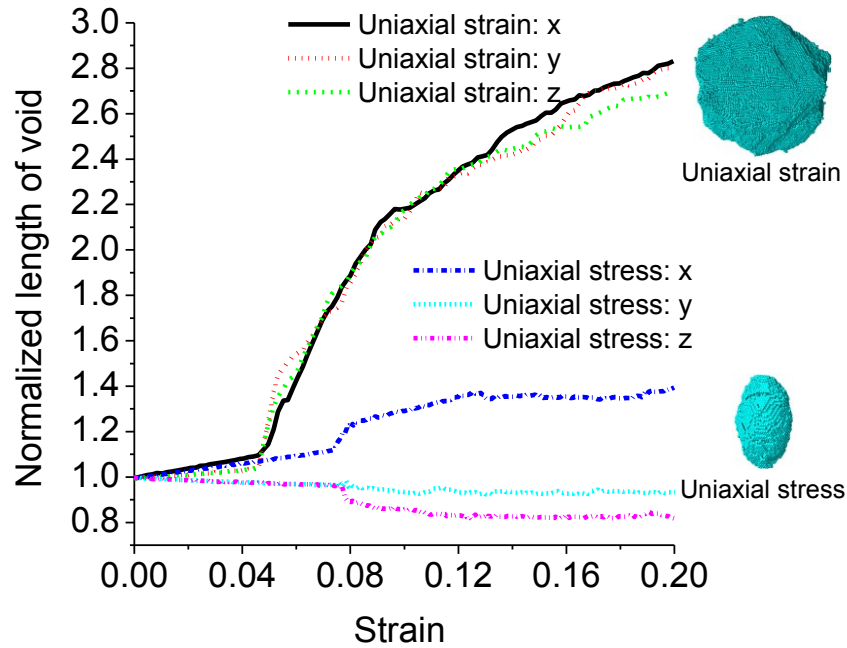


Figure 4.11: Shape evolution of the void by its size in all three directions for both the uniaxial-strain and uniaxial-stress cases under an initial temperature of 300K.

Compared with Figure 4.6, less difference among the void size in its three directions is found for the uniaxial-strain cases in Figure 4.11. Under the elastic regime, voids of both cases elongate mostly in the loading direction. Once entering the inelastic regime, the uniaxial-strain case still exhibits a much faster pace of elongation in the loading direction. But this pace is not as rapid as that in Figure 4.6 due to the difference in the dislocation structure between the two uniaxial-strain cases with different simulation temperature. It appears that the shear curves grow the void surface more efficiently once they form a large frustum-like structure. The simultaneous void growth in all the three directions of the uniaxial-stress case within a short range in Figure

4.11 appears weaker, resulting in a lower increase of the corresponding void volume fraction than that in Figure 4.6. The final void shapes at the end of loading are shown inside Figure 4.11. The much higher simulation temperature results in a deviation of the void shape from the octahedron shape for the uniaxial-strain case. For the uniaxial-stress case, the void still evolves into a prolate ellipsoid along the loading direction.

4.3.3. Miscellaneous Factors in Simulation

Other factors may influence the simulation results. Here we only focus on the simulation case at 0.1K without barostat to evaluate the effects of different equilibration duration, simulation size and strain rate. If not mentioned, the typical simulation parameters are 20ps for equilibration, 26.03nm for the initial length of cubic simulation box and $2 \times 10^8 \text{ s}^{-1}$ for the strain rate.

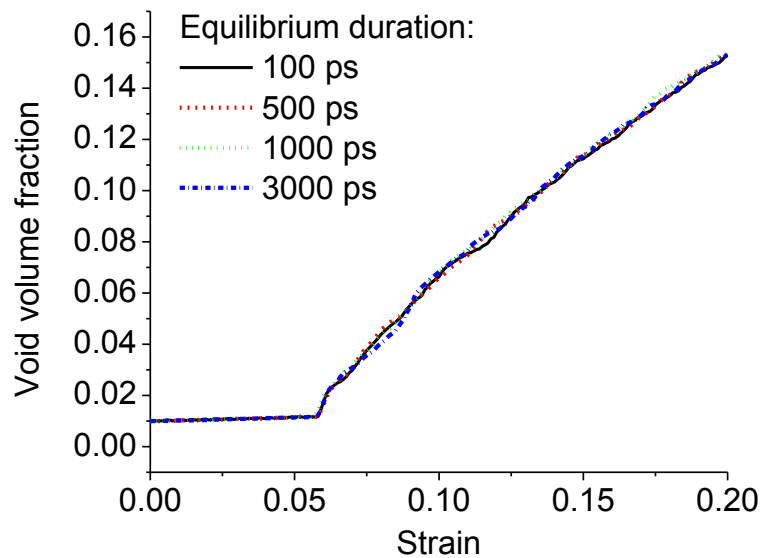


Figure 4.12: The void volume fraction with different equilibration durations.

To ensure that the MD simulation is not sensitive to the selected duration for equilibrating the system before dynamic loading, additional dynamic simulations are first run upon the configuration equilibrated with different durations. Figure 4.12 along with Figure 4.2b demonstrates that void growth simulation is insensitive to the applied equilibration duration. The strain at the onset of dislocation emission is almost independent of the duration. Difference is also trivial in terms of the formed dislocation structure. More importantly, the equilibration duration has no impact on the material transport pattern inside the frustum-like dislocation structures.

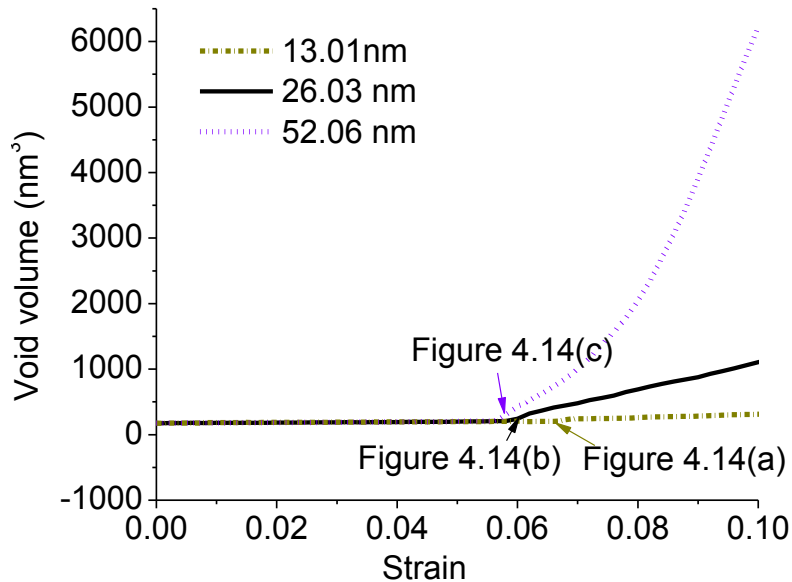
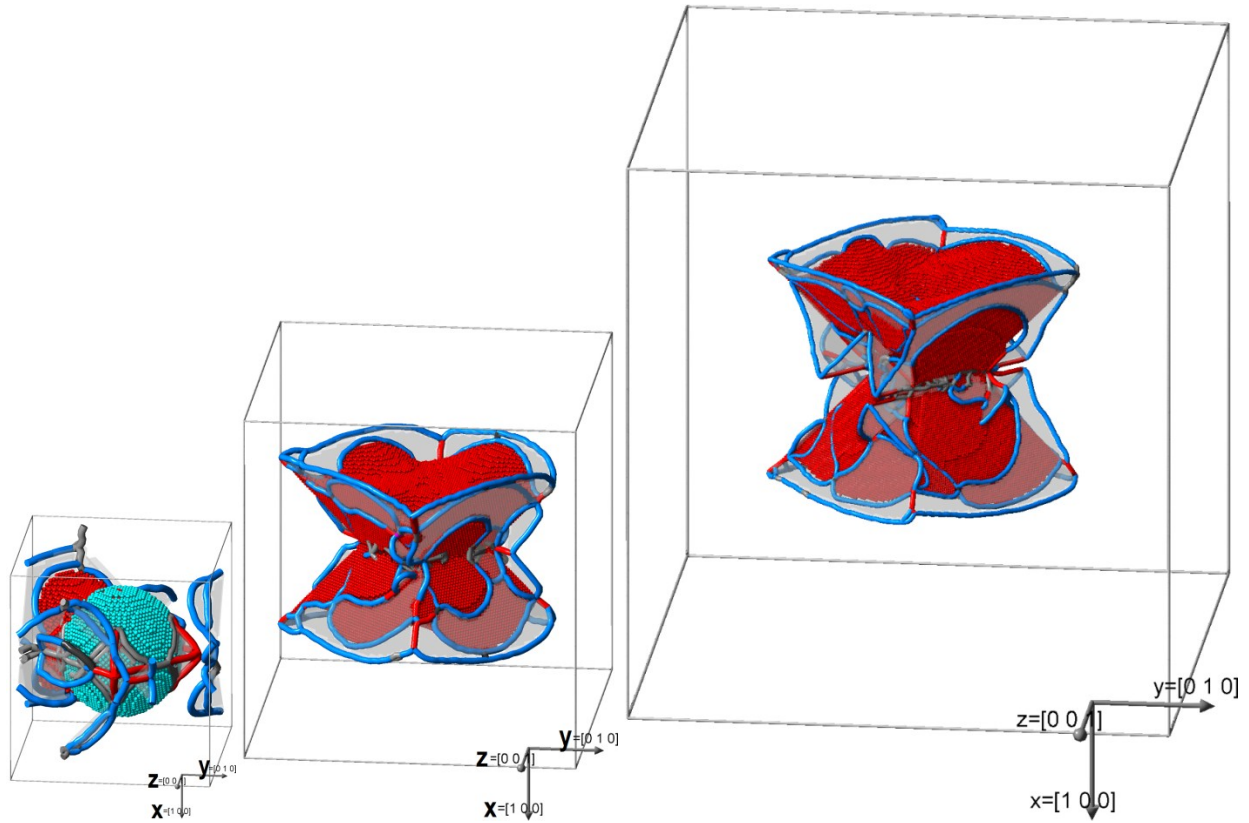


Figure 4.13: The void volume evolution with different sizes of simulation box.

Next focus is the size of the simulation box. Given the void size unchanged, the box size determines the distance between the central void and the periodic boundary. A too small simulation box may hinder the growth of dislocation structures as they reach the periodic boundary too soon. To assess the influence of periodic boundary on void growth, simulations with a half-sized simulation box and a double-sized simulation box will be examined.



(a) $l_{\text{box}}=13.01\text{nm}$ ($V_{\text{fr}}=8\%$) (b) $l_{\text{box}}=26.03\text{nm}$ ($V_{\text{fr}}=1\%$) (c) $l_{\text{box}}=52.06\text{nm}$ ($V_{\text{fr}}=0.125\%$)

Figure 4.14: Material transport visualized by the RFT atoms with different sizes of simulation box. Light blue atoms in (a-c) represent the void surface (almost invisible in (b) and (c)). The red and blue lines represent dislocation lines. The stacking fault areas are colored in light gray. The critical length is set at 2.0 \AA to identify the RFT atoms. The strains in (a-c) are 6.7%, 5.9% and 5.8%, respectively. The snapshots are not proportional to their actual sizes. Equilibration duration in (b) is 3 ns.

First of all, void growth depends heavily on the relative spacing among the voids. In Figure 4.13, the final void inside the double-sized simulation box is about 20 times that inside the half-sized simulation box. The onset of dislocation is strongly delayed in the case of half-sized simulation box. The frustum-like dislocation structure fails to form as shown in Figure 4.14a. Despite the partly-grown dislocation structure, the RFT atoms are still induced by the shear dislocation curves at the upper corner of the simulation box, as shown in Figure 4.14a. For simulation box size 26.03 and 52.06 nm, both the onset strain (4.8% and 4.7%) and the dislocation structure formed are quite similar. Red RFT atoms are seen inside the upper and lower frustum-like structures in Figures 4.14b and c. The RFT atoms fill up the inner shear curves. The dislocation structure and related mass transport become insensitive to the simulation size once the initial void volume fraction decreases below about 1%.

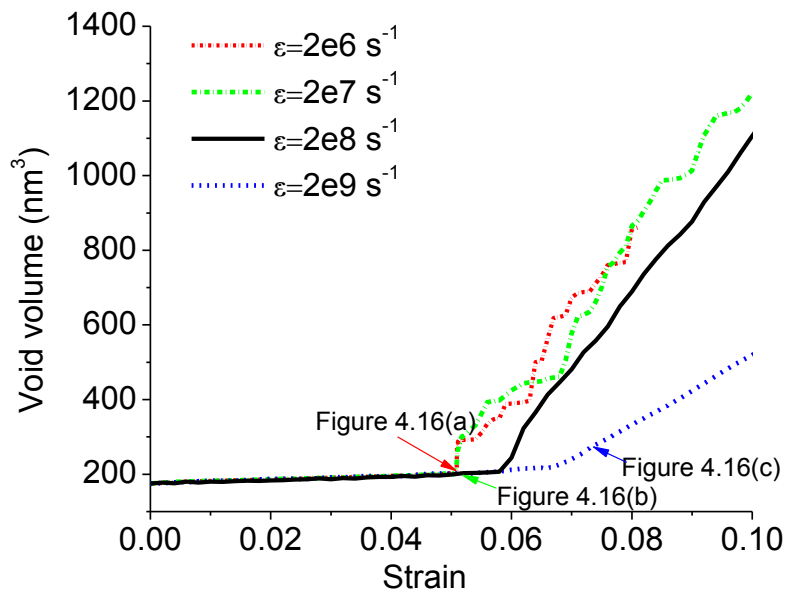


Figure 4.15: The void volume evolution at different strain rates.

For a given final strain of the tensile test, the strain rate determines the time duration of the simulation. The achievable strain rate by MD simulation is in the range of a ballistic loading or a

spall test. Dislocation nucleation can be sensitive to strain rate for a voided specimen in a certain strain rate range [103]. Thus, three additional cases with strain rates from $2 \times 10^6 \text{s}^{-1}$ to $2 \times 10^9 \text{s}^{-1}$ were simulated to examine the difference in the predicted dislocation structure and mass transport.

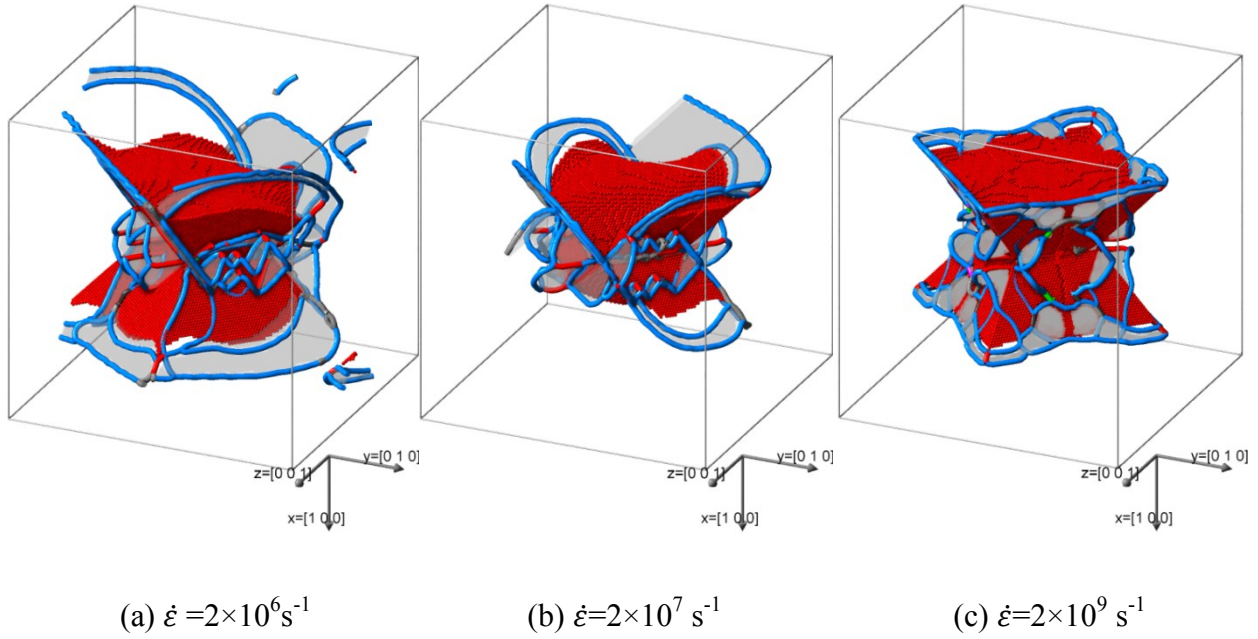


Figure 4.16: Material transport visualized by the RFT atoms with different strain rates. Light blue atoms in (a-c) represent void surface (almost invisible). The red and blue lines represent dislocation lines. The stacking faults areas are colored in gray. The critical length is set at 2.0 \AA to identify the RFT atoms. The strains in (a-c) are 5.09%, 5.1% and 7.4%, respectively. The case of $\dot{\epsilon} = 2 \times 10^8 \text{s}^{-1}$ is shown in Figure 4.14b.

The dislocation structure of $\dot{\epsilon} = 2 \times 10^9 \text{s}^{-1}$ has the most regular and symmetric shape among the four strain rate cases. This is attributed to its short duration of only 50 ps. With much longer durations such as 80 ns for the $\dot{\epsilon} = 2 \times 10^6 \text{s}^{-1}$ case, any small heterogeneity in atomic motion would be magnified and thus results in a highly irregular, asymmetric dislocation structure. The onset

strains at dislocation emission are almost the same (4.75% and 4.76%) for the cases $\dot{\epsilon}=2\times 10^6\text{s}^{-1}$ and $\dot{\epsilon}=2\times 10^7\text{s}^{-1}$. Even their void volume curves coincide when the burst of void growth occurs at $\epsilon=5.1\%$ as seen in Figure 4.15. A higher strain rate results in a lower void growth rate. Last but not least, the red RFT atoms in Figures 4.16a-c and Figure 4.14b demonstrate that mass transport within the dislocation structures exhibits similar pattern at different strain rates.

4.4. Conclusions

The mechanical constraint in molecular dynamics simulation has considerable influence on the dislocation emission, void size and shape evolution. The main conclusions can be drawn as follows:

1. Under the uniaxial-strain loading with NVT ensemble applied, frustum-like dislocation structures consisting of shear dislocation curves are formed. The identified dislocation emission angles of the NVT case are close to those predicted by the Lubarda model. Under the uniaxial-stress loading with NPT ensemble applied, the resulted slip systems are quite different from the NVT case. The identified emission angles under the uniaxial-stress considerably deviate from the Lubarda model. The difference in dislocation pattern for these two cases stems from the different system volume caused by either strain or stress-confined lateral boundaries. The respective uniaxial-strain/uniaxial-stress simulations under $T_0= 300\text{K}$ (with NVE and NPH ensembles) result in highly asymmetric/scattered dislocation pattern, which is mainly influenced by the higher simulation temperature. The calculated dislocation densities agree qualitatively with the theoretical models [131, 131] in terms of the saturation feature under the increasing strain. Quantitatively, they agree with that from a recent MD simulation ($\sim 10^{17}\text{m}^{-2}$) [129].

2. Compared to the uniaxial-strain cases, the void growth under uniaxial-stress state is very limited. The different way to constrain the lateral boundaries is responsible for the difference in void shape evolution. The final void shape of the uniaxial-strain case is close to an octahedron shape. The final void shape under the uniaxial-stress case is a prolate ellipsoid along the loading direction, which resembles that observed in a normal tensile test despite the high strain rate applied. The void growth simulated here might somehow provide hints on the correlation between the dislocation and void growth under an engineering strain rate.

3. During the transition of void growth from elastic to inelastic fashion, the material transport away from the void is induced by shear dislocation loops/curves. The material transport via shear dislocation curves/loops is not only possible but also favorable near their loop plane. Whether or not forming larger dislocation structures, the shear curves/loops are capable of inducing the local material transport. The highly-symmetric large dislocation structures formed under low temperature results in a more rapid void growth compared with their counterparts, i.e., more scattered and asymmetric dislocation structures under a much higher initial temperature.

4. The simulation box size greatly influences void volume evolution. Larger spacing, which allows for a full development of dislocation structures, remarkably accelerates void growth. For simulations with void volume fractions below 1%, the emitted dislocation structure becomes insensitive to the simulation size. Lower strain rates induce more irregular and asymmetric dislocation structures. The mass transport via frustum-like dislocation structure preserves despite the simulation box size or strain rate.

Chapter 5: Void Growth via Shear Loop Emission*

5.1. Introduction

Dislocation emission is considered as the primary cause of void growth under high strain rate [18]. Lubarda et al. [18] proposed two mechanisms regarding the dislocation-related void growth. One of these geometrically necessary dislocations is the prismatic loop and the other is the shear loop. The shear dislocation loop, by definition, has its Burgers vector inside the loop plane. In contrast, Burgers vector of a prismatic dislocation loop is not in the loop plane. Bulatov et al. [56] later claimed the impossibility of mass transport via shear loop. Our attention is initially only paid to the general correlation between the dislocation structure and void growth. However, what has been observed in our simulation clearly backs the mass transport via shear loops/curves. The MD data has been investigated through the so-called “relative displacement”, which is a newly-invented idea to exclude the homogenous elastic deformation. The gathered evidence clearly demonstrates that void growth via shear loops is true for the situation concerned. Such evidence, however, may raise further questions. Why it is the opposite for the related theoretical understanding [56]? What might have been overlooked in asserting the “shear impossibility”? To answer these questions, new theoretic understanding must be established based on a better interpretation of the MD results. Once the “shear feasibility” justified, the further task would be constructing a phenomenological model in order to describe the pattern of void growth via shear loops/curves in a large scale. As is well known, impurities such as voids inside the bulk material could trigger dislocations. Nanovoids inside the metal material can stem from a number of sources such as radiation damage [4]. These nanovoids, due to their small size,

* A version of this chapter has been published. Reprinted with permission from Cui, Y.; Chen Z. Material transport via the emission of shear loops during void growth: A molecular dynamics study. *J. Appl. Phys.* 2016, 119, 225102. Copyright 2016 IOP Publishing Ltd.

are very suitable for MD simulation. Seppälä et al. [132] studied the effect of stress triaxiality on the void growth and pointed out that the dislocations from the void surface are responsible for carrying material away. Traiviratana et al. [26] performed the MD simulation to study the void growth in both monocrystalline and bicrystalline copper. The emission and reaction of the dislocation by the presence of the void are detailed in their work. Their results also supported the idea of void expansion by shear loop formation. Zhao et al. [120] studied the effect of multi-axial stress state on the nano-porous single crystalline copper. In their simulation, quadrangular-prismatic dislocation loops form under hydrostatic loading, while square-frustum dislocation structures appear under uniaxial loading. Bringa et al. [38] studied the effect of loading orientation and nanocrystalline on the void initiation and growth. Their simulation confirmed the mechanism of void nucleation and growth by dislocations. Rodriguez-Nieva et al. [129] recently performed the MD simulation of nano-porous gold under high strain rates. Their pores behave like isolated void at lower strain. The velocity of dislocations is found to rise at first and then reduce dramatically due to the dislocation interactions. Of all the above papers, dislocations are found to be closely related to void growth/shrinkage. However, the direct mass transport pattern and its relevance with the dislocations have not been fully clarified. This highlights our aforementioned effort to uncover the dislocation-related void growth mechanism based on a better interpretation of the MD results.

This chapter is organized as follow. First is the study of a basic case with a spherical void under an initial temperature of 0.1K. Second, the case of an irregular-shaped void will be examined to reflect the effect of initial void shape. Additionally, a simulation under room temperature will help to elucidate the influence of initial temperature. Third, the feasibility of

mass transport via shear loop/curve will be clarified. Fourth, a new phenomenological description of how the dislocation network grows the void will be proposed.

5.2. The Molecular Dynamics Simulation Methodology

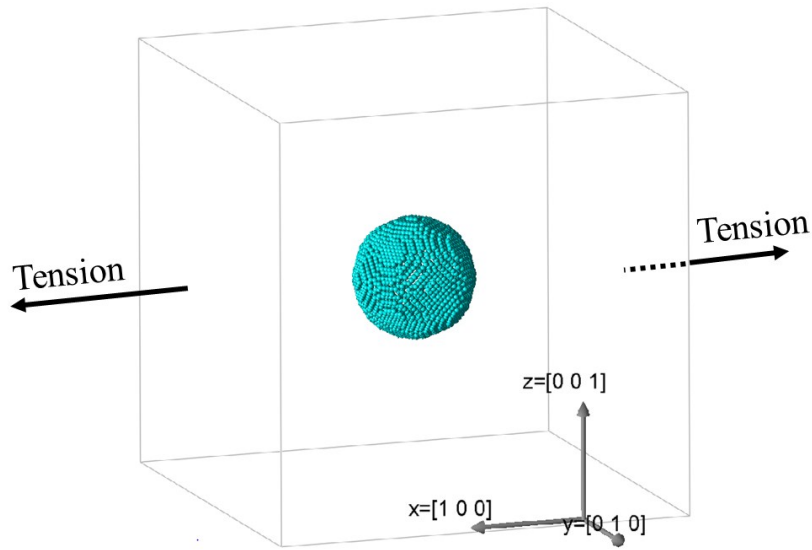


Figure 5.1: Initial configuration of simulation box ($26\times 26\times 26$ nm) and central spherical void ($r=3.5$ nm) inside (only atoms on the surface of void are shown).

The NVE integration updates the position and velocity for atoms at each time step, which creates a system trajectory consistent with the microcanonical ensemble. The applied time integration schemes closely follow the time-reversible measure-preserving Verlet and rRESPA integrators as derived by Tuckerman et al. [128]. The Large-scale Atomic/Molecular Massively Parallel Simulator (LAMMPS) is used in the simulation. Atomic interaction is modeled by the EAM potential [110]. It is crucial that the EAM potential chosen for atomistic simulations must accurately reproduce the pertinent features of the resulted energy curves such as the unstable stacking fault energy [80]. Mishin, et al. [112, 113] reported the EAM potentials for aluminum and copper, respectively. These potentials demonstrated accurate pertinent features of the

resulted energy such that they have been extensively applied in MD simulations [26, 38, 102, 114]. Hence, this EAM potential for copper [113] is chosen to carry out the simulations here.

The void-embedded geometry is created by removing the atoms of a spherical region inside the cubic simulation box as shown in Figure 5.1. The total atom number is approximately 1.5 million. The initial void volume fraction is always 1%. The boundaries of the simulation box are made periodic for all the three directions. A fixed time step of 1 fs is applied in the simulation. Energy minimization is first performed by using a conjugate gradient algorithm to attain a minimum energy configuration, followed by a relaxation step at 0.1 K to reach an equilibrium-state configuration. The uniaxial load with a strain rate of $2e8 \text{ s}^{-1}$ is then applied at both ends in the x direction. The software ATOMVIEWER [85] is employed in post-processing the MD data to identify the dislocation network and Burgers vectors. It combines the modified Nye-tensor method and the dislocation line extraction method to derive Burgers vectors and dislocation network without constructing Burgers circuits explicitly [85]. We refer to the work of Begau et al. [85] for details.

5.3. Material Transport Observation: Void Growth and Material Transport

5.3.1. The Basic Case

A direct visualization of the dislocation network becomes difficult once the dislocation forest spreads all over the whole simulation box. It is then more convenient to characterize the dislocation curves by their density. The dislocation density by definition is the length summation of the entire dislocation population divided by the containing volume. The software ATOMVIEWER outputs the dislocation network file, which contains the number of dislocations and the node information for each dislocation. The dislocation density could then be obtained by

summing up the distance between the nodes belonging to each dislocation segment and dividing it by the current system volume. In finding the length of individual dislocation segment, attention has been paid to prevent misconnecting the nodes due to the periodicity of the simulation box. Quantitatively, the calculated total dislocation density agrees with that of a recent MD simulation [129] ($\sim 10^{17} \text{m}^{-2}$). Similar to Seppälä et al. [132], the 3D void is recognized by identifying the atoms belonged to its surface. Then, the Delaunay triangulation method [86] is applied to calculate the void volume through the recognized nodes. This volume calculation method has been validated under a quasi 2D case as it is then alternatively feasible to measure the void size through image processing.

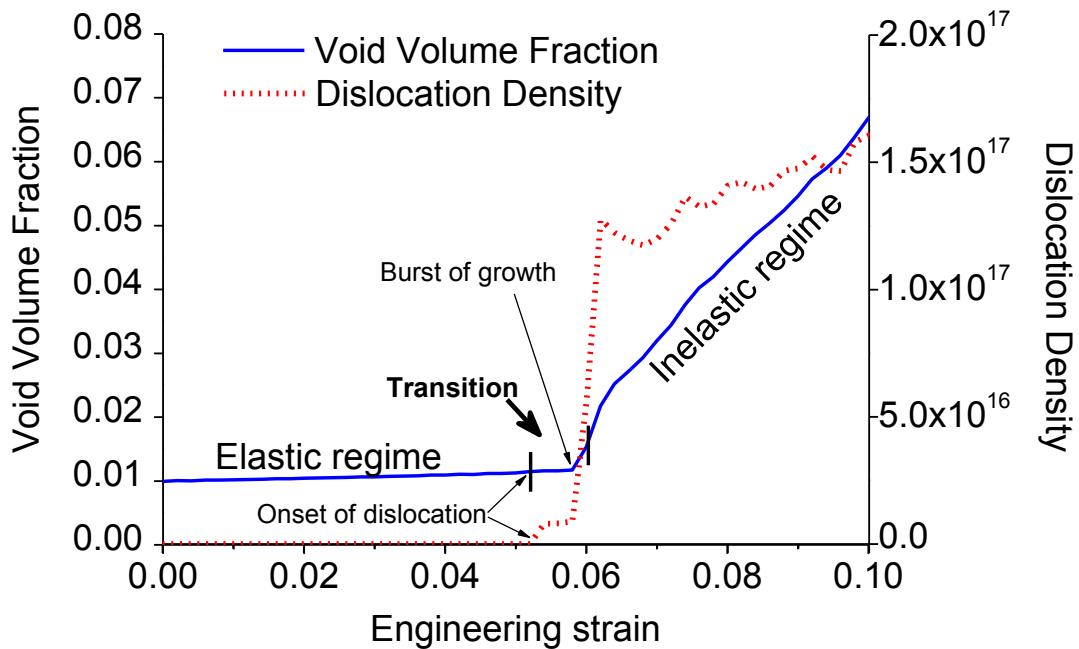


Figure 5.2: The correlation of void growth and the dislocation density. Engineering strain is used.

Figure 5.2 illustrates the general correlation between the dislocation and the void growth. Marked by the dislocation emission, the void growth can be divided into two regimes: elastic and

inelastic. During the elastic regime, the void growth is caused by stretching the lattice. Even after the onset of dislocation emission, the dominating growth pattern is still elastic. This can be seen from the void volume fraction curve in Figure 5.2 and also from the material transport pattern in Figure 5.3b. Only at some point after the onset of dislocation emission will the void growth become highly inelastic. This burst of void growth starts at the strain 0.058, accompanied with a sharp increase of the dislocation density. During the burst of void growth, the void gains more volume than the total volume gained by the simulation box. This implies that the tightened atomic bonds in some region have been relaxed. The volume increase rate of void gradually approaches that of the simulation box. From the standpoint of strain gradient plasticity theory, Wu et al. [130] suggested that a void with radius under 10nm as embedded in an infinite large material would stop growing. One fact is that the simulation box is periodic and its size could not be deemed as infinitely large compared with the void. Since the plastic deformation is volume-preserving, the significant increase of the simulation box volume inevitably leads to the significant growth of the nanovoid.

In the next few subsections, we will further investigate the localized material transport within the strain range from 0.05 to 0.06. This strain range is chosen based on two considerations: 1) the transition of the void growth pattern is within this range; and 2) the dislocation structure will start to reach the periodic boundaries and interact with those from its periodic neighbors afterwards. The re-entering dislocations as periodic images make the situation much more complicated, which is then out of the scope of this study.

5.3.1.1. The End of the Elastic Regime

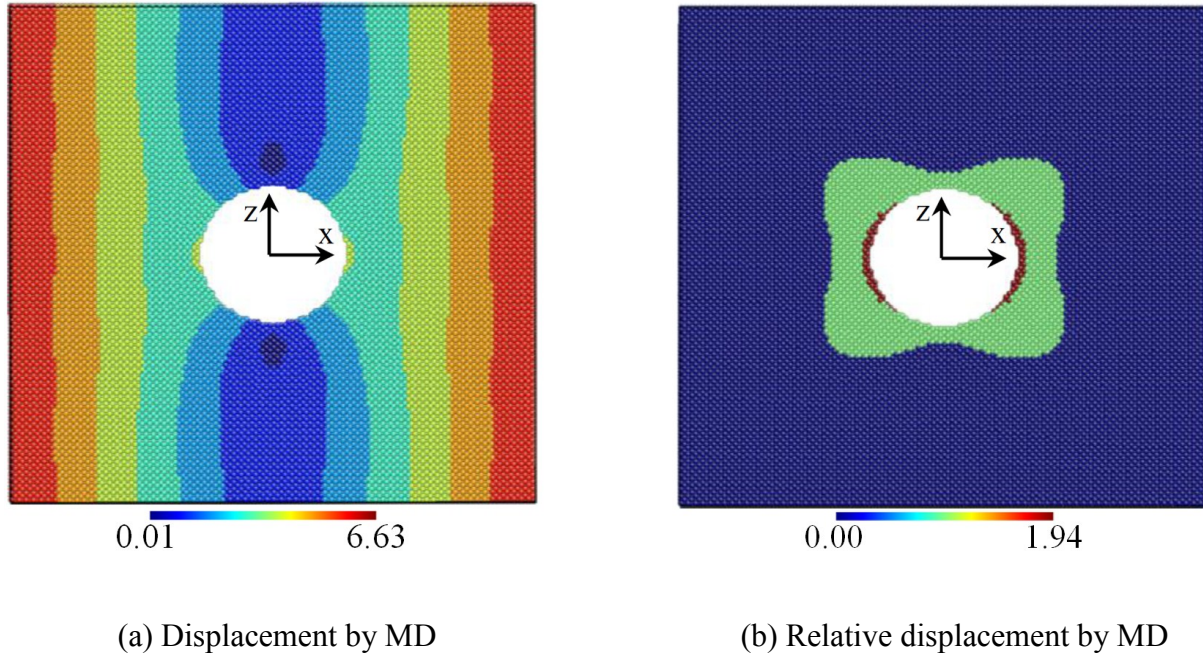


Figure 5.3: The Displacement field (magnitude) by MD simulation and the relative displacement field (magnitude) by MD simulation at the strain 0.05 (right before the dislocation emission). All the colored scale bars are in the unit of Å. The cutting plane is the xoz plane at the simulation box center.

Atomic displacement can be calculated by the difference between the current position and the initial position of atoms. This type of atomic displacement in Figure 5.3a depends on the selection of the coordinate origin. However, the “relative displacement” field in Figure 5.3b does not depend on the choice of the coordinate origin as long as the origin being attached on the stretching simulation box (see Appendix). Once the homogenous elastic deformation is excluded by using the relative displacement, the remains are the deformation (both elastic and inelastic) due to the presence of the void. At this strain, a number of disordered atoms are seen near the dislocation sites prior to the event of dislocation emission. However, these disordered atoms do not affect the relative mass transport in Figure 5.3b. Figure 5.3 indicates that (1) the elastic displacement from the MD simulation is close to that predicted by the elasticity theory and (2)

the material transport at the end of the elastic regime is dramatically different from that under the influence of dislocation network, which will be shown later.

5.3.1.2. The Beginning of the Inelastic Regime

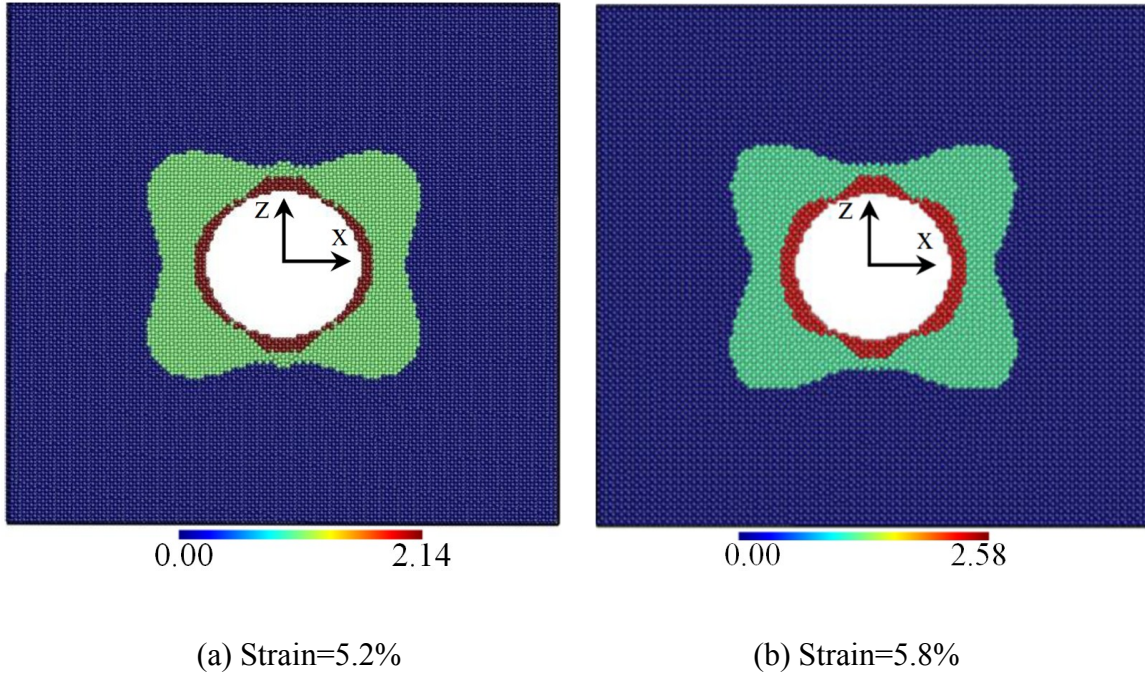


Figure 5.4: The relative displacement field (magnitude) by MD simulation at the strain 0.052 (the onset of dislocation emission) and 0.058. All the color bars are in the unit of Å. The cutting plane is the xoz plane at the box center.

The dislocation emission starts at the strain 0.052, which marks the beginning of the plastic regime. At the strain 0.052, the dislocation lines form small-scale structures at the four corners on the void surface. From the strain 0.052 to 0.058, these small-scale structures undergo virtually no change. Therefore, only Figure 5.5a is shown for brevity. These incipient dislocation structures have limited impact on the mass transport pattern. Figures 5.4a and b differ from Figure 5.3b only at the “polar areas” on the void surface where the dislocation structures at the

corners help move the atoms away from the void. From Figure 5.4a to Figure 5.4b, there is only a minor increase in the maximum relative displacement. The majority of atoms stay at lattice points and therefore results in a slow void growth in Figure 5.2.

5.3.1.3. A Burst of Void Growth during the Growing of Dislocation Structure

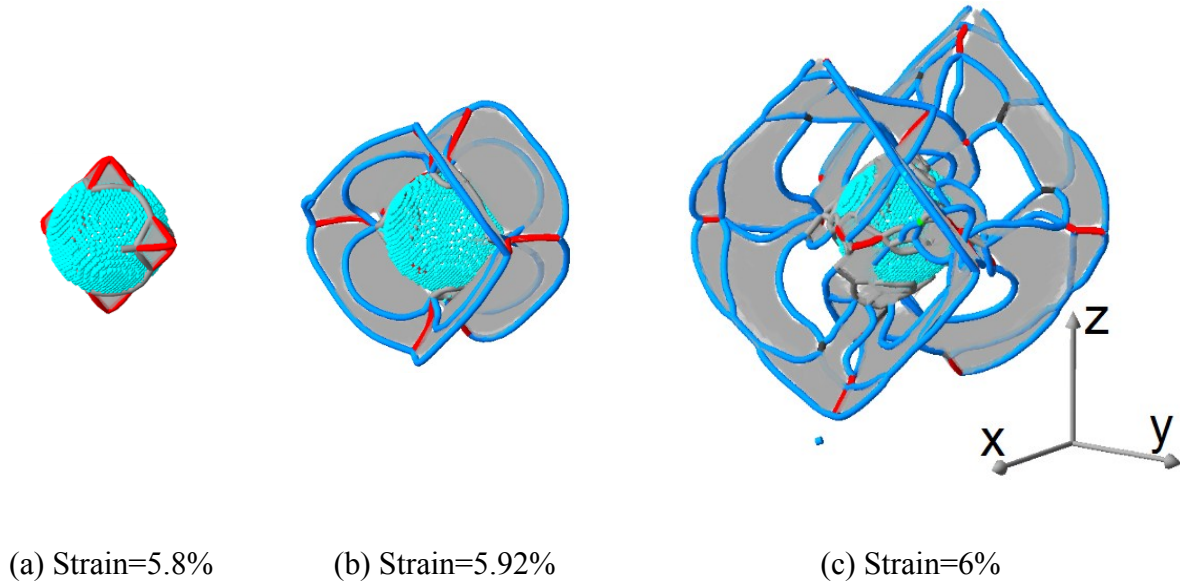
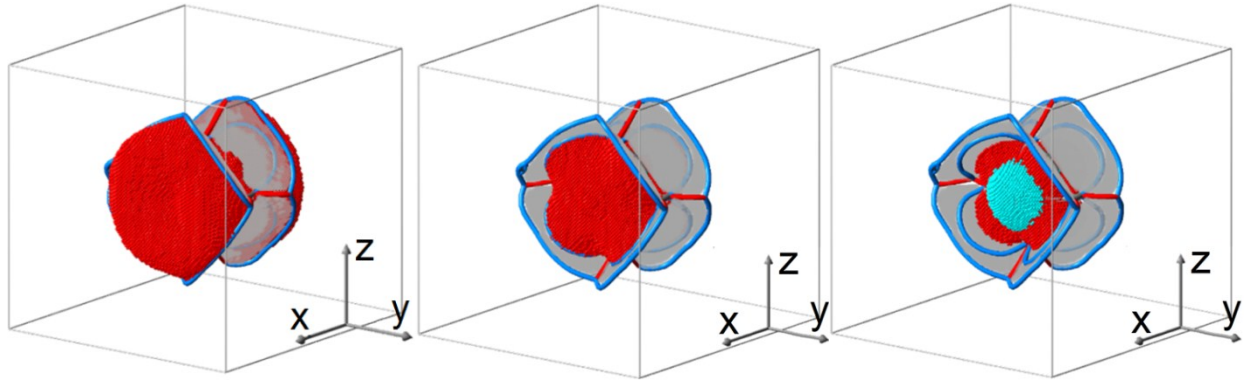


Figure 5.5: The rapid development of dislocation structure before it meets the periodic boundary. Blue atoms represent void surface while the red and blue rendered lines represent dislocation lines. The stacking faults areas are colored in gray.

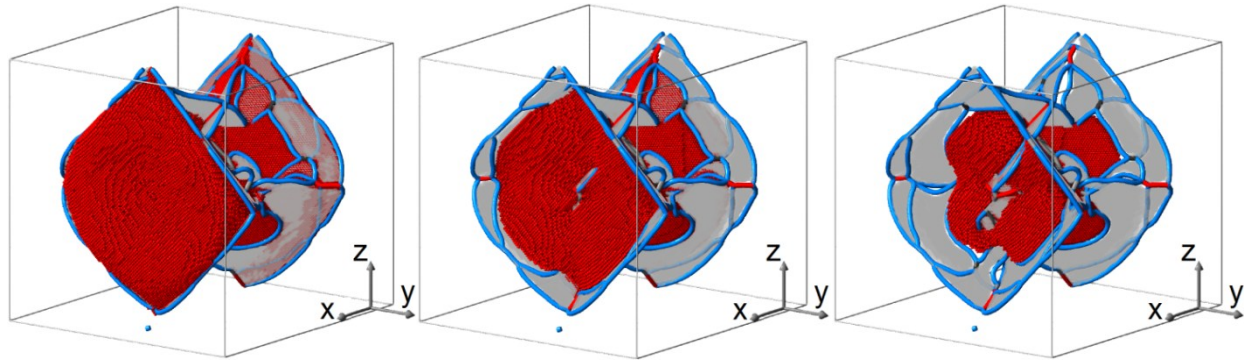
Figure 5.5 illustrates the three stages of the dislocation network development before it reaches the periodic boundaries. This rapid development of dislocation network in a large scale takes place during the strain from 0.058 to 0.06. The detached shear loop has been spotted during the growth of the dislocation network.



(a) $d_{crit} = 1.0 \text{ \AA}$ ($\epsilon = 5.92\%$)

(b) $d_{crit} = 2.0 \text{ \AA}$ ($\epsilon = 5.92\%$)

(c) $d_{crit} = 3.0 \text{ \AA}$ ($\epsilon = 5.92\%$)



(d) $d_{crit} = 1.0 \text{ \AA}$ ($\epsilon = 6\%$)

(e) $d_{crit} = 2.0 \text{ \AA}$ ($\epsilon = 6\%$)

(f) $d_{crit} = 3.0 \text{ \AA}$ ($\epsilon = 6\%$)

Figure 5.6: The “relatively farthest-travelled” atoms (in red) inside the dislocation network at the strain of 5.92% and 6%. Blue atoms in (c) represent void surface while the red and blue rendered lines represent dislocation lines. The stacking faults areas are colored in gray. Three different critical lengths, namely $d_{crit} = 1.0, 2.0,$ and 3.0 \AA , are used to identify the “relatively farthest-travelled” atoms.

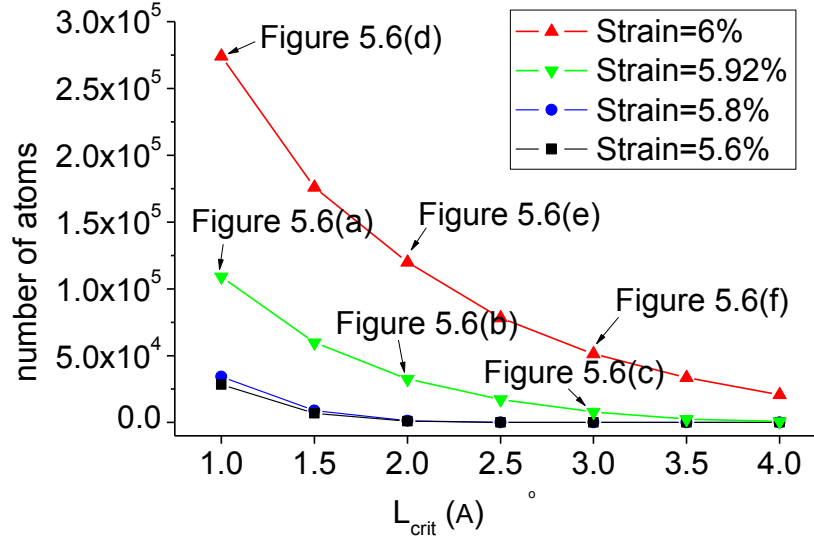
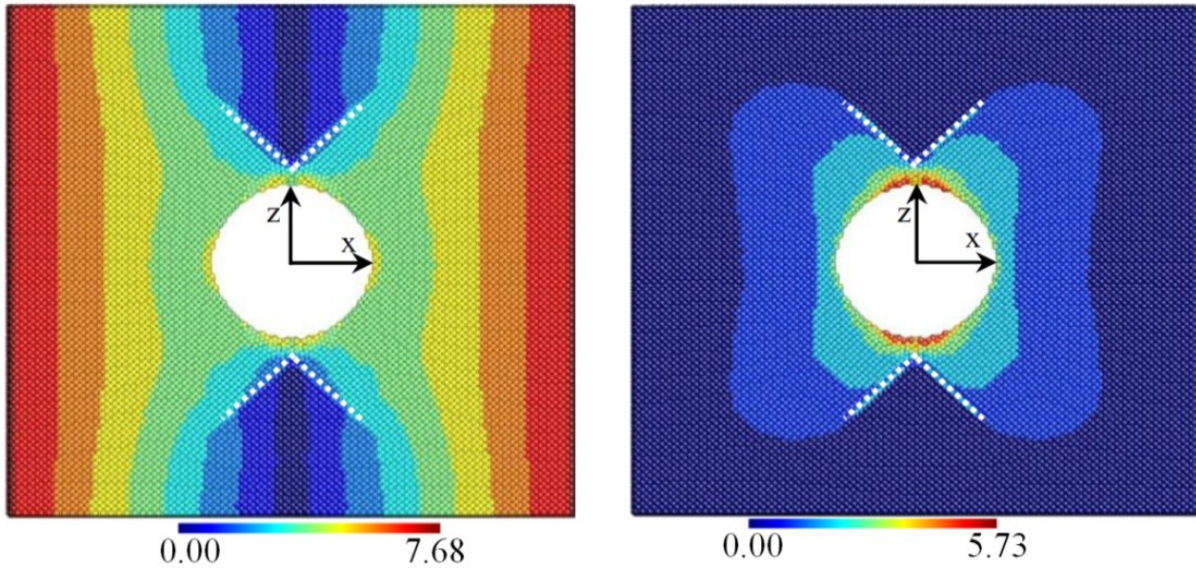


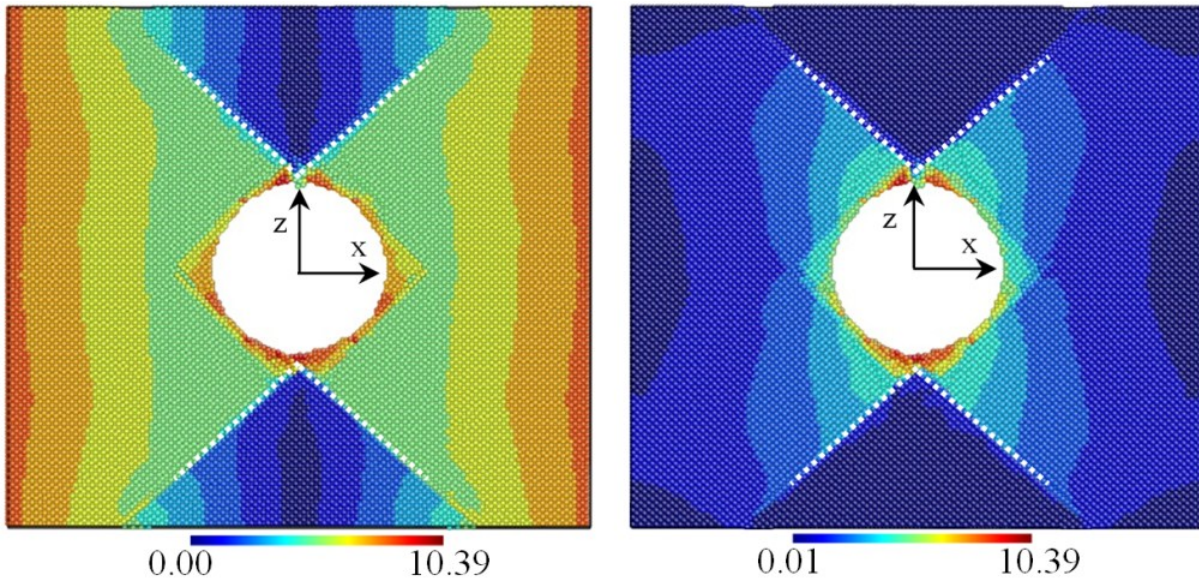
Figure 5.7: Number of the relatively farthest-travelled atoms identified by different critical length under different strains.

As summarized in Figure 5.7, the number of the relatively farthest-travelled atoms decreases with the increasing critical length. Very little difference lies between the strains 5.6% and 5.8% regarding the number of the relatively farthest-travelled atoms. This suggests that the transition of overall mass transport pattern from the “elastic” to “plastic” fashion starts from around the strain of 5.8%. As the critical length rises from 1.0Å to 3.0Å, the identified relatively farthest-travelled atoms tend to gather near the loop plane and the void surface as seen from Figure 5.6a to Figure 5.6c. The frustum-like dislocation structures are the consequence of the continuing extension of front dislocation curves and the interaction among the dislocation curves. Large pieces of material glide away from the void surface with the help of these frustum-like structures of dislocations. The detailed mechanism is that shear loops/curves help move the material away from the void surface. Indeed, the shape of the relatively farthest-travelled atoms fits the shape of the dislocation curves like those in Figures 5.6a and b. Some shear loops are observed to detach and glide away from the void surface. Whether forming complete loops or not, MD simulation

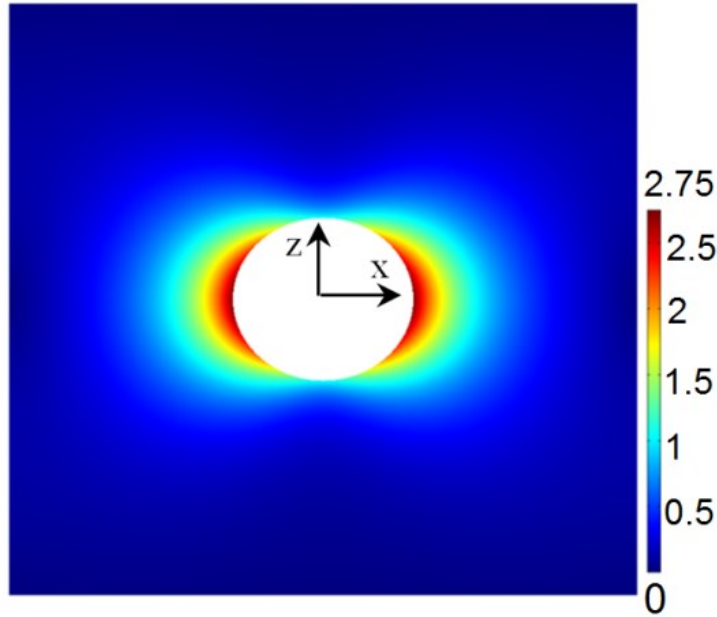
suggests that shear dislocation curves could induce the material transport. So far, the correlation between the mass transport pattern and the dislocation structure has been revealed from the MD data. Still, more cutting-plane plots help to clarify the observed material transport pattern.



(a) Displacement by MD ($\epsilon=5.92\%$) (b) Relative displacement by MD ($\epsilon=5.92\%$)



(c) Displacement by MD ($\epsilon=6\%$) (d) Relative displacement by MD ($\epsilon=6\%$)



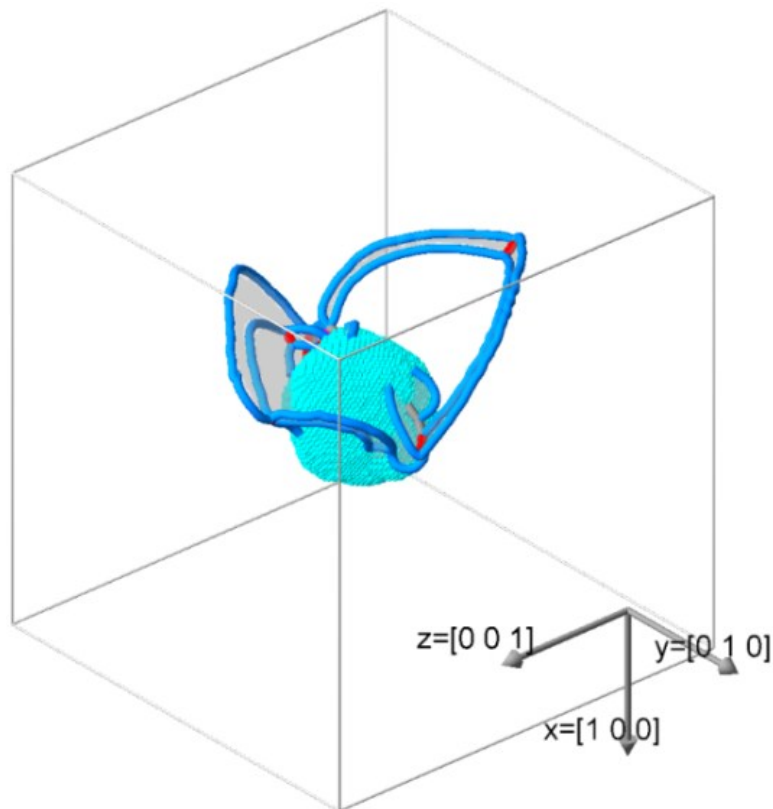
(e) Relative displacement by FE ($\epsilon=6\%$)

Figure 5.8: Displacement field (magnitude) and relative displacement field (magnitude) by the MD method plus the relative displacement field (magnitude) by the finite element (FE) simulation at the strain of 5.92% and 6%. All the color bars are in the unit of Å. White dotted lines indicate the slip planes.

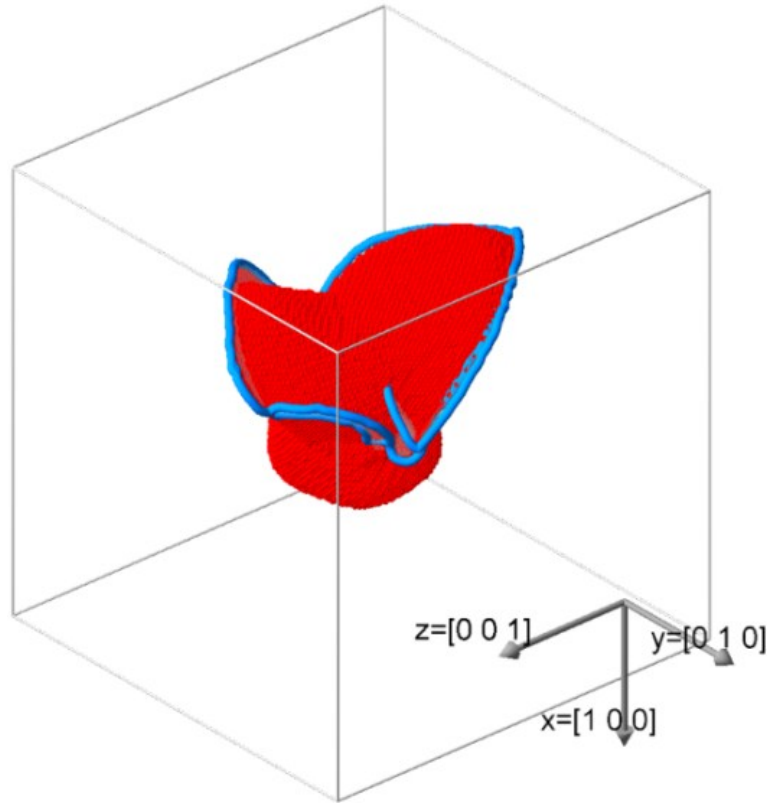
From Figure 5.3b to Figures 5.8a and c, it is evidenced that the emerging slip planes have gradually caused the discontinuity of the displacement field. From Figure 5.4b to Figures 5.8b and d, the atoms with measurable relative displacement are all inside the area between the slip planes as indicated by the dotted lines. By comparison, the FE result in Figure 5.8e shows a completely different relative displacement field. The maximum relative displacement predicted by the elasticity theory in Figure 5.8e locates at the void surface along the x direction. This feature is also shared by the MD case before the dislocation emission as seen in Figure 5.3b. After the dislocation emission, it is another story. Not only is the maximum relative displacement by MD much larger than that by FE, but also the locations of the maximums are completely

different. Figure 5.8d has this location along the z direction while Figure 5.8e has it along the x direction. To be comparable, the finite element solution only applies the elastic model and with identical 3D geometry and boundary constraints. The temperature till the strain of 0.06 is still around 0.1K and therefore thermal expansion has no contribution. Thus, we can conclude that the relative displacement is truly due to the presence of dislocation structures consisting of shear loops/curves.

5.3.2. Additional Cases



(a) Dislocation network only



(b) Relatively farthest travelled atoms inside the dislocation network

Figure 5.9: The cases of an irregular-shaped void with an initial system temperature 0.1 K. Here we show (a) the dislocation network alone with void surface depicted by light blue atoms and (b) the “relatively farthest-travelled” atoms inside the dislocation network at the strain 0.046. The critical length to identify the relatively farthest-travelled atoms is 1.0 Å. The rendered blue lines represent dislocation lines. The stacking faults areas are colored in light gray in (a).

The spherical void in the aforementioned simulation is with an ideal initial shape. In reality, the initial void shape can considerably deviate from the spherical shape. The initial shape of nanovoid was reported to considerably affect the formed dislocation structure [97]. The objective of this subsection is to examine whether or not the aforementioned findings are still true to some more general situations. Here the irregularly-shaped void, generated by a similar method for

surface roughness [133], is still with 1% initial void volume fraction. A different dislocation network is seen in Figure 5.9 for the void with irregular initial shape. The small incipient dislocation structures like those in Figure 5.5a are absent. Although the shear loops on the four main slip planes do not emit and grow in a very simultaneous fashion from, they still form a frustum-like structure at the upper side of the loading direction. In Figure 5.9b, the majority of the relatively farthest-travelled atoms are still inside the frustum-like dislocation structure. The farthest extending shear curve is the one first emitted from the void surface. Even at the time when the frustum-like structure has not been formed, the first-emitted shear curve still induced the local material transport. Therefore, the main contributors to grow the void as observed are the shear loops/curves. The forming of the frustum-like dislocation structure further facilitates this process.

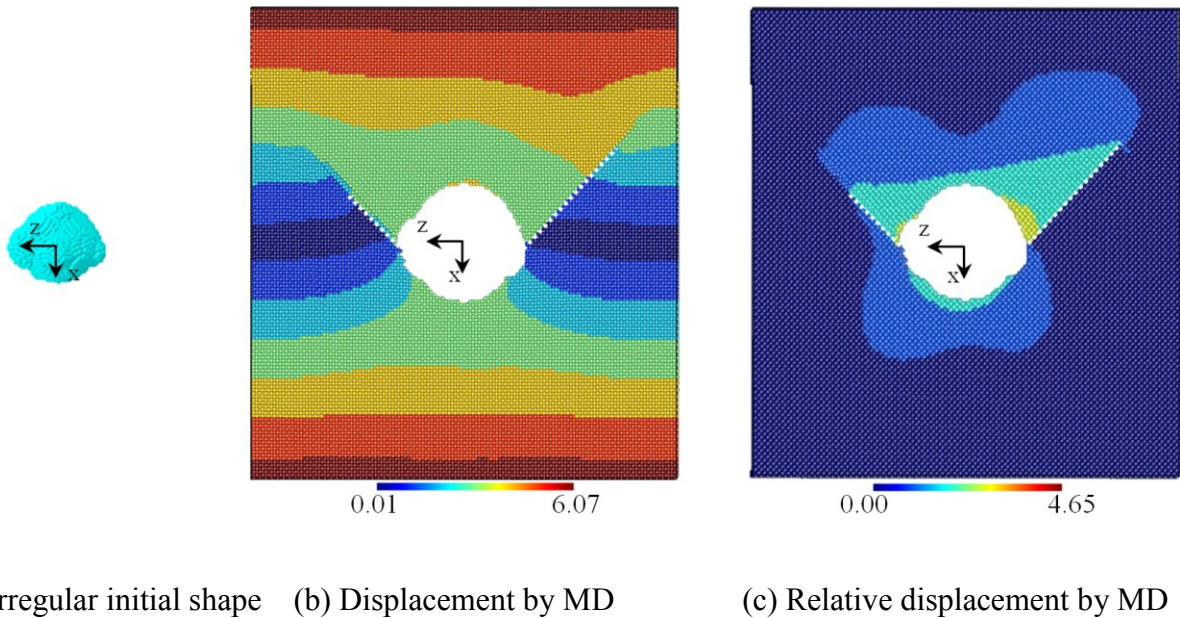
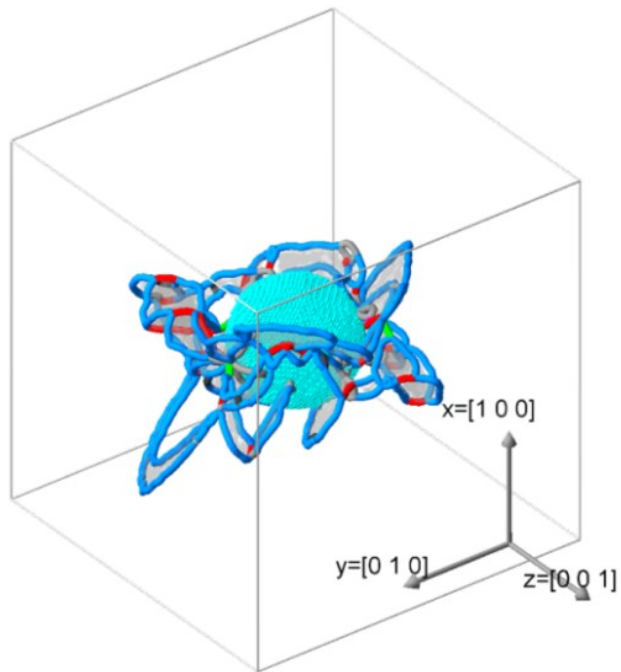


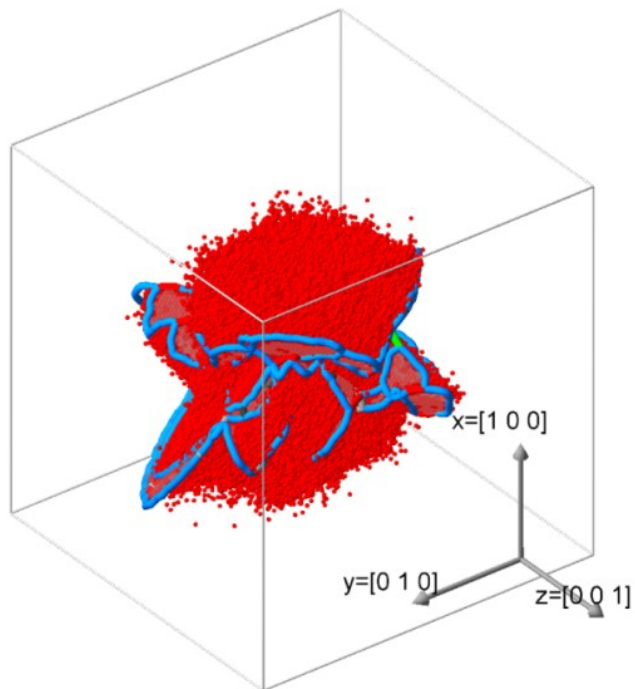
Figure 5.10: Displacement field (magnitude) and relative displacement field (magnitude) by the MD method at the strain 0.046 with an irregular initial void. All the color bars are in the unit of Å. White dotted lines indicate the slip planes.

Due to the absence of small incipient dislocation structures as those in Figure 5.5a, the maximum relative displacements in Figure 5.10c are only near the attaching points of the shear curves. Without a symmetric dislocation structure at the lower half (the positive x direction), the relative displacement field there is similar to an elastic growth as in Figure 5.3b. This clearly highlights the role of the dislocation structure which, in this case, only exists at the upper half (the negative x direction) in Figure 5.10c.

All the aforementioned simulations are conducted with an initial temperature of 0.1K. To further investigate the influence of the initial temperature, the third case runs under an initial temperature of 300K. As shown in Figure 5.11a, the overall dislocation network under higher temperature still resembles that under lower temperature. Two large dislocation structures are also formed by the emission and interaction of shear loops/curves along the loading direction. Again, the relatively farthest-travelled atoms are inside these two dislocation structures. The detailed mechanism is still the local material transport via the shear loops/curves. The initial temperature has not considerably altered the mechanism about void growth. However, there is some minor difference caused by the elevated temperature. The mass transport in a higher temperature as shown in Figure 5.11 becomes scattered at some certain locations. The transition of mass transport pattern from low temperature to high temperature has been reported for a stretched nanowire [134]. In their study, the mass transport under 10K is through the step-wise glides while that under 700K features high density of disordered atoms. Therefore, once temperature becomes much higher than 300K, atomic mass transport pattern could be altered considerably.



(a) Dislocation network only



(b) Relatively farthest-travelled atoms inside the dislocation network

Figure 5.11: The case of spherical void with initial temperature of 300K. Here shows (a) the

dislocation network along with void surface depicted by light blue atoms and (b) the “relatively farthest-travelled” atoms inside the dislocation network at the strain 0.0488. The critical length to identify the relatively farthest-travelled atoms is 1.0 \AA . The rendered red and blue lines represent dislocation lines. The stacking faults areas are colored in gray.

5.4. Theoretical Considerations

5.4.1. Material Transport Equation for the Prismatic Loop

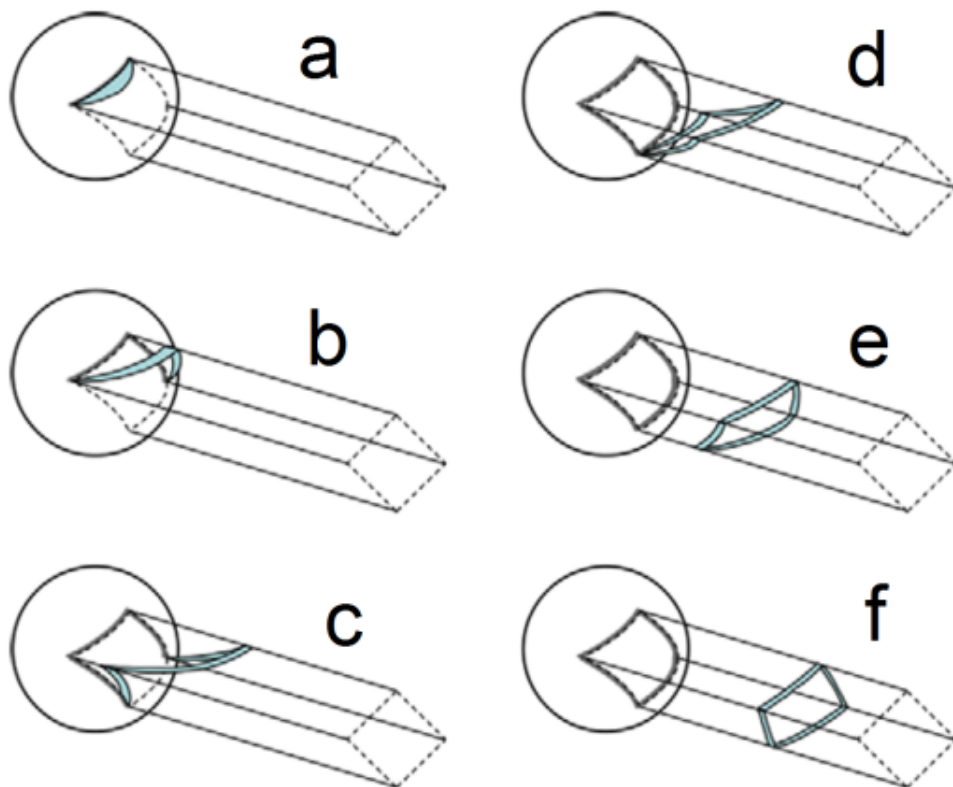


Figure 5.12: Forming of prismatic loop with quadrangular-prism slip surface. The figure is reproduced [56] (Reprinted with permission from Bulatov et al. 2010. Copyright 2010, Elsevier).

Lubarda et al. [18] proposed two mechanisms regarding void growth via dislocations. One is via prismatic loop and the other is via shear loop. The former one is relatively easy to

understand. Bulatov et al. [56], who claimed the impossibility of the shear loop to grow the void, emphasized the mass conservation as

$$\Delta V = \int_{Surface} \mathbf{b} \cdot d\mathbf{S} = \int_{Surface} (\mathbf{b} \cdot \mathbf{n}) dS \quad (5.1)$$

where

ΔV is the incremental void growth induced by the dislocation loop,

\mathbf{b} is the Burgers vector of the dislocation loop,

\mathbf{n} is the norm of the loop plane and

dS is the differential element of the surface.

The slip surface of the prismatic loop in the work of Lubarda et al. [18], following the standard definition [135], is cylindrical. Bulatov et al. [56] later extended the idea of a cylindrical slip surface to a quadrangular-prism slip surface as shown in Figure 5.12. They cited the MD work of Rudd et al. [136] to support this new understanding. This illustrated that MD simulation can be a powerful tool to improve the theoretical understanding of mass transport. It then seems reasonable to employ MD simulation to justify the role of shear loops in growing the void. Our understanding to the shear-loop growth mechanism is not limited to the observation phase. In the subsection, theoretical understanding regarding the mass transport will be presented.

5.4.2. Feasibility of Material Transport via Shear Loop Emission

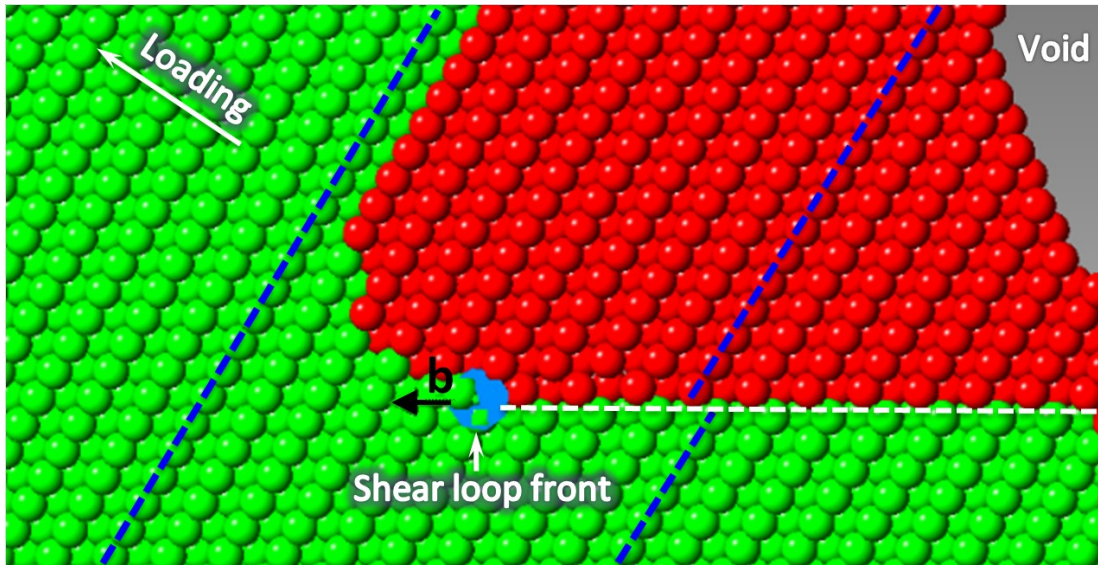


Figure 5.13: A zoomed-in snapshot of Figure 5.6 with cutting plane $[0\ 1\ -1]$ at the box center. The red atoms still represent the relatively farthest-travelled atoms while the other atoms are in green. Only a small fraction of the void is shown. The blue filled circle is the rendered shear loop front.

First and foremost, Eq. (5.1) is inadequate to deny the feasibility of material transport via shear loops. It is true that if Eq. (5.1) is performed on the loop face, ΔV would be zero at the normal-plane direction due to the fact that its Burgers vector is in the loop plane. However, this alone cannot derive the impossibility of void growth via the shear loop. The reason is as follow. For one thing, Eq. (5.1) just rules out the possibility of material transfer in the normal direction of the shear loop plane. The original definition in the textbook [57] allows the integral domain to be an arbitrary shape other than the flat face encircled by the loop, which would result in some nonzero $\mathbf{b} \cdot \mathbf{n}$. For another, Eq. (5.1) is without any consideration of the possible and probable interaction among the adjacent planes parallel to the shear loop plane. To better understand that, a zoom-in atomic plot is shown in Figure 5.13. The presence of the shear loop/curve in Figure

5.13 does induce the mass transport. These red atoms moving away from the void surface result in the growth of nanovoid.

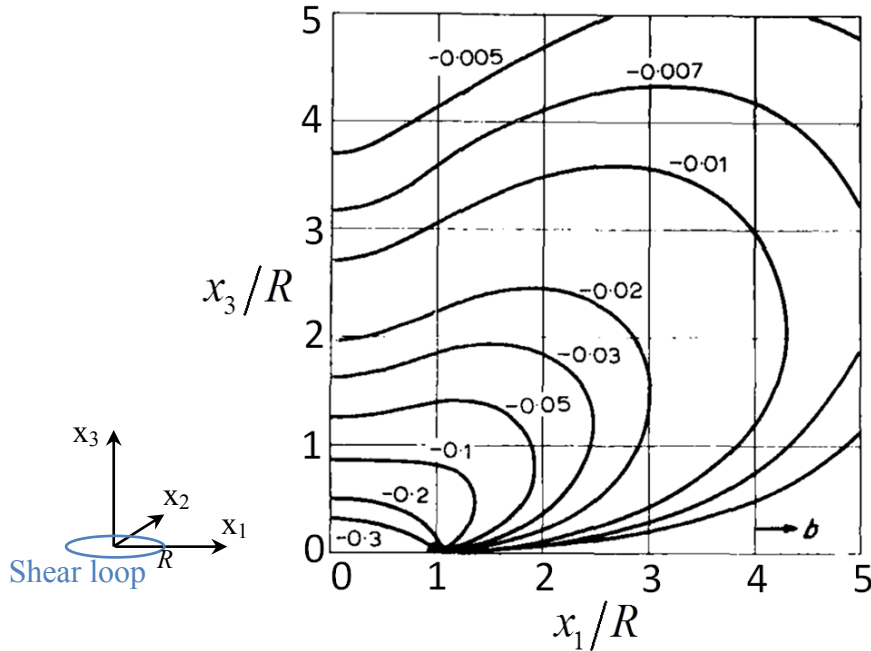


Figure 5.14: Analytical solution of displacement field caused by a circular shear loop. Here shows the contour plot of u_1 in the unit of Burgers vector at the plane $x_2=0$ for a circular shear dislocation loop, reproduced from Ohr [60] (Reprinted with permission from Ohr 1972. Copyright 1972, Taylor & Francis). The circular shear loop is inside the plane $x_3=0$ and the Burgers vector is in the x_1 direction. Here involves different convention for the Burgers vector.

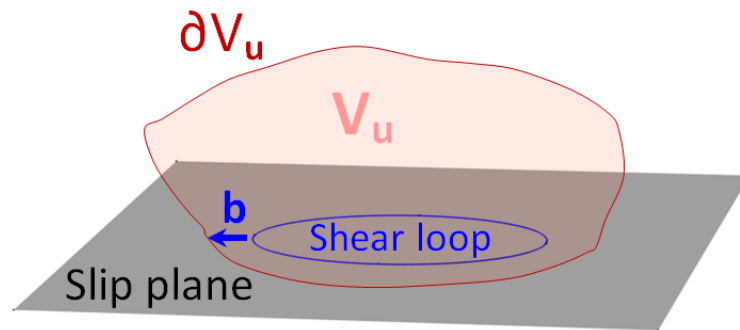
Second, elastic deformation due to formation of a shear loop could also contribute to the growth of nanovoid. This is still true even the surface in Eq. (5.1) has been taken as the loop plane. Elasticity theory is required to evaluate the material deformation for this case. Although classical elastic theory may fail at the dislocation core, modifications [137] to this approach can still lead to a physical solution. In a classical approach, Ohr [60] has applied Green's function method to derive the analytical expression for the displacement field around a circular shear loop

in an infinite isotropic medium. For brevity, the exact solution is omitted. For illustration, only u_1 of the solution [60] is shown in Figure 5.14. For one thing, the shear loop leads to nonzero displacement in certain region above the loop plane in Figure 5.14. For another, the displacement caused by the formation of shear loop approaches zero once sufficiently away from the shear loop. This is physically sound since the far-field displacement should be unaffected by the shear loop. For an isolated shear loop, the surrounding medium could be divided into two regions: one is the nearby region with nonzero displacement caused by the shear loop and the other is the unaffected far-field region. We denote $u(x,y,z)$ as the magnitude of the displacement field caused by the presence of the shear loop. It comprises two parts: one is the displacement on the surface bounding the loop [57] (not necessary the loop plane), the other is the elastic deformation due to the presence of the loop. The nearby region with mass transport can therefore be defined as the volumetric set $V_{\mathbf{u}} = \{(x,y,z) | u(x,y,z) > 0\}$. Figure 5.15a is only a schematic of how this material transport region may look like. Out of this region, there should be no material transport caused by the shear loop. For the case with a nearby void overlapped with the material transport region $V_{\mathbf{u}}$, certain area on the void surface would have nonzero displacement induced by the shear loop. It is only a rough description since the presence of the void to this displacement solution has not yet been addressed. This effective area on the void surface with shear-loop-induced displacement can be identified by the set operation $V_{\mathbf{u}} \cap S_{\text{void}}$, which is the shaded area on void surface in Figure 5.15b. The incremental void growth by the shear loop can therefore be defined as

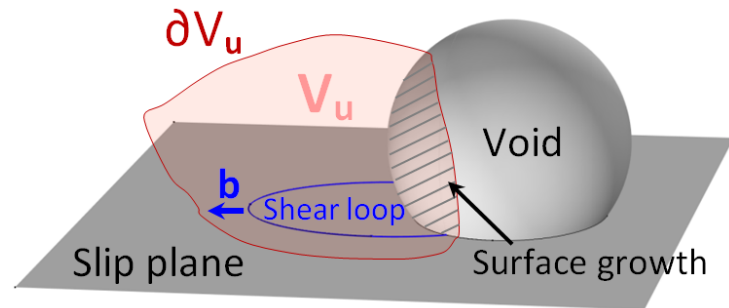
$$\Delta V_{\text{void}} = \int_{V_{\mathbf{u}} \cap S_{\text{void}}} (\mathbf{u} \cdot \mathbf{n}) dS \quad (5.2)$$

where \mathbf{u} and \mathbf{n} are the corresponding displacement vector and unit normal vector on the area $V_{\mathbf{u}} \cap S_{\text{void}}$. As shown in Figure 5.14, this induced displacement \mathbf{u} could be more significant once

near the shear loop/curve. As an inference, the void surface area near the attached shear loop should gain more growth. This point is true, for example, in Figure 5.6c. The contribution to the void growth of attached shear loops would be more significant than that of a detached shear loop far away from the void.



(a) Shear loop without void



(b) Shear loop (curve) attached on the void surface

Figure 5.15: Schematic material transport via the emission/formation of a shear dislocation loop/curve.

5.4.3. A Phenomenological Description of Void Growth by Dislocation Emission

As the previous subsection has clarified the feasibility of void growth via shear loop/curve emission, our attention here is paid to the larger-scale void growth by the dislocation structure

containing multiple and complex-shape shear dislocation curves. Our objective here is to find a phenomenological description for this larger-scale material transport near the void surface.

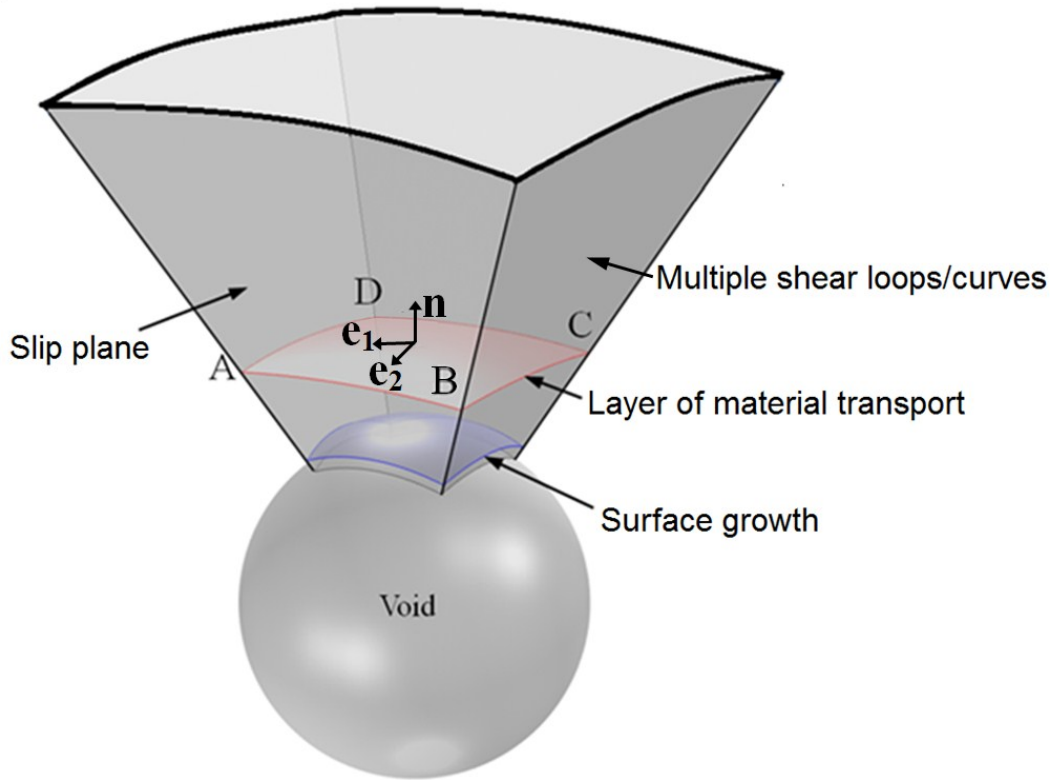
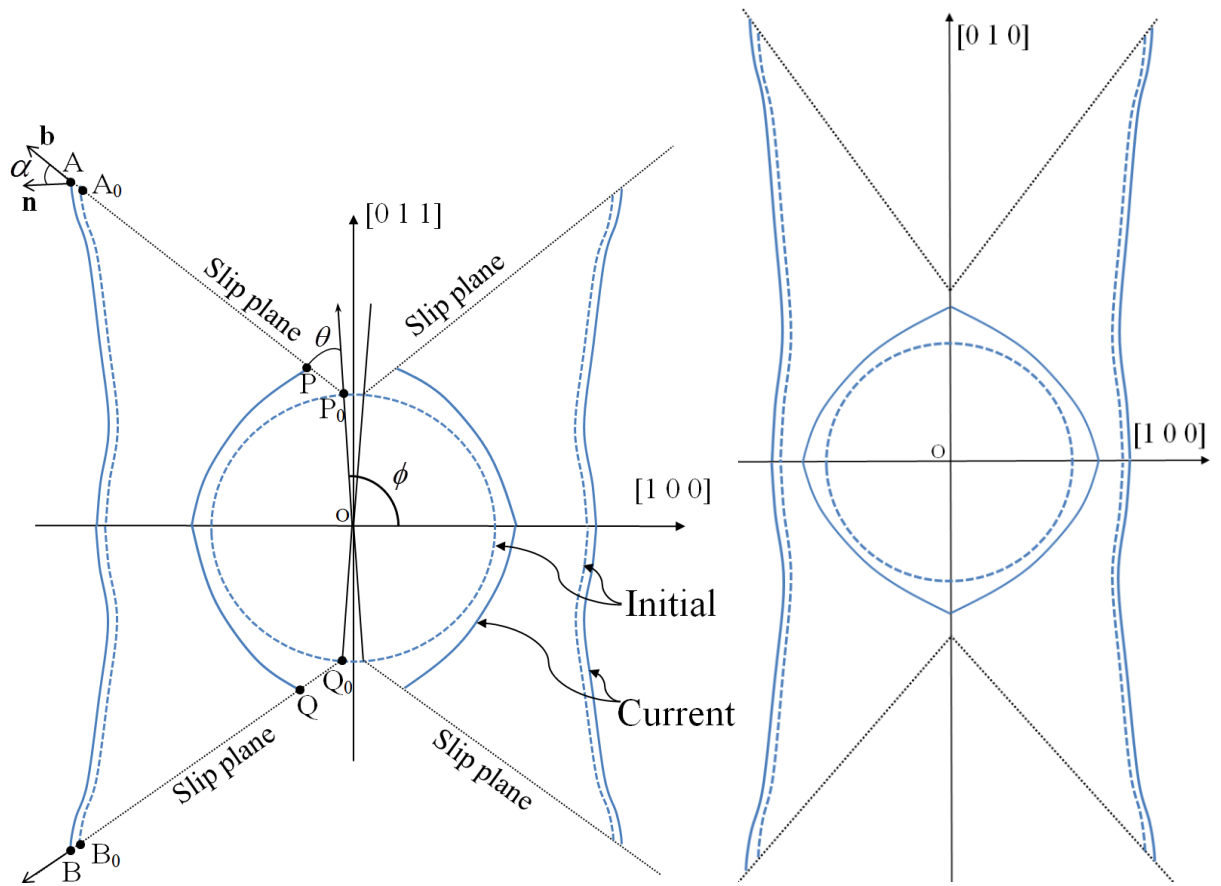


Figure 5.16: Three-dimensional schematic diagram of material transport via a square-frustum like structure consisting of dislocation loops/curves on the slip plane. Symmetry only applies for the spherical void case. The loading direction here is assumed vertical.

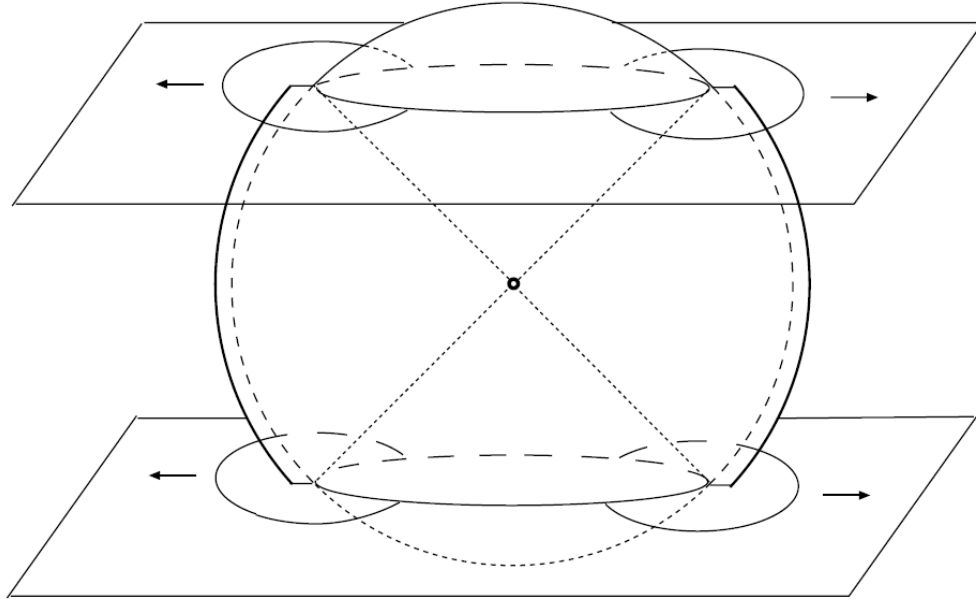
As shown previously in Figure 5.6, shear loops can interact and form frustum-like structure along the loading direction. For irregular void shape, there could be only one of this kind frustum-like dislocation structures as illustrated in Figure 5.9. Figure 5.16 is a 3D illustration of the material transport via this square-frustum structure formed by multiple shear loops/curves. Layers of material are transported away from the void via this dislocation structure. Figure 5.17 illustrates the void growth mechanism in 2D with both initial and current positions shown. The

slip planes host multiple moving dislocation curves. The idealized surface ABCD in Figure 5.16 represents a layer of material transported away from the void by the shear dislocation curves. To simplify the situation, we take the assumption that the surface normal vector at the point A is parallel to the loading direction. One can find relevance between Figures 5.17a and b to Figure 5.17c, which was theorized by Lubarda et al. [18]. They too proposed that the larger-scale material transport happens between the loop planes with simultaneously-emitted shear loops/curves. The difference between our MD observation and their description is the opening angle between the two slip planes. This angle is nonzero in our observation.



(a) With cutting plane $[0\ 1\ -1]$

(b) With cutting plane $[0\ 0\ 1]$ (xoy plane)



(c) Void growth by shear loops reproduced from Lubarda et al. [18] (Reprinted with permission from Lubarda et al. 2004. Copyright 2004, Elsevier)

Figure 5.17: Two-dimensional schematic diagram of material. Different cutting plane at the box center has been chosen in (a) and (b). Here view angle of (a) corresponds to Figure 5.13, and (b) corresponds to Figure 5.8d.

Next is a mathematical description of the proposed material transport despite some inevitable approximations. In Figure 5.17a, points P_0 and P are the initial and current positions of the cutting point on the void surface, respectively. Point A is the current position of the atom on the moved layer, while point A_0 is its initial position. Since the dislocation is emitted from the void surface, the distance AP_0 represents how far this dislocation (not the atom) has travelled. We denote the displacement of an arbitrary point on the surface as $\tilde{\mathbf{b}}$ and the unit normal vector as \mathbf{n} . According to Figure 5.13, the material transport away from the void is approximated as

$$\Delta V_{dis} = \int_{S_{ABCD}} \tilde{\mathbf{b}} \cdot d\mathbf{S} = \int_{S_{ABCD}} \tilde{\mathbf{b}} \cdot \mathbf{n} dS \quad (5.3)$$

At a first thought, shear loops/curves should grow the void in a different way compared with the prismatic loop. However, some similarity in mass transport holds between the two once regarding large structure. It is interesting that Eq. (5.1), though not true to deny the void growth by shear loop, can be referenced here for the material transport through the large dislocation structure formed by shear loops/curves. This approach has also been adopted by Ahn [55] et al. to formulate the mass transport via multiple prismatic loops. Take Figure 5.13 for example, the Burgers vector at the shear curve front does have a normal component parallel to the loading direction. The major difference between Eq. (5.1) and Eq. (5.3) lies in that the Burgers vector for the latter one is no longer parallel to the mass transport direction. The mass conservation in Eq. (5.3) implies the assumption of the volume preservation on the moved material. The surface ABCD in Figure 5.16a is not flat and we only know that

$$\tilde{\mathbf{b}} = \mathbf{b} \text{ on } L_{ABCD} \quad (5.4)$$

Here L_{ABCD} is the curve enclosing the surface ABCD. Vector \mathbf{b} is assumed to take the direction as indicated in Figure 5.17a. Next, a local orthogonal coordinate system $[\mathbf{e}_1, \mathbf{e}_2, \mathbf{n}]$ is defined on the curved surface, where \mathbf{n} is the local unit normal vector of the surface. The two vectors \mathbf{e}_1 and \mathbf{e}_2 are two orthogonal in-plane unit vectors as shown in Figure 5.16. We rewrite $\tilde{\mathbf{b}}$ as

$$\tilde{\mathbf{b}} = f\mathbf{e}_1 + g\mathbf{e}_2 + (\mathbf{b} \cdot \mathbf{n})\mathbf{n} \quad (5.5)$$

Eq. (5.5) simply satisfies $\tilde{\mathbf{b}} \cdot \mathbf{n} = \mathbf{b} \cdot \mathbf{n}$ on both the inner surface and the enclosing curve ABCD. Since

$$\mathbf{e}_1 \cdot \mathbf{n} = 0 \quad (5.6)$$

$$\mathbf{e}_2 \cdot \mathbf{n} = 0 \quad (5.7)$$

We immediately obtain the incremental void growth as

$$\Delta V_{dis} = \int_{S_{ABCD}} \tilde{\mathbf{b}} \cdot \mathbf{n} dS = \int_{S_{ABCD}} [f\mathbf{e}_1 + g\mathbf{e}_2 + (\mathbf{b} \cdot \mathbf{n})\mathbf{n}] \cdot \mathbf{n} dS = \int_{S_{ABCD}} (\mathbf{b} \cdot \mathbf{n}) dS = \int_{S_{ABCD}} |\mathbf{b}| \cos \alpha dS \quad (5.8)$$

It is more comfortable to think $\mathbf{b} \cdot \mathbf{n}$ as an average on the surface in deriving Eq. (5.8). The surface ABCD is not necessary a flat one in Eq. (5.8). The angle between the vectors \mathbf{b} and \mathbf{n} is denoted as α and satisfies $\alpha = \pi - \theta - \phi$ as shown in Figure 5.17a. Here θ and ϕ are two angles for the dislocation emission geometry [91]. A non-zero α can cause the layer to move away from the void. In this sense, the void growth has been related to the geometry of the dislocation structure. Next, further approximations will be taken to derive a simpler relation. First, the curved surface is approximated to be a flat one

$$\Delta V_{dis} \approx |\mathbf{b}| \cos \alpha |AB|^2 \quad (5.9)$$

From Figure 5.17a, the segment $|AB|$ could be related to both the segment $|AP_0|$ and dislocation emission angles as

$$|AB| = 2(r_0 \sin \phi + |AP_0| \sin \alpha) \quad (5.10)$$

A dimensionless parameter $\xi = |AP_0|/r_0$ is defined to better characterize the relative motion of the dislocation with respect to the void size. Eq. (5.10) then becomes

$$\Delta V_{dis} \approx 4|\mathbf{b}|r_0^2 \cos \alpha (\sin \phi + \xi \sin \alpha)^2 \quad (5.11)$$

Eq. (5.11) reveals that the incremental growth of the void depends on the geometry of dislocation structure, especially the dislocation emission angles. These angles are shown in Figure 5.17a and are identified from MD results. Since a number of approximations have been applied to derive Eq. (5.11), it is then necessary to compare Eq. (5.11) with the direct MD

observation in Figure 5.2. The first step is to identify the parameters in Eq. (5.11) from the MD data. At the strain 0.0592, the average magnitude of Burgers vector at the shear loop/curve front is identified as 1.06 Å. The travel distance of the shear loop front $|AP_0|$ is measured as about 62 Å. With an initial void radius of 34.8 Å, the dimensionless parameter ξ becomes 1.782. The two angular parameters ϕ and α are measured 94.3° and 49.2°, respectively. By substituting all these parameters, the incremental void volume fraction for the spherical void is found to be 0.0020 (doubled due to symmetry) by using Eq. (5.11). In Figure 5.2, this incremental increase in void volume fraction is 0.0024 from the strain 0.058 to 0.0592. This 20% deviation could stem from those aforementioned approximations.

5.5. Conclusions

The feasibility of void growth via shear loop/curves has been proved true from the MD simulation. Whether forming larger structures or not, shear loops/curves can induce material transport. A shear loop/curve close to the void surface is more readily to induce the surface growth of the void. Large frustum-like structures are formed by the emission and interaction of multiple shear loops/curves. For a spherical initial void, symmetric frustum-like structures are formed along the loading direction. For an irregular initial void, only one frustum-like dislocation structure is formed. The shear loops/curves, whether emitted in a simultaneous or sequential fashion, are capable of inducing/affecting the local material transport. The forming of larger dislocation structures further facilitates the void growth. The observed frustum-like structure features an opening angle, which is different from the one proposed by Lubarda et al. [18]. The proposed phenomenological model for void growth by frustum-like structures achieves relatively good agreement compared with that from a direct measurement of MD results.

Chapter 6: Theoretical Calculations of Void Growth due to Shear

Loops

As a step forward from the previous chapter, this chapter is dedicated to computing the exact elastic void growth due to a nearby shear loop and exploring the possible shape of the surface cut to form such a shear loop. The shear dislocation loop, by definition, has its Burgers vector inside the loop plane [135]. In contrast, Burgers vector of a prismatic dislocation loop is not in the loop plane [135]. The mass transport associated with a shear dislocation loop near a void is a nontrivial issue. Understanding of this issue can be achieved from two perspectives. First, in order to create the dislocation loop [57], the amount of mass that needs to be removed from or inserted into the bulk material can be examined. Dislocation loops/curves are prone to form and emit from void surface under loading. The creation of dislocation by removing or inserting material also introduces some displacement to the surrounding medium. This displacement causes another part of mass transport. By using a point force as a test probe, this displacement can be determined through the work done on certain surface bounding the dislocation loop [57]. For a shear loop, the second part of mass transport can be found in the work of Ohr [60]. This deformation induced by the shear loop, while is negligible for a microvoid, could be influential for a nanovoid.

We start with a brief review of the first kind of mass transport in the literature. Bulatov et al. [56] has employed the mass conservation to formulate the mass transport, based on the mass removed from or inserted into the bulk material to create a dislocation loop. However, what might have been overlooked is the definition of this bounding surface A with mass transport on it (see Figure 6.1). Although Figure 6.1 is originally generated to represent a general dislocation

loop [57], what showed in the figure is closer to, if not exactly a shear loop since its Burgers vector \mathbf{b} appears in the loop plane. Figure 6.1 comes from the same reference [57] cited by Bulatov et al. [56]. To assert the “shear impossibility”, they formulated the following equation [56]

$$\Delta V = \int_{\text{Surface}} \mathbf{b} \cdot \mathbf{n} dA \quad (6.1)$$

where \mathbf{n} is the unit normal of the infinitesimal area dA of an arbitrary, curved surface bounding the shear loop, ΔV is the mass transported. However, the original equation for material removed [57] is expressed in terms of a differential volume element

$$\delta V = \mathbf{b} \cdot \mathbf{n} dA \quad (6.2)$$

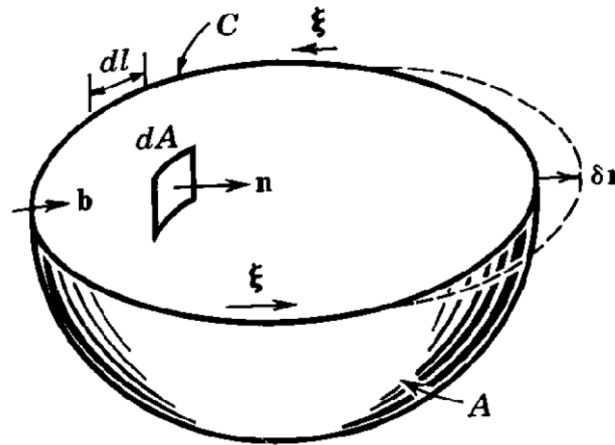


Figure 6.1: Closed dislocation loop C and its bounding surface A from [57] (Reprinted with permission from Hirth Copyright 1982, Hirth). The close loop is denoted as C , the normal of surface A is \mathbf{n} , the segment vector of loop is $d\mathbf{l} = \xi d\mathbf{l}$ and the motion of dislocation loop is $\delta \mathbf{r}$.

Figure 6.1 is the schematic corresponding to Eq. (6.2) [57]. As defined in [57], “any surface A bounded by loop C could be used for the operation”. Indeed, Figure 4-2 in the text book [57]

clearly shows that a pure edge dislocation could be generated by different possible cuts. This idea can be easily extended to a shear loop. One side of the surface cut A is displaced by \mathbf{b} relatively and the material on both side of the cut are rejoined afterwards [57, 58]. The inner product $\mathbf{b} \cdot \mathbf{n}$ therefore highly depends on the shape of surface A . In the comments of Bulatov et al. [56], the flat area encircled by the loop C was chosen as this surface A . It is only under this premise that their asserted condition $\mathbf{b} \cdot \mathbf{n} = 0$ [56] is valid and so is the “shear impossibility”. Clearly, Burgers vector \mathbf{b} and \mathbf{n} are not perpendicular to each other everywhere at least in Figure 6.1. As a result, Eq. (6.2) should be nonzero on most part of surface A . This indicates that Eq. (6.1) cannot be used to claim “shear impossibility”. Further, the integral form in Eq. (6.1) is not suitable to evaluate the local mass transport. Even if Eq. (6.1) does equal zero when symmetry in Figure 6.1 is employed, it only implies that the removed and inserted material volumes are the same. However, local mass transport is still true for specific locations on the surface as described by Eq. (6.2). Indeed, the integral to evaluate local mass transport should be operated on a small surface element. The integral is not invariant with respect to arbitrary surface cut for an incomplete dislocation loop. As long as the surface A is not presumed as the flat one encircled by loop C , there would be local mass transport. To determine the exact shape of the surface A , other information is required. Such information could, for example, come from molecular dynamics simulations. The mere overall mass conservation of Eq. (6.1), with a presumption of a flat surface A appears to be inadequate to disprove the void growth via shear loops/curves.

Next, we distinguish the mass transport caused by the formation of a shear loop and that by the motion of a shear loop. The mass transport caused by the motion of a dislocation loop is given as [57]

$$\delta V = \oint_C \mathbf{b} \cdot (\delta \mathbf{r} \times d\mathbf{l}) \quad (6.3)$$

Notably, here the integral is operated on the loop curve. If the motion is a pure slip, Eq. (6.3) is indeed zero for a shear dislocation loop since the three vectors \mathbf{b} , $\delta \mathbf{r}$ and $d\mathbf{l}$ are in the same plane. The motion other than a pure slip, as long as the projection area of the loop in the direction of Burgers vector is nonzero, should result in mass transport [57].

Second to be considered is the displacement caused by the presence of a shear loop. This part is true even if the bounding surface A is taken as the flat one encircled by the loop as shown in Figure 6.1. The presence of a shear loop introduces a strong lattice structure discontinuity to the surrounding material. Although the classical elasticity may fail at the dislocation core, modifications [137] to this approach can still lead to a solution of physical significance. A simple example of displacement field induced by an edge dislocation can be found in [59]. Similarly, but more sophisticatedly, the displacement field due to the presence of a shear loop could be obtained by the Green's function method [60]. Through integration treatment, the analytical solution \mathbf{u}^{loop} of a shear loop as shown in Figure 6.2 can be obtained as [60]

$$u_1^{loop}(x_1, x_2, x_3) = -\frac{b\zeta}{4(1-\nu)} \left[\frac{2(1-\nu)}{|\zeta|} I_0^0 + \frac{(x_1^2 - x_2^2)}{\rho^3 R^2} I_1^0 - \frac{x_1^2}{\rho^2 R^2} I_0^1 \right] \quad (6.4)$$

$$u_2^{loop}(x_1, x_2, x_3) = -\frac{bx_1 x_2 \zeta}{4(1-\nu)\rho^3 R^2} (2I_1^0 - \rho I_0^1) \quad (6.5)$$

$$u_3^{loop}(x_1, x_2, x_3) = -\frac{bx_1}{4(1-\nu)\rho R} \left[(1-2\nu)I_1^0 + |\zeta|I_1^1 \right] \quad (6.6)$$

where $\rho = \sqrt{x_1^2 + x_2^2}/R$, $\zeta = x_3/R$, R is the radius of shear loop, b is the magnitude of Burgers vector, ν is Poisson's ratio and the function I_m^n is defined as [60]

$$I_m^n(\rho, |\zeta|) = \int_0^\infty t^n J_1(t) J_m(\rho t) \exp(-|\zeta|t) dt \quad (6.7)$$

where J_m is the m th order Bessel function of the first kind. One can refer to Figure 2 in Ohr [60] for a better understanding. This elastic deformation is negligible for a microvoid since its b/R is extremely small. Nonetheless, for a small nanovoid adjacent to multiple emitted shear loops/curves, the elastic deformation induced by shear loops/curves could be a contributor. Such situation can be found, for instance, in the neutron-irradiated metals. Both nanovoids and dislocations can be formed in the metal due to irradiation. In the work of Shimomura and Mukouda [138], nanovoids of about 3 nm in diameter were observed inside the irradiated copper. In Figure 2 of Ohr [60], the influence of the shear loop extends to a relatively large area compared with its radius. To a rather nearby nanovoid, the void surface would be distorted by the shear loop and therefore develop a growth or shrinkage. Hence, an important focus of this chapter is to extend the elastic solution [60] to the case with a nearby nanovoid. The solution of the elasticity problem can be obtained by the superposition of the displacement field \mathbf{u}^{loop} caused by the shear loop and the image field \mathbf{u}^{void} due to presence of the void. This method has been adopted by Wolfer and Drugan [139] to deal with the interaction between a prismatic loop and a void. The lack of symmetry of the elasticity problem here makes it difficult to pursue any analytical solution. As an alternative, the image field is solved by the finite element method to satisfy the traction-free boundary condition on the void surface. Once \mathbf{u}^{void} is solved, the total displacement field could be expressed as

$$\mathbf{u} = \mathbf{u}^{loop} + \mathbf{u}^{void} \quad (6.8)$$

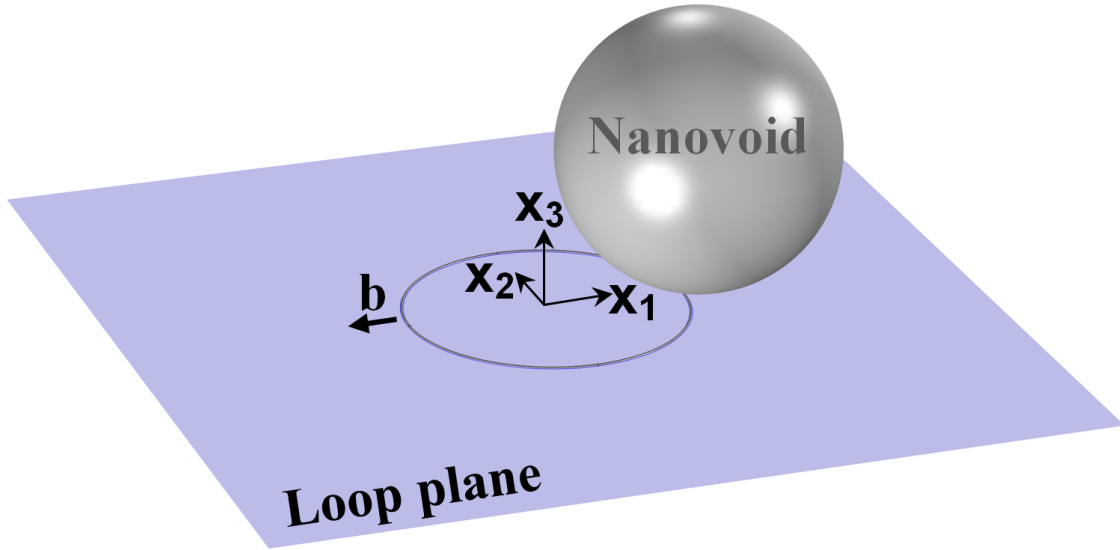


Figure 6.2: Schematic of the corresponding geometry. The center of the circular shear loop with a radius of R coincides with the coordinate origin. The spherical void of a same radius R is centered at the coordinates $(1.1R, 0, 1.05R)$. The ratio b/R is set as 0.1.

The corresponding strain field can be easily obtained through the displacement field caused by the shear loop. Next, the stress tensor $\boldsymbol{\sigma}^{loop}$ caused by the shear loop can be found through applying Hooke's law. Consequently, the boundary loading condition of the image field can be determined. The combined stress, caused by both the shear loop and the image field due to the presence of the nanovoid, must satisfy the traction-free boundary conditions on the void surface:

$$\boldsymbol{\sigma}^{void} \cdot \mathbf{n} + \boldsymbol{\sigma}^{loop} \cdot \mathbf{n} = 0 \quad (6.9)$$

where \mathbf{n} is the normal vector on the void surface. The geometry configuration is shown in Figure 6.2. Finite element calculation has been performed by modeling this geometry after a mesh

convergence test. The Young's modulus and Poisson's ratio are set to be 120 GPa and 0.33, respectively. For brevity, only the magnitude of total displacement \mathbf{u} is displayed in Figure 6.3.

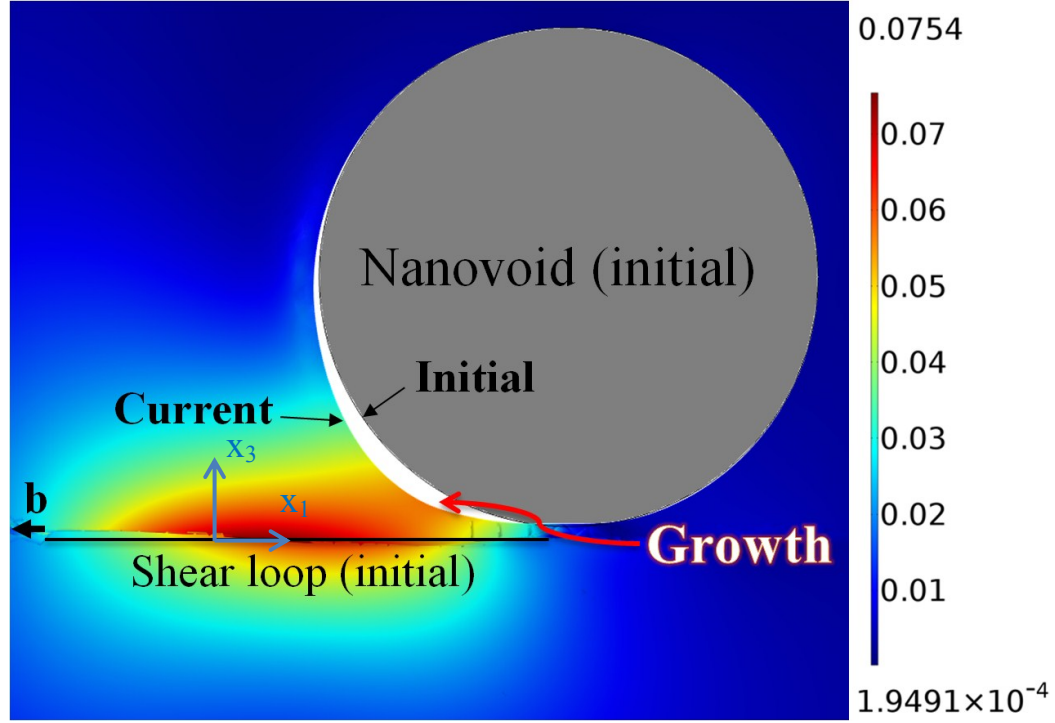


Figure 6.3: Deformed slice plot of the magnitude of total displacement \mathbf{u} with the cutting plane at $x_2=0$. Growth of the nanovoid towards the shear loop can be clearly seen (Deformation has been magnified by a scale factor of 2). The color bar is in the unit of R .

The white crescent shows the difference between the current profile and the initial profile of the nanovoid, which is displayed as a grey circle. It is worth noting that the magnitude of displacement of a single shear loop without a nearby void should be symmetric with respect to the plane $x_3=0$. Yet, the presence of the nearby void affects the displacement field and breaks this symmetry. The volume increase of nanovoid can be calculated by

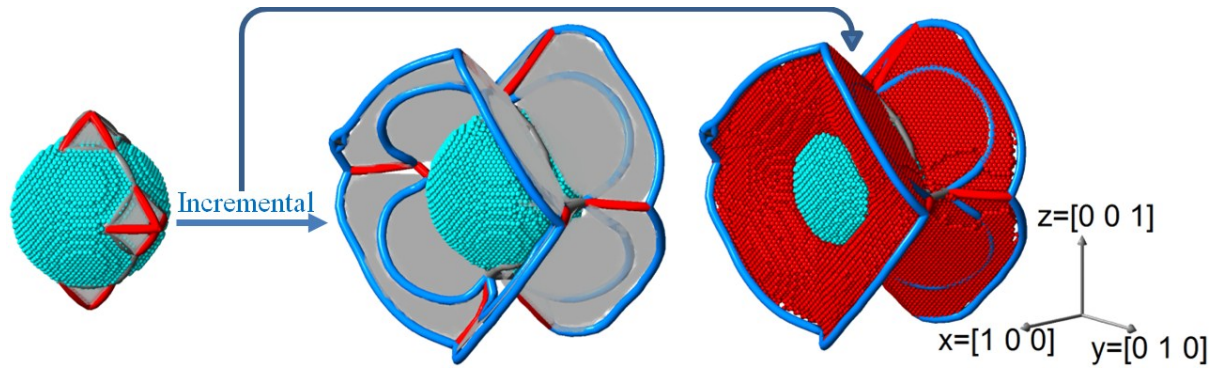
$$\Delta V_{void} = \int_{S_{void}} (\mathbf{u} \cdot \mathbf{n}) dS \quad (6.10)$$

The integral in Eq. (6.10) is directly defined on the void surface and, so is the unit normal vector \mathbf{n} . The volume increase calculated by Eq. (6.10) is 0.062 in the unit of R^3 . Hence, the ratio of increase $\Delta V_{\text{void}}/V_{\text{void}}$ is found to be 0.015. Since the solution is only for a complete shear loop [60], the modeled shear loop is assumed to be close but not attached to the void surface. Compared with the image field, the displacement field by the shear loop contributes more to the void growth.

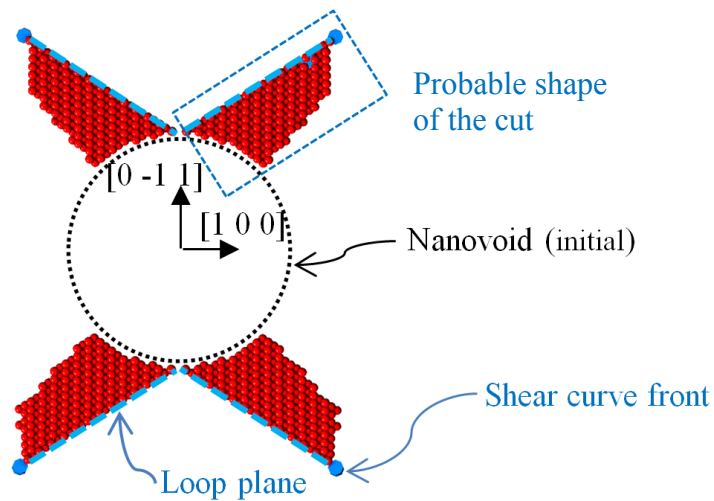
The two parts of possible mass transport induced by a shear loop have now been obtained. Once the shear loop forms, its contribution to the nearby nanovoid growth would consist of these two parts if it moves by pure slip. As mentioned, the bounding surface A can take any arbitrary shape. This shape is crucial to the mass transport. The exact shape of this surface A is out of the scope of a pure theoretical understanding. The first part of mass transport to the void growth is irreversible. The second part depends on the distance between the shear loop and the void surface.

Last but not least, atomistic simulation is examined to explore the probable shape of the surface A bounding the material transferred induced by shear loop. Recent atomistic simulations demonstrated that the local mass transport via shear loop is true through visualizing the “relative farthest-travelled (RFT)” atoms [87]. Those RFT atoms are identified by their relative atomic displacement [87]. This relative atomic displacement not only excludes the homogeneous deformation of the simulation box, but also is independent of the origin of the reference coordinate system. In the present report, we take a further step to use the incremental relative displacement to explore the probable shape of the surface A in Figure 6.1. The details of the atomistic simulation could be found in [87] for the primary case. The formation of the major frustum-like dislocation structure starts after the strain of 5.8% as shown in Figure 6.4a. The total

atomic deformation comprises four parts: the homogeneous elastic deformation due to stretch, the heterogeneous elastic deformation due to the presence of void, the elastic deformation due to dislocations and the plastic deformation due to dislocations. Since the first one can be readily excluded by using “relative atomic displacement”, the remaining task is to highlight the plastic deformation due to the shear dislocation curves. The original “relative atomic displacement” applied the initial unstrained configuration as reference [87] and considered the difference between the current and referential atomic configuration. Given that the incremental elastic deformation due to the presence of void is small in the elastic region during the simulation [87], this second part of deformation could be made insignificant once only considering the incremental deformation from $\varepsilon=5.8\%$ to $\varepsilon=5.92\%$. Since the incipient Pyramid-shape dislocations at the four corner of void remains unchanged, the incremental deformation also eliminates the deformation due to these pre-existing minor dislocations. Therefore, the remaining significant parts are only the deformations due to the shear dislocation curves. Figure 6.4c shows the incremental RFT atoms by taking Figure 6.4a as the referential atomic configuration. Figure 6.4d is the sliced snapshot with its cutting plane in the direction $[0\ 1\ 1]$. Figure 6.4d could shed some light on how the surface bounding the material transferred by shear curves/loops may look like. It is interesting to compare the shape in Figure 6.4d with the surface A in Figure 6.1 conceived by Hirth and Lothe [57]. In general, an increase of the dislocation density has been observed in atomistic simulations [87]. This implies that population growth of the shear loops/curves could magnify their contributions to the nanovoid growth. Indeed, rapid void growth is found triggered by a burst of increase in dislocation density [87]. The burst of void growth happens exactly at the strain range as in Figure 6.4.



(a) Dislocations ($\epsilon=5.8\%$) (b) Dislocations ($\epsilon=5.92\%$) (c) Incremental RFT atoms ($\epsilon=5.92\%$)



(d) Incremental RFT atoms ($\epsilon=5.92\%$) to approximate the material transport domain induced by shear curves

Figure 6.4: Incremental material transport from $\epsilon=5.8\%$ to $\epsilon=5.92\%$ during the emission of eight sets of shear curves/loops. The light blue atoms represent the current void surface while the red atoms are the incremental RFT atoms. The rendered blue and red curves are dislocation curves. The critical magnitude of displacement to identify the incremental RFT atoms is 1.02 \AA , which is the averaged magnitude of Burgers vectors belonging to the eight front shear curves. Snapshots

are plotted by software ATOMVIEWER .Loading is applied in x direction. Figure (d) shows a cutting view of (c).

Evidence and explanation for void growth via shear dislocation curve/loop can also be found in Refs. [18, 26]. Nevertheless, it should be emphasized that the formed pattern of dislocation structure is subject to the simulation conditions such as loading pattern or lattice orientation.

Chapter 7: The Influence of Ellipticity to the Void Coalescence*

7.1. Introduction

The initiation and evolution of small voids limit the formability and ductility of aluminum and its alloys. These voids grow and coalesce during the continued applied loading, causing localized coalescence and fracture. A famous constitutive model was proposed by Gurson [48] to account for the void's role in characterizing material damage. Tvergaard [140] introduced adjustment parameters to further calibrate the Gurson relation based on micromechanical studies on periodically distributed voids. So far, these models or their variants have been widely incorporated in finite element simulations and analytical calculations. Most of the constitutive models for porous metals are derived by the unit cell modeling. However, the voids in a real engineering material are not likely to be uniformly distributed. In order to capture the softening response of the porous metals with higher accuracy, it is physically necessary to characterize the heterogeneity of the void distribution. Indeed, heuristic study on the effect of void interacting in porous metals has been carried out via the FE method or the analytical approach by many researchers. Ohno and Hutchinson [141] concluded from their model, which embedding an excess of voids within a disk-shaped cluster with a uniform background distribution to an elastic-plastic solid, that non-uniform distribution of the voids lowers the ductility. Later, this conclusion was supported by Becker [142], who used a distribution of initial porosity from experiments to perform the finite element simulation. Magnusen et al. [143] examined the specimen with random or uniform distributions of macroscopic holes and developed an

* A version of this chapter has been published. Reprinted with permission from Cui, Y.; Chen Z. Molecular dynamics simulation of the influence of elliptical void interaction on the tensile behavior of aluminum. *Comput. Mater. Sci.* 2015, 108,103-113. Copyright 2015 Elsevier.

algorithm in modeling. Benson [144] applied an Eulerian finite element program to study the dynamic response of OFHC copper and 4340 steel by assuming an arbitrary random distribution of six voids with fixed total porosity. Later, Benson [145] studied the void clustering effect by modeling a discrete set of randomly distributed clusters. He found that the ultimate stress is a constant with the changing fracture strain and with the void cluster diameter. Horstemeyer et al. [115] employed the micromechanical FE method to quantify the coalescence effect based on temperature and different spatial arrangement of voids. He also proposed a critical ILD to define void coalescence. Chen et al. [146, 147] applied the FE-damage percolation model to study the damage evolution in the forming of aluminum alloy sheets. This damage percolation model adopted elliptical void shapes and employed measured particle distribution to characterize the void cluster initiated by second phase particles. Toi et al. [148] carried out a 2D mesoscale simulation to analyze the elasticity, yield stress and void-linking fracture via meshless method. Bilger et al. [149] paid attention to the specific role of the porosity fluctuations inside the representative volume element. Their results indicated the porosity fluctuations can have a strong effect on the overall yield surface of porous materials. Gărăjeu et al. [150] focused on the influence of small fluctuations of porosity on the effective properties of porous materials. They concluded that deviations of uniform distribution result in weakening the macroscopic load carrying capacity of the porous materials. The experimental research [151] using drilled-hole samples revealed different failure and strain pattern depending on the configuration of the microvoids and also highlighted the importance of void spacing and void orientation. Bandstra and Koss [152] examined the sensitivity of void growth and coalescence to the intervoid spacing, strain hardening and multiaxial stress state. They concluded that the growth of voids within the

cluster is accelerated. The work of the above researchers demonstrates the important role of the void interaction in the damage progression ranging from the microscale to the macroscale.

As for nanovoids, evidence suggests that dislocation-void interaction plays an important role in the void evolution in metals [18, 39, 40, 153-156]. Lubarda [91] extended his early work [18] to a more generalized dislocation-void interaction model under combined loading. The minimum critical stress is physically obtained by minimizing the critical stress with respect to the two angular variables. Both the dislocation emission angle and critical stress predicted in [18] were supported by MD simulations [26, 38-40]. So far, the void growth and coalescence mechanisms in face-centered cubic metals have been widely studied by the MD simulation. Potirniche et al. [37] employed the MD method to study growth and coalescence of circular nanovoids in single crystal nickel. Their results reflected the size-scale dependence of the nanovoids. Traiviratana et al. [26] performed the MD simulation in monocrystalline and bicrystalline copper. The emission of dislocation is confirmed to be the primary mechanism of void growth. Bringa et al. [38] applied the MD method to investigate the effect of loading orientation and nanocrystalline in FCC copper. Marian et al. [39] used the quasi-continuum method to study the void expansion in FCC aluminum and indicated that dislocation emission is the primary mechanism. However, the investigation of the role of void interaction including the intervoid spacing and void shape combination has not been reported. Therefore, efforts are made here to elucidate and examine the role of void interaction in the material response of the FCC aluminum.

The void interaction simulation regards the voids of elliptical shape. The elliptical void, as a generalized treatment of the initial void geometry, highlights the role of the void shape. The pertinent intervoid geometries [157] are depicted in Figure 7.1. For the empirical approach, void coalescence occurs through shear band development between the neighboring elliptical voids

when the ILD satisfies the criterion with regards to the void geometry [157]. As illustrated in Figure 7.2, the critical ILD is larger than zero for the empirical criterion as a simplification to the physical problem. However, the void coalescence process, as observed both in MD simulations and experiments, is likely to be a continued process. Therefore, a task of chapter is to investigate the continued process of void coalescence under the interaction of elliptical void via MD simulation.

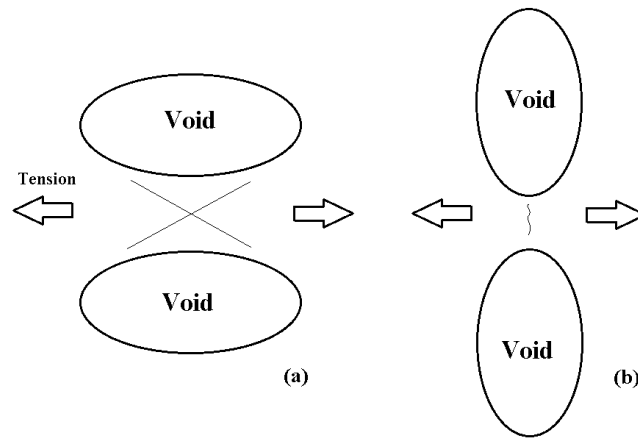


Figure 7.1: Schematic of idealized void interaction geometry reproduced from [157]: (a) oblate-oblate combination; (b) prolate-prolate combination.

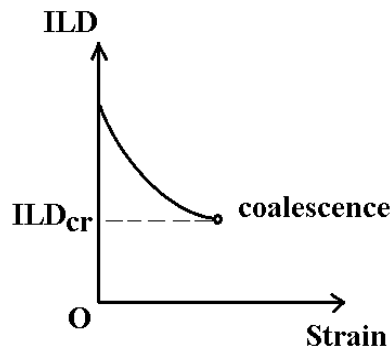


Figure 7.2: Schematic of the empirical criterion for void coalescence (the critical ILD is larger than zero).

In this work, a 3D simulation box with a thin z-direction thickness is employed. As shown in Figure 7.3, it has doubled length in y-direction based on the fact that void coalescence occurs perpendicular to the uniaxial loading direction. The simulation box can be viewed as the combination of the upper and lower square unit cells. The resulted void distribution in the simulation box is no longer uniform. A benefit of this “2D” simulation geometry is that it allows us to have a clear view of the material transport in the high strain regime when the primary growth of the voids prevails. Chang et al. [158] suggested that the yield stress simulated by MD in 2D is very close to that in 3D at 0K. Nevertheless, the extension towards a cubic 3D simulation geometry would be helpful in that it provides spacing space in the third direction for the motion of dislocations and the formation of complete dislocation loops. Some dislocation mechanisms like the prismatic loop emission induced by inclusions are more physically suitable for 3D simulations. For a spherical void in a cubic MD geometry, many authors [26, 38, 103, 154, 159-162] have contributed to uncovering the void-related material behavior over the years.

7.2. Simulation Methodology

We used the Large-scale Atomic/Molecular Massively parallel simulator (LAMMPS) in the simulations. Software ATOMEYE [84] is applied in post-processing. The interaction between the atoms is modeled by the embedded atom method [110]. It is of great importance that the EAM potential chosen for atomistic simulations must accurately reproduce pertinent features of the resulted energy curves, such as the unstable stacking fault energy [80]. The unstable stacking fault energy is a crucial parameter of the barrier for partial dislocation nucleation [81]. The accurate characterization of the dislocation nucleation and interaction relies on a qualified EAM potential. Mishin et al. [112, 113] reported the EAM potentials for aluminum and copper. These potentials demonstrated accurate intrinsic and unstable stacking fault energy such that they have

been extensively applied in MD simulations [26, 38, 111, 114, 156, 163]. Hence, the EAM potential for aluminum [112] is chosen in this work to carry out the simulations.

A periodic voids-embedded simulation box is used to represent non-uniformly distributed voids. The atoms inside the voids are removed to create specifically-shaped embedded holes. Energy minimization via a conjugate gradient algorithm is first performed to attain the minimum energy configuration, followed by the relaxation step to reach an equilibrium state configuration. Based on that, the engineering tensile strain is applied as the load. All MD simulations are performed with the isothermal-isobaric ensemble under room temperature via the Nose-Hoover thermostat [82], representing a system in thermal contact with a bath of constant temperature. According to LAMMPS user manual, the Nose-Hoover thermostat could bring the undesirable oscillation of pressure and/or temperature to the simulated system. Therefore, a proper drag force is forced upon the thermostat to damp this oscillation. In simulation, the drag force applied is determined through extensive tests such that its ability to damp the oscillation saturates.

7.3. Results and Discussions

As shown in Figure 7.3, the representative computation geometry contains two elliptical voids. As indicated by the dash lines, the rectangular simulation geometry is the combination of the upper and lower squares. Therefore, the resulted void distribution is non-uniform. For each elliptical void, the major axis is two times the minor axis. The individual void is either placed horizontally or vertically. The upper void to the lower void combination varies from oblate-oblate, to oblate-prolate and to prolate-prolate. For each void shape combination case, the initial ILD, as denoted by ILD_0 , increases from $1a_2$, as the most non-uniformly distributed case, to $2a_2$ and to $4a_2$. These nine specimens are listed in Table 7.1 for additional details. In our simulation,

uniaxial tension is applied upon the simulation box at both ends of the x-direction. The size of the simulation box corresponds to 512, 1024 and 8 atomic planes of Al in the x, y and z directions, respectively.

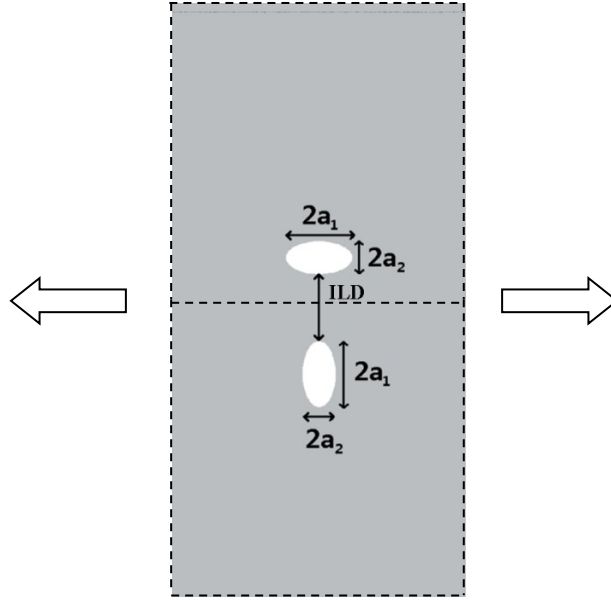


Figure 7.3: Simulation Geometry containing two non-uniformly distributed elliptical voids (Periodicity are applied on all the three dimensions).

Table 7.1: Details about the Computation Geometry

Void shape combinations (upper-lower)					
Oblate-oblate		Oblate-prolate		Prolate-prolate	
Specimen	ILD ₀	Specimen	ILD ₀	Specimen	ILD ₀
1	1a ₂	4	1a ₂	7	1a ₂
2	2a ₂	5	2a ₂	8	2a ₂
3	4a ₂	6	4a ₂	9	4a ₂
The dimensions of each specimen					
Simulation box size (nm)		Void size (nm)		Initial porosity	
Width	103.7	a ₁	11.7	0.02	
Height	207.6	a ₂	5.85	Total atom number	
Thickness	1.62			2,055,264	

7.3.1. The Onset of Dislocation Emission Compared with the Lubarda Model

Special attention was paid to identify the onset of dislocation emission from the void surface with different initial void geometry during the post-processing of MD results. On one hand, the onset of dislocation emission marks the beginning of the inelastic deformation and the rapid growth regime of the void. On the other hand, the validity of the MD method could be examined readily by comparing the predicted critical stress with those given in the literature. Lubarda [91] extended his original model [18] to account for combined loading cases. In his model, the critical stress for the initiation of dislocation emission is determined by balancing the applied stress to the image force on the dislocation exerted by the void surface. The equilibrium distance ρ in Figure 7.4 is set equal to the dislocation core cut-off radius ρ_0 [116], where ρ_0 is set equal to the magnitude of dislocation [91]. The critical stress is formulated with respect to the two angular variables, namely, ϕ and θ [91].

$$\sigma_{cr} = \frac{Gb/R}{2\pi(1-\nu)} \frac{\sin 2(\theta-\phi)}{h} \left(\frac{r_0^4}{R^2(r_0^2 - R^2) \sin \theta} - \frac{2(r_0^2 - R^2) \sin \theta}{r_0^2} \right) \quad (7.1)$$

$$h = - \left[\frac{r_0^2}{R^2} - \left(3 \frac{R^2}{r_0^2} - 2 \right) \cos 4(\theta - \phi) \right] \sin 2(\theta + \phi) - \left[\left(3 \frac{R^2}{r_0^2} - 2 \right) \sin 4(\theta - \phi) \right] \cos 2(\theta + \phi) + \sin 2(\theta - \phi) \quad (7.2)$$

$$r_0^2 = R^2 + \rho_0^2 + 2R\rho_0 \cos \theta \quad (7.3)$$

$$\sin(\theta - \phi) = R \sin \theta / r \quad (7.4)$$

Where

G is the shear modulus, and $G=25.5$ GPa [117] for aluminum,

b is the magnitude of dislocation, and $b=0.286$ nm [118] for aluminum,

ν is Poisson's ratio, and is set as 0.33; and other geometry quantities are as illustrated in Figure 7.4.

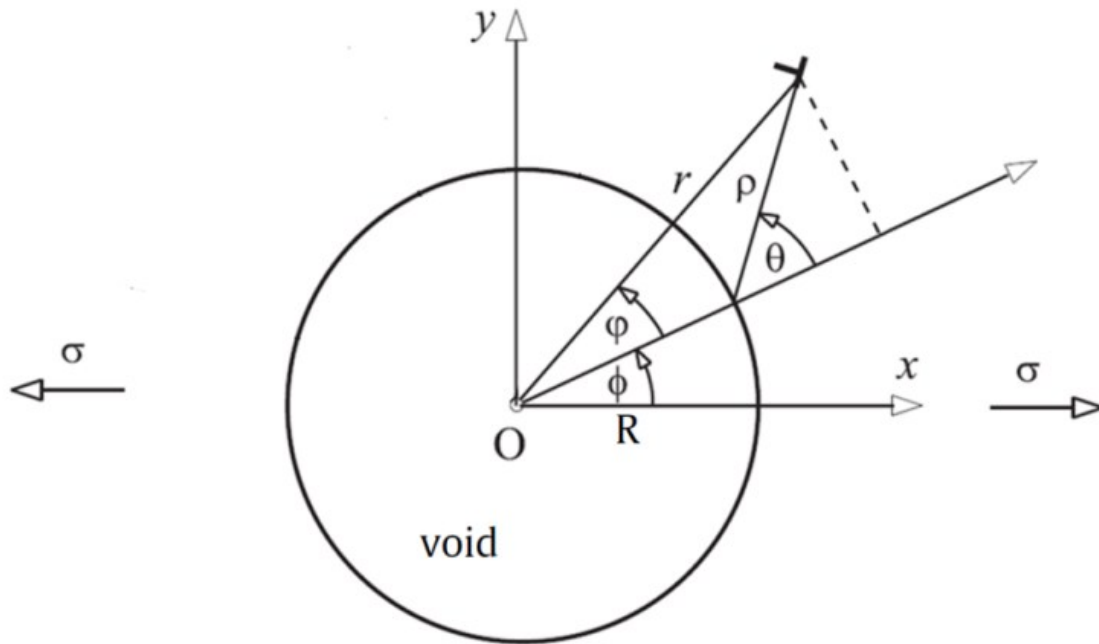


Figure 7.4: The void-dislocation geometry under uniaxial tension reproduced from [91]

(Reprinted with permission from Lubarda. Copyright 2011, Elsevier).

The simulated critical stresses by MD method are compared to the minimum value predicted by Eq. (7.1). The minimum critical stress is determined by minimizing the function $\sigma_{cr} = \sigma_{cr}(\phi, \theta)$ with respect to the two angular variables.

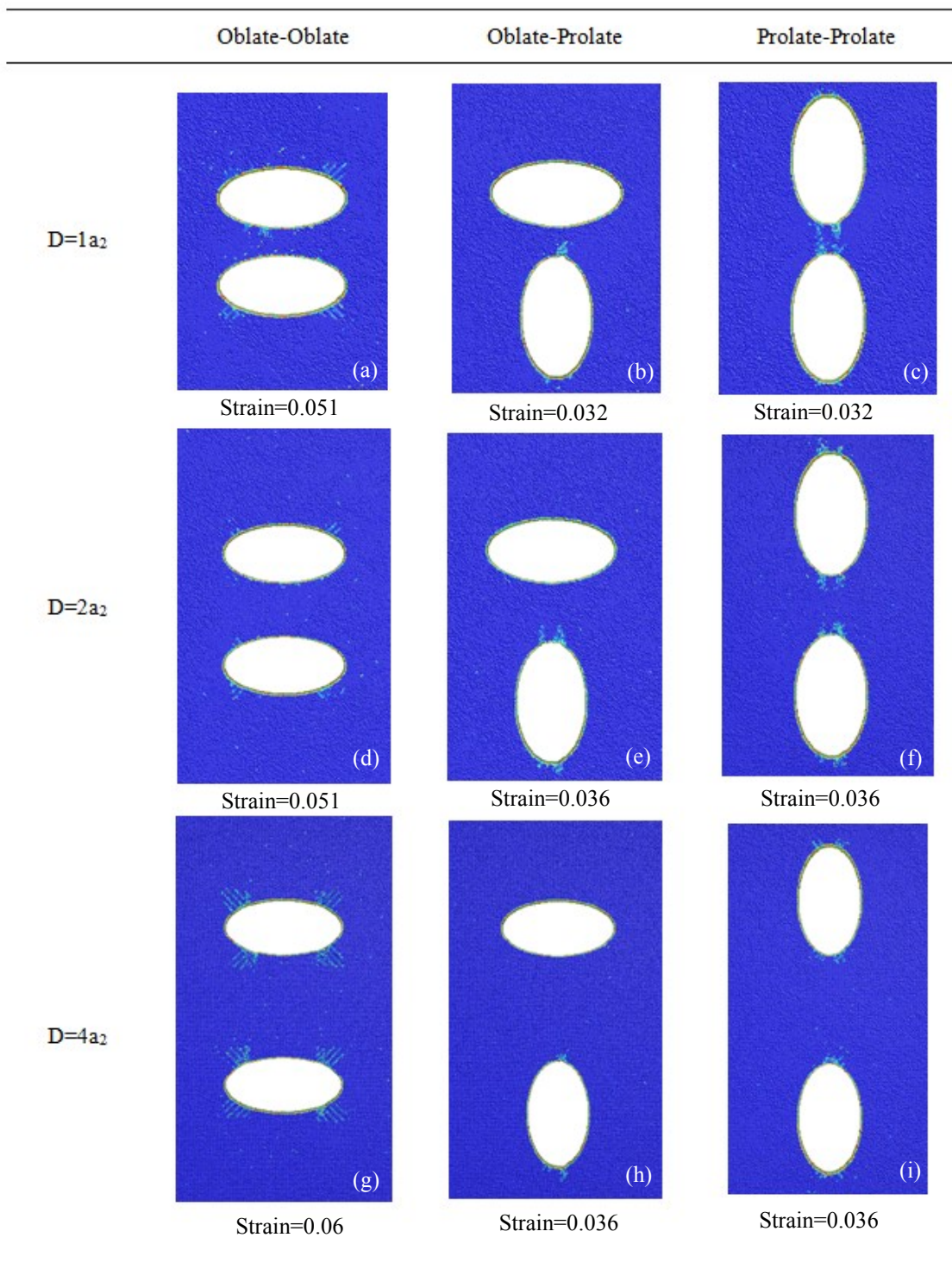


Figure 7.5: The centrosymmetry parameter coloring (CPC) plots indicating the onset of dislocation emission for each specimen.

CPC figures are plotted for the nine specimens to spot the disordered atoms. The CPC highlights the atoms according to the distances from its twelve nearest neighbors. The centrosymmetry parameter ranging from low to high identifies the atoms in the bulk lattice, partial dislocation, stacking faults and free surface, respectively. In Figure 7.5, the nine CPC plots, corresponding to the onset point of the dislocation emission, are listed with different void shape combinations and different ILD_0 . The light blue lines in the figures indicate the dislocation lines emitted from voids. From a 3D view and noticing the periodicity, these sets of lines represent the slipped areas bounded by dislocation lines. The angle between the slip planes and the x-y plane is 45° . These slip planes consist of close-packed atoms in FCC metal and thus are common directions for dislocations [135]. It can be concluded from the nine plots that the dislocation emission, as a localized event, is strongly affected by the void shape and is also influenced by the ILD_0 to some degree. For the largest ILD_0 cases as in Figures 7.5g-i, the dislocation emission patterns from the voids are free from the influence of the nearest neighbor. The number of dislocation sites emitted from the oblate void surface is four as shown in Figure 7.5(g), while the number of dislocation sites on the prolate void surface is either three or four as shown in Figures 7.5h and i. However, when it comes to the three cases with the smallest ILD_0 , the void shape determines whether dislocation emission would be inhibited or promoted. For Figure 7.5a, i.e. oblate-oblate combination with the smallest ILD_0 , the two dislocation emission sites, supposed to be on the intervoid side, are disturbed and no longer resemble the “regular” pattern for the oblate void like that in Figure 7.5g. In subsequent CPC plots following Figure 7.5a, which are not displayed for brevity, the disturbed dislocation lines quickly interlink to form a cleavage and lead to an imminent void coalescence. For Figure 7.5b and its subsequent CPC plots, the rapid dislocation emission from the prolate void largely inhibits that from the intervoid

side of the oblate void. Later, the cleavage forms and develops into coalescence path without dislocation emission from the intervoid side of the oblate void. For Figure 7.5c, the scenario is different. The short ILD_0 promotes the dislocation emission from the intervoid side of both the prolate voids. No matter what the paired void shape is, the prolate void triggers the dislocation emission much earlier than the oblate void. Therefore, the onset of dislocation emission of the two-void system as a whole is mainly determined by its prolate member. Although the pattern of the dislocation emission is subject to the influence from a near neighbor, the onset of the dislocation emission does not appear so. As a result, the conclusion could be generalized that the onset of the dislocation emission of a cluster of multiple elliptical voids is mainly determined by the ones whose major axis is perpendicular to the uniaxial loading direction.

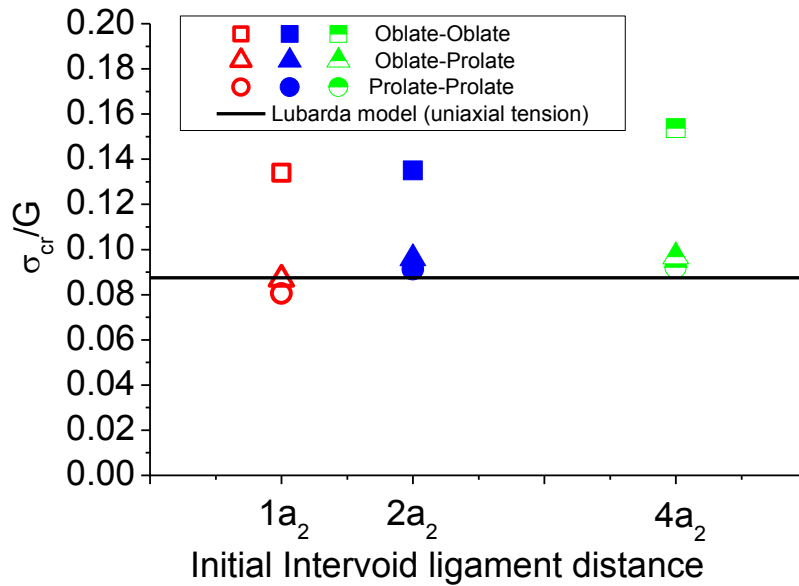


Figure 7.6: The critical stress by MD simulation compared to the minimum critical [91].

Geometric mean radius $\bar{R} = \sqrt{a_1 a_2}$ is used for the elliptical void.

The high nucleation stress acquired in Figure 7.6 can be attributed to the size effect and the high strain rate applied. Various testing techniques have demonstrated that the decreasing sample size could substantially increase the stress response of the testing material [33-36, 164-166]. Although periodicity is imposed at all three dimensions in the present study, the computation geometry is essentially of submicron size. Furthermore, the high strain rate ($2 \times 10^9 \text{ s}^{-1}$) applied in the present work, though within the commonly adopted range [26, 40], is another contributor to the high stress response. On the other hand, the spallation testing by laser driven shocks [167] suggests that such a high stress as shown in Figure 7.6 is not unrealistic in aluminum at high strain rates. Cuq-Lelandais et al. [167] measured a spall strength ranging from 1.5 GPa to 3.6 GPa with the applied strain rate increased from 10^6 s^{-1} to 10^8 s^{-1} . As for MD simulations regarding bicrystal interfaces in aluminum [111, 114], the tensile stress required to nucleate dislocation is within the range of 4.28-5.92 GPa. By comparison, the stresses required for dislocation initiation due to the presence of elliptical void are in the range of 2.04-3.92 GPa as in Figure 7.6. It should be noted that in our simulation all the elliptical voids are of the same size $\bar{R}/b = 28.9$. The minimum critical stress predicted by the Lubarda model for this void size should be 0.88 G, as plotted in Figure 7.6. In Figure 7.6, the critical stresses obtained by MD, especially the oblate-prolate and prolate-prolate cases, yield good agreement with the prediction by the Lubarda model. The simulated critical stresses by MD with different void shape combinations are plotted against the ILD_0 . A weak dependence of the critical stress on ILD_0 can be found. In general, the void shape dominates the critical stress. The oblate void requires a larger critical stress to trigger the dislocation emission, while the prolate void requires a considerably lower critical stress. In terms of void shape combination, the oblate-oblate combination results in the highest critical stress, while there is little difference between the

oblate-prolate and the prolate-prolate cases. By minimizing the critical stress, the Lubarda model also identifies the critical emission angle ϕ to be 89° for the void size concerned. Figure 7.5 indicates that the void shape also affects the angle of the dislocation emission. For the prolate voids, the dislocation emission angle ϕ is relatively close to 89° . In contrast, the dislocation emission angle from the oblate void is much smaller.

7.3.2. The Overall Stress Response

For the nine cases as a whole, the dislocation emission marks the beginning of the strain hardening region until the stress reaches the ultimate tensile strength in Figure 7.7 and Figure 7.8. The CPC plots of these nine cases illustrate the general process of dislocation development, i.e. the dislocations first emit from void surface and then propagate, partly annihilate and finally interact into a network-like structure. After reaching the ultimate strength, the accumulation of dislocations is the main cause of the deterioration of stress response. The annihilation of a certain portion of dislocations then recovers the stress to a certain level. Unfortunately, the accumulation of dislocations would regain its dominance over the annihilation such that the stress drops again. The decrease of stress is more closely linked to the dislocation development rather than the void coalescence as marked by the filled color points in the corresponding figures. Although the simulation box adopts periodical boundaries, the two-void system could be viewed as “isolated” from the neighboring voids before the strain of 0.1 as the dislocation lines have not yet reached the simulation boundary in the CPC plots. We will refer to this “isolated” range in the following context.

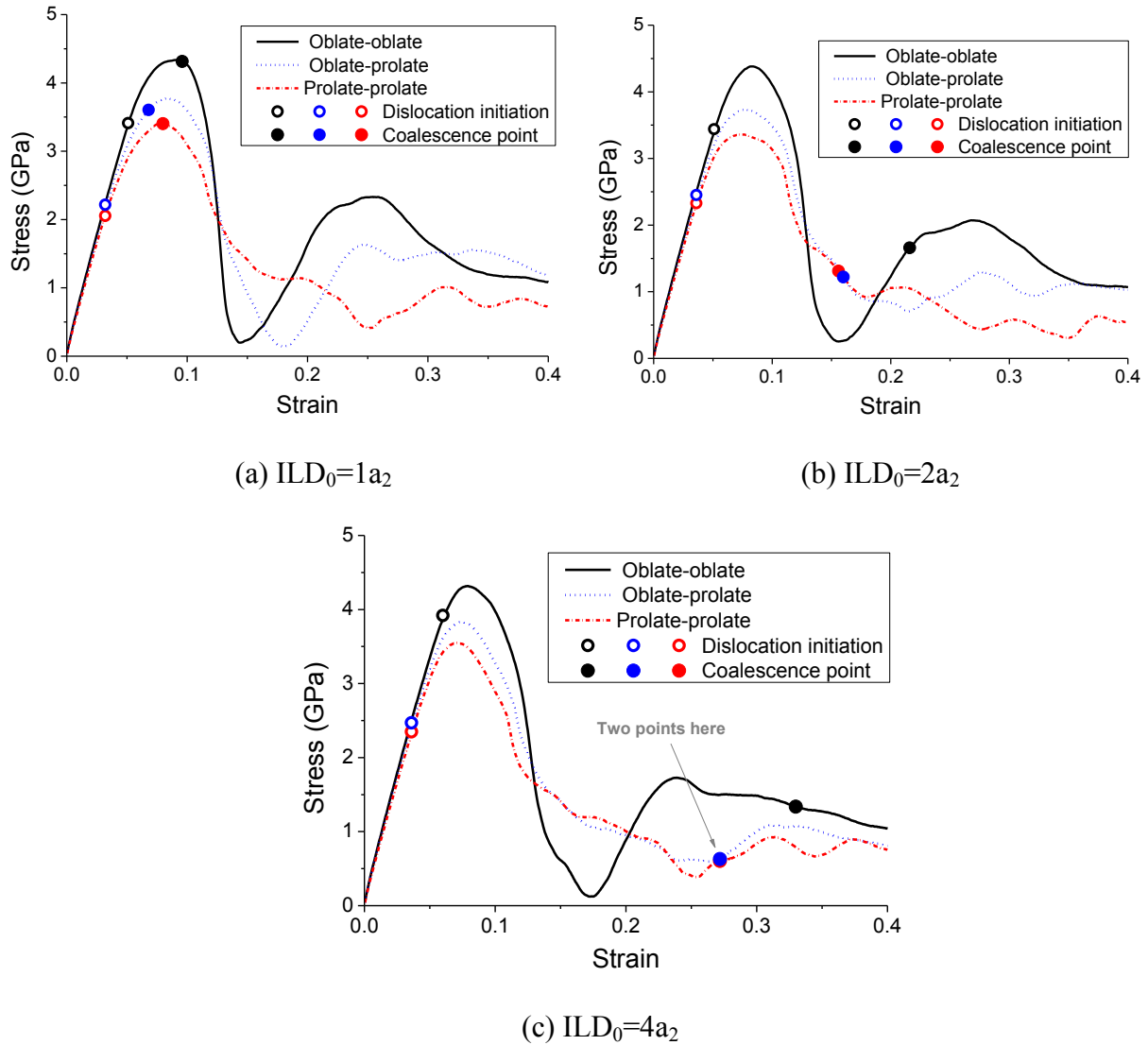
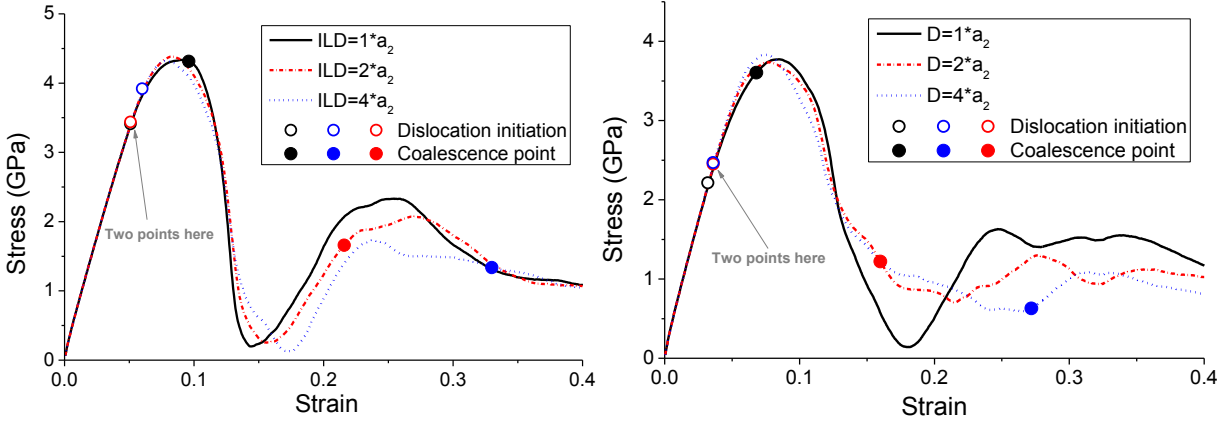


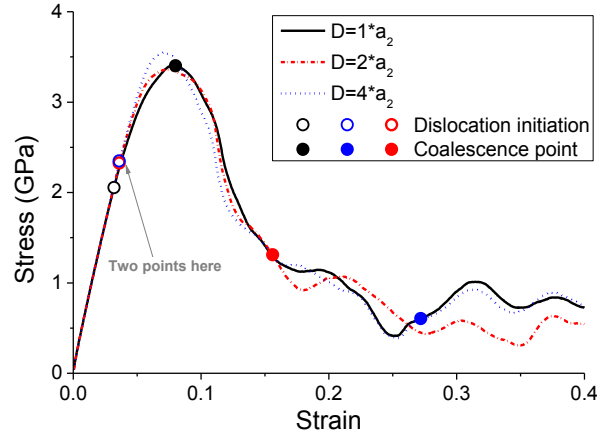
Figure 7.7: Strain-stress curves to reflect the influence of void shape combination.

In Figure 7.7, the stress curves are organized in order to reflect the role of void shape combination under different ILD_0 . The oblate-oblate cases result in the highest ultimate strength and retain a relatively high stress level at the end of loading. It is reasonable for the stress curve of the oblate-prolate cases to go between the other two cases within the “isolated” region under the strain of 0.1. Similar to the dominance of the prolate void on the dislocation emission in the previous subsection, the prolate void is also dominant in stress response such that the oblate-prolate cases are closer to the prolate-prolate cases in their stress-strain curves.



(a) Oblate-oblate

(b) Oblate-prolate



(c) Prolate-prolate

Figure 7.8: Strain-stress curves to reflect the influence of ILD_0 .

In Figure 7.8, the stress curves are organized in order to reflect the role of the ligament distance under varying void shape combinations. In Figure 7.8c, it is predictable that the case of $ILD_0=4a_2$, as the least non-uniformly distributed case, has a higher ultimate stress. Yet, for the other two figures, the influence of ILD_0 on the stress response is much weaker than that of the void shape. The ultimate strengths appear nearly independent of the ILD_0 . This weak dependence of the ILD_0 was first discovered by Benson [145], who applied Eulerian FE method to study the effect of the cluster diameter (similar to ILD) on the ultimate stress.

7.3.3. The Porosity Accumulation and Void Shape Evolution

Void growth is one of the principal mechanisms in ductile fracture. From the standpoint of strain gradient plasticity theory, Wu et al. [130] suggested that void with radius of 10nm would stop growing in the maraging steel material. For those MD investigations with porosity accumulation reported [37, 154], voids of radius ranging from 0.5-5 nm show continued growth up to 3-10 times its initial size depending on the applied strain and other influential factors. However, this discrepancy is plausible given the difference between the two approaches. The loading in MD simulation is usually strain-controlled with high strain rate, while the dynamic loading in the work of Wu et al. [130] is stress-controlled. As a piece of work based on continuum theory, Wu et al. [130] wisely reflected the length scale effect by comparing the characteristic length associated with thermal diffusion. In the MD approach, the size scale effect comes from characterizing the lattice atoms with their interactions described by the EAM potential. Thus the different way to reflect the length scale effect is also a contributor to the different void growth patterns under high strain regime.

It has been acknowledged by the FE investigation that the initial void shape plays an important role in the porosity accumulation during the loading [43, 47]. Their researches indicate that the prolate void considerably elevates the porosity level compared to the oblate void, which is qualitatively consistent with our MD simulation. However, the discrepancy induced by the initial void shapes is relatively weaker compared to the FE results. The advantage of MD simulation is its ability to capture the dislocation behavior induced by the presence of nanovoids and dislocation-void interaction on void growth. The inelastic deformation follows the onset of dislocation emission and the rapid void growth occurs shortly after.

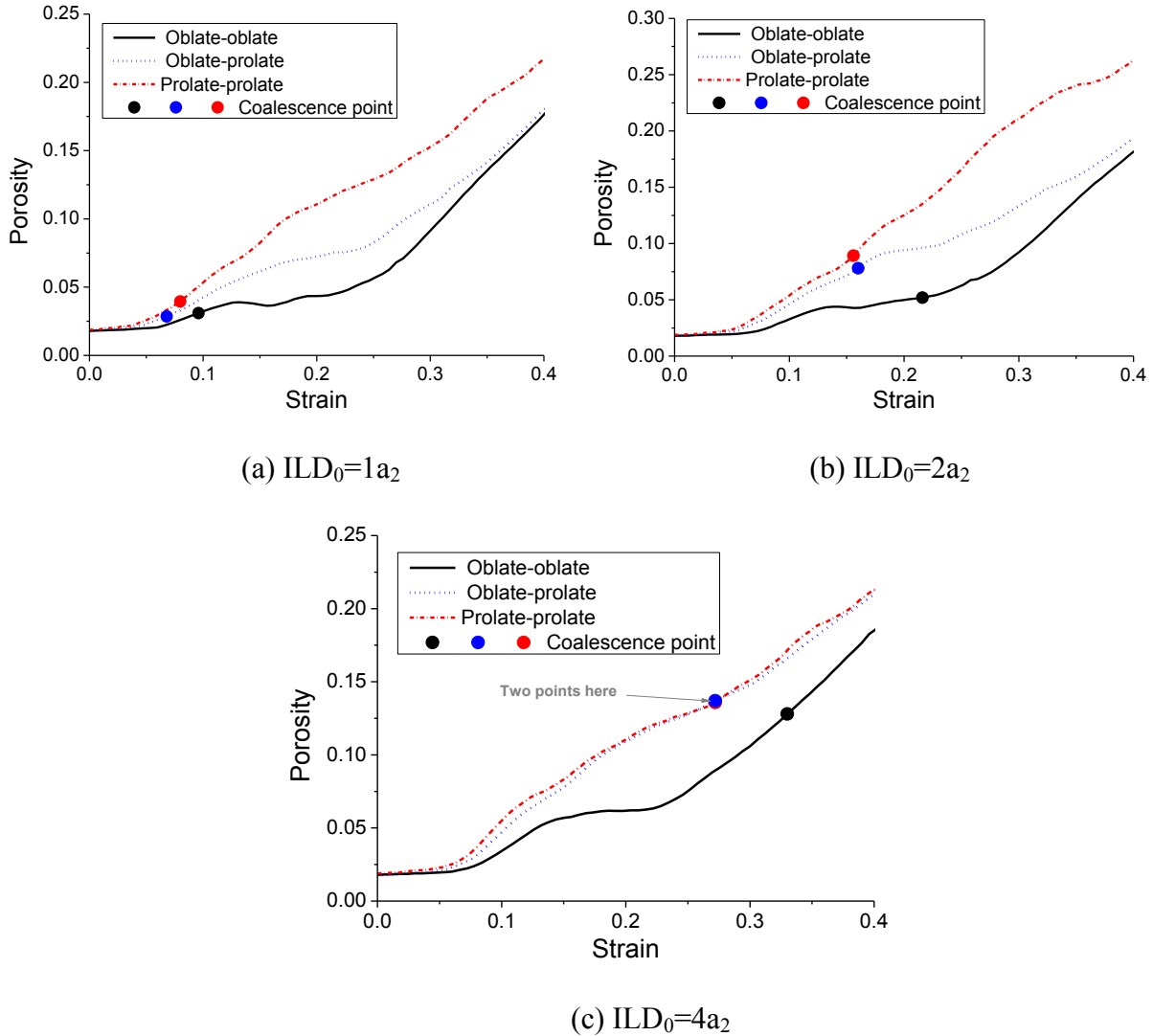
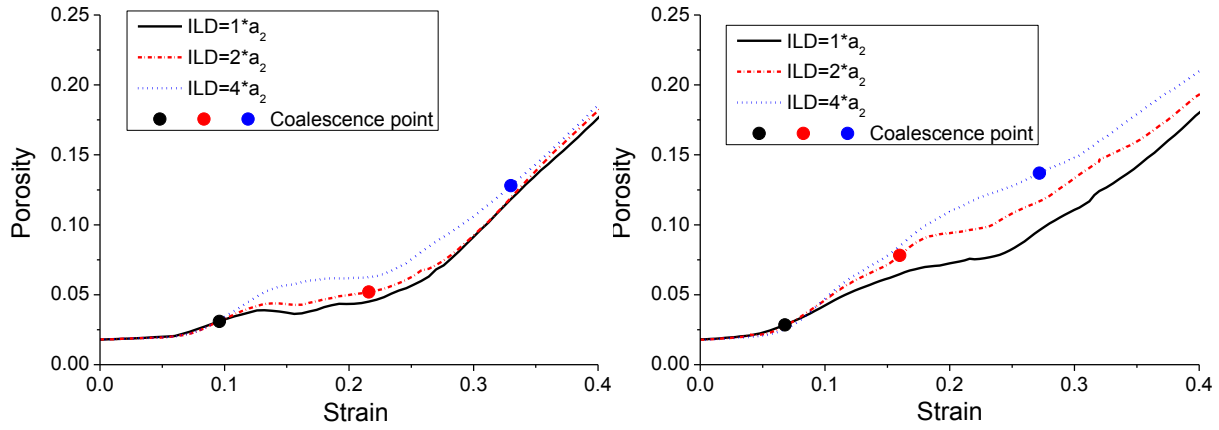


Figure 7.9: Porosity evolution reflecting the influence of void shape combination.

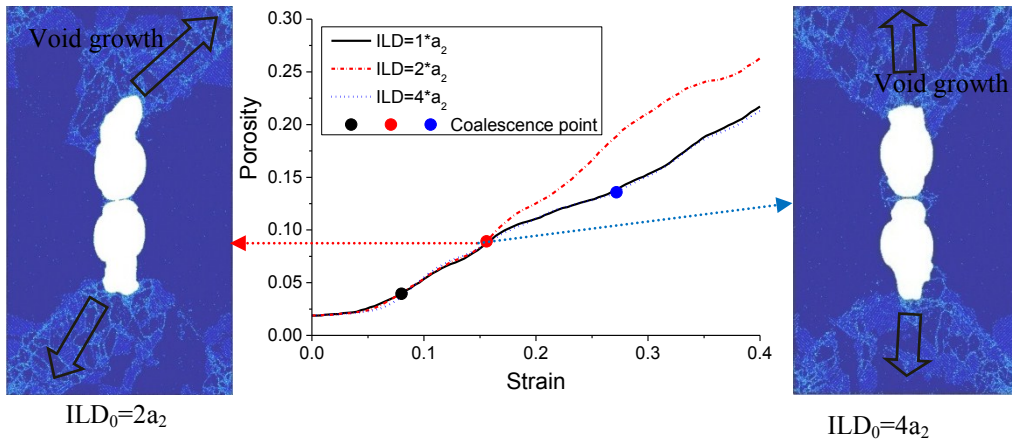
Figures 7.9a-c reveal that the prolate void shape tends to raise the porosity level of the two-void system. It is reasonable for the oblate-prolate case to be bounded by the other two cases, since it contains both oblate and prolate voids. However, it depends on ILD_0 whether the oblate-prolate combination is close to the oblate-oblate or the prolate-prolate case. From Figure 7.9a to Figure 7.9c, the oblate-prolate curve gradually shifts from about the average of the other two cases to nearly the same as the prolate-prolate case. This feature could be explained by the weakening of the clustering effect. When the ILD_0 is small, the void interaction is dominant and

thus makes the oblate-prolate combination about the average of the other two cases. However, as ILD_0 gets larger and larger, the growth of the prolate void becomes dominant over the weakened clustering effect. Also, the symmetric development of the dislocation pattern of the prolate-prolate combination with $ILD_0=4a_2$ reduces the potential porosity increase compared to the highly asymmetric dislocation in the case with $ILD_0=2a_2$ (see Figure 7.10c).



(a) Oblate-oblate

(b) Oblate-prolate



(c) Prolate-prolate

Figure 7.10: Porosity evolution to reflect the influence of ILD_0 .

Except for the prolate-prolate case with $ILD_0=2a_2$, the porosity accumulation proceeds without a sudden change induced by the void coalescence. Although ILD_0 has a minimal influence on the stress-strain curves as shown in Figures 7.8a-c, Figures 7.10a-c reveal that ILD_0 induces a notable difference during the porosity accumulations. In Figures 7.10a and b, a larger ILD_0 results in a higher porosity level. One reason is that the void easily gains more volume away from its nearest neighbor because of more spacing. It appears that the competition of gaining size in the intervoid area leads to the retarded local accumulation of the porosity there. However, Figure 7.10c is an exception. The porosity curve of the case $ILD_0=2a_2$, rather than the case $ILD_0=4a_2$, turns out to be the largest one after its coalescence point. Yet, we could find an explanation in the corresponding CPC plots. The CPC plot of the case $ILD_0=2a_2$ at its coalescence point exhibits a quite asymmetric dislocation pattern (see the left subfigure in Figure 7.10c), which links the upper prolate void through the upper-right corner of the periodic simulation box to the lower-left part of the lower prolate void. In contrast, the CPC plot of the case $ILD_0=4a_2$ at the same strain shows a more symmetric dislocation pattern (see the right subfigure in Figure 7.10c). The asymmetric dislocation pattern of the case $ILD_0=2a_2$ means the potential growth path of the upper and lower void is along the diagonal direction. Just as the void tends to grow more away from its nearest neighbor, the diagonal growth pattern provides more spacing such that the porosity accumulation is accelerated. Recalling Figure 7.8c, the stress response of this case is also considerably reduced after the coalescence point because of this asymmetric dislocation pattern.

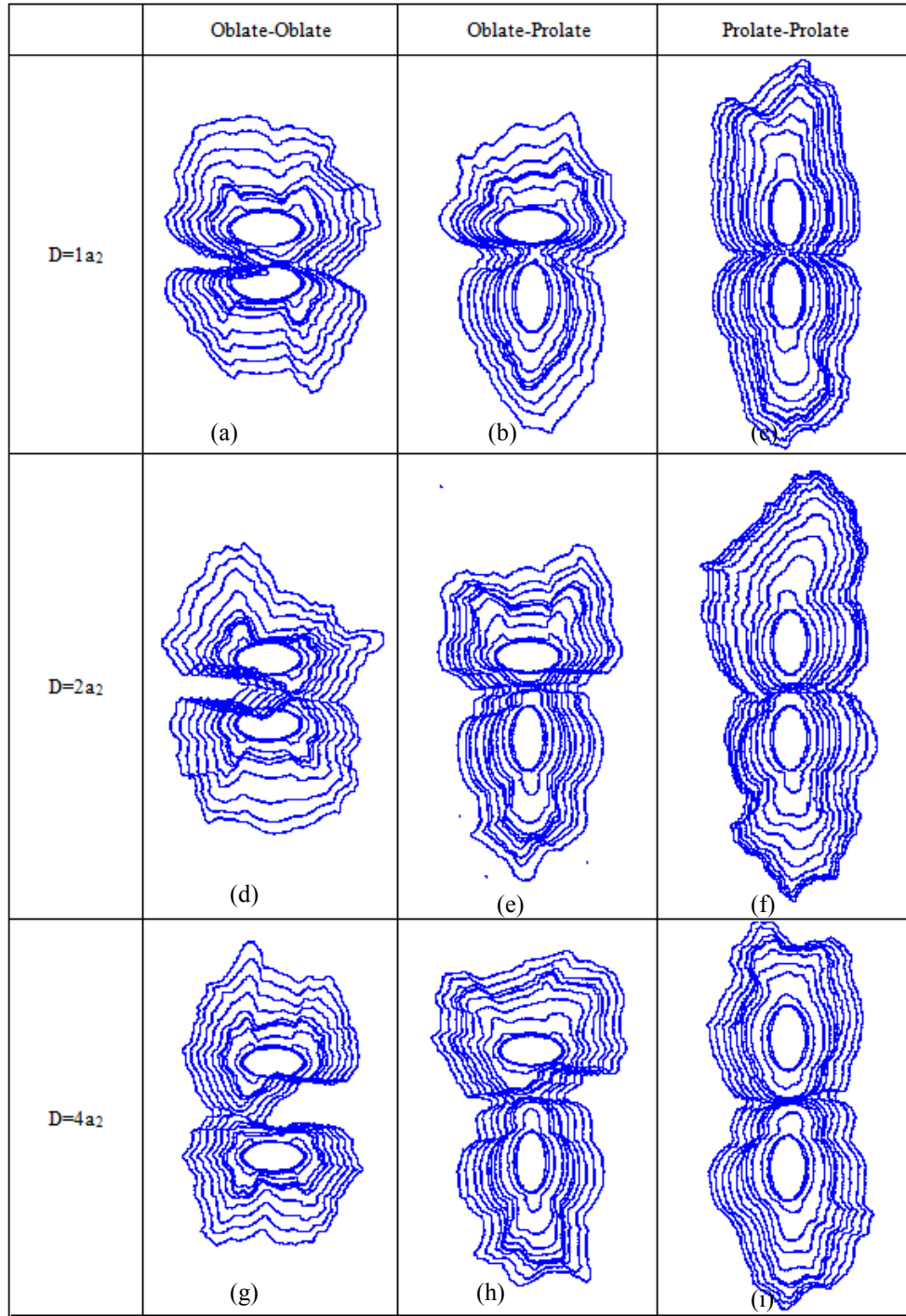


Figure 7.11: The void shape evolution of each specimen.

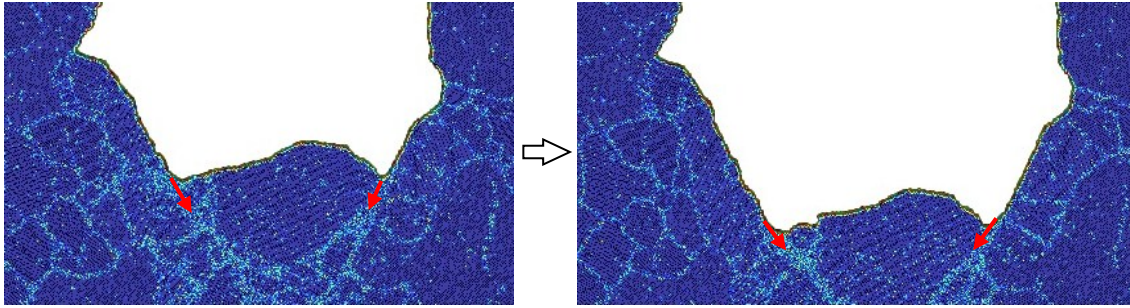


Figure 7.12: The gliding of the material along the dislocations to grow the void.

The shape of the nanovoid evolves during the continued deformation. We draw the void shape every 0.04 strain in Figure 7.11 according to the CPC plots. The individual void growth pattern, no matter which void shape combination it belongs to, is strongly influenced by its initial shape. For the oblate shape, double cleavages form at the dislocation emission site on the surface of the side away from its neighbor. For the prolate void, only one cleavage initiates on each side of the void surface due to the contiguity of the dislocation emission sites (see Figure 7.5f). However, for all the void shape combinations, only one cleavage forms at the intervoid area. Once the dominant cleavage initiates at the intervoid area, the other potential cleavage is inhibited at the incubation stage for the oblate void. Another notable feature in Figure 7.11 is that the individual void tends to grow away from its nearest neighbor because of more spacing available. By comparison, there is considerably less void growth at the middle line of the two-void system, where far less disordered atoms are found. The overlapped void shape contours in Figures 7.11a, d and g indicate that some part of the voided area could undergo shrinkage rather than expansion during the deformation. The growth of the nanovoids is found tightly associated with dislocations. Figure 7.12 illustrates a typical way of material transport by gliding along the lines with high density of dislocations. In the dislocation-free area on the void surface, the local void shape is found preserved during void growth.

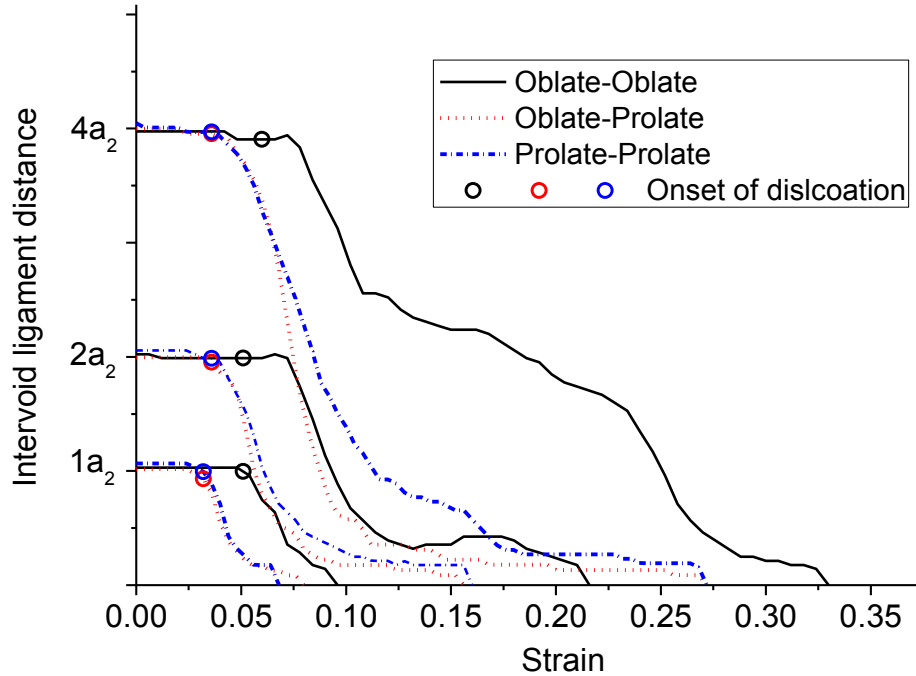


Figure 7.13: The shrinkage of the ILD during the deformation.

The ILD shrinkage curves of the specimens are plotted versus the increasing strain in Figure 7.13. Apart from the oblate-oblate void combination with $ILD_0=2a_2$ and $ILD_0=4a_2$, the onset of dislocation reduces the ILD immediately. For all the cases, the ILD shrinks faster in the initial period than near the coalescence. During the inelastic regime, the ILD shrinkage pace is subject to its initial value. For the smallest ILD_0 cases, the intervoid ligaments fracture shortly once they begin to shrink. As for the void shape influence, the oblate-oblate combination postpones the interlinkage of the voids, while there is relatively small difference between the oblate-prolate and the prolate-prolate cases. This finding can be explained by Figures 7.5d and g that the oblate void induces a dislocation emission pattern away from the ligament area and lack of immediate intervoid interaction once the ILD_0 is bigger than $1a_2$. For the larger ILD_0 , the neighboring nanovoids keep expanding with a very thin and yet not fractured intervoid ligament, as illustrated in both the left and right CPC plots in Figure 7.10c. For the MD simulation of void coalescence

in 3D, larger ILD_0 also results in a delayed intervoid ligament fracture before the complete void coalescence [136].

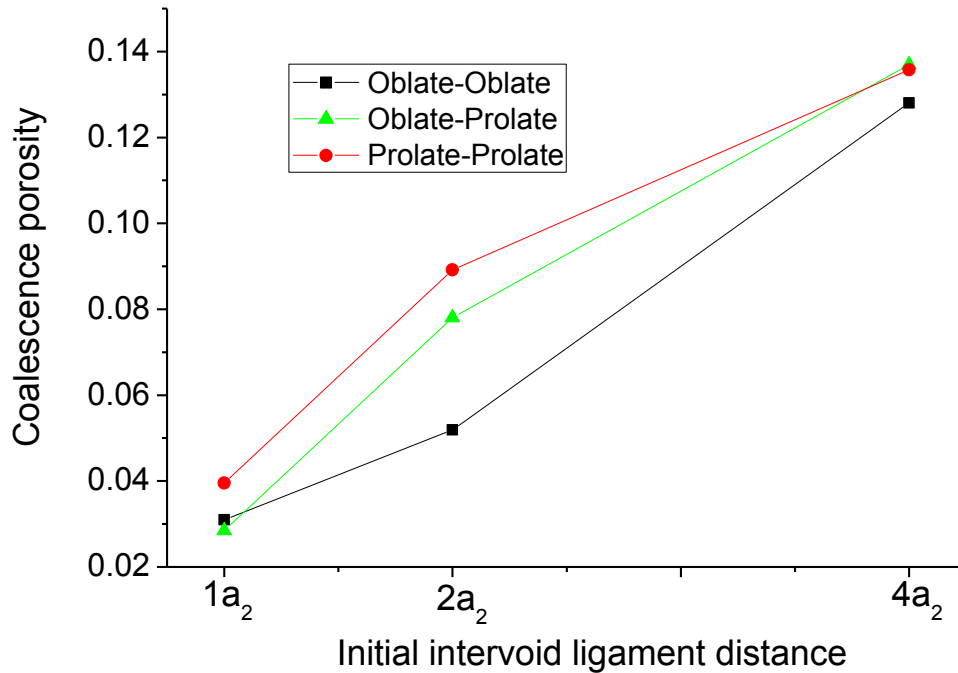


Figure 7.14: The effect of ILD_0 and void shape combination on the coalescence porosity.

The coalescence porosity, at which the intervoid ligament completely breaks, increases as the ILD_0 increases, as shown in Figure 7.14. With more spacing separating the neighboring two voids, it takes a larger strain for the coalescence to take place and therefore results in higher critical coalescence porosity. As shown in Figure 7.13, the retarded intervoid ligament fracture due to the large ILD_0 enables porosity accumulation to proceed to a higher level. In literature, a critical value of porosity is often used to predict the onset of void coalescence [3]. The results in Figure 7.14 reveal that this criterion for coalescence appears acceptable with certain ILD_0 . However, the critical porosity, as a macroscopic indicator, is not enough to determine the coalescence point for $ILD_0=2a_2$. The shape of void and the combination of different void shapes must be taken into consideration.

7.4. Conclusions

The dislocation emission and dislocation-void interaction have been studied by means of MD simulation to investigate the influence of the interaction between elliptical voids. Computation geometries with different void shape combinations and void spacings are applied in the simulation. The material response, porosity accumulation and void shape evolution are monitored during the continued loading. The main conclusions are drawn below.

1. The onset strain of dislocation emission is mainly determined by the initial void shape. The prolate void within the two-void system effectively reduces the strain required to trigger dislocation emission. The pattern of emitted dislocations is not only subject to the initial void shape but also ILD_0 . The dislocation emission of the oblate void is prone to be inhibited and disturbed at the side facing its neighbor, while it is the opposite for the prolate void.

2. Given the same ILD_0 , the void shape combination highly affects the stress response throughout the loading period. In contrast, given the same void shape combination, ILD_0 has just limited influence on the ultimate stress.

3. The void shape combination has significant influence on the porosity accumulation as well as void shape evolution. The CPC plots reveal that the asymmetric dislocation leads to asymmetric void growth, which effectively elevates the porosity level because of more spacing and could be more influential than ILD_0 . As for the void shape evolution, one typical pattern is the material transport along the lines with high density of dislocations. The initial void shape results in different cleavage pattern growing away from its nearest neighbor. The ILD shrinks faster in the initial stage and void coalescence could be considerably delayed by increasing the ILD_0 . The coalescence porosity appears to be an acceptable criterion with the ILD_0 under some

certain simulation condition concerned here. Notably, the conclusion drawn here is restricted to the cases of ILD_0 comparable to the initial void size. It is likely that ILD may play a critical role when dealing with very thin ILD_0 or thin post-loading ILD. Take Figure 7.7 for example, the ligaments become infinitesimally thin right before the coalescence points as marked in solid circles on the curves. Of all the nine stress curves, five decrease while the rest four increase before the complete fracture of the ligament. This implies that the corresponding stress state is also an influential factor when it comes to the case of very thin post-loading ILD. Hence, future systematic investigation on the void geometry with very thin ILD would be helpful to further explore the mechanism regarding void coalescence.

Chapter 8: Simulation of Nanoporous Metal with Pores Mimicking

Crystalline Arrays*

8.1. Introduction

Nanoporous materials, as a type of topological, functional nanomaterials, are emerging as strong versatile candidates with great potential in diverse applications. The inner morphology of nanoporous materials, which is the very feature to distinguish them from traditional bulk materials, can be tailored for different needs. For example, bi-continuous nanoporous metal foam, whose inner morphology reassembles a forest of nanowires, exhibit a high specific strength. The scaling law of its ligament size echoes the dogma in nanoscience “the smaller, the stronger”. Their high surface-to-volume ratio can provide more active area for reactant molecules and improve the electron mobility with solid ligaments [8-10]. Other possible applications and advantages include electrochemical sensor, energy conversion/storage system [8, 11, 12], exceptional mechanical properties with light weight [6, 13] and radiation resistance [6]. Extensive research achievements have been accumulated over the decade for bi-continuous nanoporous metal, from experimental investigation to atomistic simulation [121, 168-171]. Some recent works have focused on stress analysis of ordered nanoporous geometries such as diamond-lattice-arranged ball-and-stick structure [172] or gyroid structure [173] and compared them with disordered structures. These ideal inner structures help to examine the optimization of stress response and shed light on the novel design of nanoporous structure. Yet, the current fabrication technique limits the realistic design to only a few types of highly-ordered structures

* A version of this chapter of this thesis is submitted as Cui, Y.; Chen, Z. Simulation of nanoporous metals under compression with pores mimicking crystalline arrays: Towards stronger designs.

such as those mimicking typical crystalline arrays [174]. The crystalline-arrays-mimicking nanoporous structures are therefore our focus in this report.

Although the synthesis of ordered nanoporous metals and its rational design can be challenged by the physical need to minimize surface area in metal [174], a few advanced strategies have been invented to design and tailor pore structures of nanoporous metals [175-178]. The template-based synthesis of ordered nanoporous materials involves key steps such as template-choosing, target precursors-filling and template-removing [174]. Various nanoporous metals including Au, Pt, Ni, Cu, Co and Ag have been fabricated via the approach of hard template-based synthesis [179]. The structured pores arrangement is attributed to the self-assembly of the crystal template, which can be repeated both on the surface and throughout the bulk [180]. Through the self-assembly technique, nanopores have been structured into hexagonally close-packed, face-centered cubic (also referred as cubic close-packed) and body-centered cubic arrays [181, 182]. Apart from these structures, crystalline array such as the diamond structure is one of the most desirable structures to produce photonic crystal since its three-dimensional, complete photonic band gap could efficiently diffract light [183]. Indeed, nanoporous metals with highly-ordered array and narrow pore-size distribution are of particular interest for a wide range of important potential applications [174]. Promisingly, the self-assembly of patchy particles into diamond structures through molecular mimicry has been suggested feasible [184]. Among all the potential advantages of tailored nanoporous structure, the focus in this chapter would be the mechanical performance. Even not for load-carrying duty, the structural integrity of nanoporous metal is important since the otherwise altered inner morphology during its service could affect, for instance, its photonic and catalytic properties. During loading, the onset of plasticity is crucial since it has a great impact in the stress response

of material and triggers dislocation emission. The yield behavior is utterly important here for two reasons. First, despite being a brittle material macroscopically, the bi-continuous, nanoporous metal features concentrated plastic deformation at ligaments [185, 186]. In fact, the yield stress of bi-continuous, nanoporous metal has been extensively focused and highlighted in both experimental and simulation studies [13, 121, 168, 170, 187, 188]. Second, the mechanical test of crystalline-arrays-mimicking nanoporous metal has not yet been reported to our best knowledge. At the very least, nanoporous metals [129, 162] with random distribution of pores have demonstrated the essential role of geometrically necessary dislocations and we have no reason to presumably ignore their effect here. For the crystalline-arrays-mimicking nanopores, this should rather be a focus to examine. The active sites for dislocation emission such as surface steps and defects also play an important role in catalytic activity of nanoporous metals [121, 189]. Since atomistic simulations of bi-continuous nanoporous metal have shown consistent agreement towards experiment in terms of the mechanical behavior [121, 170, 190], it is then feasible to study the property of new type of orderly-structured nanoporous material.

8.2. Simulation Specifications

Among various metals that can produce nanoporous structure, Cu is here selected as the model material to carry out the atomistic simulation. The Large-scale Atomic/Molecular Massively Parallel Simulator (LAMMPS) is employed. The Mishin embedded-atom-method potential for copper [113] is employed. The simulation box is first filled with FCC copper atoms. The nanoporous structure is then created by removing atoms within spherical regions arranged in either diamond, BCC, FCC or HCP crystalline array. The resulted porosity is shown in Table 8.1, which is close to the estimated porosity ($\approx 78\%$) of real samples [180]. The pore size of different crystalline arrays is made the same (8.315 nm in radius) for all samples. Restricted by the pore

size, the overall size of different sample can only be made close but not the same. The difference is rather insignificant since boundaries of the simulation box are periodic for all the three directions. Once the sample is created, energy minimization is performed by using a conjugate gradient algorithm to attain a minimum energy configuration, followed by a relaxation step of 100 ps at 10 K to reach an equilibrium-state configuration. As shown in Table 8.1, the equilibrated sample size is slightly smaller than its as-created size. During the dynamic run, the uniaxial compressive load at a strain rate of $1 \times 10^8 \text{ s}^{-1}$ is applied at both ends in the z direction with strain-confined lateral boundaries.

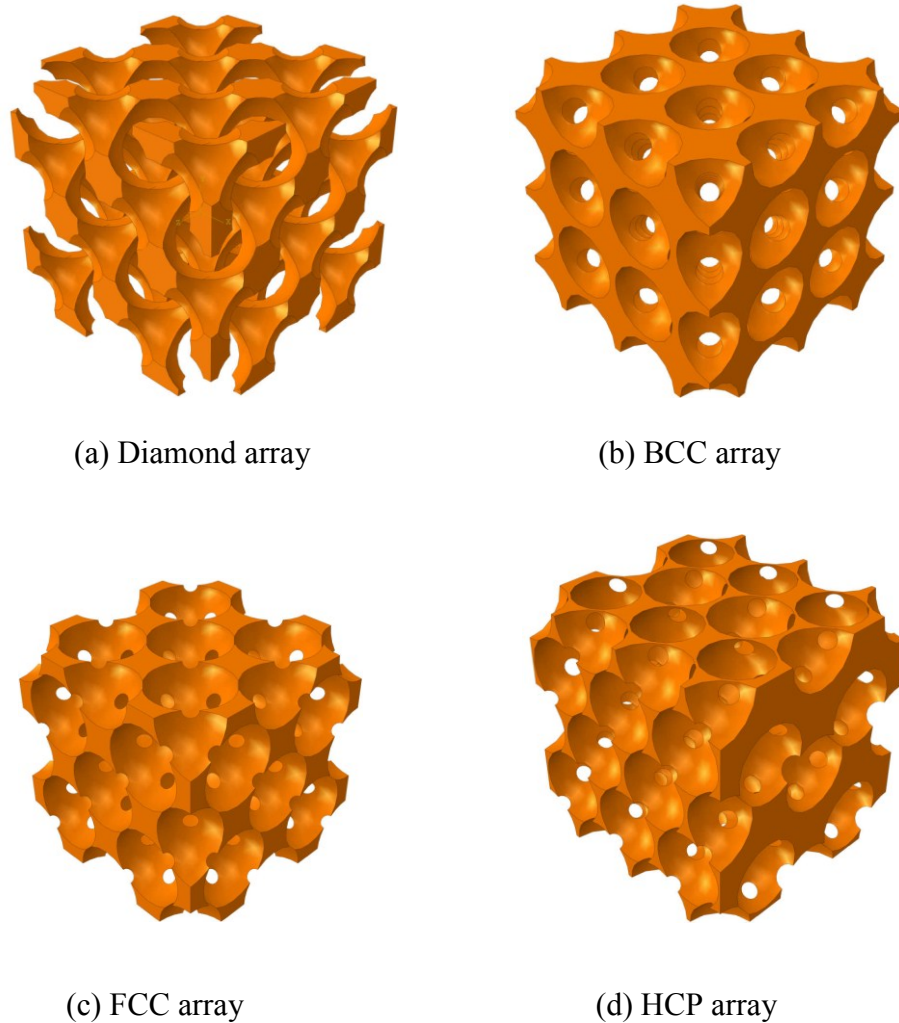


Figure 8.1: Nanoporous copper sample for atomistic simulation and finite element simulation

Table 8.1: Geometry of Nanoporous Copper Samples for Atomistic Simulation

Pore Arrays	Initial porosity	Surface/volume ratio (nm ⁻¹)	As-created sample size (nm)	Equilibrated sample size (nm)
Diamond	77.3%	1.093	52.78×52.78×52.78	52.68×52.67×52.67
BCC	77.4%	1.785	54.95×54.95×54.95	54.58×54.58×54.58
FCC	77.6%	1.983	46.27×46.27×46.27	45.94×45.94×45.94
HCP	77.5%	1.973	52.78×54.59×51.33	52.17×54.25×50.97

8.3. Results and Discussions

8.3.1. The Overall Stress Response

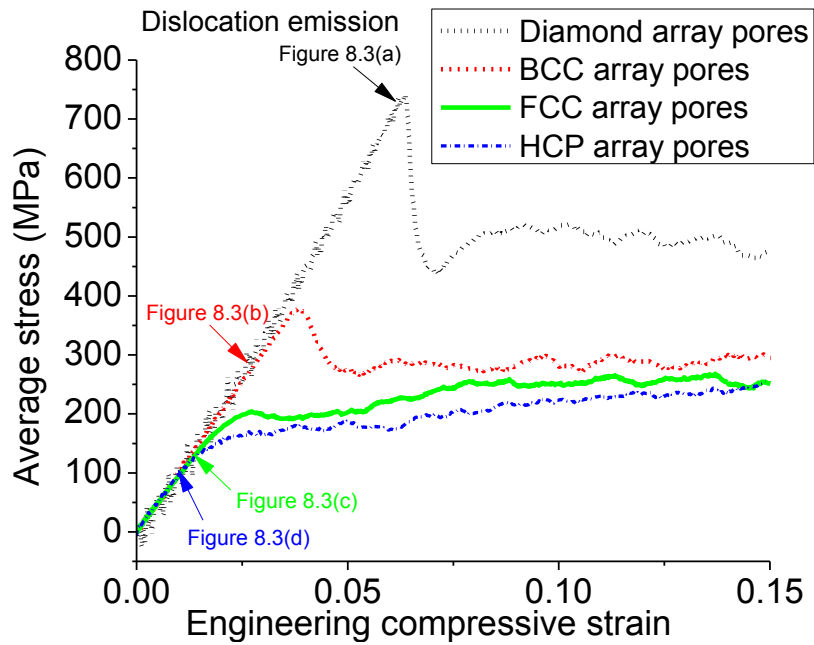


Figure 8.2: Stress-strain relation for different crystalline arrays of pores with the same initial porosity. Colored arrows indicate the start of dislocation emission correspondingly for each sample.

The stress response of nanoporous metal under compression includes three stages: an almost linear elastic regime, a plastic yielding regime and a densification regime [170]. Only the first two stages will be focused here. In Figure 8.2, the diamond-array-pore sample resulted in a superb peak stress. Its yield stress, at which dislocation emission starts, is about 8 times that of the HCP-array-pore sample. Even the BCC-array-pore sample is considerably stronger than the two samples with close-packed pores. As is well known, the high stress of diamond is not only due to its atomic lattice arrangement but also highly associated with its strong covalent bonds. Diamond lattice-mimicked macro-structure is not necessarily granted with high strength. For example, the compressive stress of diamond-oriented cellular metal lattices is found weaker than that of square-oriented ones [191]. Therefore, size effect is involved in the higher-than-expected stress response of diamond-array-pore sample. Elastic moduli of the four samples do not vary much. A strong “yield drop” is observed for the diamond-array-pore sample and a weak one for the BCC-array-pore sample. The yield stresses of the four samples, at which dislocation emission starts, have dramatic difference, which in turn affect the subsequent stress response. Understanding of this difference is non-trivial for the ordered nanoporous material. Unlike ligament size for the bi-continuous nanoporous structure, the characteristic length here appears neither easy to define nor readily to measure. Due to higher porosities than packing factors, pores of the four samples already overlap with their 1st neighbors. Thus, the inter-pore ligament toward the first neighbor is already below zero, which is certainly not a good indicator for length scale. One alternative is perhaps the averaged inter-pore distance over a number of neighboring pores. For example, the averaged inter-pore distance with up to 5th neighbors measures 5.88 nm for the diamond array pores and 10.78 nm for the HCP array pores. It is true that the shorter one

leads to a much higher yield stress, yet this distance is not a rigorous length scale as it concerns the number of neighbors in averaging.

8.3.2. The Onset of Dislocation Emission and the Comparison of Yield Stresses

As summarized by Farkas et al. [121], the highly concentrated plastic deformation is the origin of the macroscopic brittle behavior for nanoporous metal such as nanoporous Au foam [185, 186]. Indeed, yield behavior and its scaling law of bi-continuous nanoporous have been hot topics over the decade [13, 121, 168, 170, 187, 188]. Predicting yield stress can also help ensure an unaltered inner morphology which is important for photonic or catalytic function, given that elastic deformation below the yield level is totally recoverable. Another realistic consideration is the size limit imposed by MD simulation, which only allows us to capture the localized ductile behavior instead of macroscopic brittle behavior [121].

Next, we examine the atomistic snapshots for dislocation emission. Figure 8.3 shows the first ever dislocation emitted from each porous sample. The $\{1\ 1\ 1\}$ slip planes with possible twelve slip systems are activated as the primary dislocations for all the samples. This should be distinguished from the initial surface misfit due to narrow overlapping of pores. The prevailing pattern among all the four samples is that the emission of Shockley partial dislocation starts near the intersection of pore surfaces. This is the location where attractions from the two adjacent pore surfaces lessen as they are partly canceled by each other. For the diamond-array-pore sample, this position resembles the ligament in the bi-continuous porous structure, which is known to incubate the localized dislocation emission [121, 170, 190]. For the other three samples, those positions appear difficult to resemble either ligaments or nodes of the bi-continuous counterpart. For stress response, dislocation emission determines the yield stress and

the slope of stress curve is reduced immediately. The onset of dislocation emission marks the start of plastic region among samples and is essential to the ensuing stress response. To better understand this event, a theoretical understanding for simulation results would certainly be helpful.

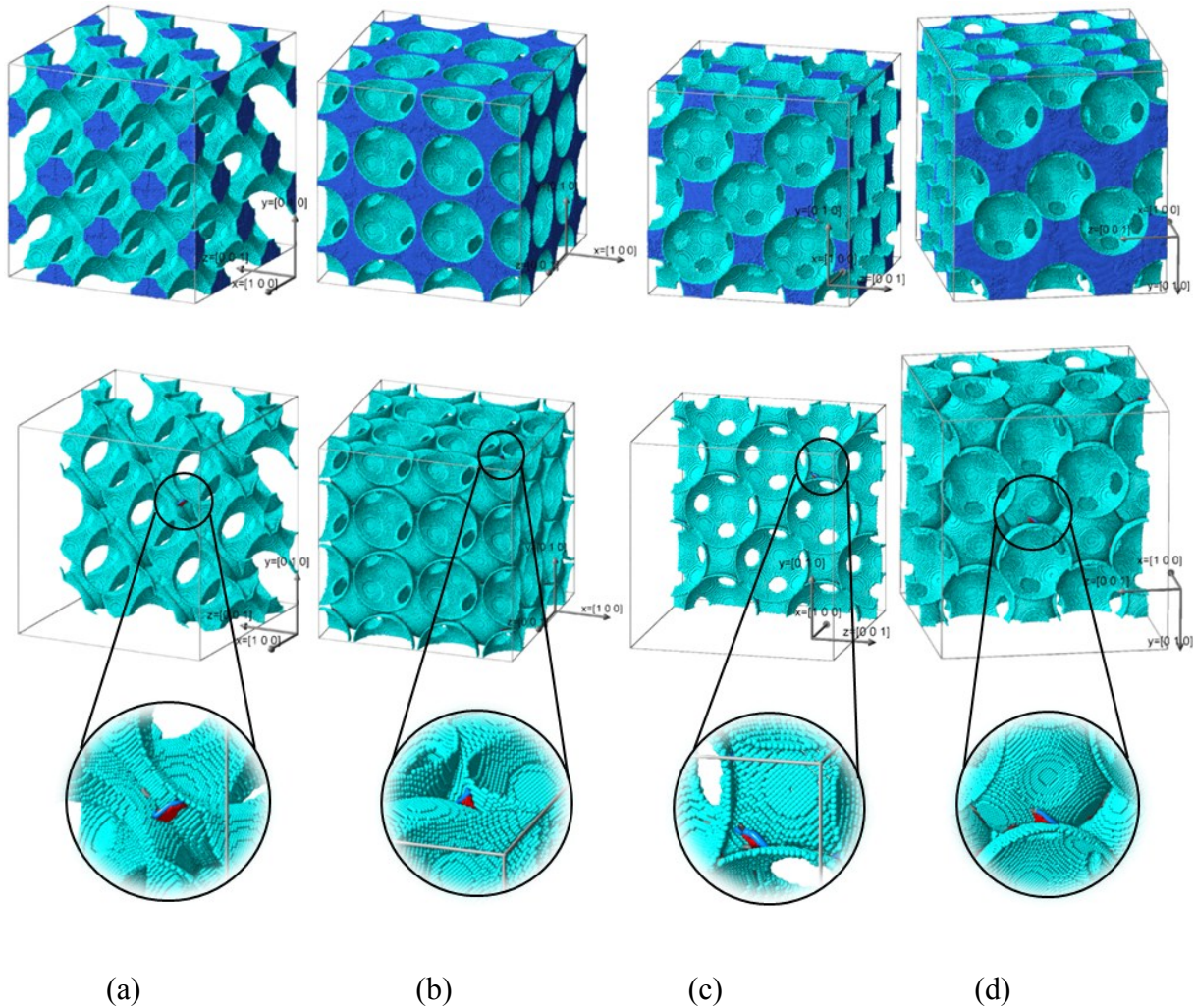


Figure 8.3: Dislocation emissions at the yield point of four samples via atomistic simulation. The post-processing software ATOMVIEWER [85] is employed. Figures (a), (b), (c) and (d) belong to the diamond, BCC, FCC and HCP array of pores, respectively. From up to down show firstly the snapshots with full atoms (bulk atoms in dark blue), secondly the cutting views with

only surface atoms left (in light blue) and thirdly the local magnification (blue rendered curves are Shockley partial dislocations and red atoms represent stacking fault). The corresponding strains are 6.24% for (a), 2.80% for (b), 1.40% for (c) and 1.05% for (d).

For dislocation emission from an isolated void, Lubarda et al. [18, 91] formulated analytical solution for the critical stress and was since widely compared and backed by atomistic simulations [38, 97, 102, 159, 192]. The Lubarda model [18] assumes an infinite-long (in the third direction) dislocation emitted from a 2D circular hole. The key feature of the model is perhaps the introduction of the core cutoff distance $w=pb$, where ρ is typically within the range from 1 to 2. Obviously, the original Lubarda model cannot be directly applied since here involve (1) 3D finite-length dislocation and (2) 3D complex porous geometry. With the finite-length dislocation and the extreme void-void interaction, analytical elastic solution appears impossible. Alternatively, we resort to the mixed analytical/numerical approach. In short, the image stress from pore surfaces is numerically computed based on the analytical solution for dislocations. The exact dislocation configuration, identical geometries and same periodic boundary conditions to the atomistic simulation will be used in the theoretical calculation hereafter. Otherwise, there would be a difference in the overall stress by applying symmetric boundary conditions instead of periodic boundary conditions, as noted by Roschning and Huber [172]. Similar to pre-defined dislocation geometry as assumed in the original Lubarda model [18], the theoretical calculation here adopts the pre-defined dislocation geometry directly from atomistic simulation. After all, the current theoretical focus is to comprehend why dislocation emits at the observed locations, not to probe those locations from scratch.

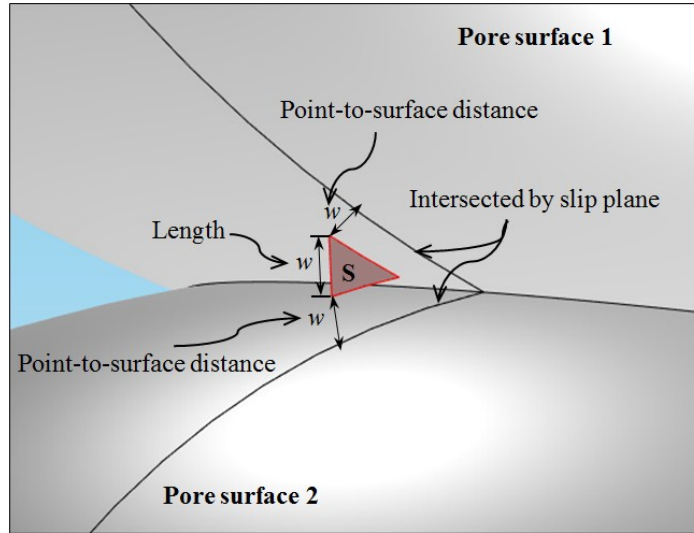


Figure 8.4: 3D Schematic of incipient curved dislocation for the theoretical calculation.

Figure 8.4 illustrates the 3D dislocation geometry for the theoretical calculation. Following the original Lubarda model, the dislocation is assumed to emit at a cutoff distance w away from the pore surfaces. Additionally, we also assume that the incipient dislocation is of w in length. This certainly makes sense since at atomic scale neither could dislocation be infinite close to pore surface nor be infinite short. Those first-ever-appeared dislocations in Figure 8.3 are already longer than w in length. To proceed, we first approximate the dislocation curve as arc by identifying its corresponding radius and circle center. Then, the arc length decreases as we shrink the radius of the circle. Meanwhile, two end points with w away from pore surfaces can be determined for any radius. The finalized arc is with such a radius that not only the inner arc is w in length but also its two ends are w away from pore surfaces like that depicted in Figure 8.4. The slip area S is formed via parallel move of the intersected curves. The finalized dislocation geometries along with Burger vectors measured from atomistic simulations are listed in Table 8.2. Due to the definition of the Burgers vector, the dislocation geometry from atomistic

simulation has been mapped back to the undeformed configuration although the difference should be trivial since the deformations at the moment are still small.

Table 8.2: Finalized Dislocation Geometries for the Theoretical Calculation. The Burgers Vector \mathbf{b} is in the Unit of Lattice Constant. The Parameter ρ is Set as 1 in $w=\rho b$

	Two end points of the arc: (x_1, y_1, z_1) and (x_2, y_2, z_2) (\AA)		Circle Center of arc (\AA)	\mathbf{b}
Diamond	145.728, 169.252, 189.201	145.252, 170.028, 188.041	92.316, 117.866, 176.417	$[1 -1 2]/6$
BCC	488.954, 528.842, 423.791	489.553, 529.442, 422.604	1252.02, -110.636, 484.374	$[1 1 -2]/6$
FCC	394.146, 300.732, 329.316	393.760, 299.953, 330.510	410.789, 285.460, 329.139	$[1 1 -2]/6$
HCP	286.505, 327.896, 259.309	286.915, 327.050, 260.448	334.011, 365.919, 272.941	$[1 -1 2]/6$

Once the dislocation geometry is identified, the stress due to dislocation can be evaluated. We refer to Mura [59] for formulating the stress induced by dislocation. The stress due to dislocation can thus be obtained from the elastic distortion [59]

$$\sigma_{ij}^{dis}(\mathbf{x}) = C_{ijkl} \left[\int_S C_{pqmn} G_{kp,ql}(\mathbf{x} - \mathbf{x}') b_m n_n dS(\mathbf{x}') + b_k n_l \delta(\mathbf{S} - \mathbf{x}) \right], \quad (8.1)$$

where C_{ijkl} is the elastic tensor, \mathbf{b} is the Burgers vector, $G_{kp}(\mathbf{x})$ is the Green function, \mathbf{n} is the normal vector of the slip area S and $\delta(\mathbf{S} - \mathbf{x})$ is the one-dimensional Dirac delta function in the normal direction of S . In practice, the sign of this surface norm is made compatible with the compressive loading. The function $C_{pqmn} G_{ip,qj}(\mathbf{x})$ can be deduced from Mura [59].

$$C_{pqmn} G_{ip,qj}(\mathbf{x}) = -\frac{1}{8\pi(1-\nu)} \left[(1-2\nu) \frac{\delta_{mi}\delta_{nj} + \delta_{ni}\delta_{mj} - \delta_{mn}\delta_{ij}}{|\mathbf{x}|^3} - 3(1-2\nu) \frac{\delta_{mi}x_n x_j + \delta_{ni}x_m x_j - \delta_{mn}x_i x_j}{|\mathbf{x}|^5} \right. \\ \left. + \frac{3(\delta_{mj}x_n x_i + \delta_{nj}x_m x_i + \delta_{ij}x_m x_n)}{|\mathbf{x}|^5} - \frac{15x_m x_n x_i x_j}{|\mathbf{x}|^7} \right] \quad (8.2)$$

The elastic constants applied in calculation are $E=120$ GPa and $\nu=0.33$ for bulk copper. For a complete loop, Eq. (8.1) can be converted into a line integral since the subtraction of plastic distortion leads to the Einstein permutation operator and enables the use of Stokes theorem. Unfortunately, the dislocations involved here are not complete loops and thus Eq. (8.1) cannot be readily converted into such a line integral. This fact also makes the nonsingular dislocation theory with stress expressed in line integral [193] not readily applicable here. In this sense, the cutoff distance can be viewed as an alternative approach to avoid the singularity regarding $|\mathbf{x} - \mathbf{x}'|$ on the denominator in Eq. (8.2). This form of singularity makes the point-to-surface distance better than the point-to-curve distance as the cutoff in a 3D situation (see Figure 8.4). The analytical expression $\sigma_{ij}^{dis}(\mathbf{x})$ is evaluated by numerical surface integration for every point on all the pore surfaces. The numerical integration approach has been validated towards the analytical solution [60] for the case of a circular shear loop. Based on σ^{dis} , we can thus numerically find the image stress σ^{image} via the finite element approach by imposing a zero traction on all the pore surfaces as

$$\boldsymbol{\sigma}^{dis} \cdot \mathbf{n} + \boldsymbol{\sigma}^{image} \cdot \mathbf{n} = \mathbf{0}. \quad (8.3)$$

Here \mathbf{n} represents the unit normal vector of pore surface. Since Eq. (8.3) only involves the surface stress, which is at least w away from the dislocation, the term $b_k n_l \delta(\mathbf{S} - \mathbf{x})$ in Eq. (8.1) can be omitted. Following Lubarda et al. [18], dislocation emission occurs when the gliding

Peach-Koehler force of the external load balances that of the image stress. The Peach-Koehler (P-K) force on the line element of dislocation [57], in a general form, is

$$d\mathbf{F} = (\mathbf{b} \cdot \boldsymbol{\sigma}) \times d\mathbf{l}, \quad (8.4)$$

where $d\mathbf{l}$ is the directed differential line element of the dislocation. By using the unit radial vector \mathbf{e}_r at the arc center, the total gliding force of the extremely short arc due to the image force is approximated as

$$F_{image} = \int_L (\mathbf{b} \cdot \boldsymbol{\sigma}^{image}) \times d\mathbf{l} \cdot \mathbf{e}_r. \quad (8.5)$$

The dislocation emission is assumed to occur once the gliding force F_{image} due to the image stress $\boldsymbol{\sigma}^{image}$ is balanced with the gliding force $F_{external}$ due to the externally applied load [18]

$$F_{external} = \int_L (\mathbf{b} \cdot \boldsymbol{\sigma}^*) \times d\mathbf{l} \cdot \mathbf{e}_r. \quad (8.6)$$

Here $\boldsymbol{\sigma}^*$ is the stress field due to external load with traction-free condition on inner boundaries. The implementation of the above mixed analytical/numerical approach is nontrivial, which involves the lengthy summation over dummy indices, creating the complex geometries and refining the local mesh for convergence, yet the key here is how to solve Eqs. (8.5,8.6) for the critical external load to induce plasticity. Fortunately, Eq. (8.6) is shown to be monotonically increasing with the applied external load. Thus, the critical external load is determined by gradually increasing the strain (the same fashion as in the atomistic simulation) until its resulted gliding force is within a relative error of 1×10^{-4} towards that of the image stress. At this critical external load, the averaged surface stress can be calculated as

$$\sigma^* = \int_{A_z'} \boldsymbol{\sigma}^* \cdot d\mathbf{S} / A_z, \quad (8.7)$$

where A'_z is the actual surface area normal to the applied load and A_z is the nominal one. The nominal area is applied here since the stress from atomistic simulation is averaged over the nominal volume. As seen in Table 8.3, the predicted critical stresses qualitatively agree with the atomistic simulations: both rows are in a descending order from the diamond array pores to the HCP array pores. However, the gliding forces due to the image stress on the dislocation segment are not in such a descending order. For diamond array pores, a lower local gliding force is induced given the even higher external load. This could be somehow associated with the stress concentration effect as geometrical narrowing and sharper corners are overwhelmingly spotted for the FCC and HCP array pores in Figure 8.3. The actual curved dislocations are very close to, but not necessarily an arc, which could be a source of discrepancy between the atomistic simulation and theoretical calculation.

Table 8.3: The Critical Stresses for Dislocation Emission Predicted by Classical Dislocation Theory Compared with those by Atomistic Simulation. The Gliding P-K Force due to Image Stress is Balanced by that due to External Load

	Diamond	BCC	FCC	HCP
The gliding P-K force due to image stress (pN)	22.57	34.90	39.92	29.88
Theoretical critical stresses σ^* (MPa)	605.4	507.5	314.4	117.3
Critical stresses by atomistic simulation (MPa)	735.0	278.2	127.5	95.3

It is obvious that the integrand in Eq. (8.6) can be converted to $\mathbf{b} \cdot \boldsymbol{\sigma}^* \cdot \mathbf{n}$, which is the shear component projected in the Burgers vector's direction. Actually, one can integrate $\mathbf{b} \cdot \boldsymbol{\sigma}^* \cdot \mathbf{n}$ for the work done to derive the Peach-Koehler force in the first place [57].

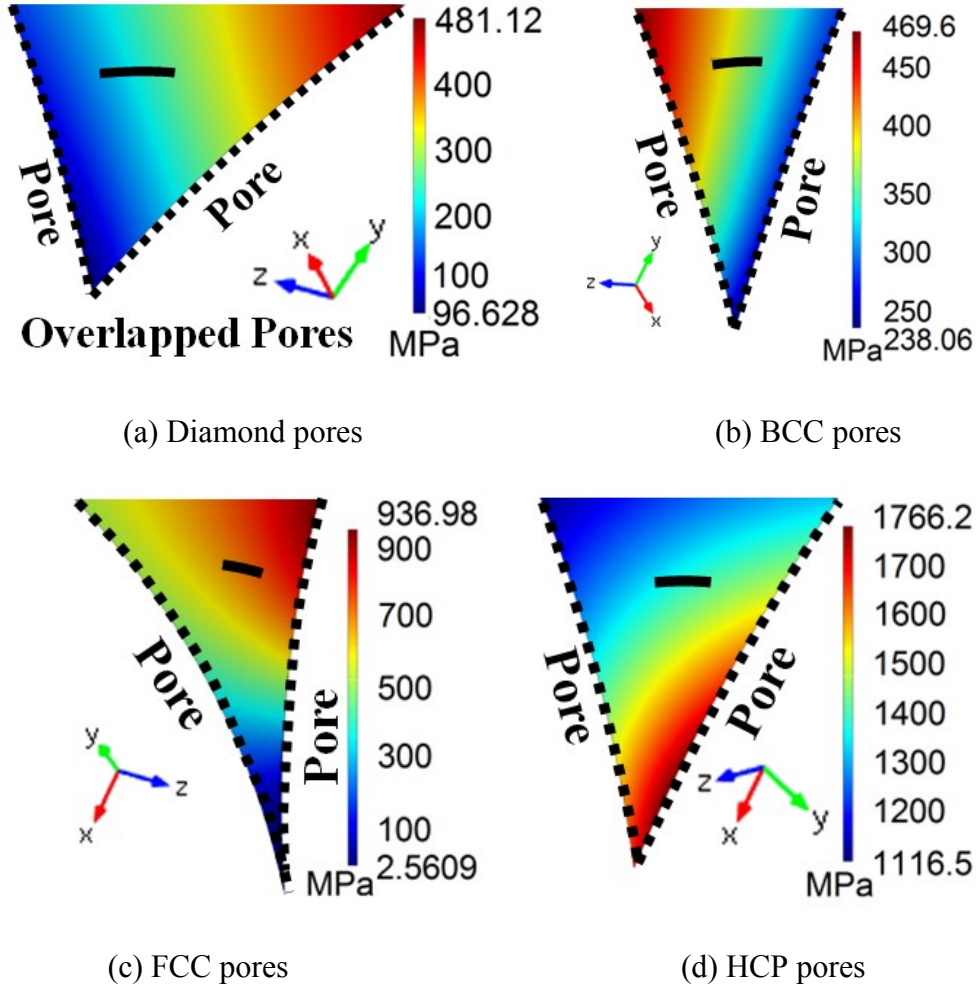


Figure 8.5: Magnitude of the shear component $\mathbf{b} \cdot \boldsymbol{\sigma}^* \cdot \mathbf{n}$ on the slip planes by finite element simulation, where $\boldsymbol{\sigma}^*$ is the stress field induced by remote stress and \mathbf{n} is the unit normal vector of slip plane. The z-direction remote stresses in (a-d) are all controlled to 117.3MPa, same to the critical stress that initiates dislocation emission for the HCP-array-pore sample. The solid black curves inside represent the dislocation segments.

Figure 8.5 shows this shear component computed by finite element method. The applied external stress 117.3MPa to each pore sample in Figure 8.5 is only high enough to trigger dislocation emission for the HCP-array-pore sample according to Table 8.3. The ratio of the maximum shear component (though on the different slip planes) versus the remote stress is the

highest for the HCP-array-pore sample while the lowest for the BCC-array-pore sample. In a sense, this ratio reflects the effective local stress concentration on corresponding slip planes. Besides, the distribution is also quite different from sample to sample. The Diamond-array-pore sample has its dislocation segment away from local maximum shear position while the FCC-array-pore sample has its dislocation segment near the local maximum position. Relative to the P-K force of the image stress, the higher the P-K force from this shear component is, the more likely the dislocation emission will be. With this in mind, it appears that the considerable discrepancy in this shear component (magnitude & distribution) from external load is more dominant in determining the yield stress level than the image stress.

8.3.3. Evolution of Dislocations, Hardening and Early Densification

To investigate the ensuing dislocation evolution, the same cutting planes as Figure 8.3 are used and the same locations for dislocation initiation are circled in Figures 8.6d, g and j to distinguish among multiple dislocations. Figures 8.6a and d correspond to the peak stress point for the diamond-array-pore and BCC-array-pore samples, while Figures 8.6b and e are at the local minimal stresses after falling from the peak stress. Figure 8.6g corresponds to the local maxima after the dislocation emission in its stress response for the FCC-array-pore sample. For comparison, the same strain as in Figure 8.6g is used for Figure 8.6j. Figures 8.6c, f, i and l show the final morphology at the end of loading for all four samples. A half of the final strain 7.8% is adopted in Figures 8.6h and k to view the changing dislocation network.

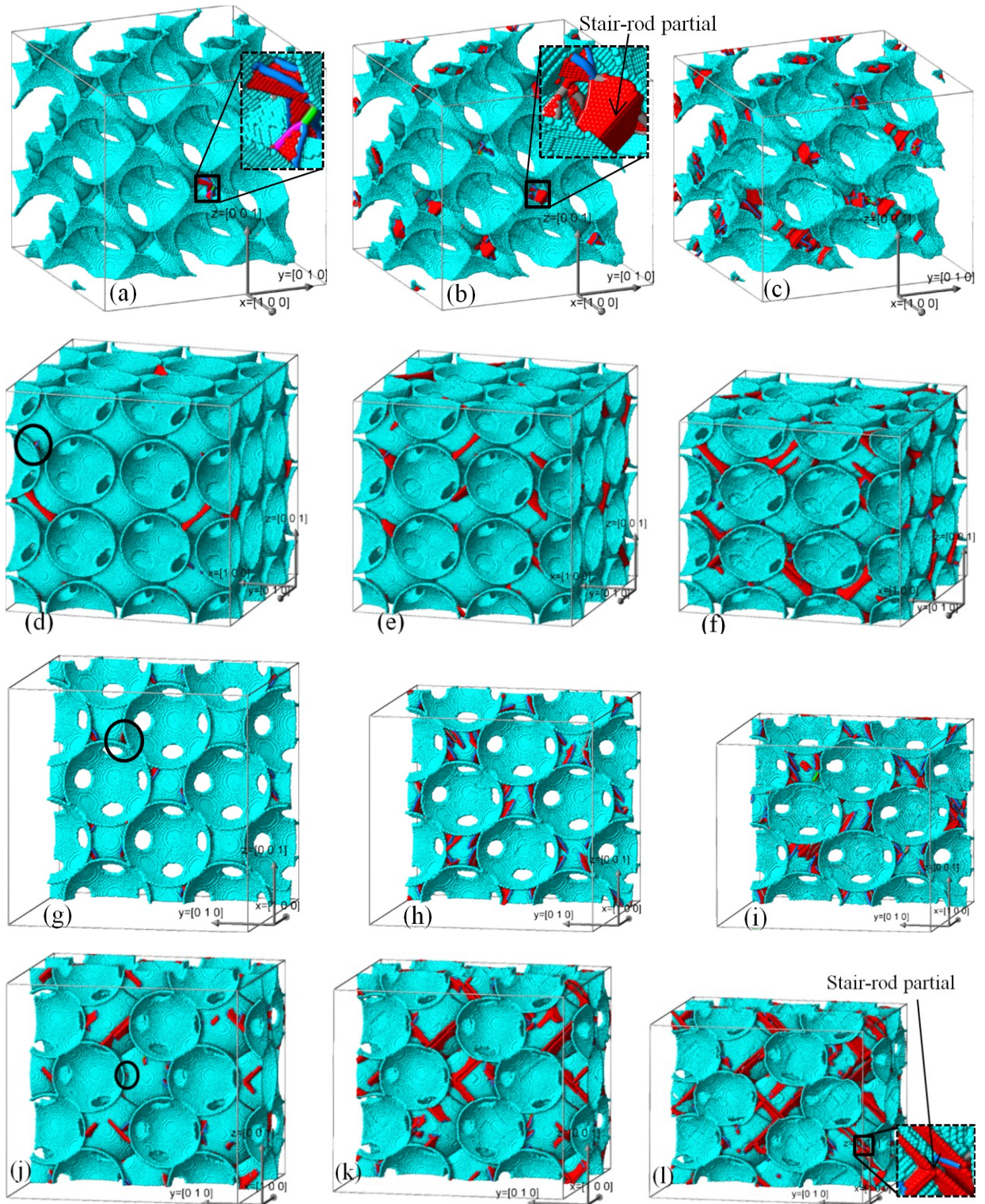


Figure 8.6: Ensuing evolution of dislocation network. Blue, pink, red and green rendered curves present Shockley partial, Frank partial, stair-rod partial and perfect dislocations, respectively.

Red atoms represent stacking fault atoms while blue atoms represent surface atoms. Diamond-array-pore specimen in (a-c) is strained to 6.36%, 7.14% and 15.6%, respectively. BCC-array-pore specimen in (d-f) is strained to 3.83%, 5.30% and 15.6%, respectively. FCC-array-pore specimen in (g-i) is strained to 2.80%, 7.80% and 15.6%, respectively. HCP-array-pore specimen in (j-l) is strained to 2.80%, 7.80% and 15.6%, respectively.

In Figure 8.6, Shockley partial dislocations are observed primarily for all four samples. Both the diamond-array-pore and BCC-array-pore samples have a rapid growth in dislocation population at the beginning of plasticity, similar to the single-void cases [38, 87, 97, 102]. As seen in Figures 8.6a and d, only the previous incipient dislocation curve of the diamond-array-pore has grown in size and even reacted. By comparison, the dislocation population of the other three samples increases at a relatively lower rate after the onset of plasticity and there appears no growth of those incipient dislocations in Figures 8.6g and j. Instead, newly-born dislocations thrive at some other locations. Dislocation reaction is spotted for the diamond-array-pore sample. The relative spacious node (an analogy to the bi-continuous counterpart) of its geometry may have facilitated such dislocation reaction. The Shockley partial and Frank partial in the inset of Figure 8.6a are forming a perfect dislocation. The reaction of Shockley partial and Frank partial to form a perfect dislocation is [49]

$$\frac{a}{3} [1 \bar{1} 1] + \frac{a}{6} [\bar{2} \bar{1} 1] \rightarrow \frac{a}{2} [0 \bar{1} 1], \quad (8.8)$$

where a is the lattice constant. The energy criterion does not specify the direction of this reaction since apparently $a^2/3 + a^2/6 = a^2/2$. The intersection of the stacking fault ribbons in the two different slip planes forms a stair-rod partial dislocation as seen in the inset of Figure 8.6b. The observed obtuse angle between the two intersected slip planes is related to the resultant vector of

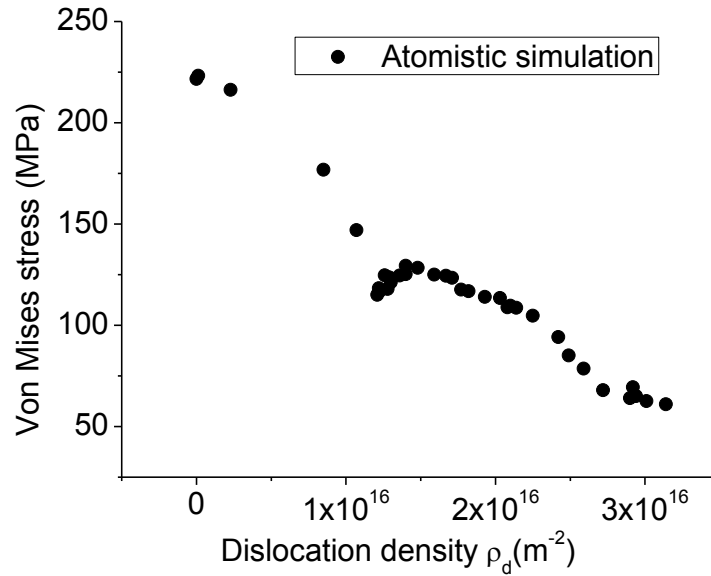
the reaction [135]. Since the Burgers vector of the stair-rod partial does not lie in either of the two intersected planes, it cannot glide along these planes and thus becomes sessile [135]. This sessile arrangement of such dislocations acts as a strong barrier to further gliding. Similar stair-rod partial is also spotted in Figure 8.6l as the joint of intersected planes stops the lower slip plane from moving upward. The formation of sessile stair-rod partial could be a reason for the stress to recover from the local minima as in Figure 8.6b, since it can harden the material by acting as a barrier to free movement of dislocations [135]. As seen from Figure 8.6, dislocations are continuously emitted and absorbed by surfaces of the four nanoporous samples, which results in constantly-changing dislocation networks.

Ruestes et al. [170] reported a significant hardening behavior of bi-continuous Au nanoporous foam: an initial power law of 0.5 at the low-strain regime and a later power law of 1.5 at the high-strain regime. However, for randomly-distributed nanopores with a lower porosity (~4%), atomistic simulation [162] showed an extremely short period of hardening right after the yield point, which is similar to the single-void cases. It then appears interesting to examine our case here, which features orderly-arranged pores yet with high porosity comparable to that of the bi-continuous nanoporous foam. The simple Taylor hardening law reads [194]

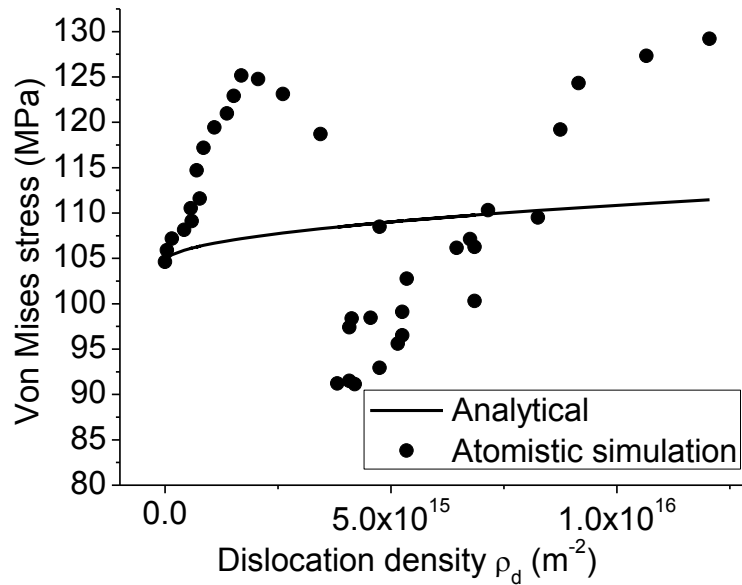
$$\sigma = C + K \cdot G \cdot b \cdot \rho_d^{1/2} \quad (8.9)$$

where C is a constant, K is a related coefficient, G is the shear modulus of copper, b is the magnitude of Burgers vector and ρ_d is the density of generated primary dislocations after dislocation emission. Since our primary dislocations are Shockley partials, $b=1.48\text{\AA}$ is chosen. Typically, K is about 0.25 for a bulk dislocation densities around 10^{16}m^{-2} [162, 195]. Since nanoporous metal with extreme high porosity is involved along with an ultra-high strain rate

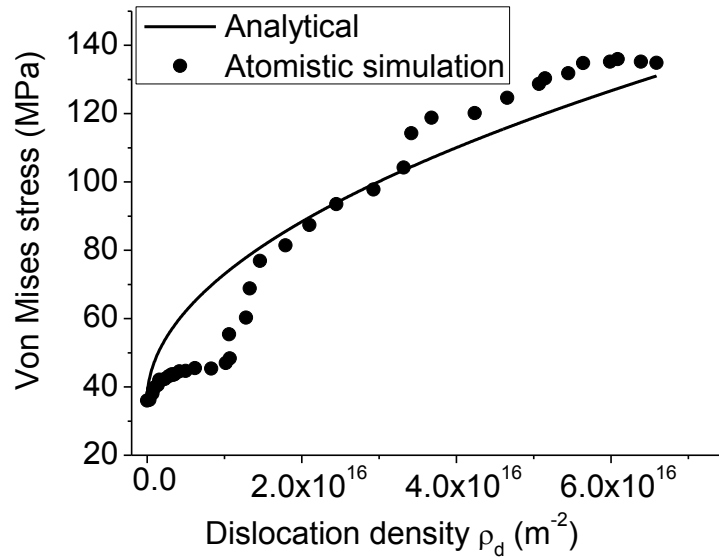
applied in the atomistic simulation, we prefer to leave K here as a fitting parameter. Following the Ludwik's equation, the constant C in Eq. (8.9) is set as the yield stress to impose the continuity. Figure 8.7 shows the simulated hardening behavior versus the Taylor hardening law for the samples (except for diamond-array-pore sample).



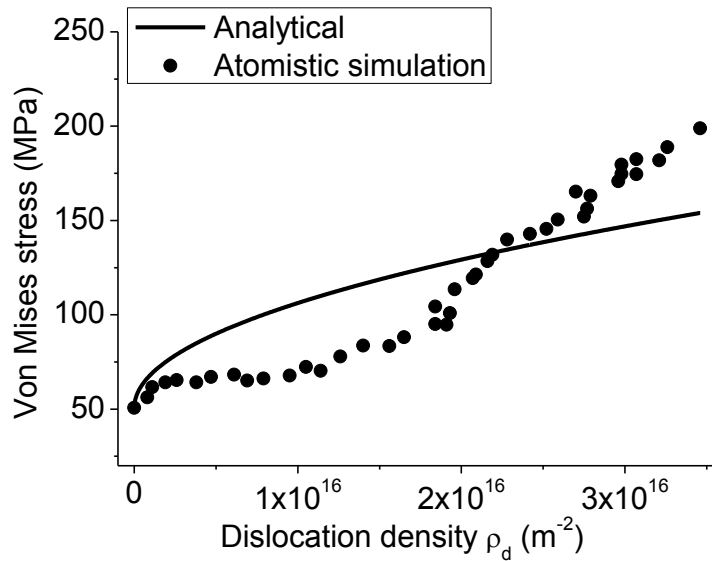
(a) Diamond-array pores



(b) BCC-array pores



(c) FCC-array pores



(d) HCP-array pores

Figure 8.7: Flow stress versus accumulated dislocation density since dislocation emission. Since the strain increment is even, wider horizontal gap between points indicates faster-pace increase in the dislocation density.

Overall, the calculated dislocation density here is close to that reported for the bi-continuous one ($\sim 5 \times 10^{16} \text{ m}^{-2}$ at 0.2 compressive strain) [170], but lower than that for the case with sparsely-distributed voids ($\sim 1 \times 10^{17} \text{ m}^{-2}$ at 0.2 compressive strain) [162]. For the diamond-array-pore sample, it only shows a hardening within an extreme short range right after onset of plasticity, similar to the case with sparsely-distributed random voids [162]. The stress recovered from the local minima around 100 MPa in Figure 8.7a can be attributed to the formation of stair-rod partial as seen in Figure 8.6b. For the BCC-array-pore sample, the fitted K is 0.0088, which is much smaller than the value 0.25 for bulk materials. Figure 8.7b along with Figure 8.2 show a slightly longer strain hardening for the BCC-array pores compared with diamond-array pores. However, a stronger strain hardening effect is observed beyond a dislocation density of $5 \times 10^{15} \text{ m}^{-2}$ in Figure 8.7b. For the rest two samples, the fitted K equals 0.0523 and 0.0784 respectively, which is considerably smaller than the value 0.25 for bulk materials. Their hardening effect is throughout the loading period since the onset of plasticity. This difference among four samples might be explained by the spacing at nodes (an analogy to the bi-continuous counterpart). The close-packing feature of FCC and HCP structure reduces the spacing at nodes and thus limits the dislocation motion (also some contribution from formed sessile dislocations). The diamond structure, with a much smaller packing factor, leaves more spacing at nodes and is thus much harder to limit dislocation motion. The BCC structure, as a non-close-packing structure but with considerably higher packing factor, is in between the two.

Under compression, significant densification ($\sim 40\%$) was observed at a strain of 0.7 for nanoporous Au foams by atomistic simulation [170], similar to the classical understanding for porous foam [196]. Although the applied maximum strain here is relatively small (primarily to capture the yield behavior), early densification is yet observable in Figure 8.8. Porosity of the

strained sample is calculated by first meshing the simulation box into small grids (close in size to the lattice constant) and then counting the voided volume [192, 197]. Due to the strain-confined lateral boundaries, the decrease rate of pore volume fraction here ($\sim 4\%$) over a span of 0.15 strain is about twice higher than that using a barostat ($\sim 4\%$) over a span of 0.3 strain [121]. Figures 8.6c, f, i and l show that pores become oblate at the end of loading, yet without collapsing. In Figure 8.8, no strong correlation is found between the dislocation emission and porosity level, different from the single-void case [192]. It is speculated that mass transfer is restrained due to the missing large dislocation structure as observed in [192], which cannot be formed at nodes due to limited spacing. Conservative motion instead of formation of dislocations will not contribute to the void shrinkage [57]. Although the generated dislocation networks are very different from the bi-continuous counterpart, crystalline-array-mimicking nanoporous metal still has its early densification in a similar linear fashion (see Figure 8.8).

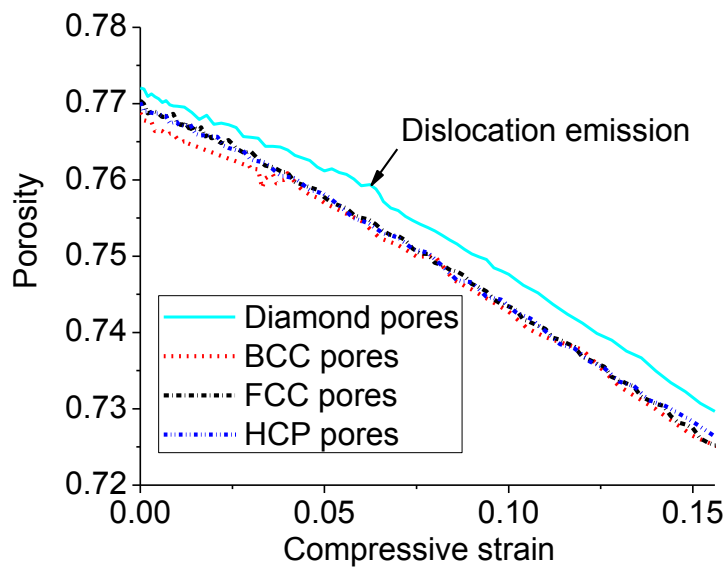


Figure 8.8: The decrease of porosity due to compression. Porosities after relaxation run is slightly smaller than the as-created values.

8.4. Concluding Remarks

The pore arrangement of nanoporous metal can be tailored to largely enhance stress response and improve structural integrity. Both the atomistic simulation and the theoretical calculation show that the inner structure can dramatically affect the yield stress. As a first attempt, our theoretical calculation adopted the dislocation configuration directly from atomistic simulation, analogous to the pre-defined dislocation configuration in the original Lubarda model. The current effort is focused on why dislocation emits on the observed locations, not to probe those locations from scratch. The cutoff distance could be replaced by using nonsingular dislocation theory with a core width to be determined, yet some adaption is needed for incomplete loops. The gliding component of P-K force due to image stress alone cannot explain the sequence of yield stresses for different samples. It appears that shear component due to remote stress, which leads to the gliding component of its P-K force is more influential to this sequence of yield stresses. Primary dislocations of all samples are Shockley partials. We observed the reaction of the Shockley and Frank partials to form a perfect dislocation, though the energy criterion does not specify its direction. Besides, the sessile stair-rod partials are formed by the intersection of the stacking fault ribbons of different slip planes. The sessile arrangement of such dislocations could be a reason for the stress to recover from the local minima for the diamond-array case. The calculated dislocation density here is closer to that in the bi-continuous nanoporous case than that in the sparsely-distributed-voids case. This difference among four samples appears to be related to the spacing at nodes (analogous to the bi-continuous counterpart). The hardening effect is found decreasing from the highest packing-factor cases (FCC and HCP array) to the lowest packing-factor case (diamond array). In all samples, pores become oblate at the end of loading, yet without collapsing. No strong correlation is established

between the dislocation emission and porosity level, which is different from the single-void cases. Crystalline-array-mimicking nanoporous metal, though inner morphology and dislocation networks dissimilar to its bi-continuous counterpart, still has its early densification in a similar linear fashion.

Our attention so far is paid to the orderly-arranged nanoporous structures, which either has been fabricated or theoretically feasible to fabricate through self-assembly of template. Yet, more flexibility in the design could be offered given the rise of novel synthesis technique in the foreseeable future, which may further improve the performance of designed nanoporous structures.

Chapter 9: Conclusions and Future Perspectives

9.1. Conclusions

Our simulations helped uncover several formerly unclear mechanisms regarding the nucleation, growth and coalescence of nanovoids. In particular, we believe that the “shear impossibility” debate was at least preliminarily settled in light of our MD investigation. This new understanding also has potential in improving the existing dislocation-based constitutive models.

For void nucleation, although the “toughness enhancement factor” indicates that the (1 0 0) silicon-copper interface is strongly “ductile”, the simulation of spherical-particle-embedded geometry suggests that the higher normal stress at the “polar” area of the silicon particle is responsible for the initial decohesion in an initially dislocation-free matrix. In terms of atomic motion, interfacial debonding features a cluster of atoms with higher-than-average displacement, whose displacement vectors form a highly-ordered alignment. The Lubarda model to evaluate the critical stress for dislocation emission for void-embedded matrix has been straightforwardly generalized to a perfectly-bonded particle case. For smaller particles, the critical stress for dislocation emission is closer to that assuming a perfectly-bonded particle, while that for larger particles is closer to that assuming an embedded void.

For void growth, initial void shape is found greatly influential to the stress-strain response. The transversely-elongated void deteriorates the ultimate strength most. Initial void shape not only alters the sites of the dislocation emission, but also determines the stress threshold for dislocation emission. The influence of initial porosity is intertwined with the influence of the initial void shape on the stress-strain relation. Our MD results demonstrate a stronger effect of the void shape on stress-strain relation than that predicted by the FE approach.

The mechanical constraint in molecular dynamics simulation has considerable influence on the dislocation emission, void size and shape evolution. The difference in dislocation pattern for these two cases stems from the different system volume caused by either strain or stress-confined lateral boundaries. Compared with the uniaxial-strain cases, the void growth under uniaxial-stress state is very limited. The different way to constrain the lateral boundaries is responsible for the difference in void shape evolution.

During the transition of void growth from elastic to inelastic fashion, the material transport away from the void is induced by shear dislocation loops/curves. The material transport via shear dislocation curves/loops is not only possible but also favorable near their loop plane. Whether or not forming larger dislocation structures, the shear curves/loops are capable of inducing the local material transport. The feasibility of void growth via shear loop/curves has been proved true from the MD simulation. The shear loops/curves, whether emitted in a simultaneous or sequential fashion, are capable of inducing/affecting the local material transport. The forming of larger dislocation structures further facilitates the void growth. The observed frustum-like structure features an opening angle, which is different from the one proposed by Lubarda et al. [18]. The proposed phenomenological model for void growth by frustum-like structures achieves relatively good agreement compared with that from a direct measurement of MD results. This new understanding is believed not only to settle the “shear impossibility” debate but also to help improve the dislocation-based constitutive models.

For void coalescence, the onset strain of dislocation emission is found mainly determined by the initial ellipticity. The transversely-elongated void within the two-void system effectively reduces the strain required to trigger dislocation emission. The pattern of emitted dislocations is not only subject to the initial void shape but also intervoid distance. The void shape combination

has significant influence on the porosity accumulation as well as void shape evolution. As for the void shape evolution, one typical pattern is the material transport along the lines with high density of defects. The coalescence porosity appears to be an acceptable criterion for void coalescence.

The pore arrangement of nanoporous metal can be tailored to largely enhance stress response and improve structural integrity. Both the atomistic simulation and the theoretical calculation show that the inner structure can dramatically affect the yield stress. As a first attempt, our theoretical calculation here adopted the dislocation configuration directly from atomistic simulation, analogous to the pre-defined dislocation configuration in the original Lubarda model. The gliding component of P-K force due to image stress alone cannot explain the sequence of yield stresses for different samples. It appears that shear component due to remote stress is more influential to this sequence of yield stresses. The calculated dislocation density here is closer to the bi-continuous nanoporous case than the sparsely-distributed-voids case. This difference among different samples appears related to the spacing at nodes (analogous to the bi-continuous counterpart). The hardening effect is found decreasing from the highest packing-factor cases (FCC and HCP array) to the lowest packing-factor case (diamond array).

Main contributions of this work can be summarized as follows. First, we show that both the shape and the arrangement of nanovoids have a great impact on the mechanical performance of nanoporous metals. Secondly, the “relative displacement” is employed to visualize atom movement during interfacial debonding and dislocation formation. Thirdly, the “shear impossibility” debate is preliminarily settled. Fourthly, the Lubarda model for critical stress to trigger dislocation emission is extended to the case of nanoporous geometry.

9.2. Future Perspectives

9.2.1. Critical Stress for Dislocation Emission

Modeling the yield stress with the presence of voids in metal is of great importance not only to the structural integrity of defected structures but also to the novel design of nanoporous structures. Currently, the Lubarda model [18, 91] is being widely used to evaluate the critical stress for dislocation emission. Despite being heuristic and concise, it contains several limitations. First, it assumes a cylindrical circular void in order to adopt the stress-function approach. In reality, bulk material can contain spherical or even ellipsoidal voids. Thus, novel analytical approach is required for a fully 3D case regarding the ellipticity of void. Second, the matrix material is assumed isotropic in the Lubarda model. Hence, anisotropy should be introduced to deal with anisotropic materials. Third, void is assumed isolated in the Lubarda model, which makes the model unable to accommodate void clusters or nanoporous structure where void interactions play an important role. Sophisticated modifications to the model could therefore be introduced in the future although it appears nontrivial.

9.2.2. Void Shape Effect with More Considerations

The void shape effect, which has been extensively studied by classical methods such as finite element simulation, is recently getting more and more attention in MD simulations. Those factors such as grain orientation, polycrystalline matrix, void orientation and alignment, multi-axis loading and large-scale clustering effect could all have combined influence with void shape effect and deserve further investigations.

9.2.3. Void Growth due to Dislocation Loops

Despite over a decade's study on dislocation-induced void growth, there is still a great need to deepen our understanding in this vital topic. The plastic void growth, which is caused by the introduction of dislocation loops or their non-conservative motion, is more important since it is unrecoverable. Several aspects can be considered in the future. First, further MD effort would help to explore the exact shape of the surface cut to create a shear loop, since it concerns the mass transferred and is inaccessible to continuum approaches. Second, we currently only observe the "spontaneous" formation of dislocation loops from void surface during the dynamic run. As a step forward, the "classical" cut-and-paste operation to create an arbitrary dislocation loop [57] could be examined by running MD simulation in the same fashion. In doing so, the simulation would be rather "quasi-static", whose insights could be valid regardless of strain rate. The third to be considered is the mass transfer during continuous formation of multiple dislocation loops.

9.2.4. Bridging the Gap between MD Results and Continuum Damage Models

The time scale (depends on strain rate applied) and the size scale are the two major concerns. For the time scale, MD simulation can readily provide insights to explosive or projectile impact problems. As suggested by MD insights, continuum damage models for the high-strain-rate regime could incorporate a stronger role of void shape effect. In general, the strain rate (beyond $1 \times 10^6 \text{s}^{-1}$) applied in classical MD approach is much higher than that in normal tensile tests. We are aware of some adapted methods in developing such as the one constructing the potential energy landscape [198]. Some interesting observation in our simulation might have already suggested viable, "effective" approaches. For example, the final void shape by imposing uniaxial-strain is close to the observation under a spall test, while that by imposing uniaxial-stress resembles the observation under a normal tensile test. This might provide hints on how to carry out "effective" MD simulation under specifically-imposed constraints to mimic that under

normal strain rates and explore relevant mechanisms. As for size scale, MD approach nowadays can readily simulate large submicron voids. Void of this size are typically found in irradiated materials as well as those secondary voids in ductile fracture. Microvoids are currently out of the scope of direct MD simulation. However, multi-scale approach which combines full-atom modeling and continuum modeling can be explored under such a situation. The key is perhaps a physically efficient transition between the multi-scaled zones, especially for capturing the migration of dislocations. For nanoporous metals, MD simulation appears an ideal tool for localized plastic deformation involving a number of pores. However, it is not yet capable of capturing the overall brittle behavior of bi-continuous nanoporous structure. The required simulation size to achieve this, which might go beyond micrometers, needs to be further explored.

9.2.5. Modeling Designed Nanoporous Structures

Our attention so far is paid to the orderly-arranged nanoporous structures, which either has been fabricated or theoretically feasible to fabricate through self-assembly of template. Yet, more flexibility in the design could be offered given the rise of novel synthesis technique in the foreseeable future, which may further improve the performance of designed nanoporous structures. In the generalized Lubarda model for the critical yield stress, the cutoff distance could be replaced by using nonsingular dislocation theory with a core width to be determined. Yet, some adaption is needed for incomplete loops. Besides, the current effort in Chapter 8 is only aimed to comprehend why dislocation emits on the observed locations, not to probe those locations from scratch. The future effort could be made to simplify the semi-analytical approach and enable probing these possible locations solely from analytical calculations.

Bibliography

- [1] Besson, J., 2010, "Continuum Models of Ductile Fracture: A Review," *Int. J. Damage Mech.*, 19(1) pp. 3-52.
- [2] Broek, D., 1973, "The Role of Inclusions in Ductile Fracture and Fracture Toughness," *Eng. Fract. Mech.*, 5(1) pp. 55-66.
- [3] Chen, Z., and Butcher, C., 2013, *Micromechanics Modelling of Ductile Fracture*, Springer, Dordrecht.
- [4] Mayer, R. M., and Brown, L. M., 1980, "Nucleation and Growth of Voids by Radiation," *J. Nucl. Mater.*, 95(1) pp. 46-57.
- [5] Feng, Z. Q., Yang, Y. Q., Chen, Y. X., 2013, "In-Situ TEM Investigation of Fracture Process in an Al–Cu–Mg Alloy," *Mater. Sci. Eng., A*, 586(1) pp. 259-266.
- [6] Bringa, E. M., Monk, J. D., Caro, A., 2012, "Are Nanoporous Materials Radiation Resistant?" *Nano Lett.*, 12(7) pp. 3351-3355.
- [7] Bai, X., Voter, A. F., Hoagland, R. G., 2010, "Efficient Annealing of Radiation Damage Near Grain Boundaries Via Interstitial Emission," *Science*, 327(5973) pp. 1631-1634.
- [8] Yamauchi, Y., Suzuki, N., Radhakrishnan, L., 2009, "Breakthrough and Future: Nanoscale Controls of Compositions, Morphologies, and Mesochannel Orientations Toward Advanced Mesoporous Materials," *Chem. Rec.*, 9(6) pp. 321-339.
- [9] Qiao, Y., and Li, C. M., 2011, "Nanostructured Catalysts in Fuel Cells," *J. Mater. Chem.*, 21(12) pp. 4027-4036.

- [10] Bae, J. H., Han, J., and Chung, T. D., 2012, "Electrochemistry at Nanoporous Interfaces: New Opportunity for Electrocatalysis," *Phys. Chem. Chem. Phys.*, 14(2) pp. 448-463.
- [11] Lang, X., Hirata, A., Fujita, T., 2011, "Nanoporous metal/oxide Hybrid Electrodes for Electrochemical Supercapacitors," *Nat. Nano*, 6(4) pp. 232-236.
- [12] Zheng, X. T., and Li, C. M., 2012, "Single Cell Analysis at the Nanoscale," *Chem. Soc. Rev.*, 41(6) pp. 2061-2071.
- [13] Biener, J., Hodge, A. M., Hayes, J. R., 2006, "Size Effects on the Mechanical Behavior of Nanoporous Au," *Nano Lett.*, 6(10) pp. 2379-2382.
- [14] Thomason, P.F., 1990, *Ductile Fracture of Metals*, Pergamon Press,.
- [15] McClintock, F. A., 1968, "A Criterion for Ductile Fracture by the Growth of Holes," *J. Appl. Mech.*, 35(2) pp. 363-371.
- [16] Liu, G., Zhang, G., Ding, X., 2003, "Dependence of Fracture Toughness on Multiscale Second Phase Particles in High Strength Al Alloys," *Mater. Sci. Tech.*, 19(7) pp. 887-896.
- [17] Zhang, Z. L., and Skallerud, B., 2010, "Void Coalescence with and without Prestrain History," *Int. J. Damage Mech.*, 19(2) pp. 153-174.
- [18] Lubarda, V. A., Schneider, M. S., Kalantar, D. H., 2004, "Void Growth by Dislocation Emission," *Acta Mater.*, 52(6) pp. 1397-1408.
- [19] Meyers, M. A., and Aimone, C. T., 1983, "Dynamic Fracture (Spalling) of Metals," *Prog. Mater. Sci.*, 28(1) pp. 1-96.

- [20] Stevens, A. L., Davison, L., and Warren, W. E., 1972, "Spall Fracture in Aluminum Monocrystals: A dislocation-dynamics Approach," *J. Appl. Phys.*, 43(12) pp. 4922-4927.
- [21] Hosokawa, A., Wilkinson, D. S., Kang, J., 2013, "Onset of Void Coalescence in Uniaxial Tension Studied by Continuous X-Ray Tomography," *Acta Mater.*, 61(4) pp. 1021-1036.
- [22] Tvergaard, V., 1982, "Ductile Fracture by Cavity Nucleation between Larger Voids," *J. Mech. Phys. Solids*, 30(4) pp. 265-286.
- [23] Sun, Y., 1995, "Constitutive Equations for Ductile Materials Containing Large and Small Voids," *Mech. Mater.*, 19(2) pp. 119-127.
- [24] Faleskog, J., and Shih, C. F., 1997, "Micromechanics of coalescence—I. Synergistic Effects of Elasticity, Plastic Yielding and Multi-Size-Scale Voids," *J. Mech. Phys. Solids*, 45(1) pp. 21-50.
- [25] Fabrègue, D., and Pardoën, T., 2008, "A Constitutive Model for Elastoplastic Solids Containing Primary and Secondary Voids," *J. Mech. Phys. Solids*, 56(3) pp. 719-741.
- [26] Traiviratana, S., Bringa, E. M., Benson, D. J., 2008, "Void Growth in Metals: Atomistic Calculations," *Acta Mater.*, 56(15) pp. 3874-3886.
- [27] Gall, K., Horstemeyer, M. F., Van Schilfgaarde, M., 2000, "Atomistic Simulations on the Tensile Debonding of an aluminum–silicon Interface," *J. Mech. Phys. Solids*, 48(10) pp. 2183-2212.
- [28] Ward, D. K., Curtin, W. A., and Qi, Y., 2006, "Aluminum–silicon Interfaces and Nanocomposites: A Molecular Dynamics Study," *Compos. Sci. Tech.*, 66(9) pp. 1151-1161.

- [29] Tomar, V., and Zhou, M., 2007, "Analyses of Tensile Deformation of Nanocrystalline α -Fe₂O₃+fcc-Al Composites using Molecular Dynamics Simulations," *J. Mech. Phys. Solids*, 55(5) pp. 1053-1085.
- [30] Noreyan, A., Qi, Y., and Stoilov, V., 2008, "Critical Shear Stresses at aluminum–silicon Interfaces," *Acta Mater.*, 56(14) pp. 3461-3469.
- [31] Dongare, A. M., LaMattina, B., Irving, D. L., 2012, "An Angular-Dependent Embedded Atom Method (A-EAM) Interatomic Potential to Model Thermodynamic and Mechanical Behavior of Al/Si Composite Materials," *Model. Simul. Mater. Sci. Eng.*, 20(3) pp. 035007.
- [32] Shadlou, S., and Wegner, L. D., 2016, "Atomistic Investigation of the Effect of Nano-Structural Shape on the Mechanical Response of SiC/Cu Interpenetrating Phase Nanocomposites," *Comput. Mater. Sci.*, 117(1) pp. 428-436.
- [33] Frick, C. P., Clark, B. G., Orso, S., 2008, "Size Effect on Strength and Strain Hardening of Small-Scale [1 1 1] Nickel Compression Pillars," *Mater. Sci. Eng., A*, 489(1–2) pp. 319-329.
- [34] Böhm, J., Gruber, P., Spolenak, R., 2004, "Tensile Testing of Ultrathin Polycrystalline Films: A Synchrotron-Based Technique," *Rev. Sci. Instrum.*, 75(4) pp. 1110-1119.
- [35] Gerberich, W. W., Tymiak, N. I., Grunlan, J. C., 2002, "Interpretations of Indentation Size Effects," *J. Appl. Mech., Transactions ASME*, 69(4) pp. 433-442.
- [36] Brenner, S. S., 1958, "Growth and Properties of "Whiskers"," *Science*, 128(3324) pp. 569-575.
- [37] Potirniche, G. P., Horstemeyer, M. F., Wagner, G. J., 2006, "A Molecular Dynamics Study of Void Growth and Coalescence in Single Crystal Nickel," *Int. J. Plast.*, 22(2) pp. 257-278.

- [38] Bringa, E. M., Traiviratana, S., and Meyers, M. A., 2010, "Void Initiation in Fcc Metals: Effect of Loading Orientation and Nanocrystalline Effects," *Acta Mater.*, 58(13) pp. 4458-4477.
- [39] Marian, J., Knap, J., and Ortiz, M., 2005, "Nanovoid Deformation in Aluminum Under Simple Shear," *Acta Mater.*, 53(10) pp. 2893-2900.
- [40] Tang, T., Kim, S., and Horstemeyer, M. F., 2010, "Molecular Dynamics Simulations of Void Growth and Coalescence in Single Crystal Magnesium," *Acta Mater.*, 58(14) pp. 4742-4759.
- [41] Benzerga, A. A., 2002, "Micromechanics of Coalescence in Ductile Fracture," *J. Mech. Phys. Solids*, 50(6) pp. 1331-1362.
- [42] Tvergaard, V., 2008, "Effects of Shape on Unstable Growth of Cavities Interacting with Surrounding Small Voids," *Philos. Mag. (London, 2003)*, 88(28-29) pp. 3357-3368.
- [43] Tvergaard, V., 2011, "Void Shape Effects and Voids Starting from Cracked Inclusion," *Int. J. Solids Struct.*, 48(7-8) pp. 1101-1108.
- [44] Pardoen, T., and Hutchinson, J. W., 2000, "An Extended Model for Void Growth and Coalescence," *J. Mech. Phys. Solids*, 48(12) pp. 2467-2512.
- [45] Gologanu, M., Leblond, J.-B., Perrin, G., Devaux, J., 1997. Recent extensions of Gurson's model for porous ductile metals. In: Suquet, P. (Ed.), *Continuum Micromechanics*, CISM Lectures Series. Springer, New York, pp. 61-130.
- [46] Keralavarma, S. M., and Benzerga, A. A., 2010, "A Constitutive Model for Plastically Anisotropic Solids with Non-Spherical Voids," *J. Mech. Phys. Solids*, 58(6) pp. 874-901.

- [47] Pardoen, T., and Scheyvaerts, F., 2010, "A New Model for Void Coalescence by Internal Necking," *Int. J. Damage Mech.*, 19(1)pp. 95-126.
- [48] Gurson, A. L., 1977, "Continuum Theory of Ductile Rupture by Void Nucleation and Growth –Part I. Yield Criteria and Flow Rules for Porous Ductile Media." *J. Eng. Mater. Technol.*, 99(1)pp. 2-15.
- [49] Gurland, J., 1972, "Observations on the Fracture of Cementite Particles in a Spheroidized 1.05% c Steel Deformed at Room Temperature," *Acta Metall.*, 20(5) pp. 735-741.
- [50] Chu, C. C., and Needleman, A., 1980, "Void Nucleation Effects in Biaxially Stretched Sheets," *J. Eng. Mater. Technol.*, 102(3) pp. 249-256.
- [51] Argon, A. S., and Im, J., 1975, "Separation of Second Phase Particles in Spheroidized 1045 Steel, Cu-0.6pct Cr Alloy, and Maraging Steel in Plastic Straining," *Metall. Trans. A*, 6(4) pp. 839-851.
- [52] Argon, A. S., Im, J., and Needleman, A., 1975, "Distribution of Plastic Strain and Negative Pressure in Necked Steel and Copper Bars," *Metall. Trans. A*, 6(4) pp. 815-824.
- [53] Argon, A. S., Im, J., and Safoglu, R., 1975, "Cavity Formation from Inclusions in Ductile Fracture," *Metall. Trans. A*, 6(4) pp. 825-837.
- [54] Ashby, M. F., 1970, "The Deformation of Plastically Non-Homogeneous Materials," *Philos. Mag.*, 21(170) pp. 399-424.
- [55] Ahn, D. C., Sofronis, P., and Minich, R., 2006, "On the Micromechanics of Void Growth by Prismatic-Dislocation Loop Emission," *J. Mech. Phys. Solids*, 54(4) pp. 735-755.

- [56] Bulatov, V. V., Wolfer, W. G., and Kumar, M., 2010, "Shear Impossibility: Comments on "Void Growth by Dislocation Emission" and "Void Growth in Metals: Atomistic Calculations",
Scr. Mater., 63(1) pp. 144-147.
- [57] Hirth, John Price, Lothe, Jens., 1967, Theory of Dislocations, McGraw-Hill, New York, pp. 97-98.
- [58] Lehto, N., and Öberg, S., 1998, "Effects of Dislocation Interactions: Application to the Period-Doubled Core of the 90° Partial in Silicon," Phys. Rev. Lett., 80(25) pp. 5568-5571.
- [59] Mura, T., 1987, Micromechanics of Defects in Solids, Martinus Nijhoff Publishers, The Netherlands,.
- [60] Ohr, S. M., 1972, "Displacement Field Around a Shear Dislocation Loop," Philos. Mag., 26(6) pp. 1307-1312.
- [61] Tvergaard, V., and Needleman, A., 1984, "Analysis of the Cup-Cone Fracture in a Round Tensile Bar," Acta Metall., 32(1) pp. 157-169.
- [62] Yi, S., and Duo, W., 1989, "A Lower Bound Approach to the Yield Loci of Porous Materials," Acta Mech. Sinica, 5(3) pp. 237-243.
- [63] Zhang, Z. L., and Niemi, E., 1994, "Studies on the Ductility Predictions by Different Local Failure Criteria," Eng. Fract. Mech., 48(4) pp. 529-540.
- [64] Zhang, Z. L., Thaulow, C., and Ødegård, J., 2000, "A Complete Gurson Model Approach for Ductile Fracture," Eng. Fract. Mech., 67(2) pp. 155-168.

- [65] Gall, K., Yang, N., Horstemeyer, M., 1999, "The Debonding and Fracture of Si Particles during the Fatigue of a Cast Al-Si Alloy," *Metall. Mater. Trans. A*, 30(12) pp. 3079-3088.
- [66] Akbarpour, M. R., Salahi, E., Hesari, F. A., 2013, "Microstructural Development and Mechanical Properties of Nanostructured Copper Reinforced with SiC Nanoparticles," *Mater. Sci. Eng., A*, 568(15) pp. 33-39.
- [67] Shehata, F., Fathy, A., Abdelhameed, M., 2009, "Preparation and Properties of Al₂O₃ Nanoparticle Reinforced Copper Matrix Composites by in Situ Processing," *Mater. Des.*, 30(7) pp. 2756-2762.
- [68] López, M., Corredor, D., Camurri, C., 2005, "Performance and Characterization of Dispersion Strengthened Cu-TiB₂ Composite for Electrical use," *Mater. Charact.*, 55(4-5) pp. 252-262.
- [69] Arico, A. S., Bruce, P., Scrosati, B., 2005, "Nanostructured Materials for Advanced Energy Conversion and Storage Devices," *Nat. Mater.*, 4(5) pp. 366-377.
- [70] Wessells, C. D., McDowell, M. T., Peddada, S. V., 2012, "Tunable Reaction Potentials in Open Framework Nanoparticle Battery Electrodes for Grid-Scale Energy Storage," *ACS Nano*, 6(2) pp. 1688-1694.
- [71] Ji, L., Xin, H. L., Kuykendall, T. R., 2012, "SnS₂ Nanoparticle Loaded Graphene Nanocomposites for Superior Energy Storage," *Phys. Chem. Chem. Phys.*, 14(19) pp. 6981-6986.
- [72] Li, S., Niu, J., Zhao, Y. C., 2015, "High-Rate Aluminium Yolk-Shell Nanoparticle Anode for Li-Ion Battery with Long Cycle Life and Ultrahigh Capacity," *Nat Commun.*, 6. pp. 7872-7878

- [73] Cuenya, B. R., 2013, "Metal Nanoparticle Catalysts Beginning to Shape-Up," *Acc. Chem. Res.*, 46(8) pp. 1682-1691.
- [74] Han, J., Fang, P., Jiang, W., 2012, "Ag-Nanoparticle-Loaded Mesoporous Silica: Spontaneous Formation of Ag Nanoparticles and Mesoporous Silica SBA-15 by a One-Pot Strategy and their Catalytic Applications," *Langmuir*, 28(10) pp. 4768-4775.
- [75] Wang, Y., Zhao, H., and Zhao, G., 2015, "Iron-Copper Bimetallic Nanoparticles Embedded within Ordered Mesoporous Carbon as Effective and Stable Heterogeneous Fenton Catalyst for the Degradation of Organic Contaminants," *Appl. Catal. B.*, 164pp. 396-406.
- [76] Long, W., Brunelli, N. A., Didas, S. A., 2013, "Aminopolymer-Silica Composite-Supported Pd Catalysts for Selective Hydrogenation of Alkynes," *ACS Catal.*, 3(8) pp. 1700-1708.
- [77] Plimpton, S., 1995, "Fast Parallel Algorithms for Short-Range Molecular Dynamics," *J. Comput. Phys.*, 117(1) pp. 1-19.
- [78] Baskes, M. I., 1992, "Modified Embedded-Atom Potentials for Cubic Materials and Impurities," *Phys. Rev. B*, 46(5) pp. 2727-2742.
- [79] Jelinek, B., Groh, S., Horstemeyer, M. F., 2012, "Modified Embedded Atom Method Potential for Al, Si, mg, Cu, and Fe Alloys," *Phys. Rev. B*, 85(24) pp. 245102-245118.
- [80] Zimmerman, J. A., Gao, H., and Abraham, F. F., 2000, "Generalized Stacking Fault Energies for Embedded Atom FCC Metals," *Model. Simul. Mater. Sci. Eng.*, 8(2) pp. 103-115.
- [81] Rice, J. R., 1992, "Dislocation Nucleation from a Crack Tip: An Analysis Based on the Peierls Concept," *J. Mech. Phys. Solids*, 40(2) pp. 239-271.

- [82] Melchionna, S., Ciccotti, G., and Lee Holian, B., 1993, "Hoover NPT Dynamics for Systems Varying in Shape and Size," *Mol. Phys.*, 78(3) pp. 533-544.
- [83] Nosé, S., 1984, "A Unified Formulation of the Constant Temperature Molecular Dynamics Methods," *J. Chem. Phys.*, 81(1) pp. 511-519.
- [84] Li, J., 2003, "AtomEye: An Efficient Atomistic Configuration Viewer," *Model. Simul. Mater. Sci. Eng.*, 11(2) pp. 173-177.
- [85] Begau, C., Hua, J., and Hartmaier, A., 2012, "A Novel Approach to Study Dislocation Density Tensors and Lattice Rotation Patterns in Atomistic Simulations," *J. Mech. Phys. Solids*, 60(4) pp. 711-722.
- [86] Sloan, S. W., 1993, "A Fast Algorithm for Generating Constrained Delaunay Triangulations," *Comput. Struct.*, 47(3) pp. 441-450.
- [87] Cui, Y., and Chen, Z., 2016, "Material Transport Via the Emission of Shear Loops during Void Growth: A Molecular Dynamics Study," *J. Appl. Phys.*, 119(22) pp. 225102.
- [88] Zhou, M., 2003, "A New Look at the Atomic Level Virial Stress: On Continuum-Molecular System Equivalence," *Proc. R. Soc. A: Math. Phys. Eng. Sci.*, 459(2037) pp. 2347-2392.
- [89] Muskhelishvili, N., I., 1963, *Some Basic Problems of the Mathematical Theory of Elasticity*, Noordhoff, Groningen,.
- [90] Dundurs, J., and Mura, T., 1964, "Interaction between an Edge Dislocation and a Circular Inclusion," *J. Mech. Phys. Solids*, 12(3) pp. 177-189.

- [91] Lubarda, V. A., 2011, "Emission of Dislocations from Nanovoids under Combined Loading," *Int. J. Plast.*, 27(2) pp. 181-200.
- [92] Wortman, J. J., and Evans, R. A., 1965, "Young Modulus, Shear Modulus, and Poisson Ratio in Silicon and Germanium," *J. Appl. Phys.*, 36(1) pp. 153-156.
- [93] Hess, P., 1996, "Laser Diagnostics of Mechanical and Elastic Properties of Silicon and Carbon Films," *Appl. Surf. Sci.*, 106(2) pp. 429-437.
- [94] Embury, J. D., 1985, "Plastic Flow in Dispersion Hardened Materials," *Metall. Trans. A*, 16(12) pp. 2191-2200.
- [95] Dighe, M. D., Gokhale, A. M., and Horstemeyer, M. F., 2002, "Effect of Loading Condition and Stress State on Damage Evolution of Silicon Particles in an Al-Si-mg-Base Cast Alloy," *Metall. Mater. Trans. A*, 33(3) pp. 555-565.
- [96] Shabrov, M. N., and Needleman, A., 2002, "An Analysis of Inclusion Morphology Effects on Void Nucleation," *Model. Simul. Mater. Sci. Eng.*, 10(2) pp. 163-183.
- [97] Cui, Y., and Chen, Z., 2015, "Molecular Dynamics Modeling on the Role of Initial Void Geometry in a Thin Aluminum Film Under Uniaxial Tension," *Model. Simul. Mater. Sci. Eng.*, 23(8) pp. 085011.
- [98] Nafar Dastgerdi, J., Marquis, G., Anbarlooie, B., 2016, "Microstructure-Sensitive Investigation on the Plastic Deformation and Damage Initiation of Amorphous Particles Reinforced Composites," *Compos. Struct.*, 142(10) pp. 130-139.
- [99] Legarth, B. N., and Niordson, C. F., 2010, "Debonding Failure and Size Effects in Micro-Reinforced Composites," *Int. J. Plast.*, 26(1) pp. 149-165.

- [100] Begau, C., Hartmaier, A., George, E. P., 2011, "Atomistic Processes of Dislocation Generation and Plastic Deformation during Nanoindentation," *Acta Mater.*, 59(3) pp. 934-942.
- [101] Ackland, G. J., and Jones, A. P., 2006, "Applications of Local Crystal Structure Measures in Experiment and Simulation," *Phys. Rev. B*, 73(5) pp. 054104.
- [102] Cui, Y., and Chen, Z., 2015, "Molecular Dynamics Simulation of the Influence of Elliptical Void Interaction on the Tensile Behavior of Aluminum," *Comput. Mater. Sci.*, 108, (Part A) pp.103-113.
- [103] Bhatia, M. A., Solanki, K. N., Moitra, A., 2013, "Investigating Damage Evolution at the Nanoscale: Molecular Dynamics Simulations of Nanovoid Growth in Single-Crystal Aluminum," *Metall. Mater. Trans. A*, 44(2) pp. 617-626.
- [104] Ho, P. S., and Kwok, T., 1989, "Electromigration in Metals," *Rep. Prog. Phys.*, 52(3) pp. 301-348.
- [105] Sauter, A. I., and Nix, W. D., 1992, "A Study of Stress-Driven Diffusive Growth of Voids in Encapsulated Interconnect Lines," *J. Mater. Res.*, 7(05) pp. 1133-1143.
- [106] Gungor, M. R., Maroudas, D., and Zhou, S., 2000, "Molecular-Dynamics Study of the Mechanism and Kinetics of Void Growth in Ductile Metallic Thin Films," *Appl. Phys. Lett.*, 77(3) pp. 343-345.
- [107] Vella, J. B., Mann, A. B., Kung, H., 2004, "Mechanical Properties of Nanostructured Amorphous Metal Multilayer Thin Films," *J. Mater. Res.*, 19(06) pp. 1840-1848.

- [108] Gungor, M. R., and Maroudas, D., 2005, "Atomistic Mechanisms of Strain Relaxation due to Ductile Void Growth in Ultrathin Films of Face-Centered-Cubic Metals," *J. Appl. Phys.*, 97(11) pp. 113527.
- [109] Kolluri, K., Gungor, M. R., and Maroudas, D., 2007, "Void Nucleation in Biaxially Strained Ultrathin Films of Face-Centered Cubic Metals," *Appl. Phys. Lett.*, 90(22) pp. 221907.
- [110] Foiles, S. M., Baskes, M. I., and Daw, M. S., 1986, "Embedded-Atom-Method Functions for the Fcc Metals Cu, Ag, Au, Ni, Pd, Pt, and their Alloys," *Phys.Rev.B*, 33(12) pp. 7983-7991.
- [111] Spearot, D. E., Jacob, K. I., and McDowell, D. L., 2007, "Dislocation Nucleation from Bicrystal Interfaces with Dissociated Structure," *Int. J. Plast.*, 23(1) pp. 143-160.
- [112] Mishin, Y., Farkas, D., Mehl, M. J., 1999, "Interatomic Potentials for Monoatomic Metals from Experimental Data and Ab Initio Calculations," *Phys. Rev. B*, 59(5) pp. 3393-3407.
- [113] Mishin, Y., Mehl, M. J., Papaconstantopoulos, D. A., 2001, "Structural Stability and Lattice Defects in Copper: Ab Initio, Tight-Binding, and Embedded-Atom Calculations," *Phys. Rev. B*, 63(22) pp. 224106.
- [114] Spearot, D. E., Jacob, K. I., and McDowell, D. L., 2005, "Nucleation of Dislocations from [0 0 1] Bicrystal Interfaces in Aluminum," *Acta Mater.*, 53(13) pp. 3579-3589.
- [115] Horstemeyer, M. F., Matalanis, M. M., Sieber, A. M., 2000, "Micromechanical Finite Element Calculations of Temperature and Void Configuration Effects on Void Growth and Coalescence," *Int. J. Plast.*, 16(7-8) pp. 979-1015.
- [116] Lubarda, V. A., and Markenscoff, X., 2007, "Dual Conservation Integrals and Energy Release Rates," *Int. J. Solids Struct.*, 44(11-12) pp. 4079-4091.

- [117] Crandall, S.H., Dahl, N.C., and Lardner, T.J., 1959, *An Introduction to the Mechanics of Solids*, McGraw-Hill, Boston,.
- [118] Totten, G.E., and MacKenzie, D.S., 2003, *Handbook of Aluminum*, Marcel Dekker, New York,.
- [119] Zhao, K. J., Chen, C. Q., Shen, Y. P., 2009, "Molecular Dynamics Study on the Nano-Void Growth in Face-Centered Cubic Single Crystal Copper," *Comput. Mater. Sci.*, 46(3) pp. 749-754.
- [120] Zhao, K., Fan, L., and Chen, C., 2009, "Multiaxial Behavior of Nanoporous Single Crystal Copper: A Molecular Dynamics Study," *Acta Mech. Solida Sin.*, 22(6) pp. 650-656.
- [121] Farkas, D., Caro, A., Bringa, E., 2013, "Mechanical Response of Nanoporous Gold," *Acta Mater.*, 61(9) pp. 3249-3256.
- [122] Gahagan, K. T., Moore, D. S., Funk, D. J., 2000, "Measurement of Shock Wave Rise Times in Metal Thin Films," *Phys. Rev. Lett.*, 85(15) pp. 3205-3208.
- [123] Komanduri, R., Chandrasekaran, N., and Raff, L. M., 2001, "Molecular Dynamics (MD) Simulation of Uniaxial Tension of some Single-Crystal Cubic Metals at Nanolevel," *Int. J. Mech. Sci.*, 43(10) pp. 2237-2260.
- [124] Makke, A., Perez, M., Lame, O., 2009, "Mechanical Testing of Glassy and Rubbery Polymers in Numerical Simulations: Role of Boundary Conditions in Tensile Stress Experiments," *J. Chem. Phys.*, 131(1) pp. 014904.
- [125] Andersen, H. C., 1980, "Molecular Dynamics Simulations at Constant Pressure and/or Temperature," *J. Chem. Phys.*, 72(4) pp. 2384-2393.

- [126] Martyna, G. J., Tobias, D. J., and Klein, M. L., 1994, "Constant Pressure Molecular Dynamics Algorithms," *J. Chem. Phys.*, 101(5) pp. 4177-4189.
- [127] Shinoda, W., Shiga, M., and Mikami, M., 2004, "Rapid Estimation of Elastic Constants by Molecular Dynamics Simulation Under Constant Stress," *Phys. Rev. B*, 69(13) pp. 134103.
- [128] Tuckerman, M., Berne, B. J., and Martyna, G. J., 1992, "Reversible Multiple Time Scale Molecular Dynamics," *J. Chem. Phys.*, 97(3) pp. 1990-2001.
- [129] Rodriguez-Nieva, J. F., Ruestes, C. J., Tang, Y., 2014, "Atomistic Simulation of the Mechanical Properties of Nanoporous Gold," *Acta Mater.*, 80(1) pp. 67-76.
- [130] Wu, X. Y., Ramesh, K. T., and Wright, T. W., 2003, "The Effects of Thermal Softening and Heat Conduction on the Dynamic Growth of Voids," *Int. J. Solids Struct.*, 40(17) pp. 4461-4478.
- [131] Schall, P., Feuerbacher, M., Bartsch, M., 1999, "Dislocation Density Evolution upon Plastic Deformation of Al-Pd-Mn Single Quasicrystals," *Philos. Mag. Lett.*, 79(10) pp. 785-796.
- [132] Seppälä, E. T., Belak, J., and Rudd, R. E., 2004, "Effect of Stress Triaxiality on Void Growth in Dynamic Fracture of Metals: A Molecular Dynamics Study," *Phys. Rev. B*, 69(13) pp. 134101.
- [133] Romanova, V. A., Balokhonov, R. R., and Schmauder, S., 2009, "The Influence of the Reinforcing Particle Shape and Interface Strength on the Fracture Behavior of a Metal Matrix Composite," *Acta Mater.*, 57(1) pp. 97-107.

- [134] Huang, P., and Kuo, J., 2011, "Thermal Stretching of Defective Nanowires: The Coupled Effects of vacancy Cluster Defects, Operating Temperature, and Wire Cross-Sectional Area," *Appl. Phys. A*, 103(4) pp. 1083-1092.
- [135] Hull, D., and Bacon, D.J., 1984, *Introduction to Dislocations*, Butterworth-Heinemann, London,.
- [136] Rudd, R. E., Seppälä, E. T., Dupuy, L. M., 2007, "Void Coalescence Processes Quantified through Atomistic and Multiscale Simulation," *J. Comput. Aided Mater. Des.*, 14(3) pp. 425-434.
- [137] Lazar, M., 2013, "The Fundamentals of Non-Singular Dislocations in the Theory of Gradient Elasticity: Dislocation Loops and Straight Dislocations," *Int. J. Solids Struct.*, 50(2) pp. 352-362.
- [138] Shimomura, Y., and Mukouda, I., 2000, "Development of Vacancy Clusters in Neutron-Irradiated Copper at High Temperature," *J. Nucl. Mater.*, 283–287, (Part 1) pp. 249-254.
- [139] Wolfer, W. G., and Drugan, W. J., 1988, "Elastic Interaction Energy between a Prismatic Dislocation Loop and a Spherical Cavity," *Philos. Mag. A*, 57(6) pp. 923-937.
- [140] Tvergaard, V., 1981, "Influence of Voids on Shear Band Instabilities Under Plane Strain Conditions," *Int. J. Fract.*, 17(4) pp. 389-407.
- [141] Ohno, N., and Hutchinson, J. W., 1984, "Plastic Flow Localization due to Non-Uniform Void Distribution," *J. Mech. Phys. Solids*, 32(1) pp. 63-85.
- [142] Becker, R., 1987, "The Effect of Porosity Distribution on Ductile Failure," *J. Mech. Phys. Solids*, 35(5) pp. 577-599.

[143] Magnusen, P. E., Dubensky, E. M., and Koss, D. A., 1988, "The Effect of Void Arrays on Void Linking during Ductile Fracture," *Acta Metall.*, 36(6) pp. 1503-1509.

[144] Benson, D. J., 1993, "An Analysis of Void Distribution Effects on the Dynamic Growth and Coalescence of Voids in Ductile Metals," *J. Mech. Phys. Solids*, 41(8) pp. 1285-1308.

[145] Benson, D. J., 1995, "The Effects of Void Cluster Size on Ductile Fracture," *Int. J. Plast.*, 11(5) pp. 571-582.

[146] Chen, Z. T., Worswick, M. J., Cinotti, N., 2003, "A Linked FEM-Damage Percolation Model of Aluminum Alloy Sheet Forming," *Int. J. Plast.*, 19(12) pp. 2099-2120.

[147] Chen, Z., Worswick, M. J., Keith Pilkey, A., 2005, "Damage Percolation during Stretch Flange Forming of Aluminum Alloy Sheet," *J. Mech. Phys. Solids*, 53(12) pp. 2692-2717.

[148] Toi, Y., and Kang, S., 2005, "Mesoscopic Natural Element Analysis of Elastic Moduli, Yield Stress and Fracture of Solids Containing a Number of Voids," *Int. J. Plast.*, 21(12) pp. 2277-2296.

[149] Bilger, N., Auslender, F., Bornert, M., 2005, "Effect of a Nonuniform Distribution of Voids on the Plastic Response of Voided Materials: A Computational and Statistical Analysis," *Int. J. Solids Struct.*, 42(2) pp. 517-538.

[150] Gărăjeu, M., and Suquet, P., 2007, "On the Influence of Local Fluctuations in Volume Fraction of Constituents on the Effective Properties of Nonlinear Composites. Application to Porous Materials," *J. Mech. Phys. Solids*, 55(4) pp. 842-878.

[151] Weck, A., and Wilkinson, D. S., 2008, "Experimental Investigation of Void Coalescence in Metallic Sheets Containing Laser Drilled Holes," *Acta Mater.*, 56(8) pp. 1774-1784.

- [152] Bandstra, J. P., and Koss, D. A., 2008, "On the Influence of Void Clusters on Void Growth and Coalescence during Ductile Fracture," *Acta Mater.*, 56(16) pp. 4429-4439.
- [153] Rudd, R. E., and Belak, J. F., 2002, "Void Nucleation and Associated Plasticity in Dynamic Fracture of Polycrystalline Copper: An Atomistic Simulation," *Comput. Mater. Sci.*, 24(1–2) pp. 148-153.
- [154] Seppälä, E. T., Belak, J., and Rudd, R. E., 2005, "Three-Dimensional Molecular Dynamics Simulations of Void Coalescence during Dynamic Fracture of Ductile Metals," *Phys. Rev. B*, 71(6) pp. 064112.
- [155] Seppälä, E. T., Belak, J., and Rudd, R. E., 2004, "Onset of Void Coalescence during Dynamic Fracture of Ductile Metals," *Phys. Rev. Lett.*, 93(24) pp. 245503.
- [156] Marian, J., Knap, J., and Ortiz, M., 2004, "Nanovoid Cavitation by Dislocation Emission in Aluminum," *Phys. Rev. Lett.*, 93(16) pp. 165503.
- [157] Worswick, M. J., Chen, Z. T., Pilkey, A. K., 2001, "Damage Characterization and Damage Percolation Modelling in Aluminum Alloy Sheet," *Acta Mater.*, 49(14) pp. 2791-2803.
- [158] H-J Chang and J Segurado and O Rodríguez de la Fuente and B M Pabón and J.LLorca, 2013, "Molecular Dynamics Modeling and Simulation of Void Growth in Two Dimensions," *Model. Simul. Mater. Sci. Eng.*, 21(7) pp. 075010.
- [159] Tang, Y., Bringa, E. M., and Meyers, M. A., 2012, "Ductile Tensile Failure in Metals through Initiation and Growth of Nanosized Voids," *Acta Mater.*, 60(12) pp. 4856-4865.
- [160] Tang, F., Cai, H., Bao, H., 2014, "Molecular Dynamics Simulations of Void Growth in γ -TiAl Single Crystal," *Comput. Mater. Sci.*, 84(1) pp. 232-237.

- [161] Shao, J., Wang, P., He, A., 2013, "Spall Strength of Aluminium Single Crystals Under High Strain Rates: Molecular Dynamics Study," *J. Appl. Phys.*, 114(17) pp. 173501.
- [162] Ruestes, C. J., Bringa, E. M., Stukowski, A., 2013, "Atomistic Simulation of the Mechanical Response of a Nanoporous Body-Centered Cubic Metal," *Scr. Mater.*, 68(10) pp. 817-820.
- [163] Meyers, M., Traiviratana, S., Lubarda, V. A., 2009, "The Role of Dislocations in the Growth of Nanosized Voids in Ductile Failure of Metals," *JOM*, 61(2) pp. 35-41.
- [164] Huang, Y., Zhang, F., Hwang, K. C., 2006, "A Model of Size Effects in Nano-Indentation," *J. Mech. Phys. Solids*, 54(8) pp. 1668-1686.
- [165] Page, T. F., Oliver, W. C., and McHargue, C. J., 1992, "Deformation Behavior of Ceramic Crystals Subjected to very Low Load (Nano)Indentations," *J. Mater. Res.*, 7(2) pp. 450-473.
- [166] Yu, D. Y. W., and Spaepen, F., 2004, "The Yield Strength of Thin Copper Films on Kapton," *J. Appl. Phys.*, 95(6) pp. 2991-2997.
- [167] J P Cuq-Lelandais and M Boustie and L Berthe and T de Ressaiguier and P Combis and J P Colombier and M Nivard and A Claverie, 2009, "Spallation Generated by Femtosecond Laser Driven Shocks in Thin Metallic Targets," *J. Phys. D: Appl. Phys.*, 42(6) pp. 065402.
- [168] Hodge, A. M., Biener, J., Hayes, J. R., 2007, "Scaling Equation for Yield Strength of Nanoporous Open-Cell Foams," *Acta Mater.*, 55(4) pp. 1343-1349.
- [169] Pia, G., and Delogu, F., 2015, "Coarsening of Nanoporous Au: Relationship between Structure and Mechanical Properties," *Acta Mater.*, 99(15) pp. 29-38.

- [170] Ruestes, C. J., Farkas, D., Caro, A., 2016, "Hardening Under Compression in Au Foams," *Acta Mater.*, 108(15) pp. 1-7.
- [171] Sun, X., Xu, G., Li, X., 2013, "Mechanical Properties and Scaling Laws of Nanoporous Gold," *J. Appl. Phys.*, 113(2) pp. 023505.
- [172] Roschning, B., and Huber, N., 2016, "Scaling Laws of Nanoporous Gold Under Uniaxial Compression: Effects of Structural Disorder on the Solid Fraction, Elastic Poisson's Ratio, Young's Modulus and Yield Strength," *J. Mech. Phys. Solids*, 92(1) pp. 55-71.
- [173] Mangipudi, K. R., Epler, E., and Volkert, C. A., 2016, "Topology-Dependent Scaling Laws for the Stiffness and Strength of Nanoporous Gold," *Acta Mater.*, 119(15) pp. 115-122.
- [174] Zhang, J., and Li, C. M., 2012, "Nanoporous Metals: Fabrication Strategies and Advanced Electrochemical Applications in Catalysis, Sensing and Energy Systems," *Chem. Soc. Rev.*, 41(21) pp. 7016-7031.
- [175] Kloke, A., von Stetten, F., Zengerle, R., 2011, "Strategies for the Fabrication of Porous Platinum Electrodes," *Adv. Mater.*, 23(43) pp. 4976-5008.
- [176] Velev, O. D., Tessier, P. M., Lenhoff, A. M., 1999, "Materials: A Class of Porous Metallic Nanostructures," *Nature*, 401(6753) pp. 548-548.
- [177] Braun, P. V., and Wiltzius, P., 1999, "Microporous Materials: Electrochemically Grown Photonic Crystals," *Nature*, 402(6762) pp. 603-604.
- [178] Yamauchi, Y., and Kuroda, K., 2008, "Rational Design of Mesoporous Metals and Related Nanomaterials by a Soft-Template Approach," *Chem. Asian. J.*, 3(4) pp. 664-676.

- [179] Jiang, P., Cizeron, J., Bertone, J. F., 1999, "Preparation of Macroporous Metal Films from Colloidal Crystals," *J. Am. Chem. Soc.*, 121(34) pp. 7957-7958.
- [180] Velev, O. D., and Kaler, E. W., 2000, "Structured Porous Materials Via Colloidal Crystal Templating: From Inorganic Oxides to Metals," *Adv. Mater.*, 12(7) pp. 531-534.
- [181] Stein, A., Li, F., and Denny, N. R., 2008, "Morphological Control in Colloidal Crystal Templating of Inverse Opals, Hierarchical Structures, and Shaped Particles," *Chem. Mater.*, 20(3) pp. 649-666.
- [182] Rechtsman, M. C., Stillinger, F. H., and Torquato, S., 2006, "Self-Assembly of the Simple Cubic Lattice with an Isotropic Potential," *Phys. Rev. E*, 74(2) pp. 021404.
- [183] Maldovan, M., and Thomas, E. L., 2004, "Diamond-Structured Photonic Crystals," *Nat. Mater.*, 3(9) pp. 593-600.
- [184] Zhang, Keys, A. S., Chen, T., 2005, "Self-Assembly of Patchy Particles into Diamond Structures through Molecular Mimicry," *Langmuir*, 21(25) pp. 11547-11551.
- [185] Balk, T. J., Eberl, C., Sun, Y., 2009, "Tensile and Compressive Microspecimen Testing of Bulk Nanoporous Gold," *JOM*, 61(12) pp. 26-31.
- [186] Biener, J., Hodge, A. M., Hamza, A. V., 2005, "Nanoporous Au: A High Yield Strength Material," *J. Appl. Phys.*, 97(2) pp. 024301.
- [187] Dou, R., and Derby, B., 2008, "The Strength of Gold Nanowire Forests," *Scr. Mater.*, 59(2) pp. 151-154.

- [188] Pia, G., and Delogu, F., 2015, "A Phenomenological Approach to Yield Strength in Nanoporous Metal Foams," *Scr. Mater.*, 103(1) pp. 26-29.
- [189] Fujita, T., Guan, P., McKenna, K., 2012, "Atomic Origins of the High Catalytic Activity of Nanoporous Gold," *Nat. Mater.*, 11(9) pp. 775-780.
- [190] Ngô, B. D., Stukowski, A., Mameka, N., 2015, "Anomalous Compliance and Early Yielding of Nanoporous Gold," *Acta Mater.*, 93(1) pp. 144-155.
- [191] Queheillalt, D. T., and Wadley, H. N. G., 2005, "Cellular Metal Lattices with Hollow Trusses," *Acta Mater.*, 53(2) pp. 303-313.
- [192] Cui, Y., and Chen, Z., 2017, "Void Initiation from Interfacial Debonding of Spherical Silicon Particles Inside a Silicon-Copper Nanocomposite: A Molecular Dynamics Study," *Modell. Simul. Mater. Sci. Eng.*, 25(2), pp. 025007.
- [193] Cai, W., Arsenlis, A., Weinberger, C. R., 2006, "A Non-Singular Continuum Theory of Dislocations," *J. Mech. Phys. Solids*, 54(3) pp. 561-587.
- [194] Taylor, G. I., 1934, "The Mechanism of Plastic Deformation of Crystals. Part I. Theoretical," *Proc. R. Soc. A: Math. Phys. Eng. Sci.*, 145(855) pp. 362-387.
- [195] Brown, L. M., 2012, "Constant Intermittent Flow of Dislocations: Central Problems in Plasticity," *Mater. Sci. Tech.*, 28(11) pp. 1209-1232.
- [196] Meyers, M.A., and Chawla, K.K., 2009, *Mechanical Behavior of Materials*, Cambridge University Press, Cambridge,.

[197] Mi, C., Buttry, D. A., Sharma, P., 2011, "Atomistic Insights into Dislocation-Based Mechanisms of Void Growth and Coalescence," *J. Mech. Phys. Solids*, 59(9) pp. 1858-1871.

[198] Fan, Y., Kushima, A., Yip, S., 2011, "Mechanism of Void Nucleation and Growth in Bcc Fe: Atomistic Simulations at Experimental Time Scales," *Phys. Rev. Lett.*, 106(12) pp. 125501.

Appendix A: The Relative Displacement

1. The Uniaxial Strain Case

In this appendix, the “relatively farthest-travelled atoms” will be defined. The simulation box being stretched as shown in Figure A.1 is with strain-confined lateral boundaries. The material transport described by the current and initial frames for the homogeneous elastic solution is given as

$$x' = \frac{l_1}{l_0} x, \quad y' = y, \quad z' = z \quad (\text{A1})$$

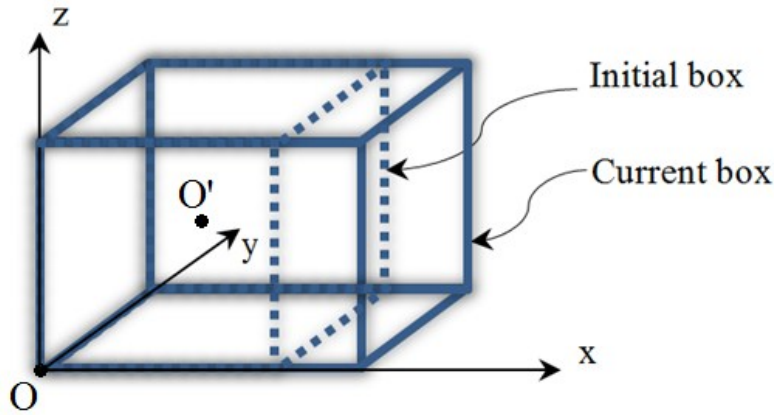


Figure A.1. Schematic of the simulation box under uniaxial stretching

Here the current configuration is denoted by the Cartesian coordinates (x', y', z') , while the initial configuration is denoted by the Cartesian coordinates (x, y, z) . The box length in the x direction is increased from l_0 to l_1 , while the box lengths in the lateral directions are fixed. Equation (A1) automatically satisfies the stress equilibrium equation and the boundary constraints under an imaginary void-free condition. The corresponding elastic solution with a

central void inside will certainly be different. However, the difference is found insignificant once away from the void surface as shown in Figure 5.8e. Now we denote the current configuration of the atoms dumped by LAMMPS as (x'', y'', z'') and the initial configuration as (x, y, z) . The magnitude of the “relative displacement” of any individual atom could be defined as the deviation from its homogeneous elastic displacement as

$$d = \sqrt{\left(x'' - \frac{l_1}{l_{10}}x\right)^2 + (y'' - y)^2 + (z'' - z)^2} \quad (\text{A2})$$

A notable feature of Eq. (A2) is that this relative displacement d does not depend on the origin of the coordinates. The dumped file of LAMMPS sets this origin at the corner of the simulation box. To calculate the “absolute” atomic displacement as in Figure 5.3a, the coordinates (x'', y'', z'') are converted with respect to the box center O' as shown in Figure A.1. However, the magnitude of the “relative displacement” under this new origin O' is still unchanged since

$$d' = \sqrt{\left[\left(x'' - \frac{l_1}{2}\right) - \frac{l_1}{l_{10}}\left(x - \frac{l_{10}}{2}\right)\right]^2 + \left[\left(y'' - \frac{l_2}{2}\right) - \left(y - \frac{l_2}{2}\right)\right]^2 + \left[\left(z'' - \frac{l_3}{2}\right) - \left(z - \frac{l_3}{2}\right)\right]^2} = d \quad (\text{A3})$$

As implied by Eq. (A3), any origin as long as attached on the simulation box will result in the same “relative displacement”. The IDs of the atoms are employed to relate the current configuration to the initial configuration. Thus, the “relatively farthest-travelled atoms” are identified once their “relative displacement” (magnitude) are bigger than the critical length d_{crit} . In this way, the set of the “relatively farthest-travelled atoms” can be identified by their IDs as

$$\Phi_{ID} = \{ID | d(ID) \geq d_{crit}\} \quad (\text{A4})$$

2. The Uniaxial Stress Case

Above is for the uniaxial-strain case. As for the uniaxial-stress case, Eq. (A1) should be replaced with

$$x' = \left(1 + \frac{\sigma_x}{E}\right)x, \quad y' = \left(1 - \frac{\nu\sigma_x}{E}\right)y, \quad z' = \left(1 - \frac{\nu\sigma_x}{E}\right)z \quad (\text{A5})$$

Here σ_x is the normal stress component in the x direction, E is the Young's modulus and ν is the Poisson ratio. Due to the fact that it is the box dimensions rather than the stresses are directly dumped at each time step, this homogeneous deformation could be expressed more conveniently as

$$x' = \frac{l_1}{l_{10}}x, \quad y' = \frac{l_2}{l_{20}}y, \quad z' = \frac{l_3}{l_{30}}z \quad (\text{A6})$$

The x-direction length is increased from l_{10} to l_1 while the y-direction and z-direction lengths shrink from l_{20} and l_{30} to l_2 and l_3 . Hence, the magnitude of relative displacement of any individual atom becomes

$$d = \sqrt{\left(x'' - \frac{l_1}{l_{10}}x\right)^2 + \left(y'' - \frac{l_2}{l_{20}}y\right)^2 + \left(z'' - \frac{l_3}{l_{30}}z\right)^2} \quad (\text{A7})$$

Again, any origin as long as attached on the simulation box will make no difference to the magnitude of this relative displacement. In a continuum view, the strain corresponding to the relative displacement is the one whose trace excludes the dilatation of the simulation box. The relative displacement is a compromise to avoid taking derivative of the displacement field containing strong discontinuity.

Appendix B: List of Publications during PhD thesis work

Journal Publications

Yi Cui, Zengtao Chen. “Simulation of mechanical response of nanoporous FCC copper under compression with pores mimicking some crystalline arrays”, *Journal of Applied Physics*, 2017 (under revision)

Yi Cui, Zengtao Chen. “Void growth via atomistic simulation: will the formation of shear loops still grow a void under different thermo-mechanical constraints?”, *Philosophical Magazine*, 2017 (under revision)

A. H. Akbarzadeh, **Y. Cui**, Z. T. Chen, “Multiscale simulation of thermal wave: From non-local continuum to molecular dynamics”, *RSC advance*, 25 (2017) 1-11

Yi Cui, Zengtao Chen. “Void initiation from interfacial debonding of spherical silicon particles inside a silicon-copper nanocomposite: A molecular dynamics study”, *Modelling and Simulation in Materials Science and Engineering* 25 (2017) 1-11

Yi Cui, Zengtao Chen. “Material transport via the emission of shear loops during void growth: a molecular dynamics study”, *Journal of Applied Physics*, 119 (2016) 225102

Yunmei Zhao, Xin Gong, **Yi Cui**, Shurong Ding "Simulation of the fission-induced swelling and creep in the CERCER fuel pellets", *Materials & Design*, 89 (2016) 183-195

Yi Cui, Zengtao Chen. “Molecular dynamics modeling on the role of initial void geometry in a thin aluminum film under uniaxial tension”, *Modelling and Simulation in Materials Science and Engineering* 23 (2015) 085011

Yi Cui, Zengtao Chen. “Molecular dynamics simulation of the influence of elliptical void interaction on the tensile behavior of aluminum”, *Computational Materials Science*, 108 (2015) 103-113

Yi Cui, Shurong Ding, Zengtao Chen, Yongzhong Huo “Modifications and applications of the mechanistic gaseous swelling model for UMo fuel”, *Journal of Nuclear Materials*, 457 (2015) 157-164

Conference Publications

Yi Cui, Zengtao Chen (2017), “Nanovoid growth under different mechanical and thermal constraints”, The 29th Canadian Materials Science Conference, Ottawa, Ontario, Canada. June 20-23 (only abstract and presentation)

Yi Cui, Zengtao Chen (2017), “Shear feasibility: new theoretical understanding regarding the growth of nanovoid”, The 26th Canadian Congress on Applied Mechanics, Victoria, British Columbia, Canada. May 29-June 1 (Best sessional presentation award)

Yi Cui, Zengtao Chen (2016), “Molecular dynamics study of the interfacial debonding due to cylindrical nano-inclusion”, The 24th International Congress of Theoretical and Applied Mechanics, Montreal, Quebec, Canada. August 21-26

Yi Cui, Zengtao Chen (2016), “Molecular dynamics insights into the coalescence of closely-packed voids”, The 24th International Congress on Theoretical and Applied Mechanics, Montreal, Quebec, Canada. August 21-26

K. Niu, **Y. Cui**, Z. T. Chen, (2015) "Experimental investigation and micromechanical modeling of hot-rolled steels considering the effects of Micro-voids." The 2015 AUTO21 Scientific Conference, Ottawa, Ontario, Canada. May 26-27